THE UNIVERSITY *of* EDINBURGH

Isolating the impact of North American and European anthropogenic aerosol emissions since the early Instrumental Period

Sabine Undorf

Doctor of Philosophy

The University of Edinburgh

2018

Abstract

Anthropogenic aerosols have been identified as an important driver of global and regional climate. Globally, aerosols are estimated to have offset much of the positive forcing due to greenhouse gases; regionally, their effect can be dominating, and can potentially drive climate anomalies far from the emission sources due to changes in the atmospheric circulation. Aerosols emitted from North America (NA) and Europe (EU) dominated the global aerosol loading until the late twentieth century. Despite recent progress, our knowledge of the climate imprint of NA and EU aerosols is still incomplete, especially regarding the decades before the mid-twentieth century, in which emissions were still lower and did not yet change as rapidly as later, but might have been more effective due to non-linearities in the aerosol-cloud interactions. The overarching goal of this work is thus to determine robust features of the impact of NA and EU aerosols on regional and large-scale climate and to advance current understanding of the underlying mechanisms, compared to those generated by other forcing agents as well as aerosols from other geographical regions. The study focuses mainly on the period of increasing sulphur dioxide (SO_2) emissions -precursor of sulphate aerosols, the most abundant anthropogenic aerosol species- from NA and EU sources (1850-1975), and on identifying the aerosol impact over the Atlantic and Eurasian domain, where North American and European aerosols are presumed to have relevant impact. Along with observations, existing historical simulations from a range of coupled climate models are studied and complementary experiments performed and analysed.

First, the boreal summer climate response to North American and European (NAEU) anthropogenic aerosol emissions during the twentieth century is characterised using a suite of models from the Coupled Model Inter-Comparison Project 5 (CMIP5). Supported by the co-variability of aerosol optical depth and near-surface climate, long-term variations in aerosol-only and all-forcing simulations are attributed to NAEU aerosol forcing if they undergo a significant reversal coinciding with the peak in NAEU SO_2 emissions, measured by inter-model agreement on the sign of linear trends before and after 1975. Regionally, robust aerosol impact is found on Eurasian near-surface temperature, pressure, and diurnal temperature range; remotely, robust aerosol impact is found on the Inter-Tropical Convergence Zone (ITCZ) position and the subtropical jet stream. The contribution of anthropogenic aerosol forcing to the forced component of simulated inter-decadal climate variability of European-mean near-surface temperature is furthermore estimated to be more than a third throughout the twentieth century. Observed variations also of European-mean sea level pressure and diurnal temperature range tend to agree better with simulations that include aerosols. These findings highlight significant aerosol impact on Eurasian climate already in the first half of the twentieth century.

The aerosol impact on observed West African and South Asian monsoon precipitation is then investigated by using a detection and attribution (D&A) approach. The aerosol source regions (NAEU, South Asia, or China) which are most important for explaining the observed 1920-2005 changes are identified. For this, fingerprints of the response to regional-aerosol forcing are derived from historical simulations with the GFDL-CM3 model along with CMIP5 simulations. It is found that in precipitation observations for West Africa, the only anthropogenic forcing which can be detected are NAEU emissions. In precipitation observations for South Asia, in contrast, local emissions are the only external forcing detected. Changes in West Africa are related to a meridional shift in the ITCZ due to aerosol-induced changes in the inter-hemispheric temperature gradient. Changes in South Asia, in contrast, are associated with a weakening of the monsoon circulation, driven by the increase of remote NAEU aerosol emissions until 1975 and since then by the increase in local emissions offsetting the

decrease in NAEU emissions. These findings show for the first time that the aerosol forcing from individual emission regions is strong and distinct enough to be detected in the presence of internal variability.

Finally, the dynamical impact of NA and EU sulphate aerosol emissions is fully analysed in the coupled Community Earth System model (CESM1-CAM5), focusing on the Atlantic. For this, multi-member ensemble simulations covering the period 1850-1975 are performed, and the response to emissions from NA and EU is contrasted. The results show that sulphate aerosols from either source cause a long-term cooling of North Atlantic sea-surface temperatures (SSTs), with the patterns a combination of atmospheric aerosol effects and an aerosol-induced strengthening of the Atlantic Meridional Overturning Circulation (AMOC). The North Atlantic response to NA emissions is larger than that to EU emissions, with stronger indirect aerosol effects due to a wider aerosol spread over the Atlantic and collocation with climatological cloud cover. A southward shift of the ITCZ, affecting tropical precipitation globally, is also found. The (multi)decadal variability components of Atlantic SSTs and of the AMOC are furthermore both found to be externally forced. A suppression of Atlantic Tropical Hurricane frequency and a north-eastward shift of Atlantic extra-tropical storms in response to both NA and EU emissions are finally shown. The analysis provides novel insights into the mechanisms of aerosol impact on the Atlantic.

Overall, the results from this work represent a significant contribution to advance our understanding of the historical impact of anthropogenic aerosols over the entire twentieth century and in particular that of aerosols from NA and EU by finding robust signals across models, using statistically rigorous methods to detect forced impact in observations, and analysing new model experiments. The findings emphasise the importance of historical anthropogenic aerosol emissions already before the late twentieth century and shed light on differences in the climate response to aerosols depending on their emission region, which will also be relevant for understanding future patterns of change related to further emission reductions.

Lay Summary

Atmospheric aerosols are little particles in the lower atmosphere which can influence climate by interacting with solar radiation and clouds. While some aerosols are emitted by natural sources (e.g. sea salt, dust), others are mainly emitted by human, e.g. industrial, activity. It is known that these anthropogenic aerosols had impact on our climate especially since the industrialisation, but many details are still very uncertain.

This work aims to identify the impact of anthropogenic aerosol emissions from North America and Europe since the mid-nineteenth century. The focus in on sulphate aerosols, which North America and Europe emitted most of until recently. The study uses historical climate observations and a range of simulations with global climate models. The simulations are based on a physical representation of the climate system and estimates of historical anthropogenic factors (greenhouse gases, anthropogenic aerosols) and natural factors (volcanic aerosols, solar variability).

It is found that sulphate aerosols from North America and Europe had a substantial effect on simulated near-surface summer climate over Europe, Asia, and North Africa during their 1850-1975 increase and their subsequent decrease in the models. A comparison with climate observations confirms further the importance of aerosols also for more short-term climate variations over Europe. The models also show sulphate aerosol impact on monsoon rainfall over West Africa and South Asia, which is then further investigated. It is found that aerosol emissions from North America and Europe are the only anthropogenic influence which can be statistically detected in historical monsoon rainfall observations from West Africa, and that the changes are part of a large-scale tropical rainfall shift due to aerosol-induced temperature changes

between the northern and southern hemisphere. For South Asia, in contrast, the only statistically detectable external influence are South Asian aerosol emissions, and the changes there are associated with weakened monsoon winds. Finally analysing the separate impacts of sulphate aerosols from North America and Europe, respectively, on the Atlantic ocean, it is found that in the model analysed, sulphate aerosols from both regions caused a decrease in Atlantic temperatures, and caused large ocean currents to bring in turn more heat into the North Atlantic. Sulphate aerosols from North America caused larger changes than those from Europe, but emissions from both regions made Tropical Hurricanes over the Atlantic less likely and impacted the likelihood of different storm paths over Europe in the model.

The results from this work advance our understanding of the historical climate impact of aerosols in general and that of those from North America and Europe in particular, and emphasise their importance already before the late twentieth century, when their negative impact on air quality in North America and Europe led to policy changes. The results are also relevant for assessing the future impact of further aerosol emission reductions, which will impact ecosystems and livelihoods.

Acknowledgements

My primary thanks go to Massimo and Gabi for inviting me to Edinburgh and guiding me all the way through my PhD. I thank Massimo especially for enthusiasm for scientific discussion and for always finding time for me. I thank Gabi especially for guidance and generous support. I thank both of them as well as Simon and the other Titans for sharing their expertise with me. I also thank all of Gabi's and Simon's past and present PostDocs for support and fun, and my fellow PhD students for great company. Thanks to my family and friends both here and abroad go without saying.

For the model data, I thank the World Climate Research Program's Working Group on Coupled Modelling, the climate modelling groups (Tab. 1.1), the U.S. Department of Energy's Program for Climate Model Diagnosis and Inter-comparison and the Global Organisation for Earth System Science Portals. The CESM project is supported by the National Science Foundation and the Office of Science (BER) of the U.S. Department of Energy. I also acknowledge use of the ARCHER UK National Supercomputing Service. I further acknowledge the use of observational data from the Met Office Hadley Centre, the Climatic Research Unit at the University of East Anglia, Berkeley Earth, the NASA Goddard Institute for Space Studies, the National Oceanic and Atmospheric Administration, and the Global Precipitation Climatology Centre.

All CMIP5 and observational data used in this study are publicly available and properly cited and referred to in the reference list. The precipitation data from the GFDL-CM3 experiments used in Chapter 3 are available at `https://doi.org/10.6084/m9.figshare.5777907`, and other fields from those experiments are available upon request from Massimo Bollasina (massimo.bollasina@ed.ac.uk). The CESM1-CAM5

experiments generated for and analysed in Chapter 4 will also be made available in the future. The research was funded by the University of Edinburgh and Gabi Heger's TITAN project granted by European Research Council (EC-320691).

Declaration

I declare that this thesis has been composed by myself and that the work has not been submitted for any other degree or professional qualification. I confirm that the work submitted is my own, except where work which has formed part of jointly-authored publications has been included. My contribution and those of the other authors to that work have been explicitly indicated below. I confirm that appropriate credit has been given within this thesis where reference has been made to the work of others.

Chapter 2 is adapted from a published paper on which I am the first author, and Massimo Bollasina (first supervisor) and Gabi Hegerl (second supervisor) (both School of GeoSciences, University of Edinburgh) are co-authors: Undorf, S., M. A. Bollasina, and G. C. Hegerl (2018a), Impacts of the 1900-1974 increase in anthropogenic aerosol emissions from North America and Europe on Eurasian summer climate, *J. Clim.*, doi: 10.1175/JCLI-D-17-0850.1. I performed the data analysis and wrote the manuscript; Massimo Bollasina edited the manuscript, and he and Gabi Hegerl provided scientific advice, proofread the manuscript, and gave feedback. Sections 2.A and 2.C are not part of the published article.

Chapter 3 is adapted from a published paper on which I am the first author, and Debbie Polson (School of GeoSciences, University of Edinburgh), Massimo Bollasina, Yi Ming (NOAA Geophysical Fluid Dynamics Laboratory, Princeton), Andrew Schurer (School of GeoSciences, University of Edinburgh), and Gabi Hegerl are co-authors: Undorf, S., D. Polson, M. Bollasina, Y. Ming, A. Schurer, and G. C. Hegerl (2018b), Detectable impact of local and remote anthropogenic aerosols on the 20th century changes of West African and South Asian monsoon precipitation, *J. Geophys. Res. Atmos.*, *123*,

4871–4889, doi: 10.1029/2017JD027711. Previous work by Debbie Polson (DP) was incorporated into the article (see below). Massimo Bollasina computed the radiative forcing which I show in Figs. B.5 and B.6 and edited the manuscript, and he and Gabi Hegerl provided scientific advice, proofread the manuscript, and gave feedback. Yi Ming provided the data from the GFDL simulations. Andrew Schurer provided the detection and attribution code, contributed through scientific discussion of the interpretation of the detection and attribution results, and proofread Sections 3.2.3, 3.3.3, and 3.5.

In detail, DP's unpublished work had very similar figures to those showing precipitation trends (Figs. 3.1, 3.2, B.8, B.9), area-mean precipitation time series (Figs. B.3, 3.3, 3.4), and 1-signal detection and attribution results (Figs. 3.5, B.17), and also a more basic version of Fig. 3.6 showing the time series of latitudinal ITCZ position. I have reproduced the underlying analysis independently to create the figures shown in this thesis. Based on this analysis of precipitation data only, I have then performed an extensive analysis of the pathways by which the identified aerosol impact is caused in the simulations, using a variety of additional variables (Figs. 3.7-3.9 and B.5, B.6, and B.21-B.26). I have furthermore extended the detection and attribution study to a 2-signal analysis in order to support the interpretation of the 1-signal results (Figs. B.17-B.20). I have demonstrated the validity of the assumptions made (B.2, B.7) and shown how precipitation and circulation in the coupled experiments compare to fixed-SST experiments and reanalysis (Fig. B.27) in addition to more analysis of other aspects (e.g. Fig. B.13). I have furthermore created numerous side figures and figure elements to explain the simulations (Figs. B.1, B.4), estimate the simulated aerosol impact given simultaneous other forcings (e.g. Fig. B.13), and better visualise the results (parts of Fig. 3.6 and B.10-B.12 as well as B.14 and B.16). I wrote Section 3.4 from scratch, and have rewritten the other sections substantially in order to be clearer and to incorporate the new findings.

Chapter 4 is adapted from a paper submitted to a peer-reviewed journal on which I am the first author, and Massimo Bollasina, Ben Booth (Met Office Hadley Centre, Exeter), and Gabi Hegerl are co-authors: Undorf, S., M. A. Bollasina, B. B. B.

Booth, and G. C. Hegerl, Contrasting the effects of the 1850-1975 increase in sulphate aerosols from North America and Europe on the Atlantic in the CESM model, under review in *Geophysical Research Letters*. I set the model simulations up, ran the model, performed the data analysis, and wrote the manuscript. All co-authors provided scientific advice, gave feedback, and proofread the manuscript. Massimo Bollasina computed the lead-lag correlations I show in Fig. 4.6. Technical information on the simulations (Section 4.A) and additional results (Section 4.B) are not part of the submitted manuscript. Some material, in particular Figs. 4.2, 4.4, 4.6, and 4.8, has furthermore been moved from the supplementary material of the submitted manuscript into the main body of this thesis.

For Chapters 2, 3, and 4, the corresponding manuscripts have been modified to avoid repetition and to improve coherence.

The other parts of this thesis were proofread by Massimo Bollasina and/or Gabi Hegerl and feedback given.

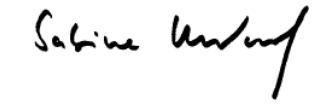

19th January 2019

Contents

List of Figures

List of Tables

Chapter 1

Introduction and Background

1.1 Motivation

Anthropogenic aerosols can drive changes in global and regional climate by impacting both the energy and water cycles. Despite intense research efforts, however, they have remained the dominant contributor to the uncertainty in total anthropogenic forcing over the industrial era in the last three IPCC reports (*IPCC*, 2013). This also hinders our ability to estimate the greenhouse gas (GHG) contribution to global temperature change (e.g., *Hegerl et al.*, 1997; *Gillett and Fyfe*, 2013) and thus climate sensitivity (e.g., *Forster et al.*, 2013; *Storelvmo et al.*, 2016) and hence increases uncertainty in predictions. The uncertainty associated with regional aerosol impact, the magnitude of which can be a multiple of their global-mean measures (*Boucher et al.*, 2013), is furthermore alarming because it includes circulation changes with the potential for high impacts on ecosystems and human populations (e.g., *Bollasina et al.*, 2011; *Dong et al.*, 2014a). Since the decline of global aerosol emissions as projected for the next decades (*Clarke et al.*, 2014) is expected to reverse some of the changes introduced by their previous increase (e.g., *Rotstayn*, 2013; *Acosta Navarro et al.*, 2016), an improved understanding of the historical aerosol impact is vital for both mid- and long-term climate projections.

1.2 Background

1.2.1 Atmospheric Aerosols

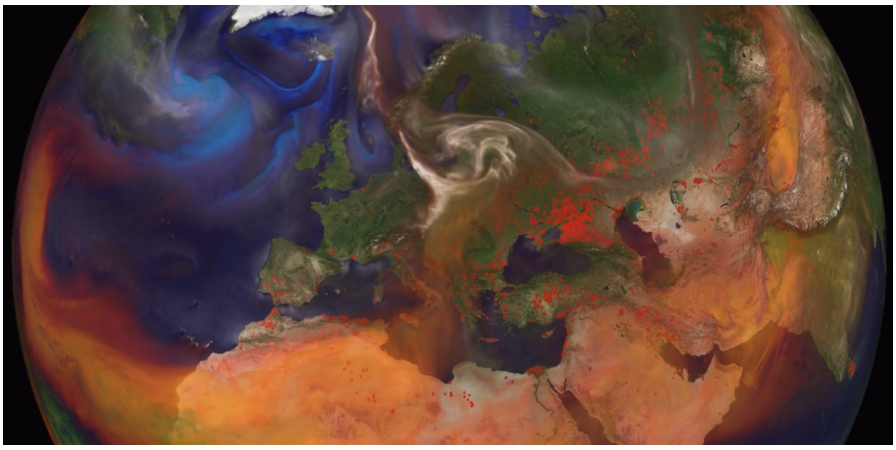

Figure 1.1: Atmospheric aerosols: A snapshot of an arbitrary day/time between May 2005 and May 2007 of *NASA/Goddard Space Flight Center* (2007)'s visualisation of the distribution of (white) sulphate, (green) black and organic carbon, (red) dust, and (blue) sea salt aerosols based on simulations with the GEOS-5 Atmospheric Model on the Cubed-Sphere and the Goddard Chemistry Aerosol and Transport (GOCART) as well as (orange dots) biomass burning from Terra and Aqua/MODIS data.

A range of different aerosols -suspensions of particulate matter[1]- are found commonly in our atmosphere due to various land-ocean-surface processes (Fig. 1.1). Prominent are sulphate aerosols, which are emitted into the stratosphere from volcanic eruptions, but also into the troposphere naturally from marine emissions of Dimethyl sulfide (DMS) (*Penner et al.*, 2001). Other natural aerosols include sea salt and dust which get mixed into the troposphere over oceans and deserts, respectively (*Prather et al.*, 2008), and organic carbon (OC) is emitted by plant transpiration and especially by biomass burning; if burnt incompletely, the latter also emits black carbon (BC), which denotes different compounds including soot (*Buseck et al.*, 2012).

[1]Technically, "aerosol" is the word for the mixture (colloid) of the particles or droplets in air. In this thesis, I will talk of the effect of "aerosols" to mean the effect of the emitted substances including the chemical and physical processes they undergo in the atmosphere, as is common in the literature (*Salby*, 2012; *Boucher et al.*, 2013). I refer to sulphate aerosols as SO_4 as in *Taylor et al.* (2012).

Once in the atmosphere, the aerosol particles can interact with water vapour and with each other, forming particles of different size (*Salby*, 2012). After residence times of a few days, they are removed from the atmosphere by dry or wet deposition (precipitation) (*Hanrahan*, 2012). The amount of aerosols in the atmosphere at any time can be characterised by their mass concentration or using optical properties, e.g. aerosol optical depth (AOD). AOD is the hypothetical optical depth of the atmospheric column if filled with the aerosol particles, where optical depth (τ, dimensionless) is a material's physical parameter determining the fraction of incoming radiation that is transmitted when passing the material; if ϕ_{trans} and ϕ_{in} denote the incoming and transmitted radiant fluxes, respectively, it is $\phi_{trans}/\phi_{in} = exp(-\tau)$ (Lambert-Beer law). AOD, a function of radiation wavelength, is commonly given at 550 nm (e.g., *Taylor et al.*, 2012). Measurements from satellites and field campaigns can inform on contemporary aerosol distributions (*CCSP*, 2009; *McNeill*, 2017), but aerosol distributions before the mid-twentieth century are usually estimated from emission inventories.

1.2.2 History of Anthropogenic Aerosol Emissions

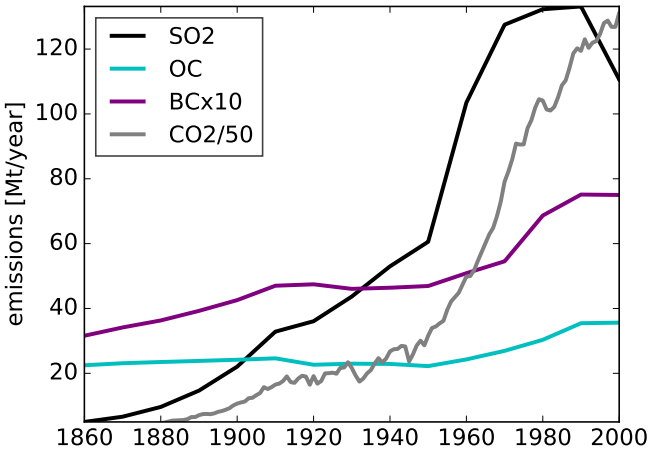

Figure 1.2: Atmospheric aerosols: Global sum of emissions of annual-mean emissions of the sulphate aerosol precursor SO_2, organic (OC) and black (BC) carbon, and carbon dioxide (CO_2)as the single most relevant anthropogenically emitted greenhouse gas. Note that BC and CO_2 data are scaled by a factor of 10 and 1/50, respectively, for better visibility. Data and estimates from (aerosols) *Lamarque et al.* (2010) and (CO_2) *Boden et al.* (2010).

An increase in aerosol emissions has been caused by human activity, through land use changes and industry. These anthropogenic aerosols include sulphate aerosols -apart from a low percentage being emitted directly, they mainly originate from industrial sulphur dioxide (SO_2) emissions- as well as carbonaceous aerosols (OC and BC) from biomass burning and fossil fuel combustion (*Lamarque et al.*, 2010; *Hoesly et al.*, 2018). While anthropogenic emissions of all aerosol species are now substantially larger than those at pre-industrial times, their evolution over the last 150 years has not been linear nor the same between species. While SO_2 emissions in particular have increased substantially, they are distinct in increasing earlier and peaking in the second half of the century (Fig. 1.2). Regional differences in emission histories (within a species) are additionally relevant in shaping the aerosol climate signal due to the spatially heterogeneous forcing patterns resulting from the short residence times of aerosols in the atmosphere.

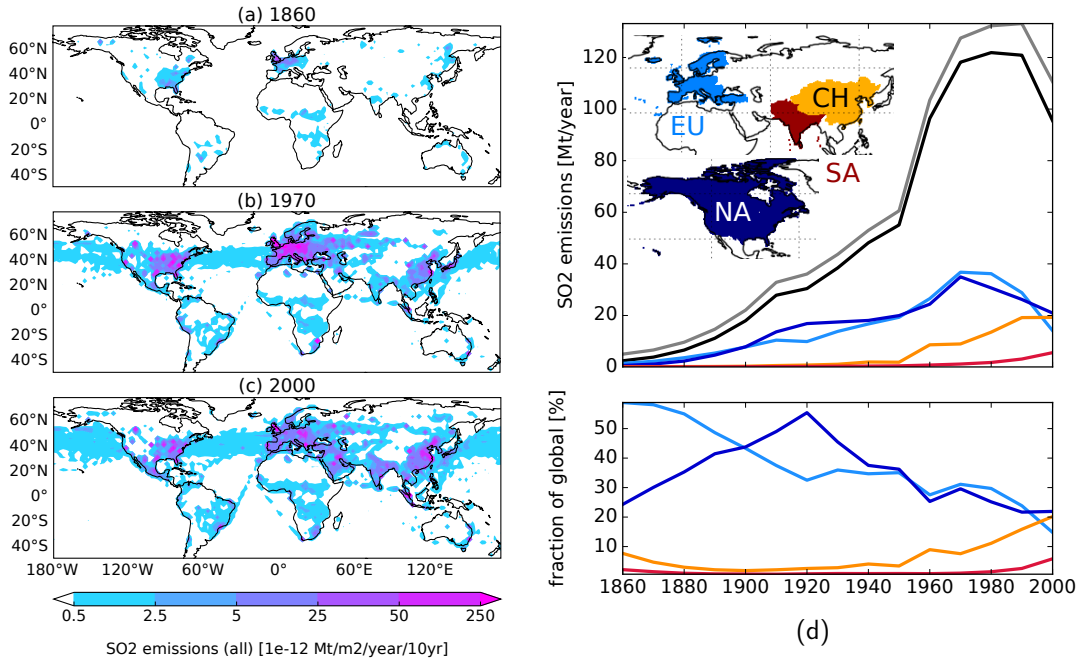

Figure 1.3: SO_2 emission history: (a-c) Emissions for the (a) 1860s, (b) 1970s, and (c) 2000s from all sectors (anthropogenic sources, biomass burning, and shipping) and (d) global-mean emissions from (grey) all sectors, (black) anthropogenic sources only, and from anthropogenic sources in (light blue) Europe, (dark blue) North America, (yellow) China, and (red) South Asia as sketched in the figure. Annual means are calculated before the analysis. Data and estimates from (*Lamarque et al.*, 2010).

This time evolution of global SO_2 emissions results mainly from a combination of changes over two macroregions, namely North America and Europe (NAEU) and Asia (Fig. 1.3). Although emissions from North America (NA) increased more in the 1920s and peaked slightly earlier than emissions from Europe (EU), they both increased steadily from pre-industrial times to the peak in the 1970s, when air quality legislation started to decouple industrial activity from aerosol emissions and led to their reduction. While dominating global emissions until the late twentieth century, the relative contribution from NAEU emissions decreased also due to increasing emissions elsewhere; Asian emissions, in particular, started to increase in the 1950s as a result of rapid economic development and kept increasing throughout the century (*Lamarque et al.*, 2010; *Hoesly et al.*, 2018).

1.2.3 Aerosol Effects on Climate

Atmospheric aerosols can impact climate by interacting with radiation and with clouds (Fig. 1.4). The aerosol-radiation interactions (ARIs) consist of the direct effect (*Charlson et al.*, 1992) of scattering or absorbing solar radiation as well as associated rapid adjustments, which include the response to altered surface energy budgets and atmospheric temperature profiles due to the direct effect (*Boucher et al.*, 2013). Black carbon, for instance, cools the surface while heating the atmosphere, which increases vertical stability and can cause cloud evaporation (the semi-direct effect; *IPCC*, 2007).

The aerosol-cloud interactions (ACIs) consist of a cloud albedo increase due to aerosols acting as cloud condensation and ice nuclei (CCN) leading to smaller cloud droplets (first indirect effect; *Twomey*, 1977), the associated cloud lifetime increase by precipitation suppression (second indirect effect; *Albrecht*, 1989), and other rapid adjustments. Non-linearities in these ACIs -in CCN number as a function of aerosol emissions, in cloud droplet concentration as a function of CCN number, and in cloud albedo as a function of cloud drop concentrations- can cause the aerosol impact to depend on the background concentration (*Carslaw et al.*, 2013; *Wilcox et al.*, 2015).

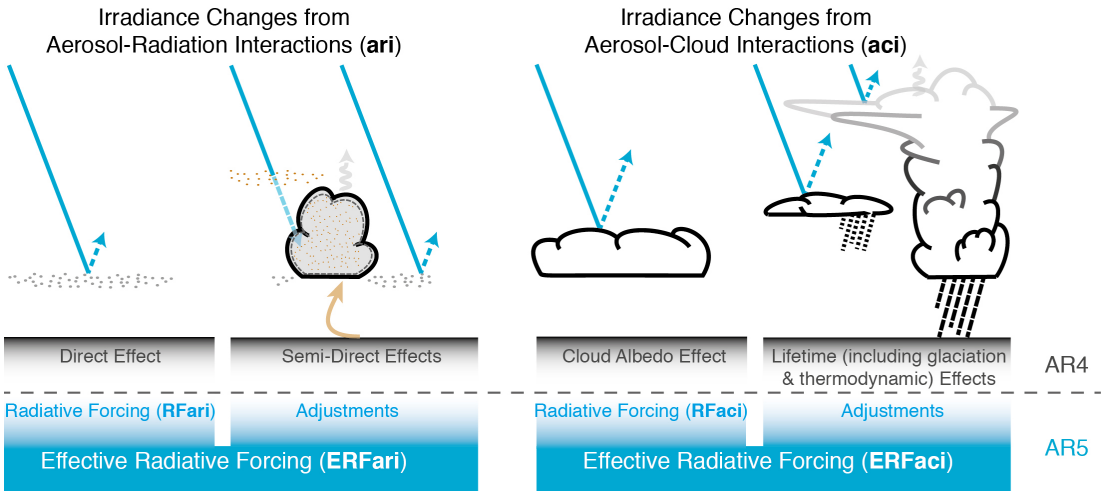

Figure 1.4: Aerosol effects on climate: (Left) aerosol-radiation and (right) aerosol–cloud interactions involving (blue arrows) solar radiation, (grey arrows) terrestrial radiation, and (brown arrow) surface-cloud layer coupling. The black and blue labels refer to the terminology used in the Forth (AR4) and Fifth (AR5), respectively, Assessment Report of the Intergovernmental Panel on Climate Change (*IPCC*, 2007, 2013). Figure taken from *Boucher et al.* (2013).

A measure allowing comparison of the global-mean climate impact of aerosols with that of other forcing agents is their effective radiative forcing (ERF). ERF is the net change on the Earth system's energy balance after allowing for rapid adjustments in atmospheric temperature, water vapour, and clouds, but excluding any temperature-mediated feedbacks (Fig. 1.5; *Myhre et al.*, 2013; *Forster et al.*, 2016). Aerosol-radiation and aerosol-cloud interactions together have been estimated to exert an ERF of -0.9 W/m^2 (-1.9 to -0.1 W/m^2 at the 90% confidence level) compared to the total anthropogenic ERF of 2.29 W/m^2 (1.13 to 3.33 W/m^2) in present-day (2011) climate compared to pre-industrial (1750) times (*Boucher et al.*, 2013). Natural aerosols of volcanic origin, in contrast, have a longer residence time in the stratosphere but occur only episodically, resulting in large, but short-term forcing. Anthropogenic aerosols are thus estimated to be the agent with the second-largest forcing besides GHGs in present-day climate, with their ratio to GHG forcing even higher earlier in the twentieth and in the nineteenth century (Fig. 1.5).

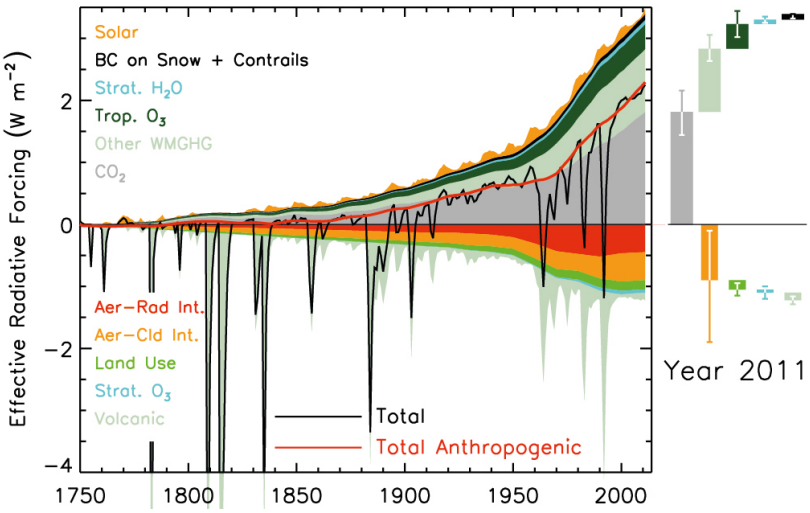

Figure 1.5: Effective radiative forcing (ERF) (in W/m^2) for natural and anthropogenic forcing agents in 2011 compared to 1750, including (red, bottom) aerosol-radiation interactions and (yellow, bottom) aerosol-cloud interactions. Also shown are the ERFs for (yellow, top) solar irradiance changes, (black, top) black carbon on snow and contrails, (blue, top) stratospheric water vapour, (dark green, top) tropospheric ozone, (grey, top) CO_2, and (green, top) other well-mixed GHGs, and (green, bottom) land use changes, (blue, bottom) stratospheric ozone, and (green, bottom) volcanic aerosols. The forcings and their uncertainties (5 to 95 % confidence level) for the year 2011 are shown to the right. Figure from *Myhre et al.* (2013).

1.2.4 Implementation of Aerosol Effects in Climate Models

Even larger than the anthropogenic aerosols' contribution to our best estimate of ERF is their contribution to its uncertainty (Fig. 1.5, right). This is largely due to limitations in our understanding, and difficulties in the model representation, of the complex aerosol-cloud interactions (*Stevens and Feingold*, 2009; *Zelinka et al.*, 2014) as well as of cloud feedbacks in general (*Boucher et al.*, 2013). Additional uncertainties in quantifying the historical aerosol impact originate from uncertainties in pre-industrial aerosol concentrations (e.g., *Carslaw et al.*, 2013) and historical aerosol emissions (e.g., *Bond et al.*, 2007; *Lamarque et al.*, 2010; *Granier et al.*, 2011; *Hoesly et al.*, 2018). But even when emissions are prescribed, global climate models of the same generation produce vastly different aerosol forcing both globally and in terms of the spatial pattern (*Taylor et al.*, 2012; *Boucher et al.*, 2013; *Myhre et al.*, 2013). Reasons for this are meteorological and chemical model differences which

cause different aerosol distribution patterns, for example in terms of how far they are transported (*Wilcox et al.*, 2015), but also, crucially, different parametrisations of aerosol effects.

Some models still neglect aerosol indirect effects altogether, but even those with the more comprehensive representations (most in Tab. 1.1) vary substantially (*Ekman*, 2014): In GFDL-CM3 and NorESM1-M, aerosol micro-physics and chemistry including cloud droplet number concentration (CDNC; first indirect effect) are simulated online, and precipitation formation depends on this CDNC (second indirect effect). Other models also have online aerosol schemes, but use diagnostic CDNC formulations, on which precipitation does (CSIRO-Mk3.6.0, HadGEM2-ES) or does not (CanESM2) depend. Yet other models prescribe aerosol fields from offline calculations and use diagnostic CDNC representations, on which precipitation does (GISS-E2-R) or does not (IPSL-CM5A-LR) depend. On top of these differences, the chemistry models used and/or the way of the diagnostic derivation of CDNC may vary as well.

Table 1.1: CMIP5 models used in this work and whether they include any representation of the first and second indirect aerosol effects (x: yes, -: no). The listed ensemble size is used for the all-forcing experiment and for each single-forcing experiment (except *) only 2 members for the GHG-only experiment). The models with the number typed in regular font are used in Chapter 2, those in italic used in Chapter 3, and those in bold used in both. An overview of the experiment design is given in *Taylor et al.* (2012).

Institute ID	Model Name	ens. size	aerosol indirect effects		Reference
			1st	2nd	
CCCMA	CanESM2	5	x	-	*von Salzen et al.* (2013)
CSIRO-QCCCE	CSIRO-Mk3.6.0	**5**	x	x	*Jeffrey et al.* (2013)
IPSL	IPSL-CM5A-LR	1	x	-	*Dufresne et al.* (2013)
MOHC	HadGEM2-ES	**4**	x	x	*Collins et al.* (2011)
NASA GISS	GISS-E2-R	**5**	x	x	*Schmidt et al.* (2014)
NCC	NorESM1-M	**1**	x	x	*Iversen et al.* (2013)
NOAA GFDL	GFDL-CM3	**3**	x	x	*Donner et al.* (2011)
NSF-DOE-NCAR	CESM1-CAM5	*3**	x	x	*Hurrell et al.* (2013)

1.3 Introduction to the Subtopics

Numerous studies have suggested that historical anthropogenic aerosols had an important impact on climate over various regions (*Boucher et al.*, 2013; *Bindoff et al.*, 2013). Emissions of aerosols from human activities predominantly located in the northern hemisphere (NH) have been linked to a variety of climate features, from Atlantic storms (*Booth et al.*, 2012; *Dunstone et al.*, 2013) to monsoon precipitation (e.g., *Rotstayn et al.*, 2012; *Polson et al.*, 2014; *Dong et al.*, 2014a; *Li et al.*, 2016) and the width of the tropics (*Allen and Ajoku*, 2016) to Arctic sea ice (*Acosta Navarro et al.*, 2016). The areas on which my work focuses and their significance are introduced in the following.

1.3.1 Aerosols and Eurasia in the Twentieth Century

Located upstream of the large Eurasian landmass and just north of Africa, European aerosols in particular have potential impact on huge inhabited areas, both through local impacts and through remote impacts mediated by atmospheric circulation adjustments. Over Europe, changes in surface temperature and diurnal temperature range (DTR) have been related to an aerosol-induced shift in the surface solar radiation regime from dimming to brightening (*Wild et al.*, 2007; *Makowski et al.*, 2008, 2009), and other studies found the recent reduction in aerosols to have increased the frequency of light precipitation events despite no changes in total precipitation in observations (*Stjern et al.*, 2011) and an increase in the ratio between convective and stratiform precipitation in a global climate model (*Stjern and Jón Egill Kristjánsson*, 2015). Complex interactions underpin furthermore the relationship between European aerosol loading and the North Atlantic Oscillation (NAO) (*Chiacchio et al.*, 2011; *Pausata et al.*, 2014).

Yet, many of these findings are associated with large uncertainties and are, at times, controversial, resulting in vivid discussions across the scientific community. *IPCC* (2013) noted that the "lack of agreement across studies prevents generalisation of

findings to project aerosol-induced changes in regional atmospheric circulation or precipitation in the near term". A large part of this is due to the existence of counteracting effects between GHGs and aerosols which can make it difficult to robustly distinguish the influence of one from another (*Xie et al.*, 2013; *Wang et al.*, 2016), especially at regional scale. Given additionally internal variability, using a multi-model suite with large ensemble size increases the signal-to-noise ratio and can thus be very useful to identify forced changes. Changes due to anthropogenic aerosol forcing throughout the twentieth century, however, have not been consistently investigated so far in this framework, particularly for the earlier part of the century when aerosol effects might have been disproportionately large (*Carslaw et al.*, 2013).

1.3.2 Aerosols and Summer Monsoon Precipitation

The global monsoon system is a climate phenomenon with vital importance as a critical resource for economy, agriculture, water resources, and ecosystems for more than 2/3 of the world's population. Observational records have shown that monsoon rainfall underwent substantial decadal-scale and even longer-term variations during the past 150 years (*Turner and Annamalai*, 2012; *Gallego et al.*, 2015), sometimes resulting in catastrophic impacts for these vulnerable societies, and a role of anthropogenic aerosols in these variations has been indicated.

In modelling studies, anthropogenic aerosols were found to drive or contribute to the monsoon precipitation reductions in East Asia (*Li et al.*, 2016; *Guo et al.*, 2013), South Asia (*Bollasina et al.*, 2011, 2013; *Guo et al.*, 2015), and North West Australia (*Rotstayn et al.*, 2012). Anthropogenic aerosols have been equally found to reduce precipitation over West Africa and the Sahel (*Ackerley et al.*, 2011; *Dong et al.*, 2014a; *Held et al.*, 2005) by changing the inter-hemispheric temperature contrast through preferential cooling of the NH and thereby causing a southward shift of the ITCZ (*Chiang and Friedman*, 2012; *Hwang et al.*, 2013).

But while we have been able to attribute observed temperature changes to anthropogenic forcings in a statistically rigorous manner explicitly taking climate variability

into account (*Hegerl et al.*, 2010) for over two decades now (e.g., *Hegerl et al.*, 1996; *Barnett et al.*, 1999), this is more challenging for precipitation, despite the fact that anthropogenic forcing, both from GHGs and aerosols, is also expected to have distinct impacts on the hydrological cycle (e.g, *Held and Soden*, 2006; *Ramanathan et al.*, 2001). Reasons for this include larger internal variability for example due to impacts of remote circulation, sparser observational coverage, and potential model deficiencies. After *Zhang et al.* (2007) detected the anthropogenic forcing in observed precipitation changes, *Polson et al.* (2014) were one of the first to detect aerosol forcing separately. Their results showed a key role for aerosols in modulating northern hemisphere summer monsoon precipitation.

Since the precipitation response tends to be heterogeneous (e.g., *Polson et al.*, 2013), and the spatial forcing pattern has moreover been found to matter even for the simulated temperature response (*Shindell and Faluvegi*, 2009; *Shindell et al.*, 2015), aerosol emissions from different source regions can be expected to have different impacts on precipitation over different monsoon regions. While a role for both local and non-local aerosols in weakening monsoons have been suggested from modelling studies for Asia (*Cowan and Cai*, 2011; *Guo et al.*, 2015; *Dong et al.*, 2015) and West Africa (*Dong et al.*, 2014a), local aerosol emissions are suggested to be predominantly responsible for the drying of the South Asian monsoon (*Ganguly et al.*, 2012; *Bollasina et al.*, 2014; *Salzmann et al.*, 2014; *Guo et al.*, 2016). Other studies looked at the effect of the simultaneous increase of Asian emissions and decrease of North American and European emissions (*Tsai et al.*, 2016), but the relative influence of aerosols from different regions on the various monsoon systems remains largely unclear.

1.3.3 Aerosols and Atlantic Variability

Low-frequency variations of sea surface temperature (SST) in the North Atlantic, commonly referred to as Atlantic Multidecadal Variability (AMV), have a significant impact on regional and global climate (*Christensen et al.*, 2013) due to their basin-wide spatial scale and persistence. These include, for example, links with changes

of Sahel rainfall (*Knight et al.*, 2006; *Ting et al.*, 2011), North and South American hydroclimate (*Nigam et al.*, 2011; *Kavvada et al.*, 2013), and Atlantic Hurricane frequency (*Zhang and Delworth*, 2006; *Dunstone et al.*, 2013). Identifying the mechanisms behind North Atlantic SST variations is both crucial to provide reliable decadal predictions (*Smith et al.*, 2010; *Steinman et al.*, 2015) and to assess future projections of ocean circulation feedbacks (*Rahmstorf et al.*, 2015; *Swingedouw*, 2015).

On the factors driving North Atlantic variability, however, substantial research in the last decade has brought more controversy than consensus. A key issue are the roles of internal variability vs. external forcing during the historical period (*Knight*, 2009; *Ting et al.*, 2009, 2014), and the extent of their interaction (*Tandon and Kushner*, 2015). A dominant role for external forcing, especially from volcanic eruptions, has for instance been concluded from models, observations, and last millennium proxies (e.g., *Otterå et al.*, 2010; *Knudsen et al.*, 2014; *Wang et al.*, 2017; *Bellomo et al.*, 2017), but the assessment is complicated by the short observational record and the complex spatio-temporal nature of North Atlantic SST variability, making findings controversial.

Another side of the debate are the relative roles of the ocean and the atmosphere – while a number of studies have emphasised the role of the ocean circulation as the key driver of the AMV via density fluctuations associated with the Atlantic Meridional Overturning Circulation (AMOC) (*Delworth et al.*, 1993; *Knight et al.*, 2005; *Marini and Frankignoul*, 2013; *Zhang et al.*, 2016; *Zhang*, 2017), other studies have proposed changes in atmospheric circulation, including stochastic forcing (*Clement et al.*, 2015, 2016) or variability of the North Atlantic Oscillation (NAO) (*Gulev et al.*, 2013), to drive North Atlantic SST variations through air-sea interactions, or both on different time scales (*Bjerknes*, 1964). An important contribution from the AMOC and/or the NAO (*Delworth et al.*, 2017), however, does not necessarily exclude a key role for external forcing, since they might themselves be impacted by forcing (*Stenchikov et al.*, 2009; *Ding et al.*, 2014). *Tandon and Kushner* (2015), for instance, showed that a forced and an unforced component of the AMV (also *Ba et al.*, 2014) coexist in a range of CMIP5 models.

The role of anthropogenic aerosols, and sulphate in particular, in modulating North Atlantic SST variability during the twentieth century are especially debated. *Booth et al.* (2012) argued that the AMV during the instrumental period was primarily driven by aerosols, with an imprint also on Atlantic atmospheric variability (*Dunstone et al.*, 2013). However, *Zhang et al.* (2013) subsequently pointed out discrepancies in the simulated subsurface fields and ocean circulation, questioning the realism of the aerosol dominance inferred from the model. More recently, however, most of the SST variance over the Atlantic was found to be radiatively forced also in other models (*Bellomo et al.*, 2017; *Murphy et al.*, 2017), with a distinct contribution of anthropogenic aerosols on both temporal and spatial variability. Note that aerosol impact on SSTs elsewhere, possibly including decadal ENSO variability, has also been suggested (e.g., *Sutton and Hodson*, 2007; *Westervelt et al.*, 2018).

In addition to the studies focussing on the AMV, others found a longer-term impact of anthropogenic aerosols on downward surface solar radiation over the Atlantic and consequently SSTs (*Dallafior et al.*, 2015), affecting the inter-hemispheric SST gradient and thereby causing a shift of the Atlantic ITCZ (e.g., *Chang et al.*, 2011; *Hwang et al.*, 2013). Long-term anthropogenic aerosol forcing has furthermore been suggested to have strengthened the AMOC (*Delworth and Dixon*, 2006; *Cowan and Cai*, 2013; *Menary et al.*, 2013) and to have delayed ocean heat content increase and associated sea level rise in response to GHGs (e.g., *Delworth et al.*, 2005) during the twentieth century.

Interactions between the atmosphere and the ocean and also anthropogenic aerosols are thus indicated to play a key role in driving North Atlantic surface and subsurface multidecadal and longer-scale variability. The sulphate aerosol source regions North America (NA) and Europe (EU) are especially interesting in this regard not only because of their dominance of historical emissions, but also because the relative magnitude as well as the physical mechanisms of their impact may not have been the same (e.g., *Shindell and Faluvegi*, 2009; *Westervelt et al.*, 2018; *Persad and Caldeira*, 2018) despite similar emission histories.

1.4 Aims and Objectives

This thesis thus aims to improve our understanding of the climate impact of historical anthropogenic aerosol emissions from North America and Europe (NAEU), both together and in isolation.

The objectives are

- to derive a characterisation of Eurasian summer climate response to anthropogenic aerosol emissions from NAEU during the twentieth century from a suite of CMIP5 models, which includes identifying the forced response to aerosols and greenhouse gases separately in single-forcing experiments as well as their combined impact in all-forcing experiments.
- to establish whether the simulated impact of anthropogenic aerosol emissions can be detected in observations, including of European near-surface climate and monsoon precipitation over West Africa and South Asia; to establish whether this impact can specifically be attributed to emissions from NAEU or other regions; and to analyse the physical mechanisms driving these changes in global climate models (GCMs).
- to analyse the historical impact of sulphate aerosol emissions from North America (NA) and Europe (EU) separately in targeted GCM simulations, focussing on the mechanisms of aerosol impact on North Atlantic sea surface temperatures including aerosol-cloud interactions and atmospheric as well as oceanic circulation responses.

Addressing these objectives promises also an improved understanding of the response to regional aerosol forcing as well as to other external forcings, with benefits for the resolution of model discrepancies and conflicting findings in addition to the implications for near-future regional climate change and policy decisions. The objectives are addressed in Chapters 2, 3, and 4, before conclusions are drawn in Chapter 5.

Chapter 2

Impacts of the 1900-1974 Increase in Anthropogenic Aerosol Emissions from North America and Europe on Eurasian Summer Climate

2.1 Introduction

In this chapter, we provide a fundamental characterisation of the climate response to NAEU aerosol emissions expected from CMIP5 simulations. For this, we focus on the boreal summer season, when the aerosol impact on temperature and other variables mediated by temperature differences, such as the position of the ITCZ and the jet streams, is expected to be largest due to the insolation maximum in the northern hemisphere (see discussion in *Hegerl et al.*, 1997). The analysis examines changes in near-surface temperature (TAS), precipitation, diurnal temperature range (DTR), sea level pressure (SLP), and zonal wind at 300 hPa. This subset, although limited,

allows us to identify the aerosol impact on relevant surface climate features, some of which are long-term observed, and investigate the potential of aerosols to bring about changes in the atmospheric circulation.

DTR is a measure of high-frequency temperature variability and is not only important for climate impacts as diverse as crop yields (*Lobell et al.*, 2007) and human mortality and morbidity (*Kim et al.*, 2016), but has also been suggested to be a useful indicator to separate aerosol and GHG forcing (*Schnur and Hasselmann*, 2005; *Wild et al.*, 2007): Through reducing surface solar radiation, aerosols are expected to reduce maximum (Tmax) more than minimum (Tmin) temperature, causing a decrease in DTR, while GHG interact with outgoing long-wave radiation and are thus expected to impact Tmax and Tmin equally (although a preferred response of Tmin to GHG warming has also been suggested; *Rohde et al.*, 2013a).

We make use of experiments carried out as part of the Coupled Model Intercomparison Project Phase 5 (CMIP5) initiative (*Taylor et al.*, 2012). These comprise multiple realisations of experiments of all historical forcings as well as individual forcings with a range of coupled global climate models, which allows us to analyse the effect of anthropogenic aerosols and compare it to those of other forcing factors, both when acting in isolation and when combined. The availability of a large set of simulations allows the identification of robust patterns of forced climate response by (1) averaging over multiple members, thus reducing the effect of internal variability, and (2) sampling across various model formulations.

The remainder of this chapter is organised as follows: After a short description of the datasets and the analysis methods used (Section 2.2), we illustrate the spatio-temporal changes in anthropogenic aerosol emissions and the resulting atmospheric aerosol loading and AOD (Section 2.3). The linear trends in the all-forcing and single-forcing CMIP5 ensembles during the historical period of increasing NAEU sulphate emissions are then shown, contrasted by those during the later period of decreasing NAEU emissions (Section 2.4). While this captures multi-decadal to near-centennial changes, higher-frequency variability of European near-surface temperature, sea level pressure,

and DTR are analysed by means of area-mean time series also from observations, and the contribution of each single-forcing factor to the total simulated forced inter-decadal variability is estimated (Section 2.5). The chapter is completed by a summary and conclusions (Section 2.6).

2.2 Data and Methods

We use data from the CMIP5 twentieth century historical experiments, and select models which provide simulations forced only with anthropogenic aerosols (Tab. 1.1). In addition to this ensemble of aerosol-only simulations (AA), we also analyse simulations with forcing from well-mixed greenhouse gases only (GHG), natural forcings only (solar radiation and volcanoes, NAT), and all these forcings combined (ALLF) for the same set of models. Note that ALLF are the standard historical simulations, which are expected to reproduce the observations. For each model, we choose ensembles of GHG, NAT, and ALLF with the same size as the ensemble available for AA, so that the results from the different ensembles are comparable. Results from the trend analysis are shown for the multi-model mean (MMM), obtained by first averaging the individual ensemble members for each model and successively averaging these ensemble means. Given the different ensemble sizes -ranging from one to five- this ensures that each model is given equal weight.

The models considered span the full range of CMIP5 spread in climate sensitivity (*Flato et al.*, 2013): Out of the 7 models, 2 (5) and 3 (4) have an equilibrium climate sensitivity (ECS) and transient climate response (TCR), respectively, smaller (larger) than the CMIP5 multi-model mean, and the CMIP5 models with the smallest ECS (GISS-E2-R) and the largest TCR (HadGEM2-ES) are both included (*Forster et al.*, 2013). The ensemble thus represents the CMIP5 model diversity in fundamental climate system characteristics controlling the response to atmospheric CO_2. It further represents the diversity in the effective radiative forcing due to (combined direct and indirect) aerosol effects (*Zelinka et al.*, 2014).

While the chosen subset has a more comprehensive representation of aerosol effects compared to the full suite of CMIP5 models (*Taylor et al.*, 2012), there is still substantial variation amongst the models (Section 1.2.4; *Ekman*, 2014). Given that all models are forced with the same aerosol emission inventories (based on decadal aerosol emissions with an annual cycle; *Lamarque et al.*, 2010), the use of multiple models does thus not only reduce the contribution from internal variability, but allows us moreover to identify features which are robust to these model differences, and in particular to the models' representation of indirect aerosol effects as well as their aerosol distribution and background (pre-industrial) aerosol concentrations (*Wilcox et al.*, 2015). This is important since these inter-model differences have been found to cause a large spread in the aerosol responses (*Boucher et al.*, 2013; *Kasoar et al.*, 2016). Robustness is assessed by comparing the sign of the response in the MMM with that in the models' ensemble means.

The model's historical all-forcing MMM reproduces the climatology and observed changes in surface temperature patterns, and simulates the climatology of many large-scale circulation features reasonably well (*Flato et al.*, 2013; *Kumar et al.*, 2016). For DTR, too, the all-forcing simulations from chosen CMIP5 models separately as well as the MMM of all models' all-forcing simulations agree well with observations over Europe both in terms of climatology (*Lindvall and Svensson*, 2014; *Cattiaux et al.*, 2015; *Liu et al.*, 2016) and long-term trends (*Lewis and Karoly*, 2013).

We compute boreal summer (June, July, and August, JJA) means from monthly-mean data, and all model data is re-gridded prior to further analysis to match the model with the lowest resolution, which is 3.75°x2.8°. For the comparison with observations, we instead interpolate the model data to the observational resolution and mask according to the observational coverage. Anomalies from the climatological state are considered, and the climatologies are computed from the models' pre-industrial control simulations.

Simulated temperature and sea-level pressure changes are compared to those derived from available observational data. For near-surface temperature anomalies, we use

the HadCRUT dataset version 4.5 (HadCRUT; *Morice et al.*, 2012), the CRUTS dataset Version 3.24.01 (CRU; *Harris et al.*, 2014), the gridded Berkeley Earth Surface Temperature dataset (BEST; *Rohde et al.*, 2013b), and GISS Surface Temperature Analysis (GISTEMP; *GISTEMP Team*, 2017; *Hansen et al.*, 2010). For DTR, we use CRU and BEST, and for sea level pressure we use the Met Office Hadley Centre mean sea level pressure data set HadSLP2 (1850-2004, HadSLP; *Allan and Ansell*, 2006).

We compute DTR from the CMIP5 model data as the difference between monthly-mean Tmax and monthly-mean Tmin, as provided by the modelling groups (Tab. 1.1), and follow the same procedure for the BEST dataset; for the CRU data, monthly-mean DTR is used as provided by *Harris et al.* (2014). Note that the observational datasets differ in their station input sources, time sampling, quality control, homogenisation, and area-averaging; for a comprehensive analysis of the relevance of these differences see *Thorne et al.* (2016).

Long-term changes in climate are investigated by computing linear trends, calculated as least-squares regressions, and displayed as change per decade. The robustness of the simulated trends is measured by the agreement among the various models: Stippled areas are regions where at least all but one of the models' ensemble means (i.e. 5 out of 6 or 6 out of 7, depending on the availability of the variables) agree on sign. The time period common to all model simulations is 1860-2005, but we limit the analysis to 1900 onward when observations are less sparse (*Morice et al.*, 2012). Trends in the NAT ensemble are not shown for brevity unless otherwise stated, as they are found to be small compared to those in the AA and GHG ensembles as well as barely anywhere robust across models for the variables, time periods, and regions considered in this analysis.

In order to support the use of linear trends to identify the link between aerosol loading and near-surface temperature, a joint empirical orthogonal functions (EOF) analysis is also performed (*Deser and Blackmon*, 1993; *Wang et al.*, 2016). This method, which is an ordinary EOF analysis of the two variable fields combined in space, decomposes the data into orthogonal modes each consisting of one pattern per variable and a

common time series, ordered by the fraction of combined variance explained. In contrast to a regression analysis, this identifies covarying patterns without the need to presume timeseries or spatial patterns. Prior to the EOF analysis, the data are temporally smoothed in order to suppress inter-annual variability. This is done by taking subsequent 11- and 7-year running means which improves filter characteristics relative to taking running means only with a single window length (e.g., *von Storch and Zwiers*, 1999). For a sensitivity analysis see Section 2.B.

2.3 Spatio-Temporal Changes in Aerosol Emissions and Associated Near-Surface Temperature

Sulphur dioxide (SO_2) is the main component of anthropogenic aerosol emissions (*Lamarque et al.*, 2010; *Hoesly et al.*, 2018). The time series of total SO_2 emissions from various regions illustrate the dominance of NAEU emissions from pre-industrial times until the mid-twentieth century and show the peak in the 1970s, with the trend reversing in Europe around 1975, following a slightly earlier reversal in the US (Fig. 2.1). While Asian (incl. eastern Russian) emissions also started to increase before 1970, they do not exhibit strong (Japan, Russia) or any (China, India, etc.) downward trends afterwards. This is also visible in the spatial pattern of the linear trends of SO_2 emissions during 1900-1970 and 1971-2010 (Fig. 2.2).

The corresponding trend patterns in column-integrated sulphate content (sulphate loading) and aerosol optical depth at 550 nm (AOD) in the CMIP5 model ensemble show that aerosols spread further east of the source region towards central Eurasia as a result of transport by the climatological westerlies (Fig. 2.2). Although CMIP5 models use the same aerosol emission inventories, the simulated aerosol distribution patterns may vary from model to model due to differences in meteorology, chemical parametrisations, and pre-industrial background concentrations (*Carslaw et al.*, 2013; *Wilcox et al.*, 2015; *Kasoar et al.*, 2016, Fig. 2.A.1). Nonetheless, there is considerable

agreement on the sign of the trends over Eurasia (Fig. 2.2c-d). The emissions of other aerosol species (black carbon, organic carbon) changed over time less homogeneously in space (Figs. A.1-A.4), but the simulated changes in AOD, which integrates the amount and optical properties of all simulated aerosol species, are very similar to those in sulphate loading, thus reflecting the dominance of sulphate aerosols (Figs. 2.2e-f, 2.A.1).

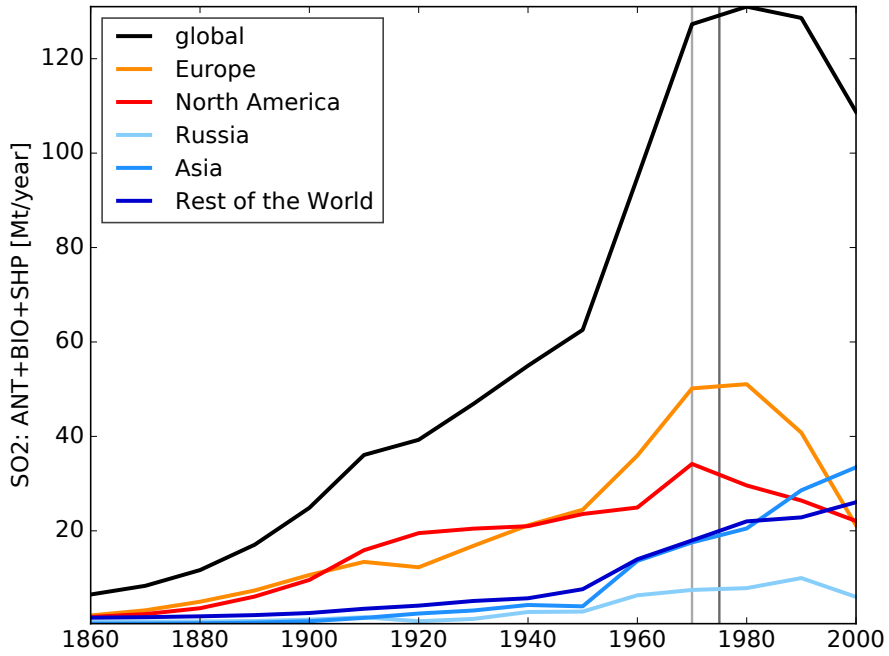

Figure 2.1: Total SO_2 emissions (kg/s) during boreal summer (JJA) from all sectors (anthropogenic, biomass burning, shipping) from Europe (EU) (30-75°N, -15-45°E; orange), North America (NA) (15-75°N, 135-60°W; red), eastern Russia (RU) (45-75°N, 45-180°E; light blue), Asia (0-45°N, 60-150°E; medium blue), and the remaining parts of the globe (dark blue). Global emissions are also shown (black). The areas are chosen based on their emission time series, and do not conform strictly to political or geographical boundaries. NA, EU, and RU are similar to the respective Tier 1 regions from the Hemispheric Transport of Air Pollution 2 experiments (*Koffi et al.*, 2016), but include for convenience other parts with negligible emissions (Arctic regions in NA, EU, RU; northern Mexico in NA; Mongolia and Kazakhstan in RU). The Asian region includes mainly India, most of China, Japan, and southern Central Asia. The vertical lines indicate the year dividing the first and second time period for which trends are calculated: 1970 (light grey) for emissions (which are decadal), and 1975 for simulated variables (dark grey). Data from *Lamarque et al.* (2010).

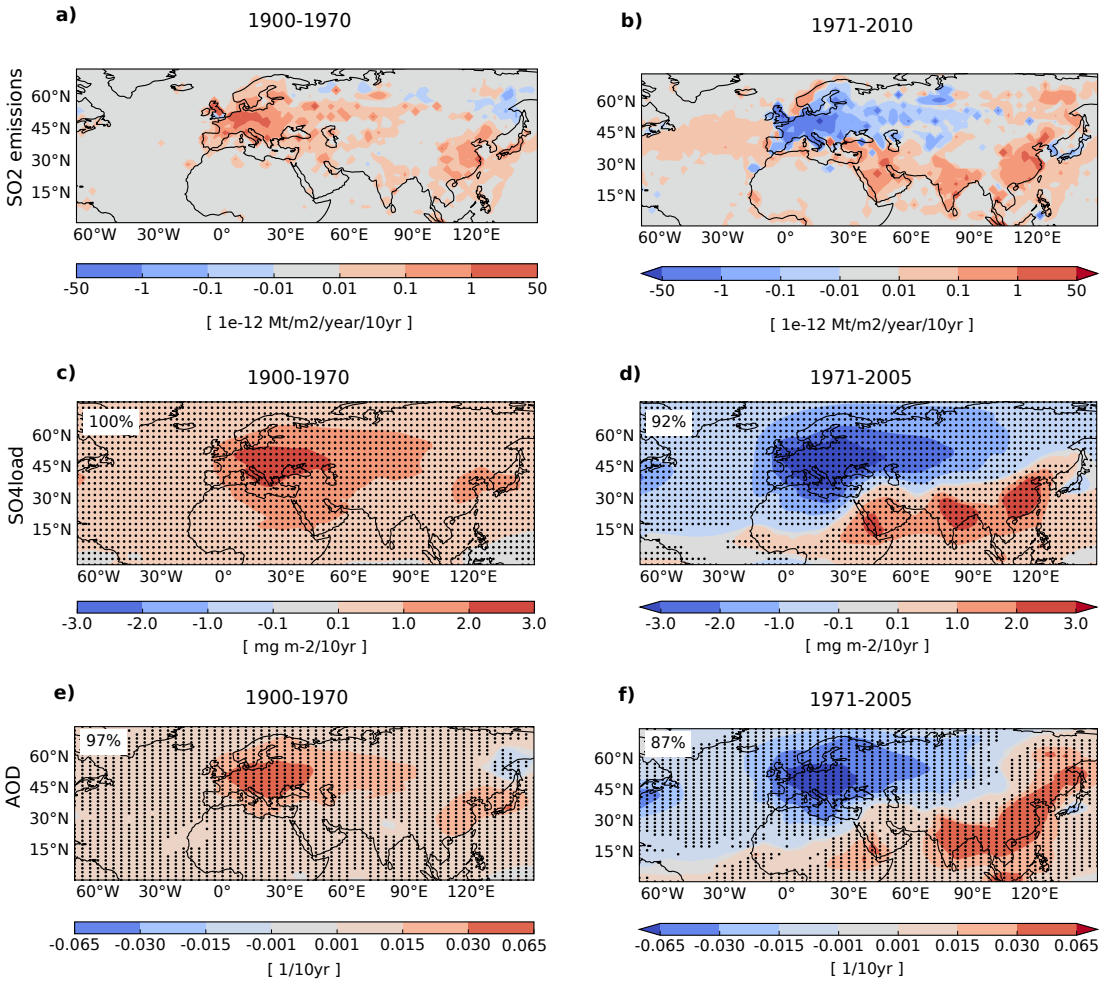

Figure 2.2: Linear trends of JJA (top) total SO_2 emissions (Mt/m^2/year/decade) from all sectors, (middle) column-integrated sulphate loading (mg/m^2/decade), and (bottom) AOD (1/decade) during (left) 1900-1970 and (right) (b) 1971-2010 and (d,f) 1971-2005. Emission data are decadal, so we use 1970 here instead of 1975 as in later figures. For sulphate loading and AOD, the multi-model mean (MMM) of the aerosol-only simulations from the models listed Tab. 1.1 is shown except for (c-d) HadGEM2-ES and (e-f) CanESM2, respectively, due to data unavailability. Stippling indicates where at least 5 out of the 6 models' ensemble means agree on sign, and the fraction of stippled grid points within 0-90°N, -30-120°E is given in the top left corner. Trends in the all-forcing ensemble are very similar (not shown). Data from *Lamarque et al.* (2010) (emissions) and *Taylor et al.* (2012) (CMIP5). Note that trends during the second period exceed the colourbar range, as indicated by triangular colourbar ends.

A joint EOF analysis reveals modes of covariability of sulphate loading and near-surface temperature (TAS) as simulated in the AA ensemble for summer over the NH excluding the Pacific (Fig. 2.3). The dominant temperature signature is a large-scale cooling associated with an overall increase in sulphate aerosols until they peak in the 1970s (Fig. 2.3a). The first mode's patterns and time series for both sulphate loading and TAS are very similar to those of the first mode from EOFs of the variables separately (Fig. A.5a-b), which confirms that these patterns represent a substantial part of variability in both sulphate loading and TAS individually in the CMIP5 ensemble. Separate EOF analyses of other variables show that approximating the aerosol-related impact with linear trends captures a large fraction of their variability in the CMIP5 AA ensemble (for example precipitation and DTR, Fig. A.5c-d).

The higher modes from the joint EOF analysis reflect differences in the time series of aerosol emissions and associated temperature impacts at smaller spatial scales. The sulphate loading and temperature patterns of the second mode (Fig. 2.3b), for instance, has opposite signs in North America and Europe compared to Asia. The principal components accordingly resemble the time series of the difference in sulphate loading over these regions. However, since only a very small fraction of the covariance is explained by the higher modes, we focus here on the dominant behaviour as reflected in the first mode.

An additional analysis of area-mean sulphate load, AOD, and near-surface temperature as a function of each other shows that the potentially stronger cooling in the first decades relative to aerosol emissions caused by non-linearities in the indirect aerosol effects (Section 1.2.3), which we might expect to find based on *Wilcox et al.* (2015)'s analysis of the model's aerosol effect parametrisations, is hardly discernible on the large regional scales considered here (Section 2.A).

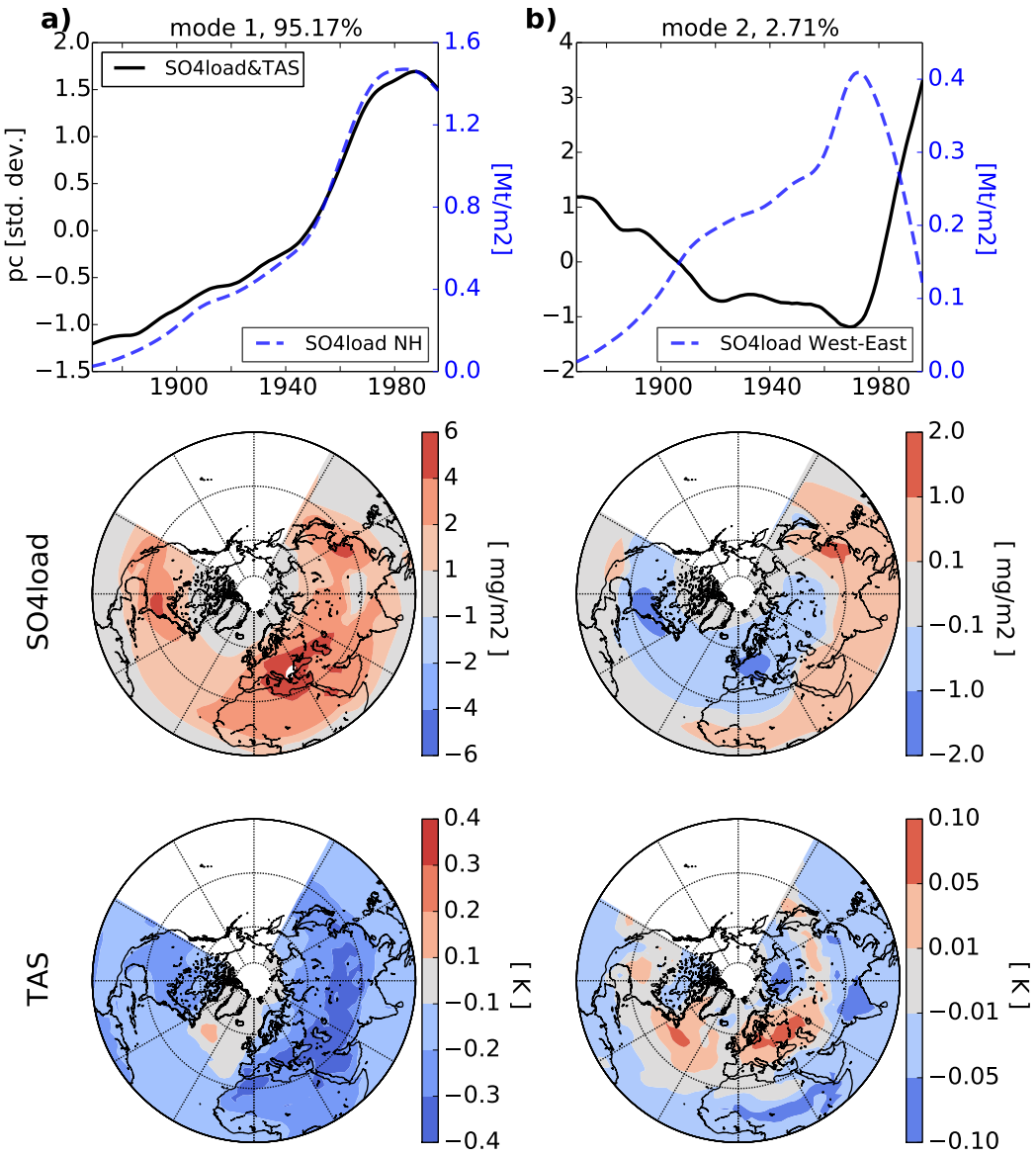

Figure 2.3: Joint EOF analysis for JJA sulphate loading (SO4load) and near-surface temperature (TAS) from the multi-model mean of the aerosol-only CMIP5 simulations. The (top) principal components of the (a) first and (b) second mode are shown along with the respective patterns for (middle) SO4load and (bottom) TAS. For comparison, the (a) total SO4load over the northern hemisphere and (b) difference between SO4load over a western (NAEU) region (the sum of 20-90°N, -130-0°E; 30-90°N, 0-30°E; and 45-90°N, 30-60°E) and an eastern region (0-45°N, 30-135°E) are also shown (blue, dashed lines). The models used are those in Tab. 1.1 except for HadGEM2-ES (no data available; separate EOFs show the other results are not sensitive to the inclusion of this model (not shown)). We apply a 11-7 year filter prior to the analysis.

2.4 Simultaneous Long-Term Changes in Emissions from North America and Europe and Near-Surface Climate

Given the strong opposite trends in SO_2 emissions from NAEU before and after the peak in the 1970s (Section 2.3), it is reasonable to expect their climate signature to also show a trend reversal around the same time. Emissions from elsewhere, e.g. Asia, in contrast, started to increase in the 1950s and might thus have perturbed the climate during the first period, but we expect their continued increase during the second period to result in changes of the same sign in both periods, albeit of different magnitudes. This also holds true for GHG forcing, which has increased during both periods. We thus identify changes during 1900-1974 in the ALLF ensemble as dominantly driven by NAEU aerosol forcing if they are robust and have the same sign as those in the AA but different to those in the GHG or NAT ensembles. This approach is further validated by contrasting the trends with those during 1975-2005, when we expect the decreasing NAEU emissions to drive changes of the opposite sign. Note, however, that the impact of emissions from, say, Asia is not negligible during 1975-2005, so that the effect of decreasing NAEU emissions might be offset by Asian emissions.

Despite clear limitations, this approach allows us to disentangle the NAEU aerosol imprint in presence of other forcings (provided they changed monotonously during the whole record). The advantage over other methods (e.g., EOF analysis) is that it allows us to assess inter-model consistency and to compare with the other ensembles and observations, for which aerosol data are not available.

Based on the timing of the trend reversal in simulated sulphate loading, we choose 1900-1974 and 1975-2005 as the time periods with increasing and decreasing aerosols, respectively. Note that choosing instead the partition year 1970, as done for the trends in emissions because they are decadal only, does not affect the results reported below (not shown). The first time period includes the slow increase in emissions (Fig. 2.1), so that trends per decade are smaller during the first than the second period; European

area-mean (35-60°N, 0-60°E) trends in the aerosol-only MMM amount to +2.0 and -2.6 mg/m2/decade for sulphate loading and +0.028 and -0.046 1/decade for AOD during 1900-1975 and 1975-2005, respectively.

Because emissions from both North America and Europe reversed sign around this time, we will in the following attribute the changes to NAEU emissions. The larger trends in European emissions and their closer proximity to the area studied, however, might suggest them to have a larger share of the impacts at least on Eurasian near-surface temperature.

2.4.1 Near-Surface Temperature & Sea Level Pressure

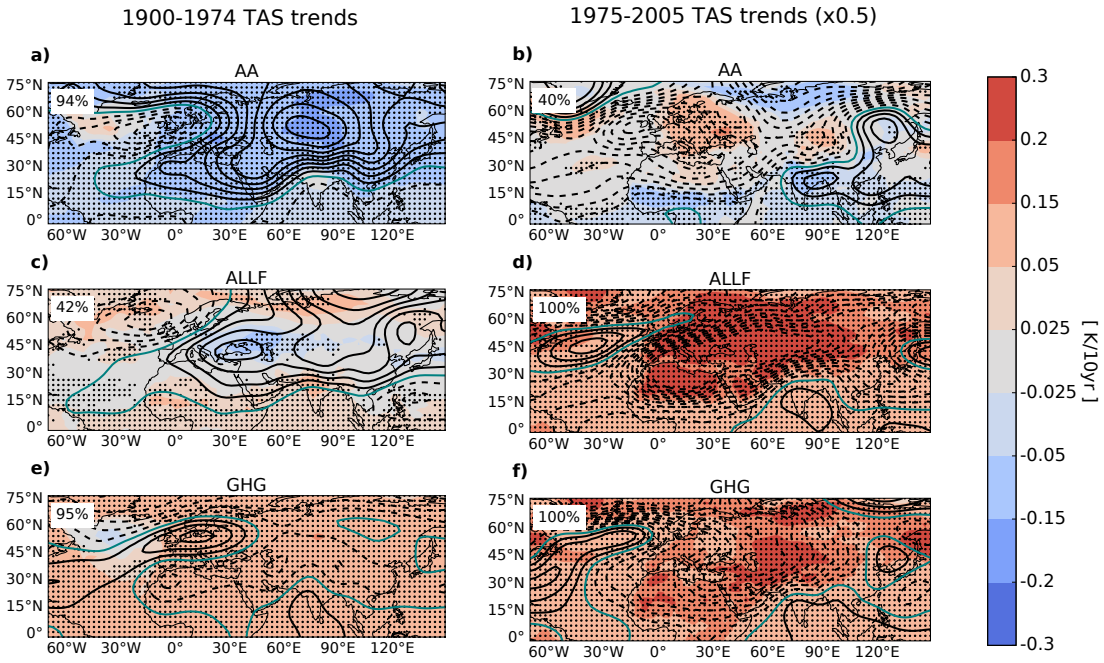

Figure 2.4: Linear trends in JJA near-surface temperature (TAS, colour shading, in K/decade, and sea level pressure (SLP, contour lines, Pa/decade) during (left) 1900-1974 and (right) 1975-2005 for the multi-model mean of the (top) AA, (middle) ALLF, and (bottom) GHG simulations. Stippling indicates where at least 6 out of the 7 models' ensemble means agree on sign for TAS, and the fraction of stippled grid points within 0-90°N, -30-120°E is given in the top left corner. Dashed contour lines indicate negative sea level pressure trends; the zero contour line is drawn in turquoise. The contour interval is 1.25 Pa/10yr. See Fig. A.7 for the robustness of the SLP trends. Note that both temperature and SLP trends during the second period are scaled by 1/2 for easier comparison with those during the first period.

The CMIP5 AA ensemble shows a widespread decrease in near-surface temperature over the Atlantic-Eurasian region during the period of increasing NAEU emissions (Fig. 2.4a). This trend is reversed in the later period with a warming of similar magnitude as the earlier cooling over central Europe, and a slightly weaker warming over the Asian mid-latitudes (Fig. 2.4b). Note that over eastern China, temperatures decrease during both periods consistent with trends in local aerosol emissions (Fig. 2.2a,c), so NAEU emissions are not the (sole) driver of the cooling over this region in the CMIP5 models. The larger trends during the second period -shown in Fig. 2.4 scaled by a factor of one half- compared to those during the first period are consistent with the larger trends in emissions, sulphate loading, and AOD (Fig. 2.2).

GHG forcing produces warming during both periods (Fig. 2.4e-f), and both the AA and the GHG signature are robust across the models in the whole region. In the ALLF ensemble, which has the two anthropogenic forcings counteract each other in the first period, the models agree on the mid-latitude cooling as well as the warming at higher and lower latitudes. The zonally extended temperature anomalies are consistent with *Shindell et al.* (2010), who found the influence of inhomogeneous radiative forcing to extend three to four times further in the zonal than in the meridional direction. The vertical cross-section of temperature trends averaged over 30-60°N shows moreover that although the strongest cooling is located near the surface over Europe, the temperature signal extends up to the mid- and upper-troposphere and as far eastward as central Asia (Fig. A.6a-b), suggestive of an eastward propagation from Europe. Natural forcing does not result in appreciable trends in the CMIP5 models (not shown).

Sea level pressure, consistent across the models, shows anomalous anticyclonic trends over the Eurasian mid-latitudes in the first period both in the AA and the ALLF ensemble, which is consistent with the atmospheric adjustment to the surface cooling (Figs. 2.4a,c; A.7a,c). The largest aerosol-induced anomalies in TAS and SLP east of the area of highest emission changes (Figs. 2.4, A.6, A.7) is consistent with expectations from aerosol transport as well as temperature advection by climatological westerlies (not shown). While increasing anthropogenic aerosols thus dominate the simulated Eurasian mid-latitude temperature changes during 1900-1974, simulated

tropical temperature changes appear to be more strongly influenced by GHG forcing, with a widespread warming seen both in the GHG and the ALLF CMIP5 ensembles (Fig. 2.4c-f).

2.4.2 Jet Stream Strength and Position

The zonal character of the aerosol-driven temperature changes as simulated with the CMIP5 models suggests that aerosols might also affect circulation features in the latitudinal direction via changes in the meridional temperature gradients. We find indeed that both the AA and the ALLF ensemble show a strengthening of the equatorward side of the subtropical jet over Asia, as identified from changes in 300-

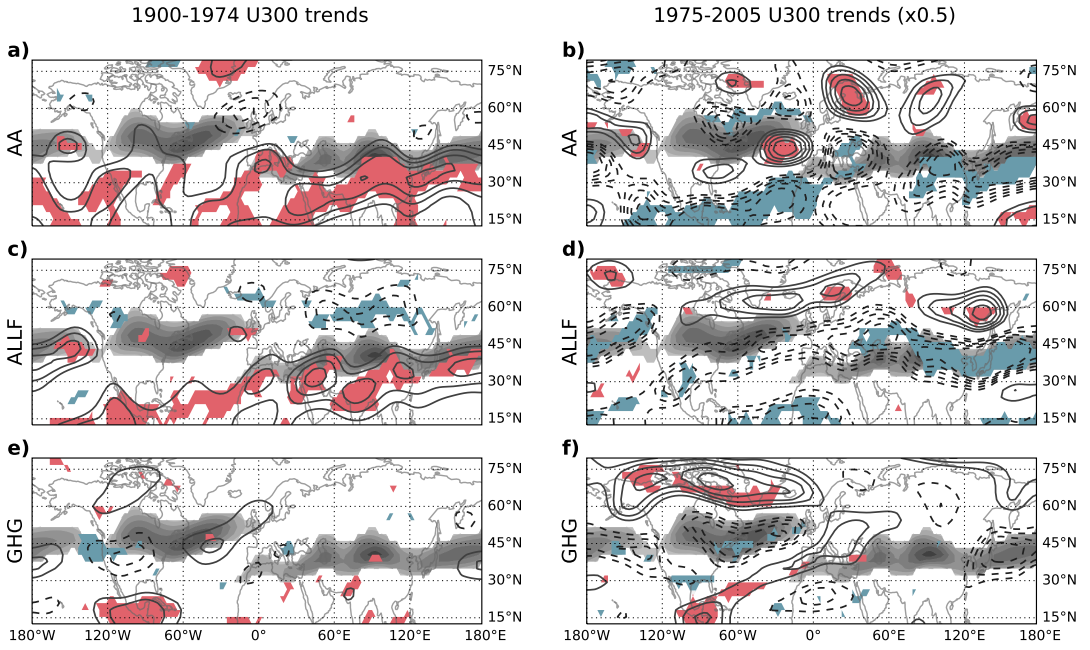

Figure 2.5: Linear trends in JJA zonal wind at 300 hPa (U300, contour lines) during (left) 1900-1974 and (right) 1975-2005 for the multi-model mean of the (top) AA, (middle) ALLF, and (bottom) GHG simulations. Dashed contour lines indicate negative trends. The contour interval is 0.02 m/s/decade. The 0.00 and ±0.02 contours are not displayed for clarity. Grey shading indicates where the climatological zonal wind speed at 300 hPa exceeds 12.5 m/s as a rough estimate of the jet stream position. Colouring (red for positive trends, blue for negative ones) indicates where at least 6 out of the 7 models' ensemble means agree on sign. Note that trends during the second period are scaled by 1/2 for easier comparison with those during the first period.

hPa zonal wind strength, during the first time period, and a weakening during the second period (Fig. 2.5a-d). GHG (and NAT, not shown), on the other hand, show no large-scale significant or robust trends (Figs. 2.4e-f; 2.5e-f). This is consistent with the thermal wind relation, with AA cooling the mid-latitudes more than the tropics and thus enhancing the temperature gradient, which results in a strengthened zonal wind (Figs. 2.4a,c; 2.5a,c). Conversely, during the second period, the decrease in NAEU emissions warms the mid-latitudes more than the tropics, thus reducing the gradient and weakening the zonal wind (Figs. 2.4b,d; 2.5b,d). The significant positive wind speed anomalies on the southern flank of the climatological jet position during the first period, and negative ones during the second, can be additionally interpreted as a southward and northward, respectively, displacement of the circulation in response to the changing meridional temperature gradients.

2.4.3 Precipitation

Another feature associated with the change in the meridional circulation is the shift of the inter-tropical convergence zone in response to variations in the inter-hemispheric temperature gradient, driven by the aerosols' preferential cooling of the Northern vs. the Southern hemisphere (*Chiang and Friedman*, 2012; *Hwang et al.*, 2013). In the CMIP5 models, we also see an aerosol signal on precipitation over western Africa, where rainfall is largely controlled by the ITCZ: A drying during the period of increasing NAEU aerosols, and a wettening during the period of decreasing aerosols, both in the AA and the ALLF ensemble (Fig. 2.6a-d).

Over most of Eurasia, where climatological precipitation is relatively low and spatially heterogeneous, precipitation trends in the CMIP5 AA ensemble during 1900-1974 are small (Fig. 2.6a). Key robust features are a wettening trend over western Europe as well as a drying over the high-latitudes, including Scandinavia and Northern Russia, which is also reversed during 1975-2005 (Fig. 2.6b). The ALLF ensemble shows also that if aerosols are included, the drying over Europe as simulated for GHG forcing only is restricted to the Mediterranean (Fig. 2.6c-f).

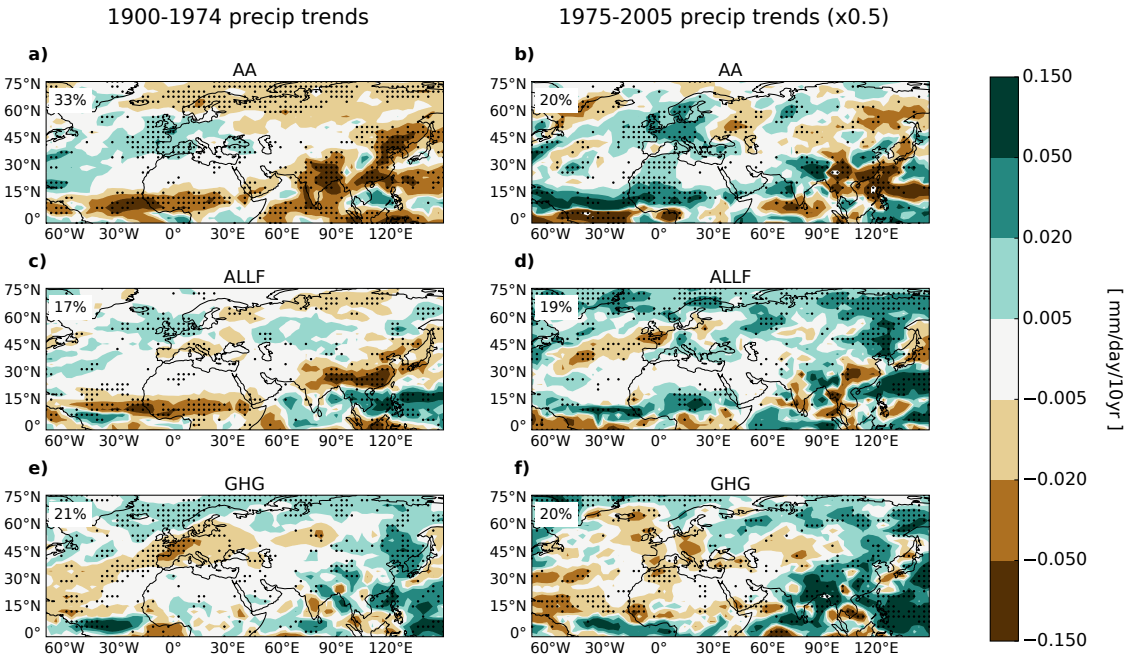

Figure 2.6: Linear trends in precipitation (precip, in mm/day/decade) for JJA during (left) 1900-1974 and (right) 1975-2005 for the multi-model mean of the (top) AA, (middle) ALLF, and (bottom) GHG simulations. Stippling indicates where at least 6 out of the 7 models' ensemble means agree on sign, and the fraction of stippled grid points within 0-90°N, -30-120°E is given in the top left corner. Note that trends during the second period are scaled by 1/2 for easier comparison with those during the first period.

In the subtropical and tropical monsoon regions South Asia, East Asia, western Africa, in contrast, we see a robust aerosol signal during both periods (Fig. 2.6a-d). During the first period, the AA ensemble shows a drying over northern India, which reverses during the second period (Fig. 2.6a-b). This robust and significant aerosol signal also dominates -although over a smaller domain- in the ALLF ensemble, despite the counteracting effect of GHGs (Fig. 2.6c-f).

Both the AA and the ALLF ensemble also show a meridional tripole pattern of longitudinally-elongated bands featuring a drying over central China and the western Pacific, a wettening over southern China and Indochina, and again a drying over the Maritime Continent during the first period (Fig. 2.6a,c). This pattern is especially consistent between AA and ALLF over land, whereas the GHG impact appears to manifest in the precipitation increase over the Indian Ocean and the western Pacific (Fig. 2.6e). While these precipitation changes have thus been clearly driven

by anthropogenic aerosols in the CMIP5 models, our results do not allow us to unequivocally separate the role of remote and local aerosols, owing to the simplicity of the linear-trend approach: In addition to NAEU emissions, local emissions also increased -again potentially more effective than later in the century-, the effects of which presumingly added onto those from NAEU emissions (*Guo et al.*, 2013). The importance of NAEU aerosols is clear, however, from comparison with a shorter, earlier period (1900-1950) for which the assumption of negligible Asian emissions change is even more justified (Fig. 2.1): The precipitation changes during 1900-1975 when both NAEU and Asian emissions increased strongly resemble those during 1900-1950, when only NAEU emissions increased, so that the response to NAEU forcing must be a substantial part of the response to the combined forcing (Figs. 2.6, A.10). Impact from NAEU aerosols in our results is plausible, too, since the anomalous anticyclone over mid-latitude Asia, resulting from the large-scale near-surface and tropospheric cooling (Figs. 2.4, A.6-A.7) might cause northeasterly winds which oppose the climatological monsoon flow and thus induce a weakening of the East Asian summer monsoon circulation, as visible in the precipitation changes over East Asia (Figs. 2.6). During 1975-2005, on the other hand, the impact of increasing local emissions could have counteracted that of decreasing NAEU emissions (*Guo et al.*, 2013), and the continued drying suggests that NAEU emissions were not the most important factor in driving the precipitation changes over China and South-East Asia in the CMIP5 simulations during this later period (Fig. 2.6a-b).

2.4.4 Diurnal Temperature Range

DTR shows a widespread decrease over much of the European and Asian mid-latitudes both in the AA and the ALLF ensemble during the first time period (Fig. 2.7a,c). Over Europe, the trend is reversed during the second period (Fig. 2.7b,d). The trends in the GHG ensemble (and NAT, not shown) are less uniform and not consistent with ALLF (Fig. 2.7e-f), which suggests that aerosols, not greenhouse gases, dominate the twentieth century DTR variations over Europe, in agreement with expectations. Interestingly, a significant, consistent aerosol signal is also noticeable at low latitudes

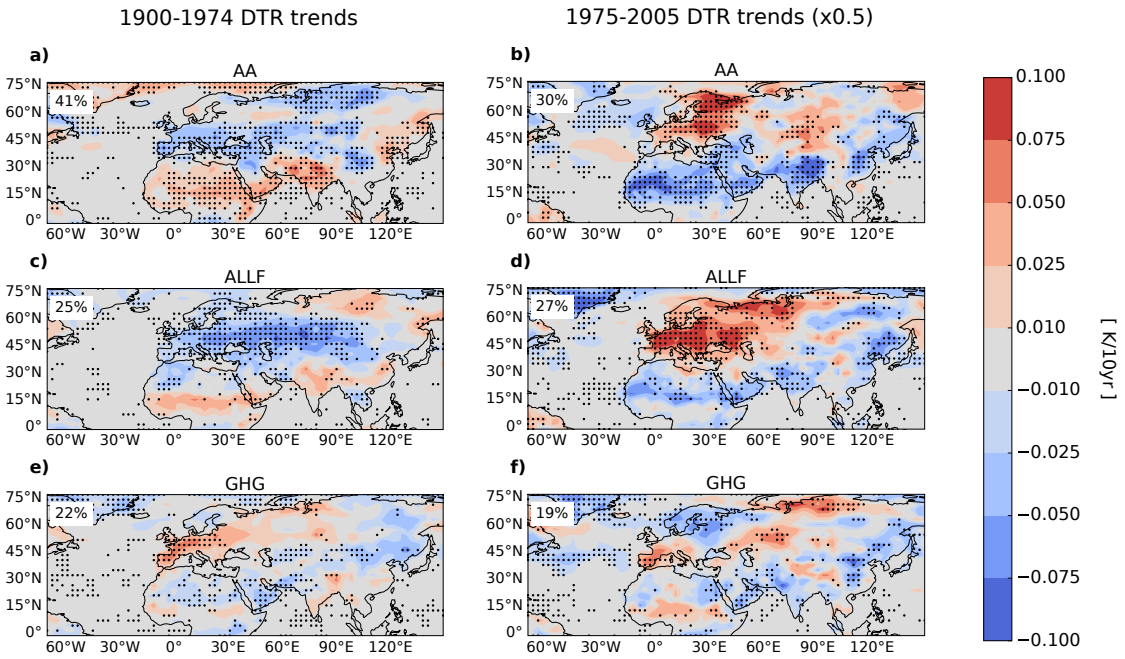

Figure 2.7: Linear trends in DTR (in K/decade) for JJA during (left) 1900-1974 and (right) 1975-2005 for the multi-model mean of the (top) AA, (middle) ALLF, and (bottom) GHG simulations for the models listed in Tab. 1.1; for AA, no HadGEM2-ES data is available, thus the MMM of the remaining six models is shown. Stippling indicates where at least 6 out of the 7 (ALLF, GHG) or 5 out of the 6 (AA) models' ensemble means agree on sign, and the fraction of stippled grid points within 0-90°N, -30-120°E is given in the top left corner. Note that trends during the second period are scaled by 1/2 for easier comparison with those during the first period.

(from northern Africa to India), but of opposite sign to that in the mid-latitudes, with GHG (and NAT) trends again much smaller, less robust, and inconsistent with those in the ALLF ensemble; coinciding precipitation trends (Fig. 2.6) hint at modulations in diurnal convection by changes in cloudiness as a possible mechanism underlying this aerosol control on DTR over these regions, which is supported by trends in total cloud fraction (Fig. A.8).

2.4.5 Sensitivity Study and Early Twentieth Century

The robustness of the trends during 1900-1974 is further ascertained by considering the shorter 1900-1950 period, during which Asian emissions increased even less and were at levels comparable to those of combined European and North American emis-

sions in 1850 (Fig. 2.1). During this period, trends of similar patterns[1] to those for 1900-1974 emerge in the CMIP5 simulations over the region considered, but with smaller magnitudes, as expected from the smaller increase in aerosols (and GHGs) which had taken place by then (Figs. A.9, A.10, A.11). For near-surface temperature, the cooling in the AA ensemble during 1900-1950 does not dominate the ALLF response, but reduces the warming trends over Europe seen in the GHG ensemble in the mid-latitude band which shows aerosol-related cooling during 1900-1974. The pattern of change in precipitation over South-East Asia described above is already recognizable in the AA trends during 1900-1950; also, DTR shows a robust narrowing over the mid-latitudes in both the AA and the ALLF ensemble.

These findings suggest that aerosols were already a key driver of regional climate anomalies before the peak aerosol increase between 1950-1970s, for some variables even dominant over GHGs. Note that saturation effects might contribute to this by potentially making the aerosol emissions less effective later in the twentieth century (e.g., *Carslaw et al.*, 2013). The similarity of the patterns and their already considerable magnitude during 1900-1950 furthermore support the notion that remote (NAEU) emissions contributed substantially to the simulated near-surface climate variation over Russia and Asia, since the amount of remote aerosol emissions dominated over that of local emissions even more in 1950 than in 1970: In 1950 (1970), there were 8 (4) times more emissions from Europe than from Asia, and from 1900-1950 (1900-1970), those from Europe increased nearly 6 (3) times faster than those from Asia (Fig. 2.1).

[1]The similarity between the patterns is judged by eye. Note that any attempt of a more quantitative comparison would have to be able to account for potential spatial shifts in otherwise similar patterns, as plausible for instance for ITCZ shifts of smaller magnitude due to smaller forcing in the earlier period compared to the later period. A simple metric measuring point-by-point similarity, for instance, would therefore not be suitable.

2.5 Temporal Evolution of European Climate

2.5.1 Comparison with Observations

The model-based findings on long-term changes associated with aerosols discussed above are now complemented by an analysis of area-mean time series for the region with the largest trends in the AA and ALLF ensembles (35°-60°N, 0°-60°E) (Fig. 2.8). We focus on near-surface temperature, sea-level pressure, and DTR, which all show a spatially homogeneous response across this region in the CMIP5 ensemble (Figs. 2.4, 2.7). The time series are also compared with observations, coverage of which is better for this region than most others especially early in the twentieth century.

The temporal change in near-surface temperature shows the contrast between the warming in the GHG-only experiments and the cooling in the AA ensemble (Fig. 2.8a). The small gradients in both ensembles in the first decades of the twentieth century is consistent with weak variations in anthropogenic emissions, while clear differences between the gradients in the two ensembles start appearing around 1925, with similar magnitudes of opposite sign until the 1970s. The largest aerosol-induced variations are found during 1940-1975, followed by a plateau and a weak recovery, reflecting the peak and subsequent decline in global aerosol emissions. In contrast, the GHG warming increased exponentially during the twentieth century, with the largest trends after 1960. The all-forcing ensemble reflects the modulation due to both drivers as well as the contribution from natural variability, for example the volcanic cooling (e.g. after the Agung eruption in 1963, e.g., *Robock and Mao*, 1995). After a few decades of negligible anthropogenic forcing at the beginning of the century, temperature variations are dominated by aerosol cooling until at least 1970, when GHG warming starts to dominate instead. Comparison with the observed changes shows that the CMIP5 models are able to capture the observed twentieth century variations of near-surface temperature over Europe (observations within the 95% range of ALLF). The most notable feature in the observations is the cooling during 1940-1980, which is consistent with the prevailing role of anthropogenic aerosols.

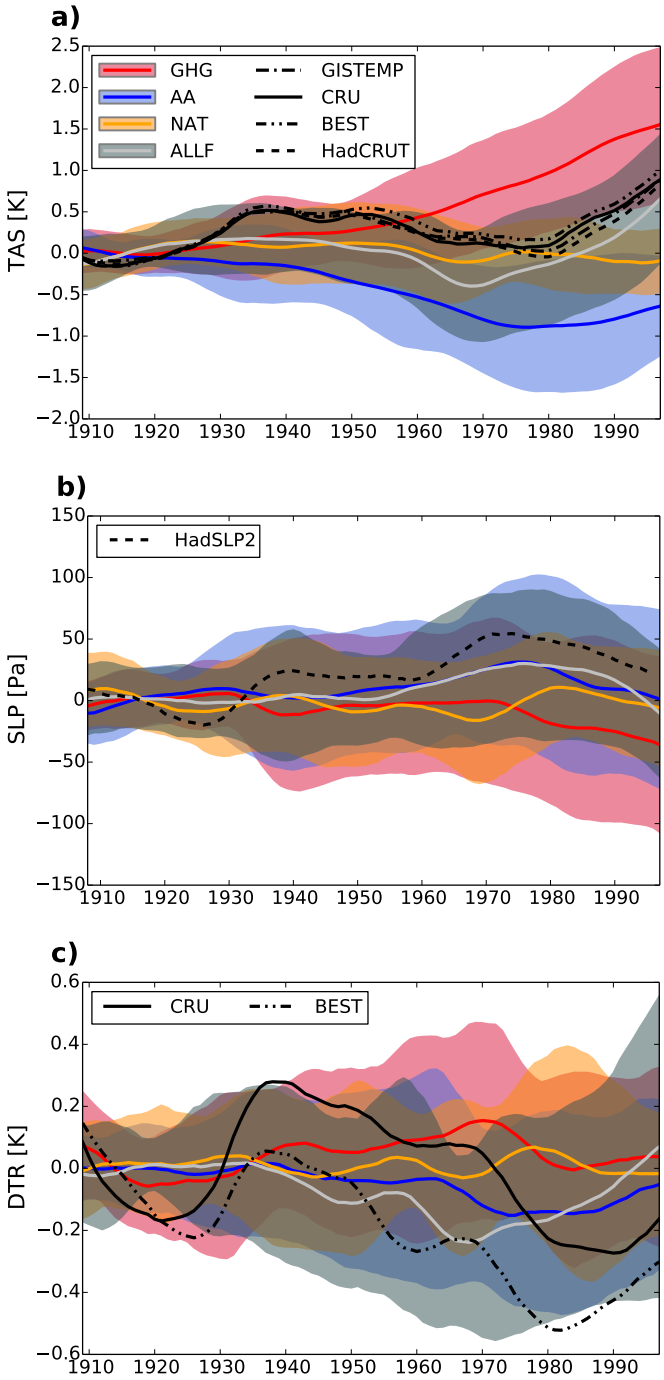

Figure 2.8: Comparison with observations over Europe (35-60°N, 0-60°E): Time series of area-mean JJA a) near-surface temperature (TAS, K), b) sea level pressure (SLP, Pa), and c) diurnal temperature range (DTR, K). Observations (black lines) are shown as well as the CMIP5 multi-model mean for single-forcing (AA in blue, GHG in red, NAT in yellow) and all-forcing simulations (ALLF in grey) along with the range of 1.96 standard deviations of the individual model simulations (shading). The CMIP5 data for TAS and DTR are masked to the coverage of the respective CRU dataset. All data are temporally smoothed with a 11-7 year filter, and anomalies with respect to 1901-1930 are plotted. For DTR, no HadGEM2-ES data is available, thus the MMM of the remaining six models is shown.

For sea level pressure (Fig. 2.8b) and DTR (Fig. 2.8c), the single-forcing ensembles diverge less clearly, reflecting higher variability, lesser model agreement, and more complex responses of these variables compared to temperature to the different forcings. For SLP, both the AA and the ALLF ensemble encompass the observations, but the GHG and NAT ensembles do not, indicating that aerosol forcing is essential to explain the observed variations.

For DTR, the two observed datasets agree on multi-decadal variability, showing a decrease until 1930, followed by a steep increase, and a subsequent decrease between the mid-1930s and the mid-1980s. They differ in their absolute anomalies, however, due to discrepancies in the first half of the century (*Thorne et al.*, 2016). While all ensembles are compatible with the CRU observations at the 95% level, the GHG and NAT ensembles are incompatible with the BEST dataset in the second half of the twentieth century. The AA and ALLF ensembles are the only ones to show a DTR narrowing over most of the twentieth century as do the observations. This overall provides further confirmation of aerosol forcing being necessary to explain historical observed variations. However, due to strong influence of internal climate variability, conclusive attribution of observed changes was not possible.

2.5.2 Contribution of Individual Forcings to Simulated European Summer Climate

The contribution of each single forcing on the forced component of simulated European inter-decadal climate variability can be estimated by calculating the gradient of the multi-model mean time series from each ensemble and comparing the magnitude of those from the single-forcing CMIP5 ensembles (AA, GHG, NAT) to their arithmetic sum as in *Wilcox et al.* (2013). This approach assumes that the role of internal variability is negligible in the multi-model mean and that the responses to the individual forcings add linearly (Fig. 2.9). The time series are smoothed prior to the analysis by consecutively taking 11- and 7-year running means to suppress variability on time scales shorter than inter-decadal (Section 2.2).

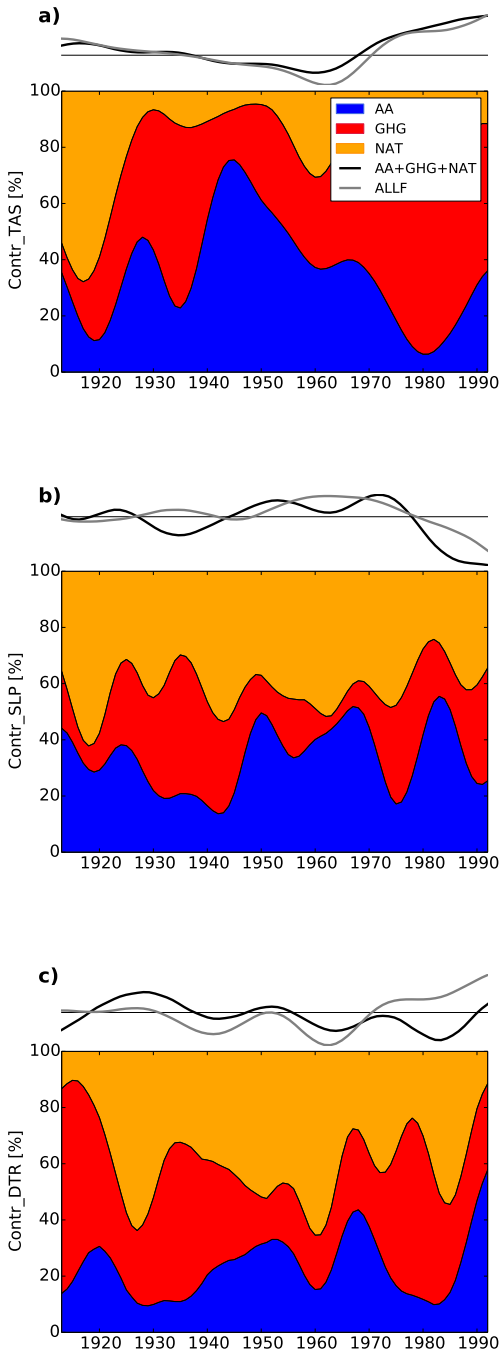

Figure 2.9: Estimates of the contribution of each single forcing on the inter-decadal variability of a) near-surface temperature (TAS, %), b) sea level pressure (SLP, %), and c) diurnal temperature range (DTR, %) for the European region as in Fig. 2.8 (here the data are not masked to the observational coverage). At the top of each panel, the instantaneous gradient of the MMM all-forcing time series (grey) and the sum of the gradients of the MMM single-forcing time series (black) are shown. At the bottom of each panel, the contributions from GHG (red), AA (blue), and NAT (yellow) are shown, derived by taking the gradient of the ensemble-mean time series for each of these forcing experiments and dividing their magnitudes by the sum of all these gradient magnitudes. All time series are temporally smoothed with a 11-7 year filter prior to the analysis and further smoothed (7-5 year filter) for plotting.

For European near-surface temperature, the sum of the gradients (AA+GHG+NAT) is a reasonable approximation to the gradient from the ALLF ensemble (Fig. 2.9a, top), and during the twentieth century, the contribution of AA to the total forced simulated variability (36%) is comparable to that of GHG (43%), and larger than that of NAT (21%). The aerosol impact is even dominant during 1940-1970, with AA explaining more than 50% of the total forced variability. The aerosol contribution to the total forced inter-decadal model variability in sea level pressure is also discernible and amounts to about a third throughout the twentieth century, and slightly more again in the period 1940-1970 (Fig. 2.9b). For DTR, AA contributes on average a forth throughout the twentieth century; this contribution grows towards the later decades, but then the sum of the gradients of the single-forcing time series approximates the all-forcing one less well (Fig. 2.9c).

2.6 Summary, Discussion, and Conclusions

The long-term signature of anthropogenic aerosol emissions mainly from North America and Europe (NAEU) on Eurasian summer climate throughout the twentieth century has been identified in an ensemble of coupled climate (CMIP5) models. The analysis was motivated by the need to advance current understanding of the effects of aerosols on regional climate, which is of utmost importance to more confidently assess and quantify the drivers of past climate variations as well as to reduce uncertainties in near-future climate projections. North America and Europe were the key aerosol emission regions worldwide for most of the twentieth century, with the potential to influence climate downstream over large inhabited regions. Yet, the topic has not been consistently investigated so far: While earlier studies have mostly focused either on individual variables or used only one climate model, robust information on the aerosol impact on a range of relevant variables across multiple coupled models is still largely unknown.

The aerosol imprint on simulated summer climate was inferred from inter-model agreement on linear trends during a period of increasing NAEU sulphate emissions (1900-

1974), contrasted with trends during the more recent period of decreasing emissions (1975-2005). This was supported by an analysis of the covariability of near-surface temperature and sulphate loading. The main findings are:

- Regionally and during the 1900-1974 period, aerosols generated a large-scale anomalous cooling stretching from Europe across most of the Eurasian mid-latitudes in the CMIP5 models. The cooling, largest at the surface, extends to the mid and upper troposphere, and is associated with a large-scale anticyclonic sea-level pressure anomaly centered over Russia, as well as with a widespread narrowing of DTR. Aerosols also strengthened the northern hemisphere subtropical jet on its equatorward side, which is consistent with changes in the meridional temperature gradient, and decreased monsoon precipitation over western Africa, northern India, and eastern China.

- During the 1975-2005 period, most of these changes are reversed, which provides support to their association with NAEU sulphate aerosol emissions – only precipitation changes over East Asia, where strong positive trends in local aerosol emissions are expected to superpose the effect of decreasing NAEU emissions, do not reverse.

- Analysis of observations averaged across Europe shows clear evidence for aerosols and GHGs both being important for models to reproduce inter- and multi-decadal variations in near-surface temperature. Observed variations in sea-level pressure are noisy, but tend to agree much better with simulations that include anthropogenic aerosols than with those without aerosols. Observed DTR has very high data uncertainty, but shows a decline over much of the century that does not occur in the CMIP5 GHG and NAT ensembles.

- Assuming linearity among the single forcing responses, anthropogenic aerosols are estimated to explain on average more than a third of the forced simulated inter-decadal variability in European near-surface temperature during the twentieth century, and more than half during 1940-1970.

The time-series analysis thus highlights the importance of aerosols in addition to GHGs for explaining temporal variations in observed European near-surface climate, in agreement with *Bindoff et al.* (2013). For DTR, our results add onto those by *Makowski et al.* (2008), providing the evidence from an ensemble of CMIP5 experiments. Furthermore, we show that regionally AA explain a substantial fraction of simulated European climate inter-decadal variability from as early on as 1900, which is even larger than that found by *Wilcox et al.* (2013) for global mean temperature.

Significant changes in strength and latitudinal position of the subtropical jet stream during the twentieth century have been discussed in a number of studies, including those focusing on variations of the tropical belt width, given that the jet stream can be interpreted as the poleward boundary of the tropics. While some studies only looked at annual means (*Archer and Caldeira*, 2008a; *Fu and Lin*, 2011; *Moore*, 2013) or the winter season (*Strong and Davis*, 2007), changes in winter and summer, if any, were generally found to be consistent in sign (*Archer and Caldeira*, 2008b; *Hudson*, 2012; *Davis and Birner*, 2013; *Pena-Ortiz et al.*, 2013; *Abish et al.*, 2015), despite the pronounced climatological seasonality. Evidence suggests a weakening and/or poleward shift of the NH subtropical jet since 1979 from satellite observations (*Fu and Lin*, 2011), reanalyses (*Archer and Caldeira*, 2008b; *Hudson*, 2012), and observations (*Davis and Birner*, 2013; *Pena-Ortiz et al.*, 2013). Together with weaker and/or even opposite trends since the mid-twentieth century (*Strong and Davis*, 2007; *Archer and Caldeira*, 2008a; *Pena-Ortiz et al.*, 2013; *Abish et al.*, 2015) and ice core proxy data (*Moore*, 2013), this indicates a strengthening before 1979. In the framework of tropical expansion/contraction, these changes have been previously linked to sulphate forcing (*Allen et al.*, 2012, 2014; *Allen and Ajoku*, 2016; *Ming et al.*, 2011), especially during the summer (*Tao et al.*, 2016), but the sign reversal associated with the evolution of aerosol forcing throughout the twentieth century has not been previously discussed in the context of jet stream changes, and the appearance of noticeable trends as early as the beginning of the century has not been shown yet.

The remote impact on monsoon precipitation found here in the CMIP5 models is consistent with *Polson et al.* (2014). For western Africa, observations show similarly a

drying during 1950-1985, and a recovery thereafter (*Nicholson*, 2013), and the region has been identified as sensitive to aerosol forcing (e.g., *Rotstayn and Lohmann*, 2002; *Ackerley et al.*, 2011). *Dong et al.* (2014a), who found both Asian and European sulphur dioxide emissions relevant for the decreased West African precipitation used a single model. Our results, based on a range of CMIP5 models, also indicate the predominant importance of NAEU emissions on summer monsoon precipitation over western Africa. The overall weakening of the South Asian monsoon during the second half of the twentieth century forced by anthropogenic aerosols has been acknowledged before (e.g., *Bollasina et al.*, 2011). While other studies found regional and remote aerosols responsible in varying ratios (e.g. *Bollasina et al.*, 2014; *Guo et al.*, 2015), we show that considering the periods with increasing and decreasing remote emissions separately indicates remote emissions to be most important. For East Asia, we found remote emissions not dominant during 1975-2005, consistent with strong impact of local aerosols (e.g., *Guo et al.*, 2013), but our results do not exclude substantial impact of remote aerosols, especially before 1975, and are not inconsistent with a mechanism of remote aerosol impact on monsoon precipitation found in earlier studies (*Cowan and Cai*, 2011; *Dong et al.*, 2015). Note also that these precipitation changes might mediate even more remote aerosol impact through associated changes in the atmospheric dynamics (Section 2.C).

The models used in this study explore the range of climate sensitivity and aerosol forcing of those CMIP5 models that include a representation of indirect effects, from those with weak (e.g. IPSL-CM5A-LR) to those with strong (e.g GFDL-CM3) indirect effects (*Zelinka et al.*, 2014). Previous studies, however, showed substantial differences between the response to historical aerosol emissions in CMIP5 models with and without a representation of aerosol indirect effects (*Wilcox et al.*, 2013; *Guo et al.*, 2015); other models, which neglect indirect aerosol effects, might therefore misrepresent the response to aerosol emissions as identified in this study.

While the use of historical single- and all-forcing simulations allows us to identify features of aerosol impact within the system of interactions and feedbacks -insofar represented in the models-, targeted simulations would allow a more rigorous disentan-

glement of the effects of aerosols from different source regions, including NA and EU. Similarly, the CMIP5 models' differing aerosol representations increase the robustness of our findings, but also prevent us from exploring the mechanisms of aerosol impact further. A future study with a different focus would thus complement our work and help understand better the physical mechanisms mediating NAEU aerosol impact.

To conclude, the findings add valuable information about the robustness of the aerosol impacts as well as new insights on their climate footprint, such as their modulation of DTR and the jet stream. The symmetry of the simulated impacts during the period of increasing and of decreasing emissions also sheds light on the changes to be expected from future reductions in aerosol emissions from NAEU and elsewhere.

Appendix 2.A Possible Non-Linearities between Simulated Sulphate Load, AOD, and Near-Surface Temperature

To (1) highlight model differences in the simulated range of sulphate loading and AOD, to (2) support further the notion of sulphate aerosol dominance of AOD, and (3) to assess whether we can see non-linearities in the relationship between aerosol content and temperature, we show how the summer (JJA) mean variables relate to each other in the historical CMIP5 aerosol-only simulations, averaged over the globe as well as over Europe and the Indian ocean as examples for regions with relatively high and low, respectively, aerosol concentrations (Fig. 2.A.1).

(1) Firstly, we note substantial inter-model differences in the absolute values as well as range and rate of change in sulphate loading and AOD. Differences between the individual simulations of the same model i.e. the influence of internal variability are much smaller.

(2) In all models, we see the near-linear relationship between sulphate loading and AOD over the regions affected by anthropogenic emissions (i.e. less so over the Indian Ocean), which, given the different emission histories of other aerosol species (Fig. 1.2), is interpreted as an indication of sulphate aerosol dominance on AOD. Note that after the peak in sulphate loading, AOD does not return exactly to the values it had during the earlier increase in sulphate loading, assumingly since the emissions of other aerosol species do not decline.

(3) Some models (e.g. GFDL-CM3, green) do seem to show a non-linear relationship between AOD and temperature over the Indian ocean. Over Europe, the sulphate loading even at 1860 is already above the range in which substantial non-linearities are expected (for IPSL-CM5A-LR, HadGEM2-ES, CSIRO-Mk3.6.0, and NorESM1-M at least; *Wilcox et al.*, 2015). Note also that some of the non-linearity happens already in the step from SO_2 emission to sulphate load (e.g., *Carslaw et al.*, 2013).

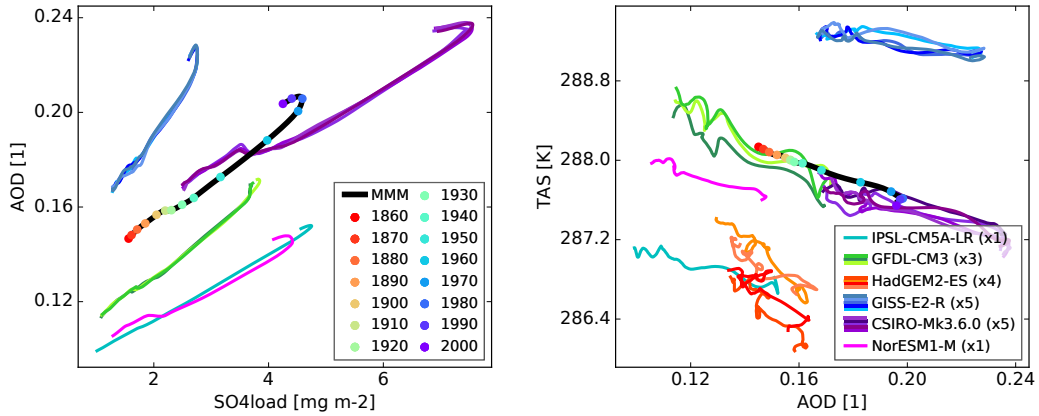

(a) globe

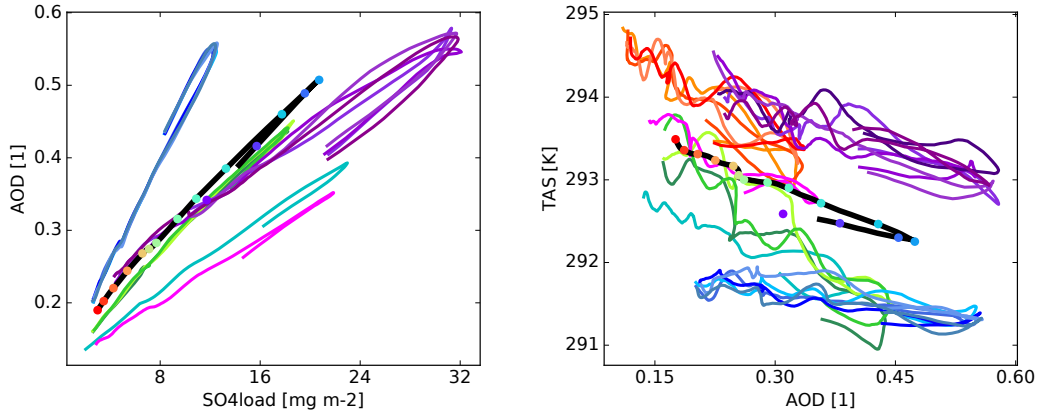

(b) Europe (35-60°N,0-60°E)

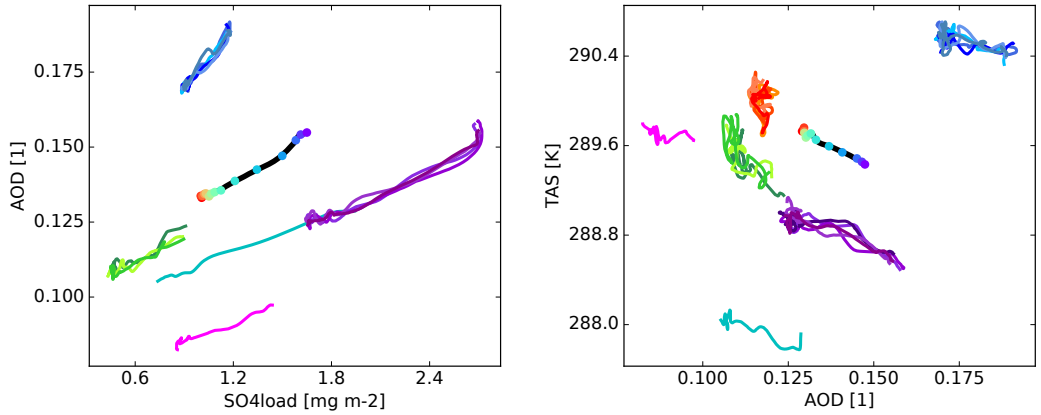

(c) Indian Ocean (0-60°S,50-100°E)

Figure 2.A.1: Relationship between JJA-mean (left) sulphate loading and AOD, and (right) AOD and near-surface temperature in the aerosol-only CMIP5 simulations, averaged over (top) the globe, (middle) Europe, and (bottom) the Indian Ocean. The relationship between the multi-model mean (MMM, black) variables is shown in addition to that in each simulation separately (coloured lines). For the MMM, decadal means are additionally plotted as coloured dots. The models used are those in Tab. 1.1 except for (left) HadGEM2-ES (no sulphate loading data available) and (left and right) CanESM2 (no AOD data available). To all data shown as lines, a 11-7 year filter is applied before the visualisation, which shortens the data compared to the decadal means.

Appendix 2.B Sensitivity Analysis for the Joint-EOF Results

For the results from the joint EOF analysis shown in Fig. 2.3, we choose the time period 1860-2004, the area of the NH excluding the Pacific (0°-80°N, 120°W-150°E), and smoothing with subsequent 11- and 7-year running means. We find in a sensitivity analysis the results to be robust to the choice of time period (e.g. until 1990 or 1970 instead of 2004 and/or starting in 1900 instead of 1860). If we use either the whole NH or Europe only, the resulting patterns and time series also look very similar. They are furthermore independent of details of the temporal filtering, tested with using running means with a single window length as well as 10- and 20-year Lanczos filters.

Appendix 2.C Further Circulation Changes Associated with the Subtropical Jet

Modelling studies found that anthropogenic aerosols can excite hemispheric-wide Rossby waves through latent heat release associated with changes in tropical convective precipitation (*Ming et al.*, 2011; *Lewinschal et al.*, 2013). Such waves, also known as "circumglobal teleconnection pattern" (*Branstator*, 2002), may be relevant for remote aerosol impact due to their association with phenomena remote to their source region such as North American cold events (*Harnik et al.*, 2016), European pressure and precipitation changes (*Saeed et al.*, 2014), and the Indian summer monsoon (*Yadav*, 2017). *Allen and Ajoku* (2016), however, found these waves neither important in historical simulations nor future projections with the CMIP5 model suite and a slab-ocean model (CAM5).

Our trend analysis shows an anomalous mid-latitude (around 45°N) zonal wave pattern across the globe in the aerosol-only ensemble if applied to meridional wind speed at 300 hPa (Fig. 2.C.1, left) and geopotential height anomalies (not shown). The wave

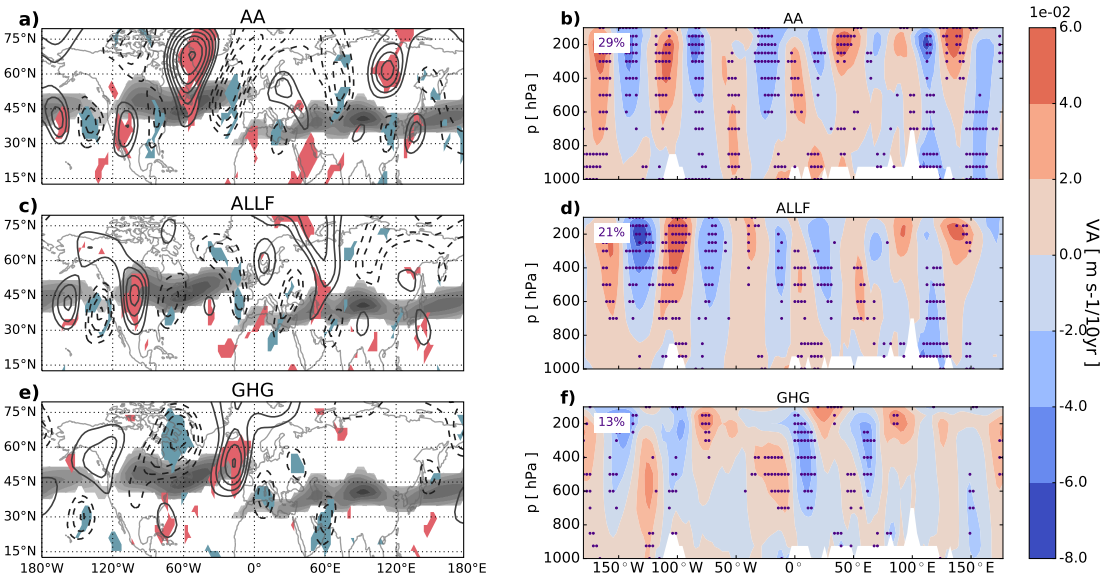

Figure 2.C.1: Linear trends in JJA meridional wind (left) at 300 hPa (contour lines) and (right) averaged over 20-50° N during 1900-1974 for the multi-model mean of the (top) AA, (middle) ALLF, and (bottom) GHG simulations. (Left) Dashed contour lines indicate negative trends. The contour interval is 0.0125 m/s/decade. The 0.0000 and ±0.0125 contours are not displayed for clarity. Grey shading indicates where the climatological zonal wind speed at 300 hPa exceeds 12.5 m/s as a rough estimate of the jet stream position. Colouring (red for positive trends, blue for negative ones) indicates where at least 6 out of the 7 models' ensemble means agree on sign. (Right) Data are masked at longitudes and pressure levels where all latitudes are masked by orography, and stippling indicates where at least 6 out of the 7 model's ensemble means agree on sign. Anomalies from the area-mean trend per level are shown.

pattern follows the subtropical jet's latitudinal variation with longitude, indicating that the jet serves as its wave guide. It is furthermore robust across all models considered in the AA ensemble (colour shading), and is also recognisable, albeit to a lesser extent, in the ALLF ensemble, especially in the western hemisphere. The GHG and NAT ensembles are much less in agreement with ALLF than AA is, nor is their trend pattern circumglobal. A longitudinal cross section (Fig. 2.C.1, right) shows that the wave pattern extends over all pressure levels similarly in the AA and ALLF ensembles.

We thus note that in the set of CMIP5 model studied here, anthropogenic aerosol emissions from NAEU might have had an additional long-term impact of a circumglobal wave pattern. This finding emphasises the possible dynamic pathways of remote aerosol impacts in addition to those reported in Section 2.4.

Chapter 3

Detectable Impact of Local and Remote Anthropogenic Aerosols on the Twentieth Century Changes of West African and South Asian Monsoon Precipitation

3.1 Introduction

In this chapter, we contrast the impact of anthropogenic aerosols from different emission source regions (NAEU, China, South Asia) on individual summer monsoon regions (West Africa, South Asia) and use the results to attribute observed precipitation changes. Using a detection and attribution approach, we determine whether -and to what extent- the different forcing fingerprints contribute to the observed changes, or whether the latter could be explained by internal variability alone. The finger-

prints are time series of regional-mean precipitation anomalies derived from global climate model simulations in which emissions from individual source regions are kept at pre-industrial levels while evolving everywhere else. In order to shed light on the dynamical mechanisms driving the detected precipitation signals, we additionally investigate changes in large-scale atmospheric circulation and temperature gradients.

The existing simulations were created with the U.S. National Oceanic and Atmospheric Administration (NOAA) Geophysical Fluid Dynamics Laboratory (GFDL) coupled climate model version 3 (CM3). It was chosen because it treats aerosol-cloud interactions and aerosol indirect effects explicitly (*Donner et al.*, 2011), simulates key climatological features of the Asian monsoon more realistically than most other models (*Sperber et al.*, 2013), and is one of the models with smallest biases in summer low-level clouds over West Africa, a key factor modulating monsoon precipitation there (*Hannak et al.*, 2017).

The remainder of this chapter is organised as follows: First we present the observational and model data used and describe the analysis methods, including an overview of the detection and attribution methodology (Section 3.2). The results from the analysis of spatio-temporal changes in precipitation over the West African and South Asian monsoon regions are then shown (Section 3.3), followed by the analysis of the underlying physical mechanisms associated with the precipitation changes, highlighting the links with variations in the large-scale atmospheric circulation (Section 3.4). A discussion concludes the chapter (Section 3.5).

3.2 Data and Methods

3.2.1 Observations and Models

Two monthly gridded observational datasets are used to calculate the mean summer (June-September, JJAS) precipitation anomalies in the West African and South Asian monsoon regions for 1920-2005: the Climate Research Unit dataset, CRUTS3.24

(CRU; *Harris et al.*, 2014), and the Global Precipitation Climatology Centre dataset (GPCC; *Schneider et al.*, 2014b). Both datasets make use of the same raw station data, but apply different methodologies to derive the gridded products. Both may contain artifacts caused by inhomogeneities such as variable number of stations per grid box over time (*Beck et al.*, 2004) and infilling. In particular, the methodology of CRU gives greater temporal fidelity while GPCC uses a larger number of stations. The analysis focuses on the West African and South Asian monsoons, which are two of the largest components of the global monsoon system and located entirely within the tropics. They have been shown to be interconnected at decadal time scales (e.g., *Feudale and Kucharski*, 2013). The availability of extensive station records in these regions dating back to the 1920s increases the detectability of the forced signals. Changes are examined for the June-September months as they encompass the entire monsoon season throughout the domain. For the analysis of the latitudinal position of the ITCZ, we use additionally satellite data from the Global Precipitation Climatology Project (GPCP; *Adler et al.*, 2003).

The model data consist of a set of four twentieth-century experiments with the 1°x2.5° GFDL-CM3 model. Each experiment is a three-member ensemble, forced with different combinations of time-evolving anthropogenic aerosol emissions (i.e., all other forcings are kept at pre-industrial levels). Three of the ensembles have global time-varying historical emissions with the exception of those from (1) North America and Europe (NoNAEU), (2) South Asia (NoSA), or (3) China (NoCH) fixed at pre-industrial levels. The fourth experiment has historical aerosol emissions for South Asia only and pre-industrial aerosol emissions in the rest of the world (SAonly) (Fig. B.1). These experiments are used to derive response patterns to regional aerosol emissions, and are interpreted in the context of additional simulations with global time-varying anthropogenic aerosol (AA), greenhouse gas (GHG), and natural (volcanic and solar; NAT) forcing individually (3 members each), as well as their combination in the all-forcing ensemble (ALL, 5 members). Taking regional emission changes away in the NoNAEU, NoSA, and NoCH simulations rather than exclusively including them, as well as the complementarity of the SAonly and NoSA cases, reduces the poten-

tial problem of non-linearities in the interactions when simulating the response to regional aerosols separately (Fig. B.2 and Section 3.2.3). Note that dust emissions from climatologically prescribed sources are a function of wind speed and direction. We also use CMIP5 simulations (Tab. 1.1; *Taylor et al.*, 2012) to compare with the results of the detection and attribution analysis from GFDL-CM3. For consistency, only the CMIP5 models are selected for which ALL, AA, GHG, and NAT simulations are available and which have a spatial resolution finer than that of the observations.

Following *Hsu et al.* (2011) and *Polson et al.* (2014), we define the monsoon domain to encompass the grid boxes for which the observed annual precipitation range (difference between the May-September and November-March averages) exceeds 2 mm day^{-1} and more than 55% of the annual total precipitation occurs during May-September (Fig. B.3). Our analysis is thus based on the climatological monsoon domain (i.e., the area is fixed throughout the period), which is a reasonable assumption as changes in monsoon precipitation associated with variations in the size or location of the region represent a minor contribution to the total precipitation change (*Polson et al.*, 2014). Both observational datasets are interpolated to the same 2.5°x2.5° grid before applying the above criteria. Grid boxes which have less than 70% land (based on a common land-sea mask) are excluded, and the South Asian region is limited to 90°E (e.g., *Wang et al.*, 2001). For each region, this procedure gives one continuous monsoon area per observational dataset, to which model data are masked before calculating regional-mean time series in order to keep consistency with the respective observational coverage.

3.2.2 Linear Trends and Aerosol Emissions

The 1920-2005 period encompasses the peak of global anthropogenic aerosol emissions around 1980, driven by the changes in the Northern Hemisphere sulphate emissions. This global signal results from the combination of very different temporal evolutions of regional emissions, each with its different time of peak -some not yet peaked- and rate of increase/decrease following regional industrial development and

air-pollution regulations. Considering continental regions, North American emissions peaked around the 1970s and European emissions a decade later, while Asian emissions started to increase rapidly only from the 1950s (Fig. B.4) and are now the largest contributor to the global aerosol loading. The simulated radiative forcing (e.g., *Hansen et al.*, 2005) in the experiments with regional aerosol emissions reflects these emission histories, both in the spatial patterns of long-term change (Figs. B.5a-d, B.6) and in the time series over the emission regions (Fig. B.5e-f).

The spatial patterns of precipitation change are shown by computing the linear trend at each grid point. Trends are calculated over the entire 1920-2005 record as well as over two shorter sub-periods, 1920-1975 and 1975-2005, separately. This allows us to not only characterise the long-term changes, but also to distinguish between periods of increasing and decreasing North American and European emissions. Note that while Asian emissions increased both before and after 1975, their trend during 1975-2005 is twice as large as that over 1920-1975. The robustness of the ensemble-mean trend at each grid point is measured by the number of ensemble members that agree on the sign of the changes. For each time period, the differences in the ensemble-mean precipitation response between the experiments with regional aerosol emissions only and the one with global aerosol emissions are also shown, with a two-tailed Student's t-test used to evaluate where the regional aerosol ensembles are inconsistent with the AA ensemble at the 95% confidence level as a measure of the significance of the differences.

3.2.3 Detection and Attribution

The 1920-2005 time series of June-September precipitation anomalies (with respect to the 1920-2005 climatology) are calculated for both observations and model simulations by averaging precipitation over each monsoon region and successively applying a 5-year running mean to reduce high-frequency variability. Total least squares regression (*Allen and Stott*, 2003) determines a scaling factor for the model ensemble-mean

time series, which defines the forced fingerprint, **F**, in observations

$$\mathbf{y} = (\mathbf{F} + \varepsilon_{\text{finger}})\beta + \varepsilon_{\text{noise}} \tag{3.1}$$

where **F** is a vector of length *I*, where *I* represents time, and **y** is a rank-*I* vector of the observed monsoon precipitation. β is the scaling factor corresponding to the magnitude of the forced fingerprint in the observations, ε_{noise} is the noise associated with internal climate variability in the observations, and ε_{finger} the internal variability associated with the finite ensemble size of the model simulations. Best estimates of just the forced component of the observations, $\tilde{\mathbf{y}}$, and of the model fingerprints, $\tilde{\mathbf{F}}$, are calculated using

$$\tilde{\mathbf{Z}} = \mathbf{Z} - \mathbf{Z}\tilde{\mathbf{v}}\tilde{\mathbf{v}}^T \tag{3.2}$$

where $\mathbf{Z} \equiv [\mathbf{F}, \mathbf{y}]$, $\tilde{\mathbf{Z}} \equiv [\tilde{\mathbf{F}}, \tilde{\mathbf{y}}]$, and $\tilde{\mathbf{v}}$ contains the eigenvector coefficients used to calculate β in Eq. 3.1.

Samples of climate noise, estimated from pre-industrial control simulations from the CMIP5 models used, are then added to $\tilde{\mathbf{F}}$ and $\tilde{\mathbf{y}}$, and β is recalculated. The distribution of β thus gives the uncertainty on the scaling factor due to internal climate variability. Where $\beta > 0$ at the 5% significance level, the forced fingerprint is said to be detected. Because climate models tend to underestimate the observed temporal variability in JJAS total precipitation by a factor of 1.5-2 over the monsoon regions considered (*Polson et al.*, 2014), we repeat the analysis, doubling the model variance when calculating the noise samples. Where a forcing is detected, we also test whether the variability of the residual, i.e. the component of the observations not explained by the forcings, is not larger than expected from the 5-95% range of internal variability from the control samples as a consistency check.

The ALL fingerprint is a combination of the response to a number of different individual forcings that for the regions considered add approximately linearly (Fig. B.7). Our main one-signal analysis tests whether this combined forcing and which individual forcing can be detected when regressing them onto the observations one at a time. We also perform a two-signal analysis to see whether we can additionally separate

the role of these individual forcings in driving the observed changes by simultaneously regressing two fingerprints onto the observations. When hereby regressing a single-forcing fingerprint simultaneously with the ALL fingerprint, we need to account for the single forcing already being present in ALL. This is done by combining the scaling factors to obtain the scaling factor for all others forcings (OTH), i.e. for forcings in ALL apart from that specific single forcing. For NoSA vs. ALL, for example, OTH would comprise the simulated response to everything except the NoSA forcing, i.e. South Asian (SA) aerosols, GHG, and NAT. For a detailed description of the implementation of the total least squares method see *Polson et al.* (2013).

3.3 Results

3.3.1 Spatial Patterns of Precipitation Change

During the whole period (1920-2005), observed precipitation exhibits a clear decrease across much of the West African and South Asian monsoon land regions (Fig. 3.1a,b), which is also present in the GFDL-CM3 ALL ensemble and further extends to the nearby oceanic regions (Fig. 3.1c). Comparison between the trends averaged over both monsoon regions (shown in blue and red in Fig. B.3a) for this period in the ALL ensemble (-0.043 mm/day/decade) with those in the single-forcing ensembles (Fig. 3.1d-f) indicates that this ALL drying pattern is dominated by the response to time-varying anthropogenic aerosols (-0.060 mm/day/decade for AA) and natural forcings (-0.015 mm/day/decade) rather than by GHGs, which cause a wettening instead (+0.032 mm/day/decade).

Across West Africa, the regional aerosol experiments that include time-evolving North American and European emissions (NoSA and NoCH, Figs. 3.1h,i, B.10h,i) produce a pattern of drying consistent with that of the global aerosol ensemble (AA, Figs. 3.1f, B.10f). In the experiments which exclude these emissions, on the other hand, precipitation changes over the region are negligible and inconsistent (Figs. 3.1g,j, B.10g,j).

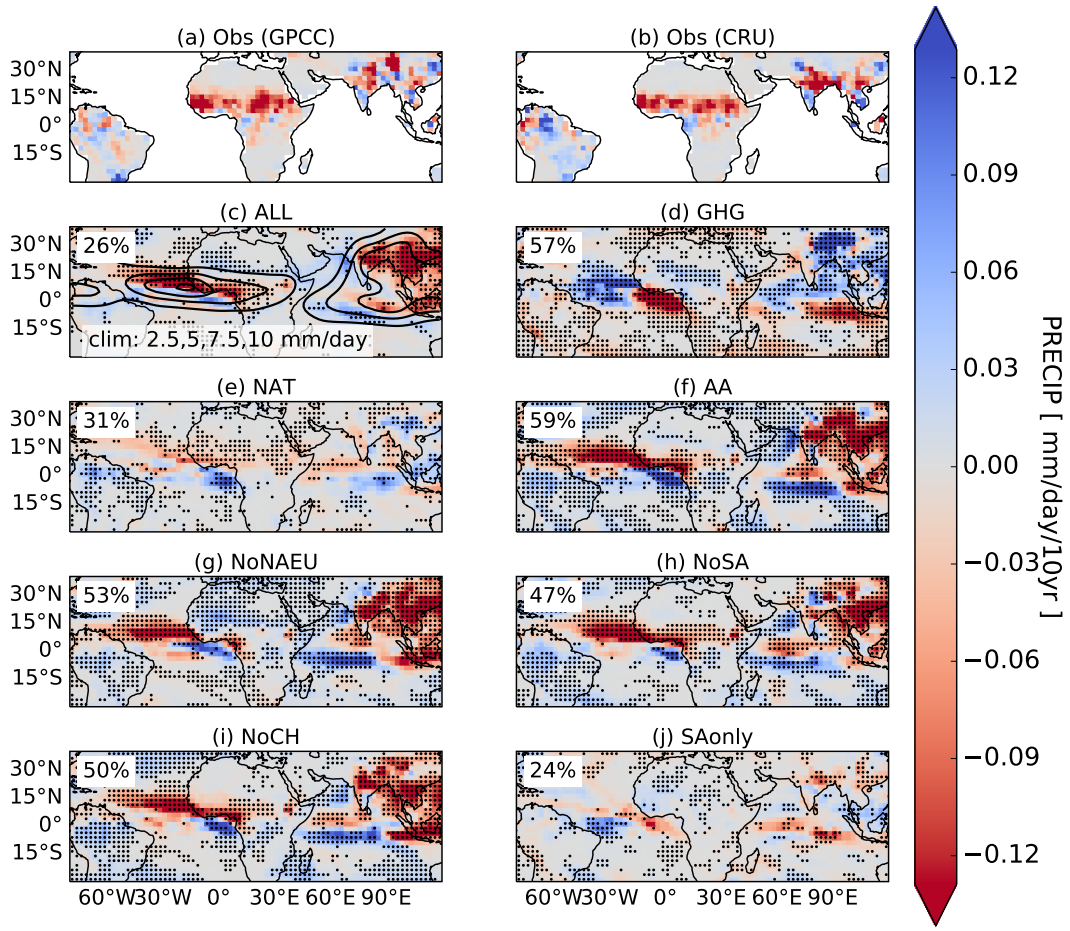

Figure 3.1: Observed and simulated summer (JJAS) precipitation linear trends (mm/day/decade) for 1920-2005. Shown are observed (a) CRU and (b) GPCC, and ensemble mean for (c) all external forcings (ALL), (d) greenhouse gas forcing (GHG), (e) natural forcing (NAT), (f) global anthropogenic aerosol forcing (AA), (g-j) global anthropogenic aerosol forcing with regional emissions set to pre-industrial levels for (g) North America and Europe (NoNAEU), (h) South Asia (NoSA), (i) China (NoCH), and (j) all but South Asia (SAonly). Stippling shows where the respective ensemble agrees on the sign of the trend, and numbers in the top left corner give the fraction of stippled points within the displayed area. In (c), black contour lines (labels at the bottom) give the climatological summer (JJAS) precipitation from a 500-year pre-industrial control simulation with the same model. See also Fig. B.10, which shows the same data only for the considered monsoon regions.

The ensemble-mean AA trend averaged over the West African monsoon region (shown in blue in Fig. B.3a) amounts to -0.031 mm/day/decade. We interpret the difference in the ensemble-mean trends of AA and NoNAEU (Fig. 3.2b) as the trend induced by North American and European aerosol emissions alone, and conclude that they cause a statistically significant trend of -0.035 mm/day/decade. This appears to be the largest contributor to the changes due to all but South Asian aerosols (-0.038 mm/day/decade for AA-SAonly, 3.2e), and thus also the AA trend, while aerosols emitted from South Asia or China play a much smaller role (0.006 mm/day/decade for AA-NoSA, 3.2c), and 0.005 mm/day/decade for AA-NoCH, 3.2d). The long-term drying over West Africa related to non-Asian anthropogenic aerosol emissions is also dominant over changes related to other forcing agents (GHG, NAT), as illustrated by the differences in the trends between the ALL and the regional-aerosol ensembles (Fig. B.13a-e vs. Fig. 3.2a-e).

The whole period (1920-2005) encompasses both the gradual increase in North American and European (NAEU) aerosols until 1975 (dominating the overall change) and the subsequent rapid decrease until 2005. Examining the two periods separately, Fig. 3.2(f-o) shows that NAEU emissions were also the most influential driver of the 1920-1975 precipitation reduction in ALL and AA: The NoNAEU and SAonly simulations are statistically different at the 95% confidence level from the AA simulations over West Africa, while the NoSA and NoCH simulations are not (Fig. 3.2g-j; also Figs. B.8, B.11). The mean trend in the global aerosol simulations over this time period (1920-1975) is 0.048 mm/day/decade over the West African monsoon region, which amounts to an overall change during 1920-1975 of nearly 10% of the climatological value of 3.4 mm/day (as calculated as the summer (JJAS) mean over the 500 years of a pre-industrial control run). During the 1975-2005 period, an increase in precipitation is seen in observations in much of the West African monsoon region, especially in the North (Figs. B.9a-b, B.12a-b). The ALL, GHG, and AA ensemble means all show a similar pattern, indicating contributions from both GHG and ALL (Figs. B.9c,d,f, B.12c,d,f). However, there is still a decreasing trend in the AA ensemble mean of -0.017 mm/day/decade area-averaged across the region, and the sign of the

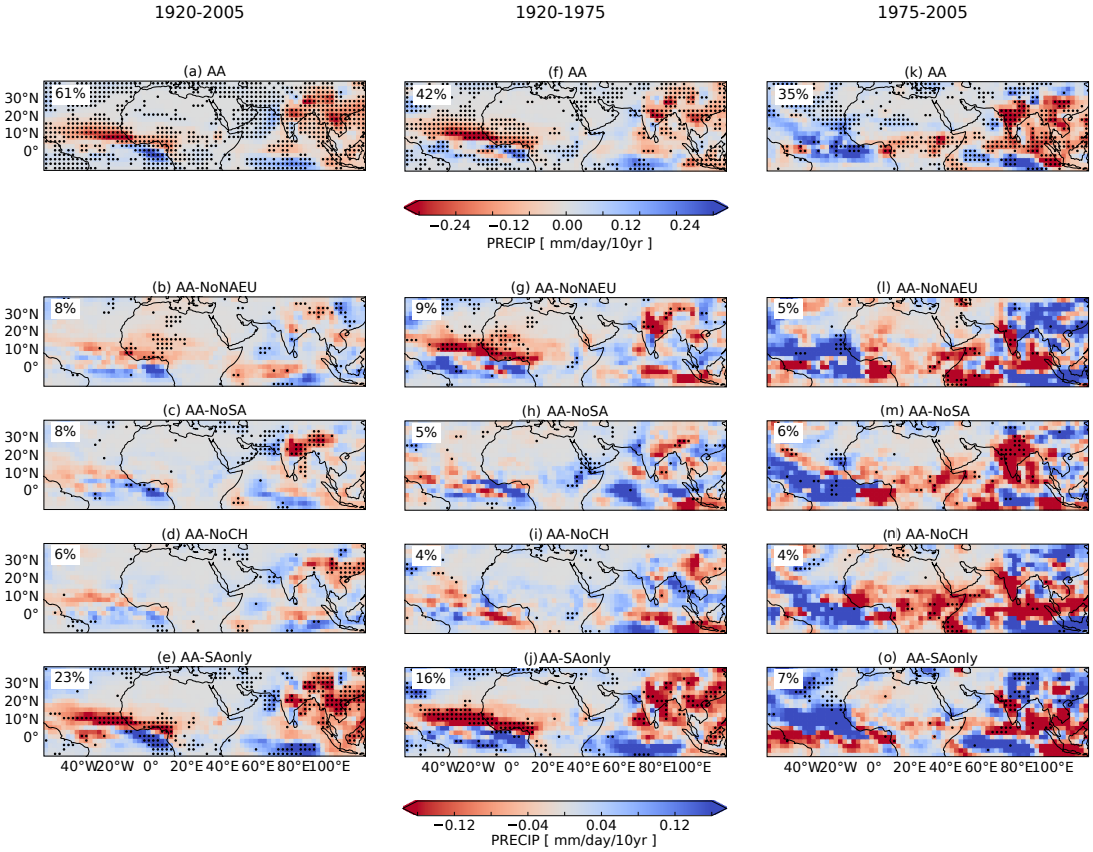

Figure 3.2: Simulated summer (JJAS) precipitation linear trends (mm/day/decade) in the global anthropogenic aerosol (AA) ensemble mean (first row) and the difference between the precipitation trends in the AA ensemble mean and the ensemble means of the regional anthropogenic aerosol simulations (mm/day/decade) for (a-e) 1920-2005, (f-j) 1920-1975, and (k-o) 1975-2005. The second row shows (b,g,l) AA-NoNAEU, indicating the impact of North American and European aerosols. The other rows show (c,h,m) AA-NoSA for South Asian aerosols; (d,i,n) AA-NoCH for Chinese aerosols; and (e,j,o) AA-SAonly for all but South Asian aerosols. Stippling in (a,f,k) shows where the AA ensemble agrees on the sign of the trend, and stippling in (b-e,g-j,l-o) shows where differences between the AA ensemble and regional aerosol ensemble are statistically significant at the 95% confidence level using a t-test. Numbers in the top left corner give the fraction of stippled points within the displayed area.

trends are not consistent across simulations, suggesting internal variability is too large compared to the forced signal during this period to clearly distinguish the influence of aerosol forcing.

Over South Asia, the largest drying trends during 1920-2005 in both the observations and the ALL and AA ensembles (Fig. 3.1a-c,f) are over northern India. From Fig. 3.2(b-e), we see that local emissions have a share in causing the aerosol-forced drying, as the NoSA and AA ensembles are statistically different. The combined influence of remote aerosols also seems to be important, as the SAonly and AA ensembles are also significantly different in northern India. Neither the NoNAEU nor the NoCH ensemble, however, show significant differences from AA in this region, which precludes the attribution of the AA trend to any specific aerosol source region. Across the South Asian monsoon region (shown in red in Fig. B.3a), global anthropogenic aerosols induce a precipitation decline of -0.089 mm/day/decade in the model, equivalent to an overall change during 1920-2005 exceeding 10% of the climatological value (7.4 mm/day). The differences between this and the ensemble means of the regional-aerosol simulations amount to -0.007 mm/day/decade for AA-NoNAEU, 0.003 mm/day/decade for AA-NoCH, and -0.064 mm/day/decade for AA-SAonly over this region (Fig. 3.2b-e). The value of -0.064 mm/day/decade for AA-NoSA indicates that local emissions are the largest single contributor to precipitation changes in the AA simulations during 1920-2005.

During the shorter periods, both observed and simulated precipitation trends over South Asia are generally more heterogeneous, and the simulated trends differ more from the observed ones (Figs. B.8-B.9, B.11-B.12). During 1920-1975, neither ALL nor AA are able to reproduce the observed wettening over western India (Figs. B.8, B.11). In the model, non-local emissions are again important to produce the AA trends (Fig. 3.2j) and can in this case be related to NAEU emissions (Fig. 3.2g), while the ensemble without South Asian emissions is not different from the AA ensemble (Fig. 3.2h). During the second period (1975-2005), the spatial trend patterns of the two observational datasets differ more from each other than during the first half of the record, with CRU (Fig. 3.2k) showing more drying in the northern

and central parts of the South Asian monsoon region than GPCC (Figs. B.9a-b, B.12a-b). The simulations are broadly consistent with either observational dataset. During this period, both the increase of local South Asian emissions and the decrease of North American and European aerosols seem important for the changes in South Asian precipitation due to global anthropogenic aerosol forcing (Fig. 3.2k-o). The changes due to local aerosol emissions alone are also dominant over the changes due to GHG and NAT forcing (Fig. B.13).

3.3.2 Time Series of Precipitation Change

The above analysis of the spatial distribution of the precipitation trends across the West African and South Asian monsoon regions is here complemented by the study of the time series of area-averaged precipitation anomalies over the two regions. This yields additional information on the timing and time scale of these precipitation variations, and provides support to the use of linear trends to estimate the changes.

Over West Africa, observed precipitation underwent a pronounced decrease from the 1960s to the mid-1980s, followed by a slight recovery until 2005 (Fig. 3.3). Simulations that include time-varying anthropogenic aerosol emissions from North America and Europe (ALL, AA, NoSA, NoCH) also show a decrease until the 1980s and a subsequent recovery, although the drying occurs here only gradually, in contrast to the observations. From 1945-1965 and in the early 1980s, the observations are only just consistent with or are outside the CMIP5 multi-model range (Fig. 3.3a). This discrepancy may be due to errors in the observations or in the models' forced response. Note also the steep decrease in observed precipitation followed by a rapid recovery in the first half of the 1980s, which is absent in the aerosol-only simulations, but visible to some extent in the simulations that include natural forcing (ALL, NAT) (Fig. 3.3a). It coincides with the El Chichón volcanic eruption in 1982, which is consistent with other studies that find drying in monsoon regions after volcanic eruptions (e.g., *Iles et al.*, 2013).

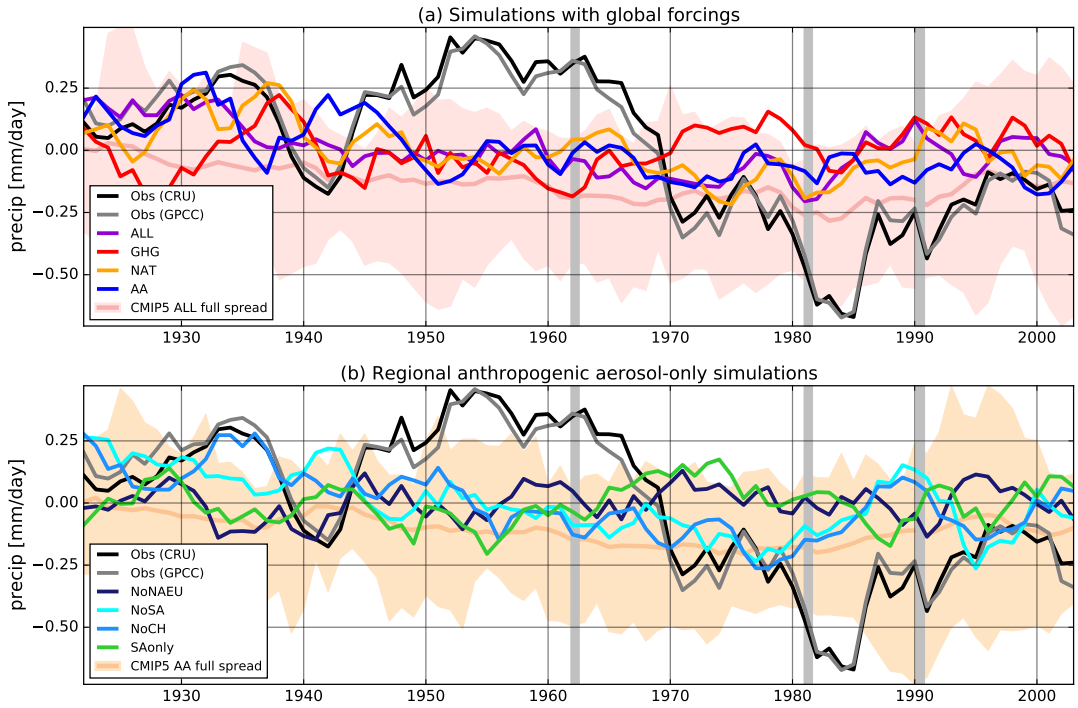

Figure 3.3: West African summer (JJAS) monsoon precipitation anomalies (mm/day) with respect to the 1920-2005 climatology for observations (CRU (black) and GPCC (grey)) and ensemble-mean anomalies for GFDL-CM3 simulations with (a) global forcings and (b) regional anthropogenic aerosol forcings (ensemble abbreviations as in Fig. 3.1). The 5-year running mean is shown for all time series; note that the simulated ones are ensemble means and have thus reduced variability compared to (single-realization) observations. Pink and orange shading, respectively, shows the model spread for all (a) CMIP5 ALL and (b) CMIP5 AA historical simulations. All model data are masked using the monsoon region derived from the CRU data. Silver vertical lines show large volcanic eruptions. Fig. B.14 shows the same time series multiplied by the respective best-guess scaling factors from the one-signal detection and attribution analysis.

Potential sources of observational errors include, for instance, human reading/writing error; historical changes in measurement technique and methodological biases; and incomplete station coverage. While the first issue can be assessed by comparing neighbouring station data, the second issue is inherently uncertain: The datasets are not independent since they partially rely on the same station data and are potentially subject to the same measurement biases. From the measurements to the gridded data used, a range of processing was done; for the CRU dataset, for instance, this includes the interpolation of rain gauge station anomalies from different sources into global gridded datasets, some of which had been homogenised (*Harris et al.*, 2014), but neither of the datasets used are published with an estimated uncertainty range (*Harris*

et al., 2014; *Schneider et al.*, 2014b). More fundamental errors in the derivation of the gridded datasets, on the other hand, are less likely given the agreement with satellite-derived precipitation products both in terms of climatology (e.g., *Sylla et al.*, 2013) and monthly-mean time series (e.g., *Zittis*, 2018) during the last 25 years over West Africa. Station coverage for CRU is relativity high for West Africa (Fig. B.15), and GPCC tends to incorporate even more station data (*Schneider et al.*, 2014b). To conclude, observational error cannot be excluded to contribute to the discrepancies between model and observations, but no evidence so far points to higher uncertainty than in precipitation observations elsewhere. Errors in the models' forced response may be due to some aspect of internal variability not captured by the models including for example low-frequency variability in the ocean. We will account for this by increasing the control model variance in the detection and attribution analysis.

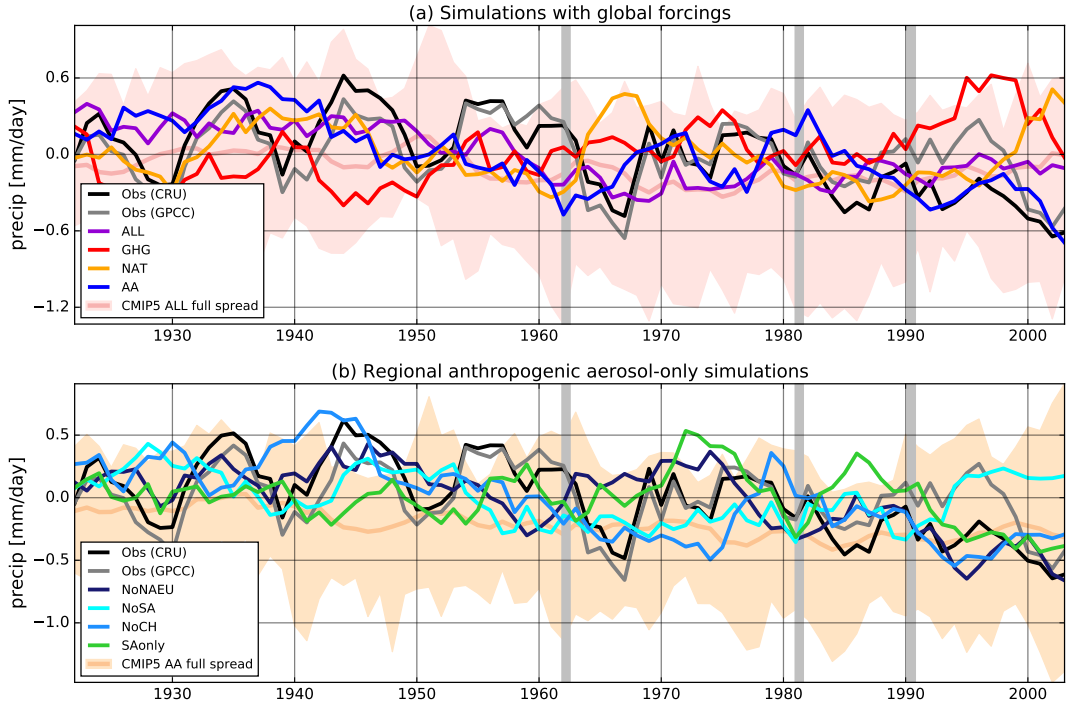

Figure 3.4: As Fig. 3.3 for South Asian monsoon precipitation anomalies (mm/day). Fig. B.16 shows the same time series multiplied by the respective best-guess scaling factors from the one-signal detection and attribution analysis.

South Asian monsoon precipitation shows a decrease during the second half of the twentieth century on top of large background decadal variability (Fig. 3.4). Only the simulations with time-varying emissions from South Asia (ALL, AA, NoNAEU, NoCH, SAonly) closely resemble this observed precipitation decrease. Note the spread

between the two observational datasets from the 1980s onwards, with noticeable differences in the 1990s. This is likely due to differences in station coverage as data availability tends to reduce towards the end of the century (*Schneider et al.*, 2014b).

3.3.3 Detection and Attribution

A detection and attribution analysis (Section 3.2.3) can link changes in monsoon precipitation and individual forcing agents in a statistically rigorous manner explicitly taking into account climate variability, which is large for precipitation. Using this approach, *Polson et al.* (2014) showed that anthropogenic aerosols are the dominant external factor influencing the observed changes in Northern Hemisphere summer monsoon precipitation during the second half of the twentieth century: Using CMIP5 multi-model mean (MMM) fingerprints to explain the observed time series of precipitation during 1951-2005 averaged over the whole Northern Hemisphere monsoon domain (thus including the South American, West Africa, South Asian, and East Asian monsoon region), the authors detected the response to global aerosol forcing in four different observational datasets, while no other external forcing was detected, and the observed changes could not be explained by internal climate variability alone either. However, the detected change was significantly larger than simulated. Motivated by these results, we test here whether global aerosol forcing also dominates the observed changes during 1920-2005 in the West African and South Asian monsoon regions separately, and whether we can distinguish the importance of the different source regions for AA by detecting the fingerprints from the different regional anthropogenic aerosol simulations in the observations. This analysis considers the time series of precipitation change rather than just the linear trend as done previously, which is especially important given the different temporal evolutions of aerosol emissions from different source regions.

For West Africa, the external forcings (ALL) both from the CMIP5 multi-model mean and GFDL-CM3 are detected in both observational datasets (scaling factors > 0; Fig. 3.5a). The observed changes are underestimated in the models, since the forced

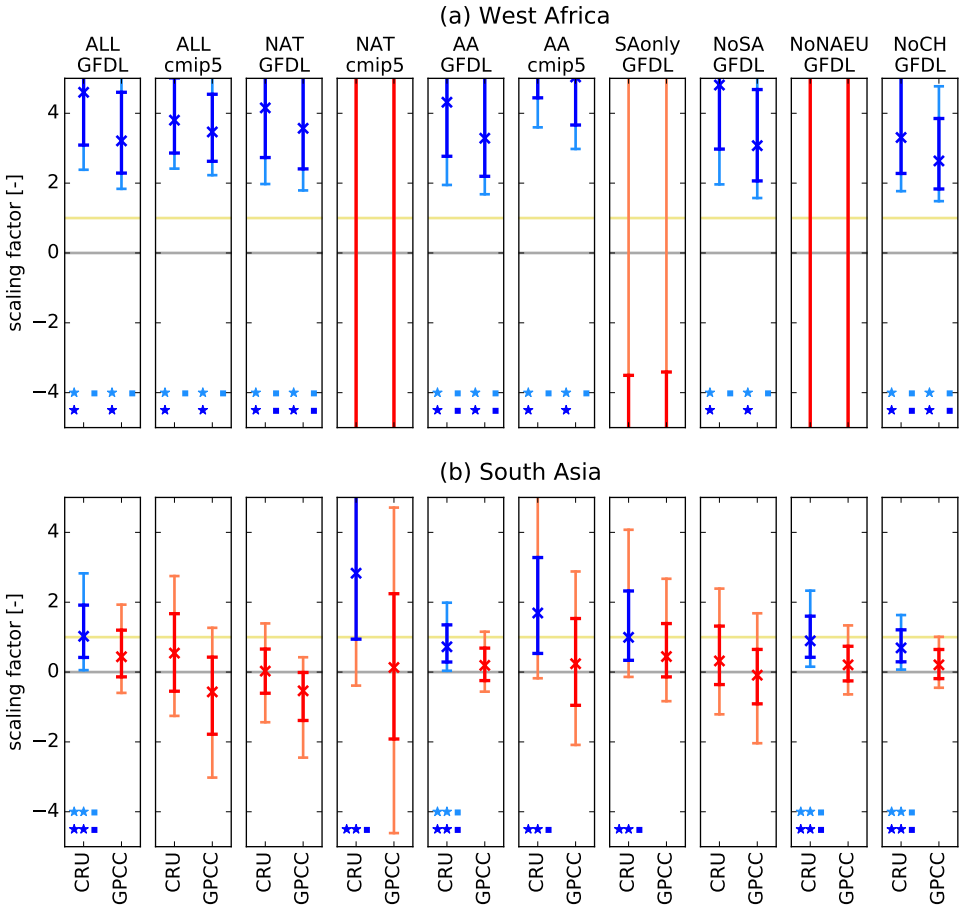

Figure 3.5: Detection and attribution of observed changes in (a) West Africa and (b) South Asia summer (JJAS) monsoon precipitation from the one-signal analysis. Scaling factors for global forcings from GFDL-CM3 (GFDL) and the CMIP5 MMM (cmip5), and regional anthropogenic aerosol-only forcing from GFDL-CM3 (ensemble abbreviations as in Fig. 3.1); results for GHG forcing in Fig. B.17. Results are shown for two observational datasets, CRU (left) and GPCC (right). Crosses show the best-guess scaling factor for the ensemble mean, thick lines are the 90% confidence interval based on the raw variance of the model control samples, and thin lines are the 90% confidence intervals when the variance has been doubled. Lines are blue when detected, red when not. The detection of a signal is further highlighted by one star (*), and two stars of the same colour next to each other (**) show where the forcing is additionally consistent with a scaling factor of 1. A filled square indicates where the variance of the residual is not larger than internal variability at the 95% confidence interval based on the raw variance of the model control samples. Light blue stars and squares as well as light blue and light red lines refer to the calculation with doubled variance.

response must be scaled up (i.e. the lower bound of the scaling factor range for ALL exceeds 1). This is consistent with the observations showing stronger trends than the all-forcing CMIP5 simulations (Fig. 3.3a). This result is robust to doubling the model internal variability, which means that the forced response is detected even if the models turned out to underestimate observed variability by a factor of two. When the variability is doubled, the residual consistency check is passed in all cases. The global aerosol (AA) fingerprints are also detected, while the GHG ones are not (Fig. B.17a), indicating the importance of aerosols rather than GHG. When using the GFDL model, NAT is also detected, while this is not the case for the CMIP5 MMM, possibly due to a stronger response to volcanic aerosols in the GFDL model compared to the other models. A two-signal analysis, performed to disentangle the role of the individual global forcings, e.g. NAT vs. AA, is inconclusive (Figs. B.18-B.20), indicating the forcings are likely too weak or the responses too similar to be detected simultaneously given internal variability. Our results nevertheless suggest that aerosols play a key role for the changes in West African monsoon precipitation. Out of the aerosol source regions, North America and Europe are found to be essential to drive these precipitation changes. That is, when emissions from these regions are included in the model fingerprints, they are detected (NoSA, NoCH, ALL, AA), otherwise they are not (SAonly, NoNAEU).

For South Asia (Fig. 3.5b), a forced response in summer monsoon precipitation is only detected if CRU observations are used (i.e., not the GPCC dataset). The difference in the detection and attribution results between these observational datasets is likely related to the previously discussed discrepancies in the time series in the 1990s, and we discuss here the results for CRU. When using the CMIP5 MMM, both the NAT and the AA fingerprint are detected, but not ALL, which is likely explained by the GHG forcing counter-acting the aerosol forcing in ALL. When using GFDL-CM3, the fingerprint of the combined forcings (ALL) is detected – while GHGs and aerosols also counter-act each other in this model, the ALL signal from GFDL-CM3 is more influenced by anthropogenic aerosols than the ALL signal from the CMIP5 MMM, likely because GFDL-CM3 has a stronger indirect aerosol forcing than most other models (*Zelinka*

et al., 2014) which are included in the CMIP5 MMM. When doubling the model internal variability, none of the signals is detected for the CMIP5 models. When using GFDL-CM3, we detect the fingerprints of all external forcings (ALL) and of global aerosols (AA), but neither those of NAT nor GHG (Figs. 3.5b, B.17b), which shows the importance of anthropogenic aerosols as simulated with GFDL-CM3 also for South Asian monsoon precipitation. The residual consistency check is passed in all cases. The scaling factors are here consistent with 1, i.e. the combination of the forcing strength and the magnitude of the model response reproduces the magnitude of the observed changes. In contrast to West Africa, local aerosol emissions seem to be the most important factor driving the observed changes in South Asia: Aerosol forcing is only detected when historical variations of South Asian aerosol emissions are included (ALL, AA, NoNAEU, NoCH, SAonly). In fact, only South Asian emissions (SAonly) are required for the aerosol forcing to be detected, at least for the best estimate of model internal variability. Conversely, aerosol forcing is not detected when emissions from South Asia are kept at pre-industrial levels (NoSA). These results are confirmed by a two-signal analysis, where we can detect the response to global-aerosol forcing versus all other forcings together (Fig. B.19) as well as the response of the simulations which include local aerosols for CRU in three out of four cases (Fig. B.20).

3.4 Pathways of Aerosol Impact

3.4.1 West Africa

The annual cycle of the West African monsoon precipitation is linked to the migration of the ITCZ, although the two phenomena have also distinct features (*Nicholson*, 2013). Yet, this classical view provides a useful framework to interpret monsoon changes in the context of large-scale circulation variations. The AA spatial pattern of 1920-2005 precipitation trends across the Atlantic shows that global aerosols caused a decrease in precipitation at the climatological northern flank of the ITCZ and an increase at its southern flank, consistent with a southward shift of the Atlantic ITCZ

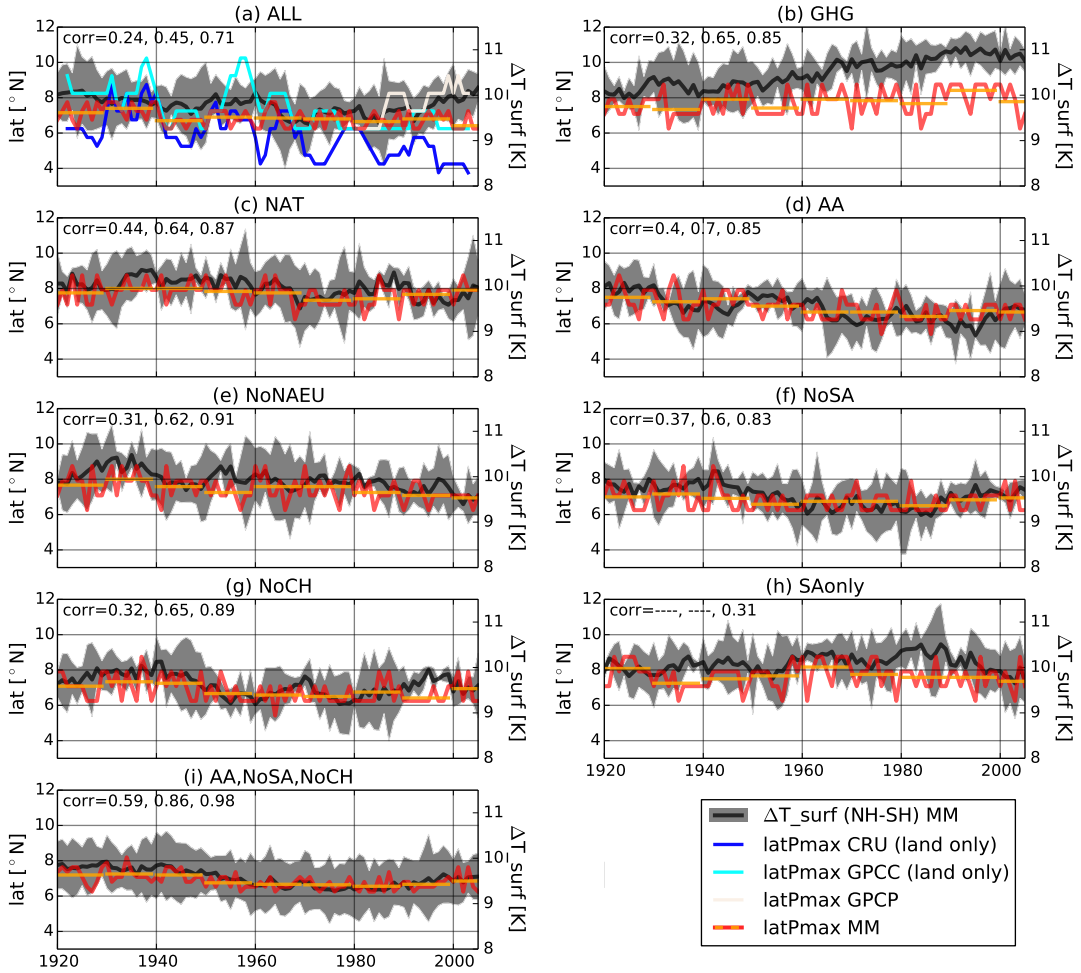

Figure 3.6: Latitude of maximum zonal mean precipitation (latPmax) over the Atlantic sector (75°W-50°E; shown by the yellow box in Fig. B.3) (left axis, in colour) as well as inter-hemispheric temperature gradient (ΔT_{surf}, land and ocean) for the same longitudes (right axis, black). The ensemble-mean time series of latPmax (annual (JJAS): red lines; decadal means: yellow lines) and ΔT_{surf} (annual (JJAS): black; 95% ensemble range: grey shading) are shown for the simulations with (a-d) global forcings and (e-h) regional-aerosol forcings (ensemble abbreviations as in Fig. 3.1); (i) shows the average across the nine simulations with evolving NAEU emissions. Numbers at the top of each panel give the correlation coefficient between ΔT_{surf} and latPmax for annual time series (as shown), the 5-year running mean, and the 11-7-year running mean, where statistically significant (pval<0.05). In (a), latPmax is also shown for the GPCP observations (creme-white), CRU observations for land only (blue), and GPCC observations for land only (cyan), all smoothed with a 5-year running mean.

(Fig. 3.1f). The aerosol signature clearly dominates the ALL pattern. Furthermore, it is also present in all regional aerosol experiments but for SAonly. For West Africa, this means a decrease in precipitation over the coastal land areas, and an increase in precipitation over the ocean to the south, thus outside the summer monsoon region.

To track the meridional displacement of precipitation across the Atlantic basin throughout the twentieth century, the latitude of maximum precipitation longitudinally-averaged over 75°W-50°E (Fig. B.3; *Philander et al.*, 1996; *Schneider et al.*, 2014a) is analysed (Fig. 3.6). The southward displacement of precipitation is notable in simulations with aerosol emissions from North America and Europe (Fig. 3.6a,d,f-g,i), with the fastest changes between the 1940s and 1960s, consistent with those in emissions (Fig. B.4). In simulations without emissions from these regions, in contrast, the shift occurs only at the end of the twentieth century (Fig. 3.6e,h). Theoretical considerations suggest that inter-hemispheric temperature differences drive the shift in the ITCZ; for aerosols, this is due to the preferential cooling of the Northern Hemisphere (*Hwang et al.*, 2013; *Rotstayn et al.*, 2015). The spatial patterns of long-term sea surface temperature (SST) change illustrate the hemispheric differences for the differently forced experiments (Fig. B.21). The time series of the inter-hemispheric temperature difference agree well with the latitudinal position of the ITCZ, with statistically significant correlations of over 0.8 for all simulations but ALL and SAonly on multi-decadal time scales (Fig. 3.6b-g), and over 0.7 for ALL (Fig. 3.6a). The much smaller correlation for SAonly (Fig. 3.6h) is not surprising given its weak forcing. Observations for land-only precipitation also show a similar tendency for a southward shift from the 1960s, while the satellite observations show a tendency for a northward shift in the latitude of maximum precipitation from the mid-1980s, similar to the models. These precipitation shifts are even clearer in the observations when the South American longitudes are excluded, and the correlations are similar if only SSTs are used to calculate the inter-hemispheric temperature gradient (not shown). The model simulations show that the northward shift in recent decades due to decreasing NAEU emissions (Fig. 3.6f) is weakened by the southward shift induced by non-NAEU emissions (Fig. 3.6h). Note that also within the non-aerosol simulations (GHG, Fig. 3.6b

and especially NAT, Fig. 3.6c), inter-hemispheric temperature difference and meridional ITCZ position correlate, consistent with a causal relationship between the two. The long-term decrease until the 1980s seen in ALL and the observations, however, is inconsistent with the increase in GHG, and much more clear in the aerosol simulations than in NAT. The classic interpretation of the West African monsoon precipitation as part of the ITCZ is thus functional here and the shift of the ITCZ, consistent with aerosol-induced changes in the inter-hemispheric temperature difference, explains part of the changes in West African monsoon precipitation.

The statistically significant difference in West African summer monsoon precipitation between the simulations including all aerosols and those excluding aerosols from anywhere but South Asia could not only point to the impact of aerosols from the major Northern Hemisphere emission regions, but also to a role of local (West African) emissions (Fig. B.22), as found for instance in recent trends for black carbon in winter (*Huang et al.*, 2009). Simulated clear-sky short-wave downward radiation and surface temperature in the West African monsoon region diverge indeed depending on whether local aerosol emissions are included (NoNAEU, NoSA, NoCH) or not (SAonly) (Fig. 3.7c,e): With local emissions, the clear-sky radiation reaching the surface decreases throughout the twentieth century concurrent with an increase in local aerosol emissions (Fig. 3.7a). All-sky downward radiation (Fig. 3.7d), which, in contrast to clear-sky radiation, takes into account cloud cover and thus also reflects circulation changes, does not show this dependency on local emissions, and neither does precipitation (Fig. 3.7f). Instead, precipitation depends on whether North American and European emissions are included (NoSA, NoCH) or not (NoNAEU, SAonly), which is consistent with the signals detected in the previous section. While local aerosol emissions may thus still have some impact on precipitation, the combined effect of remote aerosols, mainly from North America and Europe, dominates the changes in West African summer monsoon precipitation. Since clear-sky radiation over West Africa, indicative of aerosol-radiation interactions, does furthermore not change whether NAEU emissions are included (NoSA, NoCH) or not (NoNAEU), aerosols transported to West Africa, if any, are of minor importance compared to the

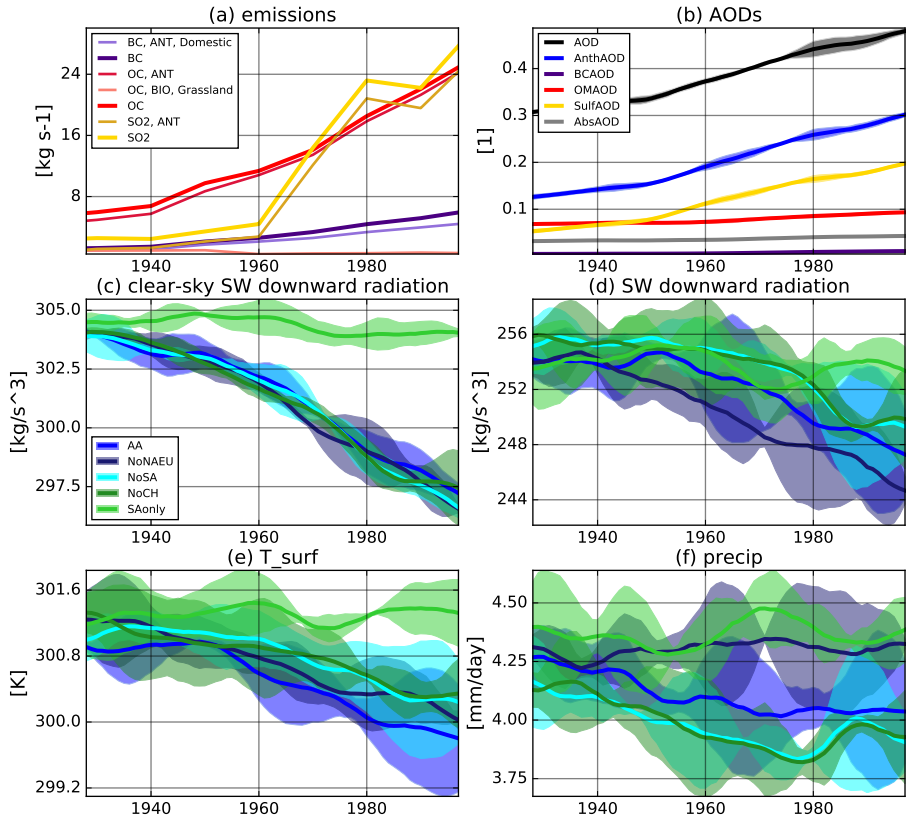

Figure 3.7: West African summer (JJAS) (a) total aerosol emissions from *Lamarque et al.* (2010) as used in the simulations, and (b) aerosol optical depth (AOD) from the aerosol-only (AA) simulations' ensemble mean as well as (c) clear-sky short-wave downward radiation, (d) all-sky short-wave downward radiation, (e) surface temperature, and (f) precipitation as simulated with global anthropogenic aerosol only forcing (AA) as well as regional-aerosol simulations (ensemble abbreviations as in Fig. 3.1). Shown are 11-7 year running means along with their respective 95% range of the individual simulations (shading). In (a), total emissions of black carbon (BC), organic carbon (OC), and sulphur dioxide (SO2) are shown along with the contributions from grassland fire emissions (BIO, Grassland) for all species and combined energy, transportation, domestic, industrial, waste treatment, and agricultural waste burning sector emissions (ANT) for OC and SO2. In (b), total AOD (black) and absorbing AOD (grey) also include other aerosol species, for instance dust aerosols, the emission sources of which are prescribed climatologically in the model. AODs due to sulphate aerosols (yellow), black carbon (purple), and organic matter (red) and their sum, the anthropogenic contribution to AOD (blue), are also shown. Area means are taken over (a) the land area within 4°N-17.5°N, 20°W-42.5°E and (b-f) the West African monsoon region (shown in blue in Fig. B.3a).

cloud changes associated with large-scale circulation patterns from remote aerosol cooling.

3.4.2 South Asia

For South Asia, the monsoon precipitation is more independent from the ITCZ, which is in this region located over the Indian Ocean, i.e further south than the considered monsoon region. The decreased precipitation detected for all simulations including South Asian aerosols (i.e. all but NAT, NoSA, and GHG in Fig. 3.5b) is related to a weakened monsoon circulation, as visible for instance in counter-climatological 1920-2005 trends of 850 hPa wind (Figs. 3.8a, B.23). This anomalous easterly flow over India and along the coasts of the Arabian peninsula and East Africa is associated with the aerosol-induced cooling of the land with respect to the ocean, and a related increase in surface pressure over land (Figs. 3.8f,k). Non-local aerosols are most important for these long-term trends (Fig. 3.8b-e,g-j,l-o), which is consistent with the findings for precipitation (Fig. 3.2b-e); note the increased importance of local aerosols in the last decades of the twentieth century (Fig. 3.2k). While the aerosols dominate the ALL response, GHGs act conversely to strengthen the circulation (Figs. B.23- B.25).

More evidence for this weakening of the circulation, and the aerosols' role in this, is seen in the time series of regional-mean sea level pressure, zonal wind, and land-sea temperature contrast, shown in Fig. 3.9 along with their respective correlation coefficients on short (annual time series) and longer time scales (time series smoothed by 11- and 7-year running means applied consecutively): Variations in zonal wind speed over India and the Arabian Sea on the one hand and precipitation on the other hand closely resemble each other on longer time scales (correlations > 0.85 for the latter for all simulations but NAT (Fig. 3.9c) and SAonly (Fig. 3.9f), second blue numbers), and sea level pressure over South Asian land and adjacent areas to the North varies in opposite phase with precipitation (Fig. 3.9, orange numbers). All simulations which include not only South Asian aerosols (Fig. 3.9a,d-g) show this

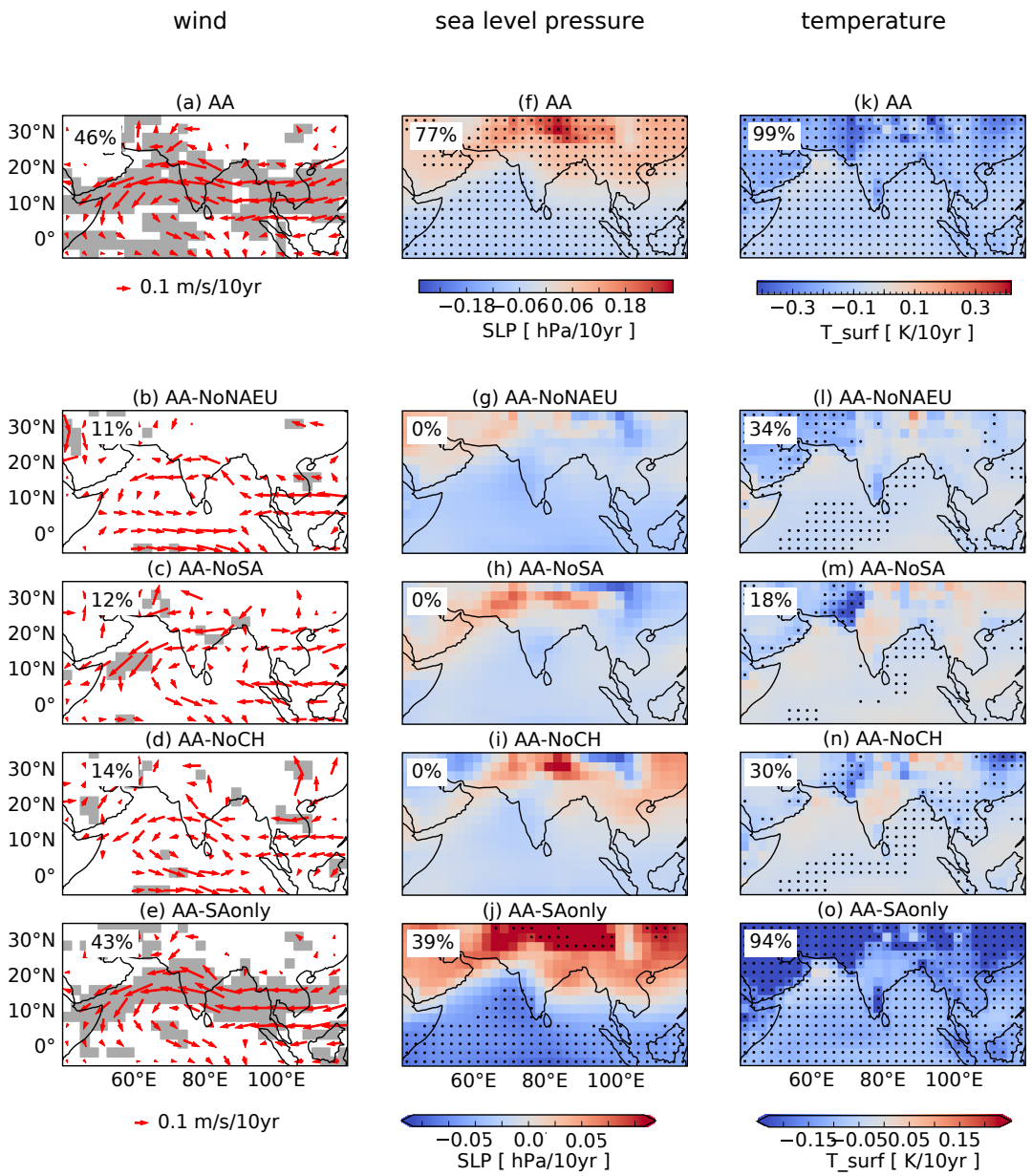

Figure 3.8: Simulated 1920-2005 summer (JJAS) ensemble-mean linear trends in the global anthropogenic aerosol simulations (AA) (first row) and differences between these and the ensemble-mean trends of the regional anthropogenic aerosol simulations (other rows) for wind speed at 850 hPa (left), sea level pressure (SLP, middle), and surface temperature (T_{surf}, right). These differences indicate the impact of aerosols from (b,g,l) North American and European, (c,h,m) South Asian, (d,i,n) Chinese, and (e,j,o) all but South Asian sources. In the first row, grey shading (a) or stippling (f,k) shows where the AA ensemble agrees on the sign of the trends in (a) zonal, meridional, and total wind speed, (f) SLP, and (k) T_{surf}. In the other rows, shading (b-e) or stippling (g-j,l-o) shows where differences between AA ensemble and regional aerosol ensemble are significant at the 95% confidence level using a t-test. Numbers in the top left corner give the fraction of stippled points within the displayed area.

weakening of the circulation until about 1970, while the inclusion of South Asian aerosols (Fig. 3.9h) is necessary to continue this trend in the later decades.

The temperature contrasts between South Asian land and ocean (Fig. 3.9) as well as between Northern and Southern Hemisphere (not shown) are crucial drivers of the monsoon and exhibit the same long-term trends as precipitation (second purple numbers in Fig. 3.9). Precipitation in the ALL simulations, however, is more clearly dominated by the aerosol forcing than is the case for the temperature gradients (Fig. B.26), which might reflect other means of aerosol impact contributing to the weakening of the monsoon circulation.

When forced with observed SSTs, the model simulates a pattern of precipitation change even closer to the observed one, and indeed more so than some reanalysis products (Fig. B.27m,n; *Compo et al.*, 2011), which improves our trust in the reliability of the model-based findings. While the observed SSTs include the slow component of the response to external forcings, the fast component of the response must also be included in order to recover the full signal (Fig. B.27o,p). The consistency in the circulation changes over the South Asian monsoon region between the fully coupled AA and ALL experiments on the one hand (Figs. B.23-B.25) and when forced with observed SSTs on the other hand (Fig. B.27a-l) shows furthermore that the contribution of long-term ocean variability as well as ocean-atmosphere coupling is of secondary importance to the aerosol-related changes shown above.

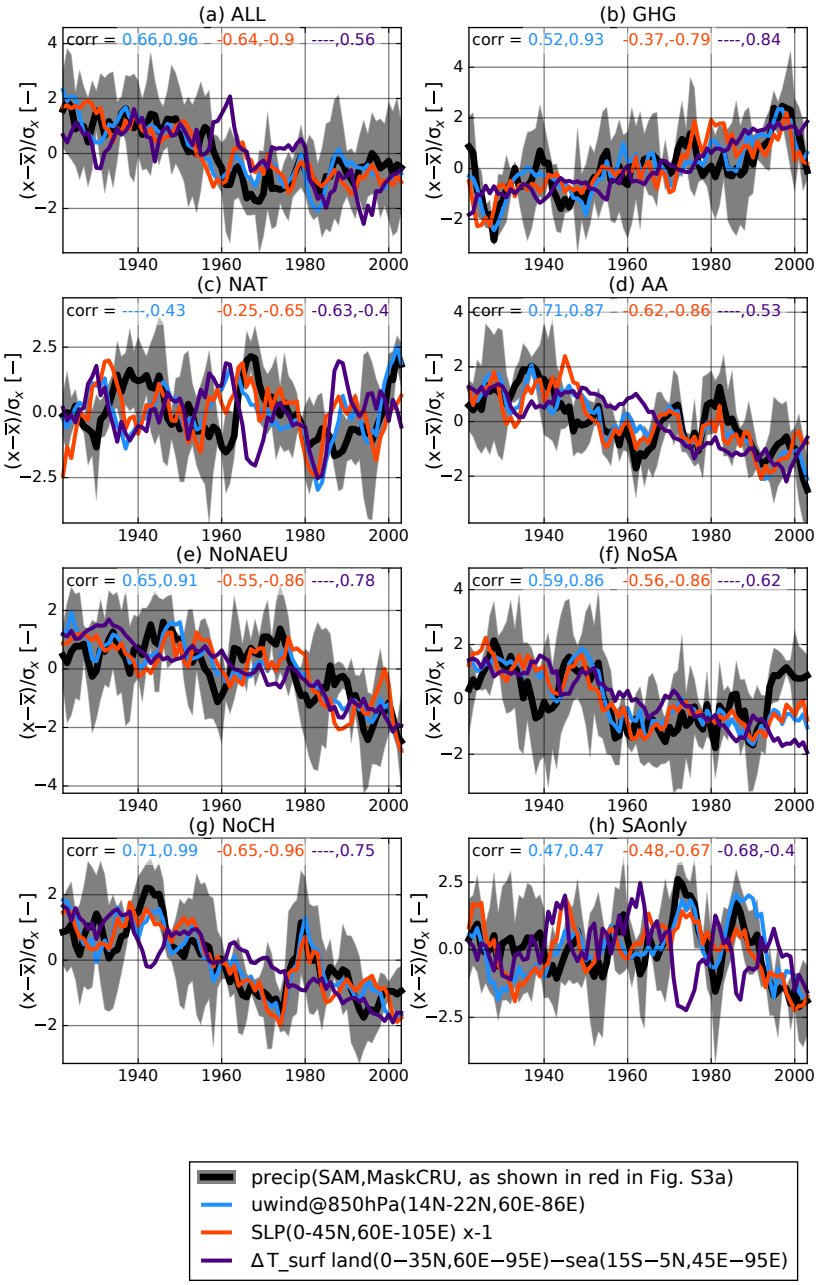

Figure 3.9: Standardised South Asian summer (JJAS) monsoon precipitation anomalies (black), zonal wind speed over India and the Arabian Sea (light blue), sea level pressure over a northerly extended South Asian land region (orange), and surface temperature difference between South Asian land and northern Indian ocean temperatures (purple) for 1920-2005 for the ensemble mean of (a-d) global forcings and (e-h) regional aerosol forcings. Shown are the 5-year running means along with their respective 95% range of the individual simulations (shading). Numbers at the top of each panel give the correlation coefficient between precipitation and each of the other variables for the non-standardised annual time series (fist number), and the 11-7-year running mean (second number), where statistically significant (pval<0.05). The correlation between near-surface (2m) rather than surface temperature (not shown) and precipitation on long time scales amounts to 0.83.

3.5 Discussion and Conclusions

A number of studies have shown that precipitation in monsoon regions across the Northern Hemisphere underwent large changes during the twentieth century. Anthropogenic aerosols have been shown to have influenced the observed changes above internal variability and dominate over GHG forcing which on its own would have led to an increase in precipitation (*Polson et al.*, 2014). By extending the analysis period back to the 1920s, we have been able to show that in two individual monsoon regions, West Africa and South Asia, anthropogenic aerosols have driven observed changes in precipitation, and that the source region of the aerosol emissions is an important factor in the detectability of anthropogenic aerosol forcing. However, the models' significant underestimate of the magnitude of the observed changes remains a concern.

For West Africa, remote aerosols from North America and Europe need to be included in order to detect the anthropogenic signal in observed monsoon precipitation. The decrease in precipitation seen from the 1950s to 1980s and the subsequent recovery agrees with the evolution of total global emissions, of which these regions are the largest contributor (Fig. B.4; *Polson et al.*, 2014). This is consistent with the changes in West African precipitation being partly related to shifts in the ITCZ due to the inter-hemispheric temperature differences caused by the aerosol preferential cooling of the Northern Hemisphere (*Hwang et al.*, 2013; *Rotstayn et al.*, 2015). Nevertheless, the models underestimate the magnitude of the observed changes, and the strong drying seen during the middle of the century is not captured by GFDL-CM3. This results in large best-estimate scaling factors which raise questions whether the models correctly capture the monsoon response to aerosol forcing (Fig. B.14). Other studies have shown that CMIP5 models tend to underestimate the observed multi-decadal trends in the Sahel (*Biasutti*, 2013), which may be due to weaker forcing or missing physical processes in the models, for example indirect aerosol effects (*Booth et al.*, 2012), changes in dust aerosols (*Ji et al.*, 2016), or land surface feedbacks (*Kucharski et al.*, 2013), or due to internal variability, such as from SSTs (*Ting et al.*, 2009). The

CMIP5 models' ability to simulate the connection between North Atlantic SSTs and Sahel precipitation varies (*Martin et al.*, 2014), but this does not seem to influence the detectability of aerosol response, since ALL and AA are detected both for GFDL-CM3 and the CMIP5 ensemble. The West African monsoon region identified in this study has some overlap with the Sahel region considered by *Dong and Sutton* (2015), who found GHGs and, to a lesser extent, aerosols, not SST trends, necessary to explain the recovery of Sahel precipitation with the HadGEM model. Volcanic eruptions in the twentieth century may also be important drivers of variability at shorter time scales, and aerosols from volcanic eruptions have also been shown to cause the shift in the ITCZ away from the hemisphere where the aerosols cooling is larger (e.g., *Iles and Hegerl*, 2015).

In contrast, in South Asia, where changes in local aerosol emissions are larger than for West Africa, local emissions are essential in order to explain observed changes in monsoon precipitation. This is consistent with increasing emissions from South Asia during the later part of the twentieth century and with studies that find that the indirect aerosol effects, acting locally, play an important role in the decline in precipitation in this region (*Guo et al.*, 2015). While our results suggest that anthropogenic aerosol forcing has played a role in driving the observed drying, this does not preclude an additional role by decadal variability, e.g. the Pacific Decadal Oscillation (*Salzmann and Cherian*, 2015), which, however, might also have been influenced by an aerosol-induced change in the Walker circulation via modulation of the trade wind strength (*Dong et al.*, 2014b; *Takahashi and Watanabe*, 2016).

For both monsoon systems, the failure to detect anthropogenic aerosol forcing from other source regions should not be interpreted as these aerosol emissions having no influence, but rather that they are not detectable above the internal variability of precipitation during the period 1920-2005. Modelling studies of the Asian monsoon (*Cowan and Cai*, 2011; *Dong et al.*, 2015), and the analysis of the spatial trends patterns here, suggest that both local and non-Asian aerosols contribute to the weakening of the monsoon, while studies of West Africa suggest that aerosol emissions from Asia also play a role in this regional reduction in monsoon precipitation (*Dong*

et al., 2014a). This analysis provides more rigorous support to the results of the modelling study by *Bollasina et al.* (2014) who suggested a predominance of local aerosols in driving seasonal mean precipitation changes over South Asia, and in particular the widespread monsoon decrease over central India. Note, they also found that non-local aerosols were of greater importance for early summer precipitation changes associated with an advanced monsoon onset, which, in terms of seasonal mean anomalies, results in the positive precipitation anomaly over north-western India.

Uniquely, we have been able to show that the influence of local anthropogenic aerosols in South Asia, and of North American and European emissions in West Africa, is not only recognisable in the model simulations, but also detectable in long-term observations of precipitation. While our results rely on simulations with the GFDL-CM3 model, we believe them to be robust, since key features of the aerosol response are also in the CMIP5 multi-model mean. However, reproduction of the study with a larger ensemble and other models would be important to provide further support to the robustness of the results. The detection of aerosol influence on past monsoon precipitation changes highlights the possible role of the decline in anthropogenic aerosol emissions expected in the near future (*Vuuren et al.*, 2011), with the interplay of aerosols from different source regions likely gaining importance due to more heterogeneous global emission patterns.

Chapter 4

Contrasting the Effects of the 1850-1975 Increase in Sulphate Aerosols from North America and Europe on the Atlantic in the CESM Model

4.1 Introduction

In this chapter, we explore the sensitivity of the climate system to historical changes in SO_2 emissions from NA and EU separately, focussing on the Atlantic region in a state-of-the-art coupled model, the National Center for Atmospheric Research (NCAR) Community Earth System Model (CESM1) with a comprehensive aerosol scheme (*Meehl et al.*, 2013; *Ekman*, 2014). We use a set of purposefully-designed historical experiments whose ensemble size of 8, larger than typically employed in CMIP5, is expected to benefit the identification of the common forced signal given internal variability (e.g., *Knight*, 2009).

In the remainder of the chapter, the model data and methods are briefly described (Section 4.2); the observed and simulated AMV are compared, the impacts of SO_2 emissions from NA and EU on simulated Atlantic SST variations identified, and relevant physical mechanisms analysed (Section 4.3); and finally the results discussed and conclusions drawn (Section 4.4).

4.2 Data and Methods

4.2.1 Model Description and Experiment Set-up

We use the coupled NCAR/NSF-DoE Community Earth System Model (CESM1) version 1.2.2 (*Hurrell et al.*, 2013) with a 1.9° x 2.5° latitude-longitude grid for the atmospheric and land components with 30 vertical levels and a model top around 40 km, and a 0.6° x 0.9° rotated-pole latitude-longitude grid for the ocean and sea-ice components with 60 vertical levels. The atmospheric component is the Community Atmosphere Model version 5.3 (CAM5; *Neale et al.*, 2012), which includes a 3-modal online tropospheric aerosol model (MAM3) with prognostic representations of both indirect aerosol effects (*Ghan et al.*, 2012; *Meehl et al.*, 2013).The other model components are an extension of the Parallel Ocean Program Version 2.1 (POP2); the Los Alamos Sea Ice Model (CICE4); the Community Land Model (CLM) version 4.0 with carbon nitrogen cycling (CN); and the river transport model (RTM). Note that this is very similar to the CMIP5 version of this model (CESM 1.0), which has the same ocean, sea ice, land model, and coupler, but no river transport model, and a slightly older version of the atmosphere model, CAM5.0 (*Taylor et al.*, 2012).

Three sets of experiments covering the period 1850-1980 are used, each an ensemble of 8 members initialised from a 200-year pre-industrial (1850) control simulation (Fig. C.1a). The first experiment (ALL) is forced with time-varying historical estimates of GHG concentrations, natural aerosols, solar irradiance, land use, and anthropogenic aerosol emissions developed for CMIP5 (*Taylor et al.*, 2012) and should reproduce the

observed climate best. The other experiments differ from ALL in that the SO_2 and SO_4 emissions from the anthropogenic sectors of energy, industry, domestic, transport, agriculture, and waste are kept at their pre-industrial level over either North America (noNA experiment) or over Europe (noEU experiment) (Fig. C.1b). The respective regions used are based on the Tier 1 regions from the Hemispheric Transport of Air Pollution 2 experiments (*Koffi et al.*, 2016), similar to *Bellouin et al.* (2016). For the technical details of the emission modifications as part of the simulation set-up see Section 4.A.

4.2.2 Observations

Two observational SST datasets are used: NOAA's Extended Reconstructed Sea Surface Temperature v4 (ERSST4; *Huang et al.*, 2015) and the Met Office Hadley Centre's HadSST.3.1.1.0 (HadSST3; *Kennedy et al.*, 2011a). HadSST3 consists of an ensemble of 100 realisations accounting for uncertainty due to possible pervasive low frequency biases, but not including other types of uncertainty (*Kennedy et al.*, 2011b). ERSST4 is infilled to give full data coverage, with a loss of resolution especially early in the record (*Huang et al.*, 2015).

4.2.3 Methods

Area-mean, annual-mean time series are computed from monthly data, and smoothed by taking 5-year running means to suppress inter-annual variability. The spatial patterns of aerosol impact are analyzed using least-square linear trends during 1850-1975. Despite its simplicity, this approximation is adequate given the near-linear increase in SO_2 emissions from both NA and EU (Fig. 1.3d) and correspondingly near-linear changes in global and regional sulphate loading, aerosol optical depth, radiative fluxes and temperature (not shown). The difference in the ensemble-mean response between ALL and noNA or ALL and noEU is interpreted as the impact of SO_2 emissions from

NA or EU, respectively, and its significance measured by a two-tailed Student's t-test at the 95% confidence level.

We calculate the AMV by regridding and masking the monthly model data to the observational (HadSST3) resolution and coverage, respectively; calculating monthly SST anomalies with respect to the 1854-1980 climatology; applying a 10-year low-pass (Lanczos) filter; removing the long-term linear trend; and averaging across the North Atlantic (0-65°N,0-80°W, area-weighted) as in *Bellomo et al.* (2017) and similar to e.g. *Knight et al.* (2005). The AMOC index as a function of latitude is calculated from the model's MOC output -the net volumetric rate of water transported northwards- in the Atlantic-Arctic ocean at its maximum at any depth (*Medhaug and Furevik*, 2011; *Tandon and Kushner*, 2015).

4.3 Results

4.3.1 North Atlantic Sea Surface Temperatures

The ALL ensemble reproduces the observed AMV well, although it slightly underestimates the observed differences between the 1910/1920 and 1970 cool periods and the warmer period in between (Fig. 4.1a). Note that the AMV resembles strongly the area-mean SST anomalies due to the lack of a large trend during this period (Fig. C.2; *Tandon and Kushner*, 2015), and shares variability with the rest of the global ocean (Figs. C.3, C.4). The AMV has the same multi-decadal variations in all 24 simulations (visually from the ensemble envelopes in Fig. 4.1a). This indicates that it is dominated by external forcing in this model, since we do not expect internal variability to create in-phase variations. While deciphering its drivers is not conclusively possible with our experiment set-up, the simulations do suggest a combination of factors, including a role for NA and EU SO_2 emissions (Fig. C.2) amongst other, for instance volcanic (Fig. 4.2), forcings.

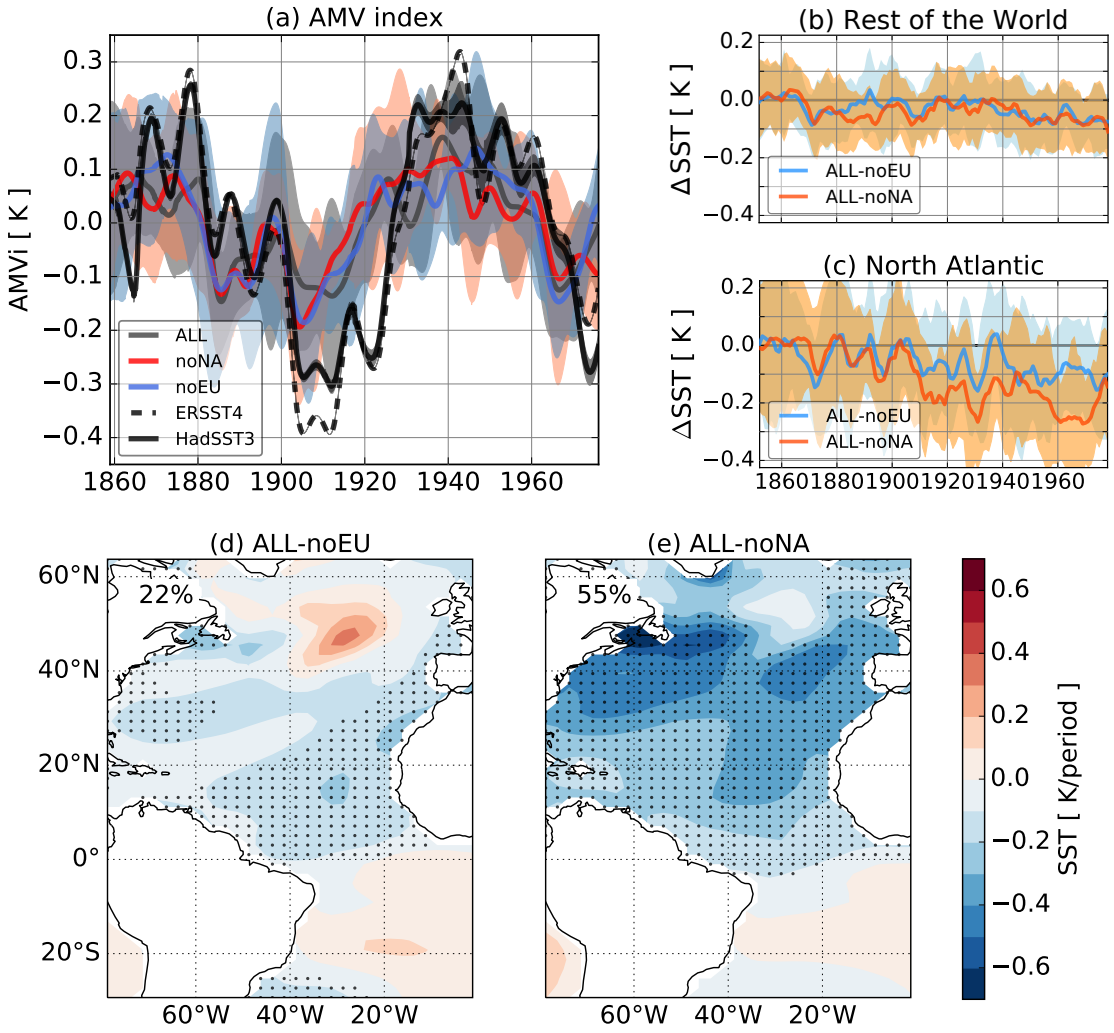

Figure 4.1: Atlantic sea surface temperatures (SSTs): (a) Observed and simulated Atlantic Multi-decadal Variability (AMV) and (b-e) simulated SST change due to regional SO_2 emissions. (a) AMV from observations ERSST4 (dashed black) and HadSST3 (solid black, with shading for the 90% range of the 100 realisations) and from the all-forcing simulations with global SO_2 emissions (ALL; grey, ensemble-mean with shading for the 90% range of the 8-member ensemble) and without anthropogenic European (noEU; blue) and North American (noNA; red) emissions. In (b-c), differences between ALL and noEU (light blue line and shading) and ALL and noNA (orange line and shading) in area-averaged SSTs over (b) everywhere but the North Atlantic and (c) only the North Atlantic are shown. In (d-e), differences in the linear trends during 1850-1975 between ALL and (d) noEU and (e) noNA are shown, with stippling for significance at the 5% level and numbers in the top left corner for the fraction of stippled points within the displayed area.

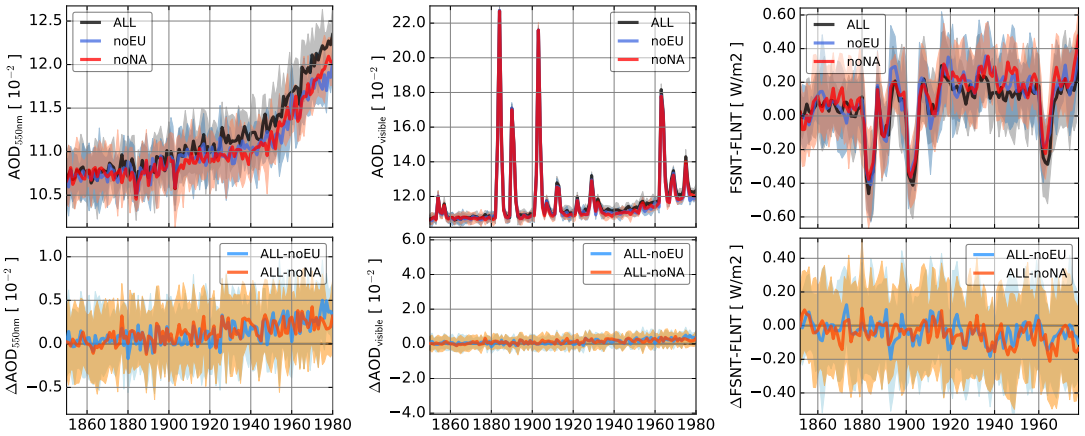

(a) AOD_{550nm} (not smoothed) (b) $AOD_{visible}$ (not smoothed) (c) FSNT-FLNT

Figure 4.2: Simulated global mean, annual mean time series of (a) AOD (at 550 nm), (b) total AOD in the visible band, and (c) net total (short-wave minus long-wave) all-sky radiation at the top of the model. The ensemble-mean values of the (top) simulations with global anthropogenic SO_2 emissions (ALL; black with grey shading for the 90% range of the 8-member ensemble) and those from the simulations without European (noEU; blue line and shading) and North American (noNA; red line and shading) anthropogenic SO_2 emissions are shown as well as the (bottom) differences between ALL and noEU (light blue line and shading) and ALL and noNA (orange line and shading).

Comparison between ALL and the regional-aerosol ensembles shows that anthropogenic SO_2 emissions from NA and EU, while not significantly affecting the "phasing" of the simulated AMV, cause a steady long-term cooling of North Atlantic SSTs (Fig. 4.1b-e). The impact of NA emissions on basin-wide SSTs during 1850-1975 ($\approx$ 0.25 K) is found to be larger than that of EU emissions ($\approx$ 0.15 K) despite their similar historical emissions with around 40% global share each (Fig. 1.3d) and their similar cooling of SSTs outside the Atlantic ($<$ 0.1 K) (Figs. 4.1b-c, C.2, C.5). Note that this is similar for sub-surface ocean temperatures, with a decrease in simulated upper-ocean heat content in the Atlantic and elsewhere (Fig. C.2).

In lower latitudes (0-40N°), the spatial patterns of the long-term Atlantic SST response to NA and EU SO2 emissions both show a cooling off the European and African west coast and across the subtropical North Atlantic and a cooling off the US-American East Coast (Fig. 4.1d-e). They also both show no cooling over the subpolar gyre (around 30°W,50°N) i.e. have a "cooling hole" which is symmetric to

the observed "warming hole" (e.g., *Drijfhout et al.*, 2012), and no cooling (insignificant warming) in the tropical South Atlantic. Apart from these similarities, however, the patterns differ substantially: NA emissions cause strong cooling along the mid latitude storm track, spreading over most of the North Atlantic, while EU emissions cause a less widespread cooling concentrated along the African coast.

4.3.2 Atmospheric Aerosol Effects

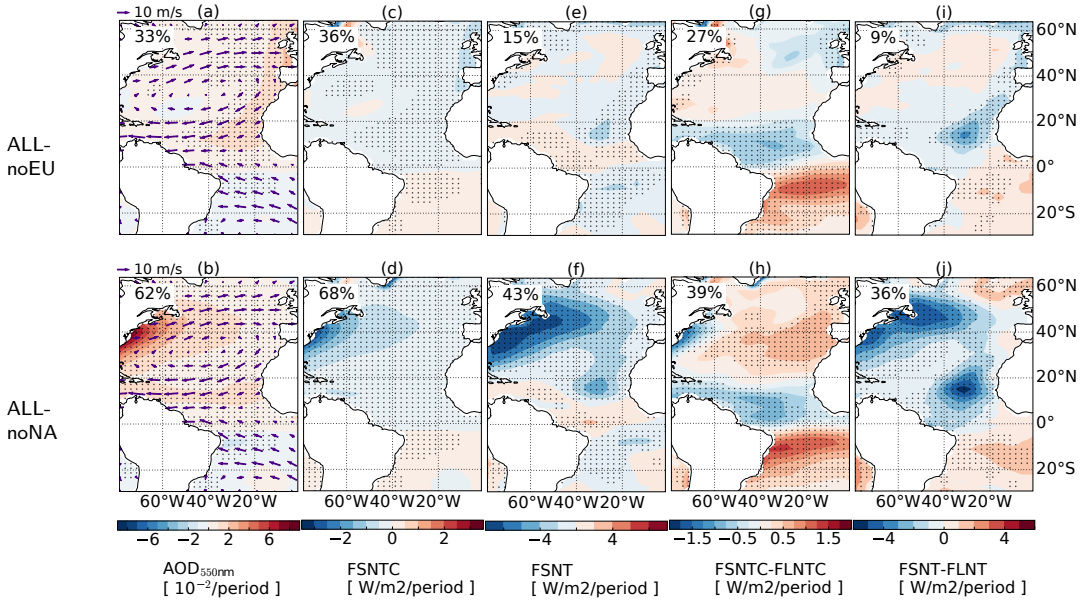

Figure 4.3: Simulated aerosol effects over the Atlantic: Linear trends as in Fig. 4.1(d-e), but for (a,b) AOD, and net (c,d) clear-sky short-wave (FSNTC), (e,f) all-sky short-wave (FSNT), (g,h) clear-sky total (FSNTC-FLNTC), and (i,j) all-sky total (FSNT-FLNT) radiation at the top of the model. In (a,b), purple arrows indicate the climatological wind near 850 hPa from the pre-industrial control run.

A linear-trend analysis of aerosol content, cloud fraction, and radiative fluxes sheds light on the atmospheric component of the mechanism generating the SST changes discussed above. The increased NA and EU SO_2 emissions result in increased sulphate loading over the North Atlantic, manifest in increased (total) AOD, with the spatial patterns largely explained by climatological circulation (Fig. 4.3a-b): NA aerosols are advected over the Atlantic by mid-latitude storm tracks, while EU aerosols are transported into the sub-tropical Atlantic by trade winds. The decrease in clear-sky short-wave radiation over the same areas shows the direct effect (scattering) of sul-

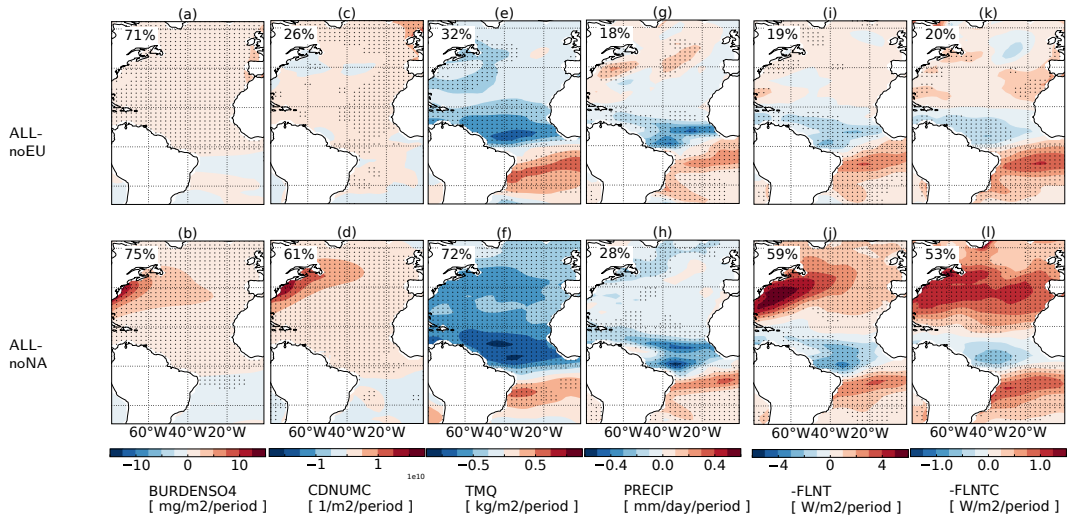

Figure 4.4: As Fig. 4.3, but for (a-f) total (vertically integrated) (a-b) sulphate aerosol load, (c-d) cloud droplet number concentration, (e-f) precipitable water as well as (g-h) total (convective+large-scale) precipitation and (i-l) net long-wave radiation at top of the model for (i-j) all sky and (k-l) clear sky over the Atlantic region. (i-l) Since the model measures long-and short-wave fluxes in different directions, the trends are shown with the sign adjusted so that positive values indicate a warming tendency as in Fig. 4.3.

phate aerosols (Fig. 4.3c-d). An increase in cloud droplet number concentration and cloud fraction over areas of large climatological cloud cover off the North American coast and in the North Atlantic strato-cumulus cloud deck (Figs. 4.4, C.6) show aerosol-cloud interactions (ACIs), which contribute substantially to the change in all-sky short-wave radiation (Fig. 4.3e-f).

This suggests that the simulated Atlantic SST response is larger for NA than for EU emissions because the prevailing winds transport NA aerosols more effectively over the Atlantic, and moreover to regions with more climatological cloud cover. Note also that significant changes in sea salt and dust aerosols over the North and tropical South Atlantic (Fig. C.7) suggest the possibility of still largely unexplored feedbacks between anthropogenic aerosols, climate, and natural aerosols (*Wang et al.*, 2012; *Martin et al.*, 2014; *Yuan et al.*, 2016).

4.3.3 Atlantic Meridional Overturning Circulation

Potential interactions between simulated North Atlantic SSTs, large-scale ocean circulation, and sulphate aerosols -as for example suggested by the simulated aerosol-induced cooling east of the Grand Banks (Figs. 4.1d-e), thought of as a key region for the North Atlantic ocean circulation (*Buckley and Marshall*, 2016)- are investigated by means of the AMOC. The simulated AMOC shows pronounced multi-decadal variability, with a strengthening until about 1920, a weakening until around 1950, and again a strengthening thereafter (Fig. 4.5a). As for the AMV (Section 4.3.1), this phasing is the same in all 24 simulations, indicating that a large fraction of the AMOC is externally forced in the model rather than due to internal variability.

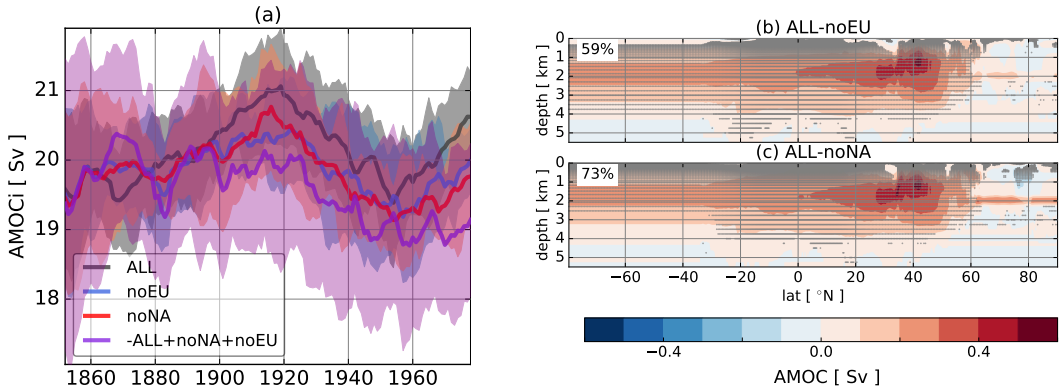

Figure 4.5: Simulated Atlantic Meridional Overturning Circulation (AMOC): (a) Annual-mean AMOC index (maximum AMOC at any depth) at 29.8°N. Colours and shading as in Fig. 4.1(a) except the AMOC response to the combined forcing of GHG, natural, and aerosols other than from NA and EU SO_2 emissions is also shown as approximated from arithmetically combining the ensemble-mean AMOC indices (purple). (b-c) Difference in the 1850-1979-mean AMOC between ALL and (b) noEU and (c) noNA. Stippling as in Fig. 4.1(d-e).

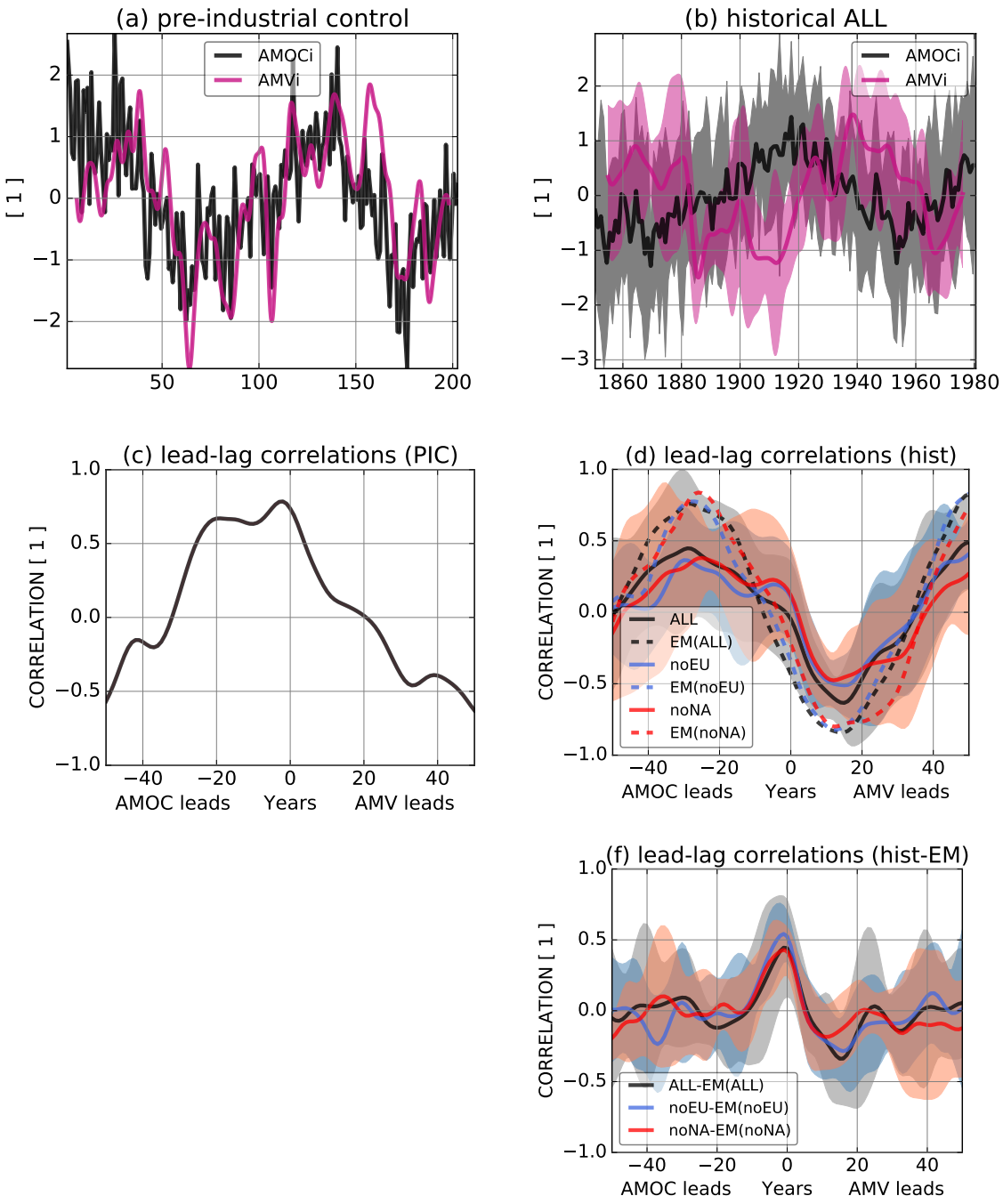

Figure 4.6: North Atlantic variability in the (left) pre-industrial control simulation and (right) historical experiments: (a-b) Standardised (black) AMOC index at 30°N and (purple) Atlantic Multi-decadal Variability (AMV) index as in Fig. 4.1a. (c-f) Lead-lag correlations between the standardised AMOC (detrended, 10-year low-pass filtered) and the AMV index. In (d) the ensemble mean of the correlations between the indices in each ensemble member is shown (solid lines) as well as the correlations between the ensemble-mean indices (EM, dashed line). In (f), the ensemble mean of the correlations of the residuals between the AMOC and AMV in each member and their ensemble means, respectively, is shown. (Right) Shading shows the 90% range of the 8-member ensemble around the ensemble mean.

Earlier research suggests this external forcing to be mediated by the AMV, with cool and warm Atlantic SSTs causing an AMOC strengthening and weakening, respectively (e.g., *Zhang and Wang*, 2013; *Tandon and Kushner*, 2015). Comparison with the AMV index (Fig. 4.1a) suggests indeed a lagged anti-correlation between the -simulated or observed- AMV and the simulated AMOC. This is confirmed by a lead-lag analysis (Fig. 4.6), which shows the ensemble-mean, i.e. forced, component of AMV and AMOC in all historical experiments to be anti-correlated with an AMV lead by 10 years (or an AMOC lead by 30 years, which we discard for physical reasons). In the unforced case, the AMOC drives the AMV near zero lag, and both mechanisms are superposed in the historical simulations. The AMV seems thus also here to mediate the external forcing of the AMOC. While the NAO (*Hurrell*, 1995) might play a role in linking the AMV with the AMOC at decadal or longer time scales (*Mignot and Frankignoul*, 2005; *Delworth and Zeng*, 2016; *Iles and Hegerl*, 2017), our simulations do not show a long-term change or significant response to the sulphate aerosol forcing in the NAO (Fig. C.8), which is unsurprising given that the connection is known to be commonly underestimated in current models (*Eade et al.*, 2014).

As with North Atlantic SSTs (Fig. 4.1c), SO_2 emissions from NA and EU have a persistent impact on the simulated AMOC strength: From 1900 onwards, the AMOC index is persistently higher by about 2.5% when either NA or EU SO_2 emissions are included (Fig. 4.5a), at all depths and latitudes up to about 55°N (Fig. 4.5b). The associated increase in northward ocean heat transport will compensate for some of the radiative cooling over the Atlantic (Figs. 4.3, 4.4). This means that magnitude and pattern of the long-term SST responses to SO_2 emissions from NA and EU described above (Fig. 4.1b-e) are a combination of atmospheric forcing and ocean feedback.

4.3.4 Large-Scale Atmospheric Adjustment and Impact on Global Precipitation

The simulations show a temperature response to NA and EU emissions not only over the Atlantic, but far downstream of the respective emission regions across most of the

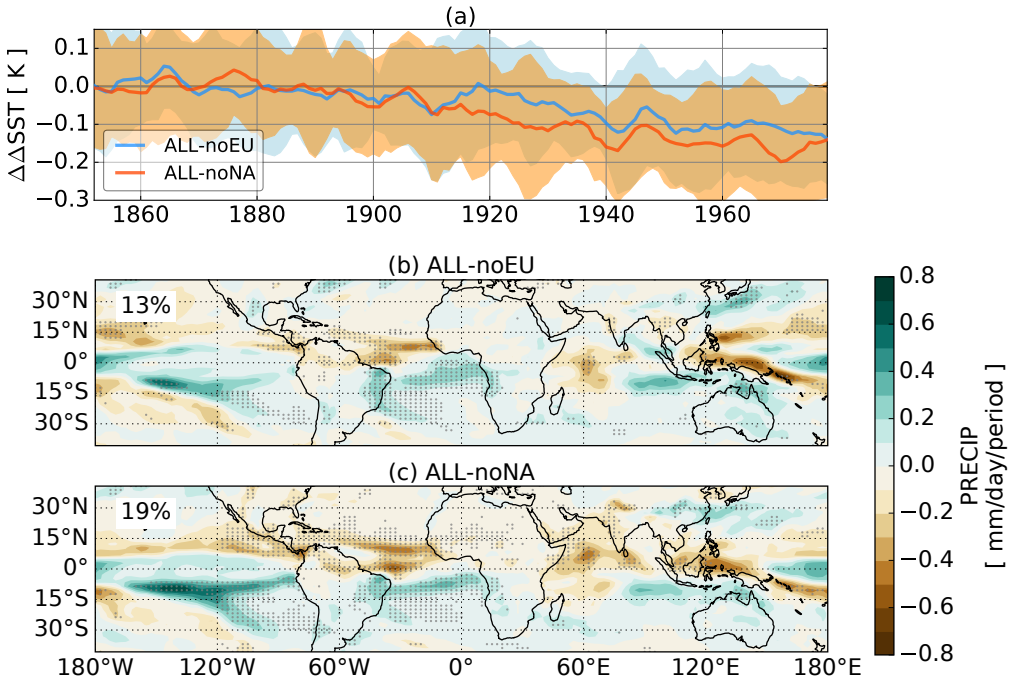

Figure 4.7: Simulated large-scale atmospheric circulation changes: (a) Time series of SST anomalies as in Figs. 4.1(a-b), but for inter-hemispheric SST difference, and (b-c) linear trends as in Fig. 4.1(d-e), but for precipitation.

northern hemisphere (NH) (Fig. C.5). The inter-hemispheric temperature contrast is thereby steadily decreased throughout the twentieth century (Fig. 4.7a). This is also relevant for the Atlantic region in that it causes an enhancement of the southern flank of the ITCZ and thus its de facto southward shift (Chapters 2, 3 and e.g., *Allen et al.*, 2015; *Westervelt et al.*, 2017).Note that this response again includes a partial compensation from the AMOC feedback (Fig. 4.5; *Dong and Sutton*, 2005; *Marshall et al.*, 2014).

The ITCZ shift is visible in equator-symmetric changes in cloud fraction, water vapour, precipitation, and radiative fluxes (Figs. 4.3e-h, 4.4, 4.8, C.6). The resulting negative and positive fluxes north and south of the equator, respectively, (Fig. 4.3i-j) can be considered a positive feedback to the Atlantic and NH cooling (e.g., *Clark et al.*, 2018). The simulated global precipitation response is dominated by this ITCZ shift, showing a prominent change of tropical rainfall pattern in all ocean basins which is remarkably similar for NA and EU emissions (Figs. 4.7b-c, 4.8).

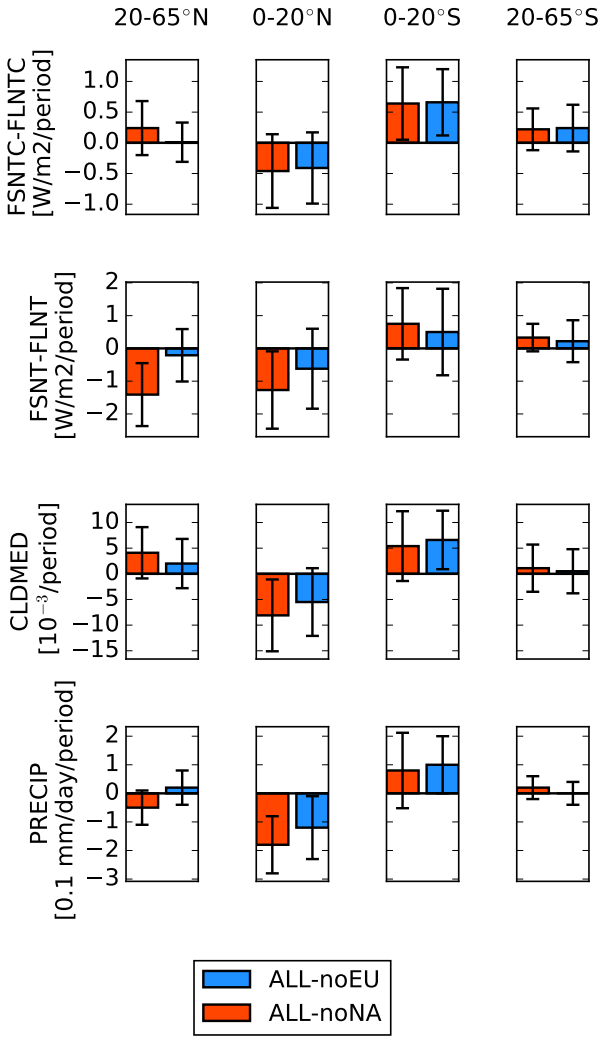

Figure 4.8: Area-means of the 1850-1975 linear trends shown in Figs. 4.4-s4.3 for (top to bottom) total (short-wave minus long-wave) radiation at the top of the atmosphere for clear-sky (FSNTC-FLNTC) and for all sky (FSNT-FLNT), mid-level cloud fraction (CLDMED), and precipitation (PRECIP) averaged over (left to right) the extra-tropical North Atlantic (20-65°N; 0-80°W), the tropical North Atlantic (0-20°N; 0-80°W), the tropical South Atlantic (0-20°S;0-80°W), and the extra-tropical South Atlantic (20-65°S;0-80°W). The ensemble-mean values of the difference between (orange) ALL and noNA and (blue) ALL and noEU are shown along with the 90% range (calculated as $1.66\sqrt{\sigma^2_{\mathrm{ALL}} + \sigma^2_{\mathrm{noNA}}}$ with σ_{ALL} and σ_{noNA} the standard deviation of the area-mean values from the 8-member distribution of the ALL and the noNA ensembles, respectively, and equally for ALL-noEU).

4.4 Summary, Discussion and Conclusions

The Atlantic climate responses to historical (1850-1975) sulphate aerosols from North America (NA) and Europe (EU) have been contrasted in a coupled climate model by comparing transient 8-member ensemble simulations with either all forcings evolving historically or anthropogenic SO_2 emissions from NA and EU separately kept at pre-industrial levels. The study was motivated by existing literature suggesting a role for anthropogenic aerosols in past multi-decadal variability of Atlantic SSTs which affects climate worldwide, and a knowledge gap concerning the relative roles of NA and EU emissions despite its relevance for policy applications.

In summary, we find that sulphate aerosols from either source cause a long-term cooling of North Atlantic SSTs, with the patterns a combination of atmospheric aerosol effects and an aerosol-induced strengthening of the AMOC. The response is larger for NA than for EU emissions, with stronger indirect aerosol effects due to a wider aerosol spread over the Atlantic and collocation with climatological cloud cover. A southward shift of the ITCZ, affecting tropical precipitation globally, and causing a small positive feedback to the North Atlantic cooling, is also found. The (multi)decadal variability components of Atlantic SSTs, i.e. the AMV, and of the AMOC are both found to be externally forced, possibly by a combination of forcings factors including NA and EU sulphate aerosols.

The external forcing of the model's AMV and the lead-lag relationships between its AMV and AMOC show that earlier findings (*Murphy et al.*, 2017; *Bellomo et al.*, 2017; *Tandon and Kushner*, 2015) hold also for simulations initialised from different ocean states. The consequential small role allowed for *internal* ocean variability in explaining AMOC variations given external forcings -historical and prospective- has received little attention in the literature so far. In showing that NA and EU emissions impact the simulated historical AMOC to similar amounts, we furthermore extend the results by *Cowan and Cai* (2013). The simulated "cooling hole" (Section 4.3.1) in response to NA and EU SO_2 emissions suggests furthermore the observed "warming

hole" (e.g., *Drijfhout et al.*, 2012) not to be aerosol driven, but due to the AMOC feedback, which seems to mute aerosol cooling as it mutes GHG warming.

Judging from their projected 21st century shifts (*Allen*, 2015), other CMIP5 models which also represent both aerosol indirect effects are expected to simulate even larger historical changes in the ITCZ. The larger response of the ITCZ to NA than to EU emissions found here (Fig. 4.8) was also found in CESM1 and two other models by *Westervelt et al.* (2018) for the precipitation response to a removal of present-day SO_2 emissions in time-slice experiments. Our model experiments suggest that NA emissions might also have had a larger share in the suppression of Atlantic tropical hurricane frequency (*Dunstone et al.*, 2013), while both NA and EU emissions might have impacted the storm tracks over the extra-tropical North Atlantic and Europe (Section 4.B).

Our findings rely on the model's representation of many complex and highly uncertain processes that may vary between models. We cannot test the historical forcing of the AMOC due to the lack of observations (*Srokosz et al.*, 2012; *Munoz et al.*, 2011), but the simulated (1920-1980) AMOC variations are consistent with the CMIP5 MMM (*Tandon and Kushner*, 2015), and the simulations capture for example historical observations of sub-polar sea surface salinity (Fig. C.9; *Friedman et al.*, 2017) in addition to Atlantic and global SSTs.

Inter-model differences in the atmospheric response arise from pre-industrial aerosol loading, historical SO_2 spread, and especially the parametrisation of ACIs (e.g., *Wilcox et al.*, 2015). The model's aerosol net total effective radiative forcing and its climate sensitivity are amongst the largest across a range of CMIP5 models, but not exceptional (*Zelinka et al.*, 2014; *Meehl et al.*, 2013; *Forster et al.*, 2013). On the other hand, CESM1 seems to underestimate the observed SST variability over the Atlantic (Fig. 4.1a), which could either imply internal variability not captured by the model, or, given the temporal covaration of the forced (ensemble-mean) signal and the observations, an underestimation of the forced response. Since some of the forced response is from (both anthropogenic and volcanic) aerosols (Section 4.3.1; *Booth*

et al., 2012), this could further suggest that the model underestimates the response to aerosols. Lower or higher aerosol forcing may result in decreased and increased, respectively, absolute values of SST cooling compared to those found here, but not necessarily affect the relative attribution to NA vs. EU emissions.

To conclude, this study sheds light on the contribution of regional aerosol emissions from NA and EU to the changes in North Atlantic SSTs during the industrial period, providing insights of the associated physical mechanisms including the large-scale atmosphere and ocean circulation. The findings are not only relevant for projections of future change related to a continued decline of SO_2 emissions (*Vuuren et al.*, 2011; *Westervelt et al.*, 2017), but also for the mechanistic understanding of the role of forcing in Atlantic variability and as such for future projections related to other forcing agents.

Appendix 4.A Technical Details of the Emission Modifications for the CESM Simulations

The aerosol emission modifications are applied to the files from the CESM model repository, which are derived from the recommended CMIP5 input files (*Lamarque et al.*, 2010), but already in the format required by the atmospheric component of the model (CAM). The original CMIP5 input files are surface emissions given as mass per area, per aerosol species, and per emission source. For sulphate, they prescribe the emission of the sulphate aerosol precursor gas sulphur dioxide. The CAM input emissions include also small amounts of sulphate to be emitted already in the form of aerosol particles (SO_4), i.e. as primary aerosol. For each emission source, their amount is assumed to be 2.5% of the amount of substance of emitted SO_2, and emitted in the aerosol mode assumed to be typical for that type: nucleation mode, Aitken mode, accumulation mode, or coarse mode, with associated diameters of $\leq$ 50 nm, 10-50nm, 50nm-1μm, and $\gtrapprox$ 1 μm respectively. For sulphate aerosols, the Aitken and accumulation modes are relevant.

For each aerosol mode and emission source, the number density of aerosol particles is prescribed in addition to the number density of molecules. The former is calculated from the latter using typical values of the number of molecules per particle (10^6 for Aitken mode particles, and 10^6-100^6 for accumulation mode particles), derived from assumed mean diameters and dry densities of the aerosol particles for each emission source and mode. While domestic, transport, waste, agriculture, and ship emissions are assumed to occur only at the surface, emissions from grass fires, forest fires, industry, energy, and volcanic eruptions are prescribed with a height coordinate. These elevated emissions were derived assuming the mean vertical profile from 1997-2002 AEROCOM data.

I create the modified emission files for the new simulations by setting all SO_2 and SO_4 variables in the CAM input files originating from anthropogenic land emission

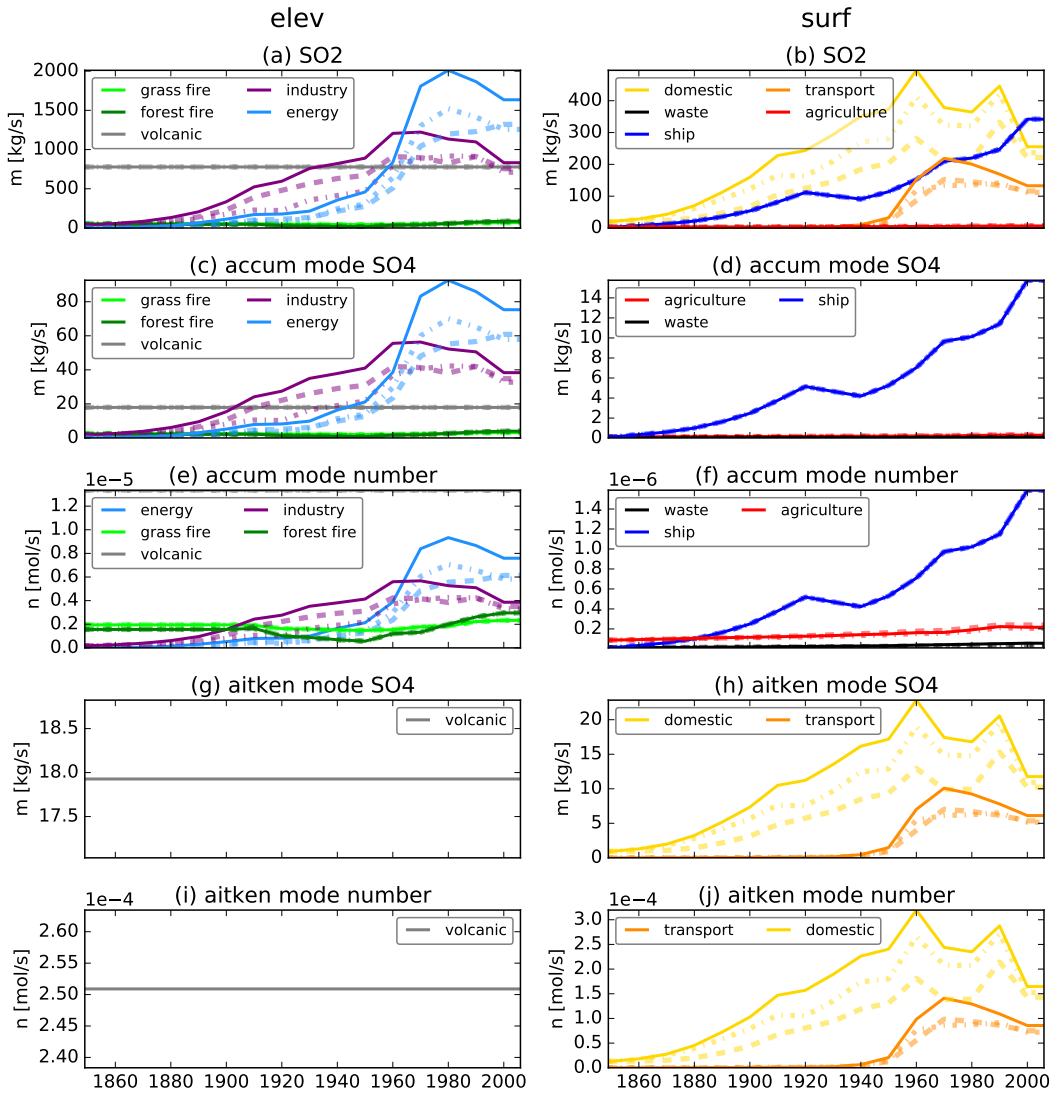

Figure 4.A.1: Global-mean, JJA-mean emissions of the (a) sulphate precursor sulphur dioxide (SO_2) and (c-j) primary sulphate (SO_4) as modified for the CESM regional-aerosol experiments: Global anthropogenic and natural emissions from (left) elevated and (right) surface sources of the different emission sources as input to the (solid lines) ALL experiments and those with anthropogenic emissions from (dash-dotted) North American and (dashed) European sources kept at their 1850 values. All CESM aerosol emission input fields which include SO_2 or SO_4 are shown: (a-b) mass concentration rates of SO_2; (c-d) mass concentration rates and (e-f) number concentration rates of SO_4 in the accumulation mode; and (g-h) mass concentration rates and (i-j) number concentration rates of SO_4 in the Aitken mode.

sources within the North American or European region, respectively (Fig. 1.3d), to their 1850 value. These are energy, industry, domestic, transport, agriculture, and waste, but not ship, forest fire, grass fire, or volcanic.

To check the resulting files, I convert the CESM-type emissions files into emissions which can be compared to those shown in the other chapters. This includes (1) changing the units from particles/cm3/s $\cdot 6.022 \cdot 10^{26}$ and particles/cm2/s $\cdot 6.022 \cdot 10^{26}$ (with $6.022 \cdot 10^{26} = 1000 \cdot \mathrm{N_A mol}$ and the Avogadro constant $\mathrm{N_A} \approx 6 \cdot 10^{23} \mathrm{mol}^{-1}$); (2) converting the emissions given as number density of aerosol particles (n_p [mol]) to number density of molecules (n_m [mol]) using

$$\begin{aligned} n_p[\mathrm{mol}] &= \frac{m_m}{m_p}\frac{1}{\mathrm{N_A}} = \frac{M n_m}{\rho_p V_p}\frac{1}{\mathrm{N_A}} = \frac{M n_m}{\rho_p \frac{4}{3}\pi(\frac{d_p}{2})^3}\frac{1}{\mathrm{N_A}} \\ &\approx 2.1 \cdot 10^{-10} \mu\mathrm{m}^3 \frac{n_m[\mathrm{mol}]}{d_p[\mu\mathrm{m}^3]} \end{aligned} \tag{4.1}$$

with the emitted particle diameters d_p [μm] of 0.261 (energy, industry, shipping), 0.134 (forest and grass fire, waste), 0.134 (accumulation mode of background volcanic emissions), and 0.0504 (domestic, transport and Aitken mode of background volcanic emissions) and the dry particle density for SO_4 $\rho_p = 1.77[g/cm3]$; and (3) converting the number density of molecules i.e. the concentration of amount of substance into the concentration of mass using $m_{SO2}[\mathrm{g}] = 1/64 n_{m,SO2}[\mathrm{mol}]$ and $m_{SO4}[\mathrm{g}] = 1/(64 \cdot 1.8) n_{m,SO4}\mathrm{mol}$ (with the molar masses of $M_{SO2} \approx 64$ g/mol and $M_{NH4HSO4} \approx 115$ g/mol).

The total sum of the resulting global-mean summer (JJA) emissions of sulphate aerosols and -precursors (Fig. 4.A.1, with column-integrated elevated concentrations) is reassuringly consistent with those from the original surface emission files (Fig. 2.1).

Appendix 4.B Atlantic Storm Activity

Large-scale storm systems, both tropical and extratropical, are impactful features of Atlantic weather (e.g., *Christensen et al.*, 2013; *IPCC*, 2012) linked to Atlantic climate variability. Recently, *Dunstone et al.* (2013) suggested the possibility of external factors, in particular anthropogenic aerosols, to be the dominant driver of historical tropical storm variability in the North Atlantic region. Their conclusion of sulphate aerosols to have suppressed Tropical Hurricane frequency by cooling Atlantic SSTs motivates this attempt to determine the contribution from North American and European SO_2 emissions, respectively.

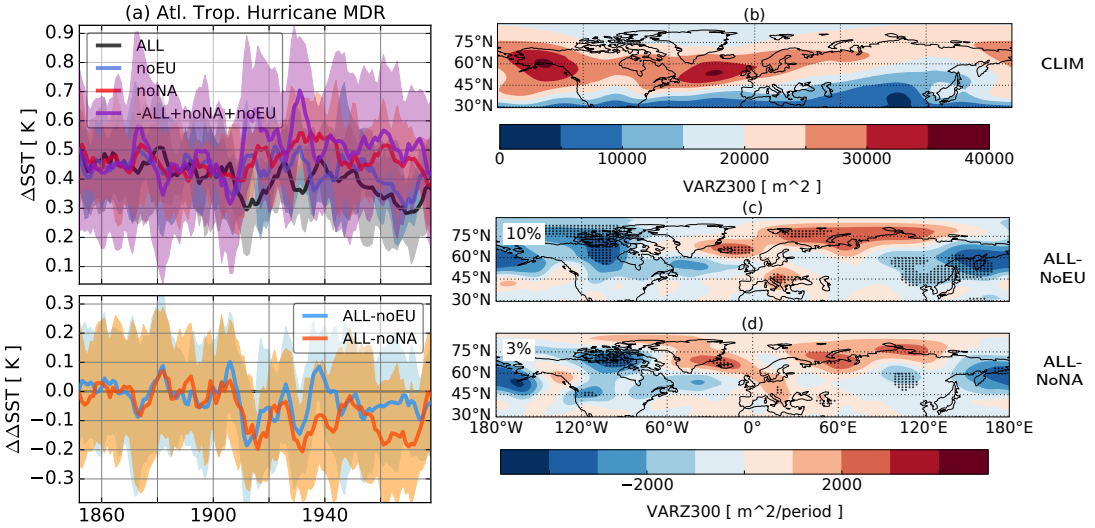

Figure 4.B.1: Indicators of simulated storm activity in the Atlantic region: (a) Time series as in Figs. 4.1(a-b) and 4.5(a), but for June-November SST of the Atlantic Hurricane Main development region (MDR; 5-25°N,80°W-20°E) relative to tropical-mean (30°S-30°N) SSTs as measure of tropical storm activity, and (b) climatology and (c-d) linear trends as in Fig. 4.1(c-d), but for winter (DJF) monthly-mean variance (VAR) of daily geo-potential height at 300 hPa (Z300) as a measure of extra-tropical storm activity.

As a measure of Atlantic Tropical Hurricane activity, we use area-mean SST of their main development region (MDR; 5-25°N, 80°W-20°E) relative to tropical-mean (30°S-°N) SST during the Hurricane season (June-November) as *Villarini et al.* (2010); *Dunstone et al.* (2013). We find that SO_2 emissions from both NA and EU decrease the simulated index substantially (Fig. 4.B.1a). During 1900-1975, it is on average around 0.1 K lower in response to NA emissions, and around 0.05 K lower in response to EU emissions. This difference is consistent with the larger NA impact on SSTs over the Western side of the MDR region (Fig. 4.1d-e) and on SSTs and upper ocean heat content over the Atlantic and elsewhere (Fig. C.2). The relative cooling for NA and EU together ($\approx$0.2 K) is of similar magnitude to historical variations in observations and the HadGEM2-ES model, which have been shown to roughly correspond to a change in annual storm frequency of a factor of two (*Dunstone et al.*, 2013). We also see, however, a strong signal from the other external forcings (purple line in Fig. 4.B.1a) with a complex time series on top of large internal variability, which complicates the interpretation e.g. of the rapid change seen around 1915.

We also examine possible sulphate aerosol impact on extra-tropical storm activity, approximated with the monthly-mean variance of daily-mean geopotential heights as *Chang et al.* (2002); *Linderholm et al.* (2011) averaged over the peak boreal mid-latitude storm season (December-February). We find that the patterns of long-term change due to NA and EU SO_2 emissions both show a north-eastward shift, with more storms taking a north-westerly path into central Europe via Southern Scandinavia (Fig. 4.B.1b-d). This is consistent with a northward shift of the jet stream and high pressure anomalies over Western Europe (not shown).

These findings -suppressed Tropical Hurricane frequency and shifted extra-tropical storm activity- further highlight the potential role played by sulphate aerosols on key targets of climate adaptation around the Atlantic.

Chapter 5

Conclusions

5.1 Summary

The aim of this work was to enhance our understanding of the climate impact of historical anthropogenic aerosol emissions. This was motivated by the large uncertainties still associated not only with the magnitude of historical aerosol cooling, relevant for climate sensitivity and thus long-term climate projections, but also with the impact of aerosol forcing on regional climate, both directly and through their influence on atmospheric and oceanic circulation. This is relevant for short- to mid-term climate projections and for the mechanistic understanding of the climate system in general. The knowledge gains expected from including the early industrial period in particular had so far been underexploited; despite being observationally more challenging than the more recent decades, the still lower greenhouse gas forcing, potential disproportionately larger aerosol effects, and improved signal-to-noise ratios due to the longer record are promising. Having been the by far most important aerosol emission source regions until around the mid-twentieth century, North America and Europe presented themselves naturally as the focus. They furthermore had enough similarities (emission history, latitudinal location) and differences (longitudinal location, position with respect to climatological circulation) to be also interesting to study in contrast to each other.

First, the boreal summer climate response to North American and European (NAEU) anthropogenic aerosol emissions during the twentieth century was characterised using a suite of models from the Coupled Model Inter-Comparison Project 5 (CMIP5). Supported by the co-variability of aerosol optical depth and near-surface climate, long-term variations in aerosol-only and all-forcing simulations were attributed to NAEU aerosol forcing if they undergo a significant reversal coinciding with the peak in NAEU SO_2 emissions, measured by inter-model agreement on the sign of linear trends before and after 1975. Regionally, robust aerosol impact was found on Eurasian near-surface temperature, pressure, and diurnal temperature range; remotely, robust aerosol impact was found on the Inter-Tropical Convergence Zone (ITCZ) position and the subtropical jet stream. The contribution of anthropogenic aerosol forcing to the forced component of simulated inter-decadal climate variability of European-mean near-surface temperature was furthermore estimated to be more than a third throughout the twentieth century. Observed variations also of European-mean sea level pressure and diurnal temperature range tended to agree better with simulations that include aerosols.

The aerosol impact on observed West African and South Asian monsoon precipitation was then investigated by using a detection and attribution (D&A) approach. The aerosol source regions (NAEU, South Asia, or China) which are most important for explaining the observed 1920-2005 changes were identified. For this, fingerprints of the response to regional-aerosol forcing were derived from historical simulations with the GFDL-CM3 model along with CMIP5 simulations. It was found that in precipitation observations for West Africa, the only anthropogenic forcing which can be detected are NAEU emissions. In precipitation observations for South Asia, in contrast, local emissions were the only external forcing detected. Changes in West Africa were found to be related to a meridional shift in the ITCZ due to aerosol-induced changes in the inter-hemispheric temperature gradient. Changes in South Asia, in contrast, were found to be associated with a weakening of the monsoon circulation, driven by the increase of remote NAEU aerosol emissions until 1975 and since then by the increase in local emissions offsetting the decrease in NAEU emissions.

Finally, the dynamical impact of NA and EU sulphate aerosol emissions was fully analysed in the coupled Community Earth System model (CESM1-CAM5), focusing on the Atlantic. For this, multi-member ensemble simulations covering the period 1850-1975 were performed, and the response to emissions from NA and EU was contrasted. The results showed that sulphate aerosols from either source cause a long-term cooling of North Atlantic sea-surface temperatures (SSTs), with the patterns a combination of atmospheric aerosol effects and an aerosol-induced strengthening of the Atlantic Meridional Overturning Circulation (AMOC). The North Atlantic response to NA emissions is larger than that to EU emissions, with stronger indirect aerosol effects due to a wider aerosol spread over the Atlantic and collocation with climatological cloud cover. A southward shift of the ITCZ, affecting tropical precipitation globally, was also found. The (multi)decadal variability components of Atlantic SSTs and of the AMOC were furthermore both found to be externally forced. A suppression of Atlantic Tropical Hurricane frequency and a north-eastward shift of Atlantic extra-tropical storms in response to both NA and EU emissions were finally shown.

5.2 Challenges and Limitations

A challenge in addressing the aim of this work was the balance between identifying aerosol impacts which are robust to inter-model differences e.g. in their aerosol effect representation and can be compared to observations, and delving into the e.g. dynamical mechanisms which cause these impacts but might be more model-dependent and are difficult to test against observations. The analysis of South Asian monsoon precipitation for instance (Chapter 3) was able to attribute observed precipitation changes clearly to aerosol forcing even by region, but missing historical observations of more process-related or large-scale circulation variables like wind speed (Section 3.4.2) keeps the mechanism of this aerosol impact more uncertain. The same is true for the suggested relationship between cloud cover and diurnal temperature range (Section 2.4.4), details of aerosol-cloud interactions over the Atlantic (Section 4.3.2), or the relationship between Atlantic SSTs and the AMOC (Section 4.3.3). Additional

challenges were associated with limitations in the available model simulations, including the limited number of modelling groups providing aerosol-only simulations, their partially small ensemble size, and the varying number of aerosol output variables available (Chapter 2).

Due to the already wide focus of this study, not much room was given to discussing the impacts of aerosol species other than sulphate aerosols. In the first part, the spatial analysis effectively constrained the impacts of sulphate aerosols by choosing to contrast linear trends during periods in which only emissions of sulphur dioxide changed distinctly (Section 2.4). In the second part, the detection and attribution study as well as the analysis of the dynamical mechanisms considered the effect of all anthropogenically emitted aerosol species together (Chapter 3). This grouping of different aerosol species together in the available "single"-forcing aerosol-only simulations can introduce additional uncertainty regarding for example the scaling of the aerosol forcing in detection and attribution studies, for example if there are inter-models differences in the proportions between the forcing from different aerosol species. In the last part, for which model simulations could be purposefully designed, the impact of sulphate aerosols was finally studied in rigorous isolation (Chapter 4). An analysis of the effect of the other aerosol species, including land-atmosphere interactions like the effects of black carbon on snow or those from land-use changes in the Tropics would however also be interesting.

A limitation of the findings on sulphate aerosol impact on the Atlantic and the associated mechanisms and feedbacks (Chapter 4) is that they are based on a single model. The model response has been tested for being realistic within the context of existing inter-model comparisons, and, where possible within the scope of this work, consistent with observations, too. Given the high degree of parametrisation and the associated uncertainties e.g. of aerosol- and cloud-related processes below the grid scale still present in current global climate models, a future reproduction of the analysis with different models would be desirable nevertheless.

5.3 Wider Implications

The identification of regional-scale historical changes in response to regional anthropogenic aerosol emissions, both in contrast to other external forcings like greenhouse gases and to anthropogenic aerosol emissions from elsewhere, is relevant for understanding also the effect of both present aerosol emissions and future emission reductions (e.g., *Vuuren et al.*, 2011). This includes the recognition of expected benefits which might provide motivation for emission reductions in addition to expected health effects from improved air quality, but also the informing of adaptation efforts where negative effects compared to present-day conditions are anticipated.

This study shows for the first time that the aerosol forcing from individual emission regions is strong and distinct enough to be detected over internal variability in a detection and attribution framework (Chapter 3). In addition to the scientific progress, this might also be relevant should the international political discourse of climate justice (*UNFCCC. Conference of the Parties (COP)*, 2015) seek the attribution of aerosol-impacted regional climate change to emission source regions (e.g., *Huggel et al.*, 2016). Some of the aerosol impacts on climate reported here are very relevant in terms of climate impacts on societies and ecosystems. This applies especially to the observed changes in monsoon precipitation over West Africa and South Asia because of the huge number of people affected and their high vulnerability (*Hewitson et al.*, 2014). This also applies to the simulated changes in Atlantic storm activity, for example because of the potentially devastating effects of storm surges caused by tropical cyclones (e.g., *Mendelsohn et al.*, 2012; *Shultz et al.*, 2018).

Relevant beyond the question of historical anthropogenic aerosols impact are also the model findings on the external forcing of the AMOC (Section 4.3.3), since the future AMOC response to GHG forcing might affect global sea level change e.g. through feedbacks on the Greenland ice sheet (*Church et al.*, 2013) and be even more relevant for the climate beyond the 21st century in the -although judged as unlikely (*Collins et al.*, 2013)- event of its collapse. The model finding of aerosol impact on

North Atlantic SSTs by modulation of the AMOC might furthermore help to reconcile seemingly conflicting views on the control of Atlantic variability (Section 1.3.3).

Some of the changes in response to historical anthropogenic aerosol emissions identified here would furthermore have to be included in any consideration of geoengineering schemes based on solar radiation management. An example is the identified aerosol impact on diurnal temperature range, which the results suggest to be more a response directly to the aerosols' radiative effect than a feedback to the resulting surface cooling and which might thus also be expected in response to stratospheric aerosol forcing (e.g., *Crutzen*, 2006; *Lo et al.*, 2016). Regarding schemes aiming at a large-scale increase in aerosol concentrations to brighten marine clouds (e.g., *Latham*, 1990; *Salter et al.*, 2008; *The Royal Society*, 2009), our results further highlight possible responses of both atmospheric and ocean circulation to spatially heterogeneous forcing.

5.4 Areas for Future Research

There are various ways in which the research presented here could be furthered, to the benefit of both foundational scientific advancements and policy applications. An obvious research question to be addressed more is the dependency of the simulated historical aerosol impact on the model representation of aerosol effects and clouds. The next climate model inter-comparison project might be helpful for this, if more modelling groups provide aerosol-only simulations with larger ensemble size as well as more available aerosol fields and better documentation. To allow judgement on each model's realistic representation of reality, however, improved observations of aerosol-cloud processes and their effect on climate will also be needed.

Such an improved process-level understanding is promised by recent developments of a new generation of models, for instance in cloud-resolving resolution (e.g., *Klocke et al.*, 2017; *Roberts et al.*, 2018), combined with new observations of cloud properties (e.g., *Bony et al.*, 2017). These tools might also enable the further study of drivers of diurnal temperature range – while the results presented here (Chapter 2) suggest large

changes and substantial aerosol impact, more quantitative analysis in this work was discouraged by huge inter-model and observational uncertainty despite the relevance of diurnal temperature range for climate impacts and its potential for separating GHG and aerosol forcing.

The recurring theme of aerosol impact on the ITCZ could also be studied further: While focussing on its large-scale atmospheric circulation aspect has been effective for the work presented here, a more detailed analysis of its interactions with more regional circulation changes would also be interesting. Another research question could focus on aerosol impact on extreme events, for example droughts or floods especially when combined with extreme temperature events. The potential feedbacks between aerosol-induced circulation changes and aerosol concentrations, also including interactions between anthropogenic emissions of the different aerosol species as well as natural aerosols (Fig. C.7), could furthermore be studied.

With regard to the presented findings on aerosol-atmosphere-ocean interactions in the CESM model (Chapter 4), a range of follow-up questions come to mind. These include the comparison with other models, both in terms of the relative impacts of North American and European aerosols and the anthropogenic aerosol impact on the AMOC, but also with regard to the more general questions of external forcing of the AMV, the AMOC, and their relationship. Further analysis of the simulated and observed North Atlantic salinity changes (Fig. C.9), for example by means of a salinity budget analysis, might allow conclusions on the realism of the simulated AMOC response. It might also help to reduce uncertainty in aerosol impact on extra-tropical precipitation. A last research question could be to follow up on the mentioned changes in Atlantic storm activity found in the model (Section 4.B).

References

Abish, B., P. V. Joseph, and O. M. Johannessen (2015), Climate change in the subtropical jetstream during 1950-2009, *Adv. Atmos. Sci.*, *32*, 140–148, doi: 10.1007/s00376-014-4156-6.1.

Ackerley, D., B. B. B. Booth, S. H. E. Knight, E. J. Highwood, D. J. Frame, M. R. Allen, and D. P. Rowell (2011), Sensitivity of twentieth-century Sahel rainfall to sulfate aerosol and CO2 forcing, *J. Clim.*, *24*, 4999–5014, doi: 10.1175/JCLI-D-11-00019.1.

Acosta Navarro, J. C., V. Varma, I. Riipinen, Ø. Seland, A. Kirkevåg, H. Struthers, T. Iversen, H.-C. Hansson, and A. M. L. Ekman (2016), Amplification of Arctic warming by past air pollution reductions in Europe, *Nat. Geosci.*, *9*, 277–281, doi: 10.1038/NGEO2673.

Adler, R. F., G. J. Huffman, A. Chang, R. Ferraro, P.-P. Xie, J. Janowiak, B. Rudolf, U. Schneider, S. Curtis, D. Bolvin, A. Gruber, J. Susskind, P. Arkin, and E. Nelkin (2003), The version-2 Global Precipitation Climatology Project (GPCP) monthly precipitation analysis (1979-present), *J. Hydrometeorol.*, *4*(6), 1147–1167, doi: 10.1175/1525-7541(2003)004<1147:TVGPCP>2.0.CO;2.

Albrecht, B. A. (1989), Aerosols, cloud microphysics, and fractional cloudiness, *Science*, *245*, 1227–1230, doi: 10.1126/science.245.4923.1227.

Allan, R., and T. Ansell (2006), A new globally complete monthly historical gridded mean sea level pressure dataset (HadSLP2): 1850-2004, *J. Clim.*, *19*(22), 5816–5842, doi: 10.1175/JCLI3937.1.

Allen, M. R., and P. A. Stott (2003), Estimating signal amplitudes in optimal fingerprinting , part I : theory, pp. 477–491, doi: 10.1007/s00382-003-0313-9.

Allen, R. J. (2015), A 21st century northward tropical precipitation shift caused by future anthropogenic aerosol reductions, *J. Geophys. Res. Atmos.*, *120*(18), 9087–9102, doi: 10.1002/2015JD023623.

Allen, R. J., and O. Ajoku (2016), Future aerosol reductions and widening of the northern tropical belt, *J. Geophys. Res. Atmos.*, *121*(12), 6765–6786, doi: 10.1002/2016JD024803.

Allen, R. J., S. C. Sherwood, J. R. Norris, and C. S. Zender (2012), Recent Northern Hemisphere tropical expansion primarily driven by black carbon and tropospheric ozone, *Nature*, *485*(7398), 350–354, doi: 10.1038/nature11097.

Allen, R. J., J. R. Norris, and M. Kovilakam (2014), Influence of anthropogenic aerosols and the Pacific Decadal Oscillation on tropical belt width, *Nat. Geosci.*, *7*, 270–274, doi: 10.1038/NGEO2091.

Allen, R. J., W. Landuyt, and S. T. Rumbold (2015), An increase in aerosol burden and radiative effects in a warmer world, *Nat. Clim. Chang.*, (November), 1–6, doi: 10.1038/nclimate2827.

Archer, C. L., and K. Caldeira (2008a), Reply to comment by Courtenay Strong and Robert E. Davis on "Historical trends in the jet streams", *Geophys. Res. Lett.*, *35*(L24807), 1, doi: 10.1029/2008GL035114.

Archer, C. L., and K. Caldeira (2008b), Historical trends in the jet streams, *Geophys. Res. Lett.*, *35*(L08803), 1–6, doi: 10.1029/2008GL033614.

Ba, J., N. S. Keenlyside, M. Latif, W. Park, H. Ding, K. Lohmann, J. Mignot, M. Menary, O. H. Otterå, B. Wouters, D. Salas y Melia, A. Oka, A. Bellucci, and E. Volodin (2014), A multi-model comparison of Atlantic multidecadal variability, *Clim. Dyn.*, *43*(9-10), 2333–2348, doi: 10.1007/s00382-014-2056-1.

Barnett, T. P., K. Hasselmann, M. Chelliah, T. Delworth, G. Hegerl, P. Jones, E. Rasmusson, E. Roeckner, C. Ropelewski, B. Santer, and S. Tett (1999), Detection and attribution of recent climate change: A status report, *Bul. Am. Met. Soc.*, *80*(12), 2631–2659.

Beck, C., J. Grieser, and B. Rudolf (2004), A new monthly precipitation climatology for the global land areas for the period 1951 to 2000, *Tech. rep.*, German Weather Service, Offenbach.

Bellomo, K., L. N. Murphy, M. A. Cane, A. C. Clement, and L. M. Polvani (2017), Historical forcings as main drivers of the Atlantic multidecadal variability in the CESM large ensemble, *Clim. Dyn.*, doi: 10.1007/s00382-017-3834-3.

Bellouin, N., L. Baker, Ø. Hodnebrog, D. Olivié, R. Cherian, C. Macintosh, B. Samset, A. Esteve, B. Aamaas, J. Quaas, and G. Myhre (2016), Regional and seasonal radiative forcing by perturbations to aerosol and ozone precursor emissions, *Atmos. Chem. Phys.*, *16*, 13,885–13,910, doi: 10.5194/acp-16-13885-2016.

Biasutti, M. (2013), Forced Sahel rainfall trends in the CMIP5 archive, *J. Geophys. Res. Atmos.*, *118*(4), 1613–1623, doi: 10.1002/jgrd.50206.

Bindoff, N. L., P. A. Stott, M. AchutaRao, M. R. Allen, N. Gillett, D. Gutzler, K. Hansingo, G. Hegerl, Y. Hu, S. Jain, I. I. Mokhov, J. Overland, J. Perlwitz, R. Sebbari, and X. Zhang (2013), Detection and attribution of climate change: From global to regional, in *Clim. Chang. 2013 Phys. Sci. Basis. Contrib. Work. Gr. I to Fifth Assess. Rep. Intergov. Panel Clim. Chang.*, edited by T. F. Stocker, D. Qin, G.-K. Plattner, M. Tignor, S. K. Allen, J. Boschung, A. Nauels, Y. Xia, V. Bex, and P. M. Midgley, Cambridge University Press, Cambridge, United Kingdom and New York, NY, USA.

Bjerknes, J. (1964), Atlantic air-sea interaction, *Adv. Geophys.*, *10*(C), 1–82, doi: 10.1016/S0065-2687(08)60005-9.

Boden, T. A., G. Marland, and R. J. Andres (2010), Global, regional, and national fossil-fuel CO2 emissions, doi: 10.3334/CDIAC/00001_V2010.

Bollasina, M. A., Y. Ming, and V. Ramaswamy (2011), Anthropogenic Aerosols and the Weakening of the South Asian Summer Monsoon, *Science*, *334*, 502–505, doi: 10.1126/science.1204994.

Bollasina, M. a., Y. Ming, and V. Ramaswamy (2013), Earlier onset of the Indian monsoon in the late twentieth century: The role of anthropogenic aerosols, *Geophys. Res. Lett.*, *40*(14), 3715–3720, doi: 10.1002/grl.50719.

Bollasina, M. A., Y. Ming, V. Ramaswamy, M. D. Schwarzkopf, and V. Naik (2014), Contribution of local and remote anthropogenic aerosols to the twentieth century weakening of the South Asian Monsoon, *Geophys. Res. Lett.*, *41*, 680–687, doi: 10.1002/2013GL058183.Received.

Bond, T. C., E. Bhardwaj, R. Dong, R. Jogani, S. Jung, C. Roden, D. G. Streets, and N. M. Trautmann (2007), Historical emissions of black and organic carbon aerosol from energy-related combustion, 1850-2000, *Global Biogeochem. Cycles*, *21*(2), 1–16, doi: 10.1029/2006GB002840.

Bony, S., B. Stevens, F. Ament, S. Bigorre, P. Chazette, S. Crewell, J. Delanoë, K. Emanuel, D. Farrell, C. Flamant, S. Gross, L. Hirsch, J. Karstensen, B. Mayer, L. Nuijens, J. H. Ruppert, I. Sandu, P. Siebesma, S. Speich, F. Szczap, J. Totems, R. Vogel, M. Wendisch, and M. Wirth (2017), EUREC4A: A field campaign to elucidate the couplings between clouds, convection and circulation, *Surv. Geophys.*, *38*(6), 1529–1568, doi: 10.1007/s10712-017-9428-0.

Booth, B. B. B., N. J. Dunstone, P. R. Halloran, T. Andrews, and N. Bellouin (2012), Aerosols implicated as a prime driver of twentieth-century North Atlantic climate variability., *Nature*, *484*(7393), 228–232, doi: 10.1038/nature10946.

Boucher, O., D. Randall, P. Artaxo, C. Bretherton, G. Feingold, P. Forster, V.-M. Kerminen, Y. Kondo, H. Liao, U. Lohmann, P. Rasch, S. K. Satheesh, S. Sherwood, B. Stevens, and X. Y. Zhang (2013), Clouds and aerosols, in *Clim. Chang. 2013 Phys. Sci. Basis. Contrib. Work. Gr. I to Fifth Assess. Rep. Intergov. Panel Clim. Chang.*, edited by T. F. Stockers, D. Qin, G.-K. Plattner, M. Tignor, S. K. Allen,

J. Boschung, A. Nauels, Y. Xia, V. Bex, and P. M. Midgley, Cambridge University Press, Cambridge, United Kingdom and New York, NY, USA.

Branstator, G. (2002), Circumglobal teleconnections, the jet stream waveguide, and the North Atlantic Oscillation, *J. Clim.*, *15*(14), 1893–1910, doi: 10.1175/1520-0442(2002)015<1893:CTTJSW>2.0.CO;2.

Buckley, M. W., and J. Marshall (2016), Observations, inferences, and mechanisms of the AtlanticMeridionalOverturning Circulation: A review, *Rev. Geophys.*, *54*, 5–63, doi: 10.1002/2015RG000493.

Buseck, P. R., K. Adachi, A. Gelencsér, É. Tompa, and M. Pósfai (2012), Are black carbon and soot the same?, *Atmos. Chem. Phys. Discuss.*, *12*(9), 24,821–24,846, doi: 10.5194/acpd-12-24821-2012.

Carslaw, K. S., L. A. Lee, C. L. Reddington, K. J. Pringle, A. Rap, P. M. Forster, G. W. Mann, D. V. Spracklen, M. T. Woodhouse, L. A. Regayre, and J. R. Pierce (2013), Large contribution of natural aerosols to uncertainty in indirect forcing, *Nature*, *503*(7474), 67–71, doi: 10.1038/nature12674.

Cattiaux, J., H. Douville, R. Schoetter, S. Parey, and P. Yiou (2015), Projected increase in diurnal and interdiurnal variations of European summer temperatures, *Geophys. Res. Lett.*, *42*(3), 899–907, doi: 10.1002/2014GL062531.

CCSP (2009), Atmospheric aerosol properties and climate impacts. A report by the U.S. Climate Change Science Program and the Subcommittee on Global Change Research, *Tech. Rep. January*, Washington, D.C., USA.

Chang, C.-Y., J. C. H. Chiang, M. F. Wehner, A. R. Friedman, and R. Ruedy (2011), Sulfate aerosol control of tropical Atlantic climate over the twentieth century, *J. Clim.*, *24*(10), 2540–2555, doi: 10.1175/2010JCLI4065.1.

Chang, E. K., S. Lee, and K. L. Swanson (2002), Storm track dynamics, *J. Clim.*, *15*(16), 2163–2183, doi: 10.1175/1520-0442(2002)015<02163:STD>2.0.CO;2.

Charlson, R. J., S. E. Schwartz, J. M. Hales, R. D. Cess, J. A. Coakley, Jr, J. E. Hansen, and D. J. Hofmann (1992), Climate forcing by anthropogenic aerosols, *Science*, *255*, 423–430, doi: 10.1126/science.255.5043.423.

Chiacchio, M., T. Ewen, M. Wild, M. Chin, and T. Diehl (2011), Decadal variability of aerosol optical depth in Europe and its relationship to the temporal shift of the North Atlantic Oscillation in the realm of dimming and brightening, *J. Geophys. Res. Atmos.*, *116*(2), 1–13, doi: 10.1029/2010JD014471.

Chiang, J. C. H., and A. R. Friedman (2012), Extratropical Cooling, Interhemispheric Thermal Gradients, and Tropical Climate Change, *Annu. Rev. Earth Planet. Sci.*, *40*(1), 383–412, doi: 10.1146/annurev-earth-042711-105545.

Christensen, J., K. K. Kumar, E. Aldrian, S.-I. An, I. Cavalcanti, M. de Castro, P. G. W. Dong, A. Hall, J. Kanyanga, A. Kitoh, J. Kossin, N.-C. Lau, J. Renwick, D. Stephenson, S.-P. Xie, and T. Zhou (2013), Climate phenomena and their relevance for future regional climate change, in *Clim. Chang. 2013 Phys. Sci. Basis. Contrib. Work. Gr. I to Fifth Assess. Rep. Intergov. Panel Clim. Chang.*, edited by T. Stocker, D. Qin, G.-K. Plattner, M. Tignor, S. Allen, J. Boschung, A. Nauels, Y. Xia, V. Bex, and P. Midgley, chap. 14, Cambridge University Press, Cambridge, United Kingdom and New York, NY, USA.

Church, J. A., P. U. Clark, A. Cazenave, J. M. Gregory, S. Jevrejeva, A. Levermann, M. A. Merrifield, G. A. Milne, R. S. Nerem, P. D. Nunn, A. J. Payne, W. T. Pfeffer, D. Stammer, and A. S. Unnikrishnan (2013), Sea level change, *Clim. Chang. 2013 Phys. Sci. Basis. Contrib. Work. Gr. I to Fifth Assess. Rep. Intergov. Panel Clim. Chang.*, pp. 1137–1216, doi: 10.1017/CB09781107415315.026.

Clark, S. K., Y. Ming, I. M. Held, and P. J. Phillipps (2018), The role of the water vapor feedback in the ITCZ response to hemispherically asymmetric forcings, *J. Clim.*, *31*(9), 3659–3678, doi: 10.1175/JCLI-D-17-0723.1.

Clarke, L., K. Jiang, K. Akimoto, M. Babiker, G. Blanford, K. Fisher-Vanden, J.-C. Hourcade, V. Krey, E. Kriegler, A. Löschel, D. McCollum, S. Paltsev, S. Rose, P. R.

Shukla, M. Tavoni, B. C. C. van der Zwaan, and D. P. van Vuuren (2014), Assessing transformation pathways, in *Clim. Chang. 2014 Mitig. Clim. Chang. Contrib. Work. Gr. III to Fifth Assess. Rep. Intergov. Panel Clim. Chang.*, edited by O. Edenhofer, R. Pichs-Madruga, Y. Sokona, E. Farahani, S. Kadner, K. Seyboth, A. Adler, I. Baum, S. Brunner, P. Eickemeier, B. Kriemann, J. Savolainen, S. Schlömer, C. von Stechow, T. Zwickel, and J. Minx, pp. 413–510, Cambridge University Press, Cambridge, United Kingdom and New York, NY, USA.

Clement, A., K. Bellomo, L. N. Murphy, M. A. Cane, T. Mauritsen, G. Radel, and B. Stevens (2015), The Atlantic Multidecadal Oscillation without a role for ocean circulation, *Science*, *350*(6258), 320–324, doi: 10.1126/science.aab3980.

Clement, A., M. A. Cane, L. N. Murphy, K. Bellomo, T. Mauritsen, and B. Stevens (2016), Response to Comment on "The Atlantic Multidecadal Oscillation without a role for ocean circulation", *Science*, *352*(6293), 1527–1527, doi: 10.1126/science.aaf2575.

Collins, M., R. Knutti, J. Arblaster, J.-L. Dufresne, T. Fichefet, P. Friedlingstein, X. Gao, W. J. Gutowski, T. Johns, G. Krinner, M. Shongwe, C. Tebaldi, A. J. Weaver, and M. Wehner (2013), Long-term climate change: Projections, commitments and irreversibility, *Clim. Chang. 2013 Phys. Sci. Basis. Contrib. Work. Gr. I to Fifth Assess. Rep. Intergov. Panel Clim. Chang.*, pp. 1029–1136, doi: 10.1017/CBO9781107415324.024.

Collins, W. J., N. Bellouin, M. Doutriaux-Boucher, N. Gedney, P. Halloran, T. Hinton, J. Hughes, C. D. Jones, M. Joshi, S. Liddicoat, F. O'Connor, J. Rae, C. Senior, S. Sitch, I. Totterdell, A. Wiltshire, and S. Woodward (2011), Model development and evaluation of an Earth-System model - HadGEM2, *Geosci. Model Dev.*, *4*, 1051–1075, doi: 10.5194/gmd-4-1051-2011.

Compo, G. P., J. S. Whitaker, P. D. Sardeshmukh, N. Matsui, R. J. Allan, X. Yin, E. Gleason, R. S. Vose, G. Rutledge, P. Bessemoulin, S. Br, G. J. Marshall, M. Maugeri, H. Y. Mok, Ø. Nordli, T. F. Ross, R. M. Trigo, X. L. Wang, S. D.

Woodruff, and S. J. Worley (2011), The Twentieth Century Reanalysis project, *Q. J. R. Meteorol. Soc.*, *137*, 1–28, doi: 10.1002/qj.776.

Cowan, T., and W. Cai (2011), The impact of Asian and non-Asian anthropogenic aerosols on 20th century Asian summer monsoon, *Geophys. Res. Lett.*, *38*, L11,703, doi: 10.1029/2011GL047268.

Cowan, T., and W. Cai (2013), The response of the large-scale ocean circulation to 20th century Asian and non-Asian aerosols, *Geophys. Res. Lett.*, *40*(11), 2761–2767, doi: 10.1002/grl.50587.

Crutzen, P. J. (2006), Albedo enhancement by stratospheric sulfur injections: A contribution to resolve a policy dilemma?, *Clim. Change*, *77*(3-4), 211–219, doi: 10.1007/s10584-006-9101-y.

Dallafior, T. N., D. Folini, R. Knutti, and M. Wild (2015), Dimming over the oceans: Transient anthropogenic aerosol plumes in the twentieth century, *J. Geophys. Res. Atmos.*, *120*(8), 3465–3484, doi: 10.1002/2014JD022658.

Davis, N. A., and T. Birner (2013), Seasonal to multidecadal variability of the width of the tropical belt, *J. Geophys. Res. Atmos.*, *118*(14), 7773–7787, doi: 10.1002/jgrd.50610.

Delworth, T., S. Manabe, and R. J. Stouffer (1993), Interdecadal variations of the thermohaline circulation in a coupled ocean-atmosphere model, *J. Clim.*, *6*(11), 1993–2011, doi: 10.1175/1520-0442(1993)006<1993:IVOTTC>2.0.CO;2.

Delworth, T. L., and K. W. Dixon (2006), Have anthropogenic aerosols delayed a greenhouse gas-induced weakening of the North Atlantic thermohaline circulation?, *Geophys. Res. Lett.*, *33*(2), 3–6, doi: 10.1029/2005GL024980.

Delworth, T. L., and F. Zeng (2016), The impact of the North Atlantic Oscillation on climate through its influence on the Atlantic meridional overturning circulation, *J. Clim.*, *29*(3), 941–962, doi: 10.1175/JCLI-D-15-0396.1.

Delworth, T. L., V. Ramaswamy, and G. L. Stenchikov (2005), The impact of aerosols on simulated ocean temperature and heat content in the 20th century, *Geophys. Res. Lett.*, *32*(24), 1–4, doi: 10.1029/2005GL024457.

Delworth, T. L., F. Zeng, L. Zhang, R. Zhang, G. A. Vecchi, and X. Yang (2017), The central role of ocean dynamics in connecting the North Atlantic Oscillation to the extratropical component of the Atlantic Multidecadal Oscillation, *J Clim.*, *30*, 3789–3805, doi: 10.1175/JCLI-D-16-0358.1.

Deser, C., and M. L. Blackmon (1993), Surface climate variations over the North Atlantic Ocean during winter: 1900-1989, *J. Clim.*, *6*, 1743–1753.

Ding, Y., J. A. Carton, G. A. Chepurin, G. Stenchikov, A. Robock, L. T. Sentman, and J. P. Krasting (2014), Ocean response to volcanic eruptions in Coupled Model Intercomparison Project 5 simulations, *J. Geophys. Res.*, *119*, 5622–5637, doi: 10.1002/2013JC009780.Received.

Dong, B., and R. Sutton (2015), Dominant role of greenhouse-gas forcing in the recovery of Sahel rainfall, *Nat. Clim. Chang.*, *5*(August), 757–761, doi: 10.1038/NCLIMATE2664.

Dong, B., and R. T. Sutton (2005), Mechanism of interdecadal thermohaline circulation variability in a coupled ocean-atmosphere GCM, *J. Clim.*, *18*(8), 1117–1135, doi: 10.1175/JCLI3328.1.

Dong, B., R. T. Sutton, E. Highwood, and L. Wilcox (2014a), The Impacts of European and Asian Anthropogenic Sulfur Dioxide Emissions on Sahel Rainfall, *J. Clim.*, *27*(18), 7000–7017, doi: 10.1175/JCLI-D-13-00769.1.

Dong, B., R. T. Sutton, E. J. Highwood, and L. J. Wilcox (2015), Preferred response of the East Asian summer monsoon to local and non-local anthropogenic sulphur dioxide emissions, *Clim. Dyn.*, *46*(5), 1733–1751, doi: 10.1007/s00382-015-2671-5.

Dong, L., T. Zhou, and X. Chen (2014b), Changes of Pacific decadal variability in the twentieth century driven by internal variability, greenhouse gases, and aerosols, *Geophys. Res. Lett.*, *41*, 8570–8577, doi: 10.1002/2014GL062269.Published.

Donner, L. J., B. L. Wyman, R. S. Hemler, L. W. Horowitz, Y. Ming, M. Zhao, J.-C. Golaz, P. Ginoux, S.-J. Lin, M. D. Schwarzkopf, J. Austin, G. Alaka, W. F. Cooke, T. L. Delworth, S. M. Freidenreich, C. T. Gordon, S. M. Griffies, I. M. Held, W. J. Hurlin, S. A. Klein, T. R. Knutson, A. R. Langenhorst, H.-C. Lee, Y. Lin, B. I. Magi, S. L. Malyshev, P. C. D. Milly, V. Naik, M. J. Nath, R. Pincus, J. J. Ploshay, V. Ramaswamy, C. J. Seman, E. Shevliakova, J. J. Sirutis, W. F. Stern, R. J. Stouffer, R. J. Wilson, M. Winton, A. T. Wittenberg, and F. Zeng (2011), The dynamical core, physical parameterizations, and basic simulation characteristics of the atmospheric component AM3 of the GFDL global coupled model CM3, *J. Clim.*, pp. 3484–3519, doi: 10.1175/2011JCLI3955.1.

Drijfhout, S., G. J. van Oldenborgh, and A. Cimatoribus (2012), Is a decline of AMOC causing the warming hole above the North Atlantic in observed and modeled warming patterns?, *J. Clim.*, *25*(24), 8373–8379, doi: 10.1175/JCLI-D-12-00490.1.

Dufresne, J.-L., M.-A. Foujols, S. Denvil, A. Caubel, O. Marti, O. Aumont, Y. Balkanski, S. Bekki, H. Bellenger, R. Benshila, S. Bony, L. Bopp, P. Braconnot, P. Brockmann, P. Cadule, F. Cheruy, F. Codron, A. Cozic, D. Cugnet, N. de Noblet, J.-P. Duvel, C. Ethé, L. Fairhead, T. Fichefet, S. Flavoni, P. Friedlingstein, J.-Y. Grandpeix, L. Guez, E. Guilyardi, D. Hauglustaine, F. Hourdin, A. Idelkadi, J. Ghattas, S. Joussaume, M. Kageyama, G. Krinner, S. Labetoulle, A. Lahellec, M.-P. Lefebvre, F. Lefevre, C. Levy, Z. X. Li, J. Lloyd, F. Lott, G. Madec, M. Mancip, M. Marchand, S. Masson, Y. Meurdesoif, J. Mignot, I. Musat, S. Parouty, J. Polcher, C. Rio, M. Schulz, D. Swingedouw, S. Szopa, C. Talandier, P. Terray, N. Viovy, and N. Vuichard (2013), Climate change projections using the IPSL-CM5 Earth System Model: From CMIP3 to CMIP5, *Clim. Dyn.*, *40*, 2123–2165, doi: 10.1007/s00382-012-1636-1.

Dunstone, N. J., D. M. Smith, B. B. B. Booth, L. Hermanson, and R. Eade (2013), Anthropogenic aerosol forcing of Atlantic tropical storms, *Nat. Geosci.*, *6*, 534–539, doi: 10.1038/ngeo1854.

Eade, R., D. Smith, A. Scaife, E. Wallace, N. Dunstone, L. Hermanson, and N. Robinson (2014), Do seasonal-to-decadal climate predictions underestimate the predictability of the real world?, *Geophys. Res. Lett.*, *41*, 5620–5628, doi: 10.1002/2014GL061146.

Ekman, A. M. L. (2014), Do sophisticated parameterizations of aerosol[U+2010]cloud interactions in CMIP5 models improve the representation of recent observed temperature trends?, *J. Geophys. Res. Atmos.*, *119*, 817–832, doi: 10.1002/2013JD020511.Received.

Feudale, L., and F. Kucharski (2013), A common mode of variability of African and Indian monsoon rainfall at decadal timescale, *Clim. Dyn.*, *41*, 243–254, doi: 10.1007/s00382-013-1827-4.

Flato, G., J. Marotzke, B. Abiodun, P. Braconnot, S. Chou, W. Collins, P. Cox, F. Driouech, S. Emori, V. Eyring, C. Forest, P. Gleckler, E. Guilyardi, C. Jakob, V. Kattsov, C. Reason, and M. Rummukainen (2013), Evaluation of climate models, in *Clim. Chang. 2013 Phys. Sci. Basis. Contrib. Work. Gr. I to Fifth Assess. Rep. Intergov. Panel Clim. Chang.*, edited by T. Stocker, D. Qin, G.-K. Plattner, M. Tignor, S. Allen, J. Boschung, A. Nauels, Y. Xia, V. Bex, and P. M. Midgley, Cambridge, United Kingdom and New York, NY, USA.

Forster, P. M., T. Andrews, P. Good, J. M. Gregory, L. S. Jackson, and M. Zelinka (2013), Evaluating adjusted forcing and model spread for historical and future scenarios in the CMIP5 generation of climate models, *J. Geophys. Res. Atmos.*, *118*(3), 1139–1150, doi: 10.1002/jgrd.50174.

Forster, P. M., T. Richardson, A. C. Maycock, C. J. Smith, B. H. Samset, G. Myhre, T. Andrews, R. Pincus, and M. Schulz (2016), Recommendations for diagnosing effective radiative forcing from climate models for CMIP6, *J. Geophys. Res. Atmos.*, *121*, 12,460–12,475, doi: 10.1002/2016JD025320.

Friedman, A. R., G. Reverdin, M. Khodri, and G. Gastineau (2017), A new record of Atlantic sea surface salinity from 1896 to 2013 reveals the signatures of climate variability and long-term trends, *Geophys. Res. Lett.*, *44*(4), 1866–1876, doi: 10.1002/2017GL072582.

Fu, Q., and P. Lin (2011), Poleward shift of subtropical jets inferred from satellite-observed lower-stratospheric temperatures, *J. Clim.*, *24*(21), 5597–5603, doi: 10.1175/JCLI-D-11-00027.1.

Gallego, D., P. Ordóñez, P. Ribera, C. Peña-Ortiz, and R. García-Herrera (2015), An instrumental index of the West African Monsoon back to the nineteenth century, *Q. J. R. Meteorol. Soc.*, *141*(October), 3166–3176, doi: 10.1002/qj.2601.

Ganguly, D., P. J. Rasch, H. Wang, and J.-H. Yoon (2012), Climate response of the South Asian monsoon system to anthropogenic aerosols, *J. Geophys. Res.*, *117*(D13209), doi: 10.1029/2012JD017508.

Ghan, S. J., X. Liu, R. C. Easter, R. Zaveri, P. J. Rasch, J. H. Yoon, and B. Eaton (2012), Toward a minimal representation of aerosols in climate models: Comparative decomposition of aerosol direct, semidirect, and indirect radiative forcing, *J. Clim.*, *25*(19), 6461–6476, doi: 10.1175/JCLI-D-11-00650.1.

Gillett, N. P., and J. C. Fyfe (2013), Annular mode changes in the CMIP5 simulations, *Geophys. Res. Lett.*, *40*(6), 1189–1193, doi: 10.1002/grl.50249.

GISTEMP Team (2017), GISS Surface Temperature Analysis (GISTEMP). NASA Goddard Institute for Space Studies. Dataset accessed 1/12/2017 at https://data.giss.nasa.gov/gistemp/.

Granier, C., B. Bessagnet, T. Bond, A. D'Angiola, H. Denier van der Gon, G. J. Frost, A. Heil, J. W. Kaiser, S. Kinne, Z. Klimont, S. Kloster, J.-F. Lamarque, C. Liousse, T. Masui, F. Meleux, A. Mieville, T. Ohara, J.-C. Raut, K. Riahi, M. G. Schultz, S. J. Smith, A. Thompson, J. van Aardenne, G. R. van der Werf, and D. P. van Vuuren (2011), Evolution of anthropogenic and biomass burning emissions of air

pollutants at global and regional scales during the 1980–2010 period, *Clim. Change*, *109*(1-2), 163–190, doi: 10.1007/s10584-011-0154-1.

Gulev, S. K., M. Latif, N. Keenlyside, W. Park, and K. P. Koltermann (2013), North Atlantic Ocean control on surface heat flux on multidecadal timescales., *Nature*, *499*(7459), 464–7, doi: 10.1038/nature12268.

Guo, L., E. J. Highwood, L. C. Shaffrey, and a. G. Turner (2013), The effect of regional changes in anthropogenic aerosols on rainfall of the East Asian Summer Monsoon, *Atmos. Chem. Phys.*, *13*(3), 1521–1534, doi: 10.5194/acp-13-1521-2013.

Guo, L., A. G. Turner, and E. J. Highwood (2015), Impacts of 20th century aerosol emissions on the South Asian monsoon in the CMIP5 models, *Atmos. Chem. Phys.*, *15*, 6367–6378, doi: 10.5194/acp-15-6367-2015.

Guo, L., A. G. Turner, and E. J. Highwood (2016), Local and Remote Impacts of Aerosol Species on Indian Summer Monsoon Rainfall in a GCM, pp. 6937–6955, doi: 10.1175/JCLI-D-15-0728.1.

Hannak, L., P. Knippertz, A. H. Fink, A. Kniffka, and G. Pante (2017), Why do global climate models struggle to represent low-level clouds in the West African summer monsoon?, *J. Clim.*, *30*(5), 1665–1687, doi: 10.1175/JCLI-D-16-0451.1.

Hanrahan, G. (2012), Air pollutants and associated chemical and photochemical processes, *Key Concepts Environ. Chem.*, pp. 215–242, doi: 10.1016/B978-0-12-374993-2.10007-X.

Hansen, J., M. Sato, R. Ruedy, L. Nazarenko, A. Lacis, G. A. Schmidt, G. Russell, I. Aleinov, M. Bauer, S. Bauer, N. Bell, B. Cairns, V. Canuto, M. Chandler, Y. Cheng, A. D. Genio, G. Faluvegi, E. Fleming, A. Friend, T. Hall, C. Jackman, M. Kelley, N. Kiang, D. Koch, J. Lean, J. Lerner, K. Lo, S. Menon, R. Miller, P. Minnis, T. Novakov, V. Oinas, J. Perlwitz, J. Perlwitz, J. Rind, A. Romanou, D. Shindell, P. Stone, S. Sun, N. Tausnev, D. Thresher, B. Wielicki, T. Wong, M. Yao, and S. Zhang (2005), Efficacy of climate forcings, *J. Geophys. Res.*, *110*, doi: 10.1029/2005JD005776.

Hansen, J., R. Ruedy, M. Sato, and K. Lo (2010), Global surface temperature change, *Rev. Geophys.*, *48*(RG4004), 1–29, doi: 10.1029/2010RG000345.

Harnik, N., G. Messori, R. Caballero, and S. B. Feldstein (2016), The Circumglobal North American wave pattern and its relation to cold events in eastern North America, *Geophys. Res. Lett.*, *43*(20), 11,015–11,023, doi: 10.1002/2016GL070760.

Harris, I., P. D. Jones, T. J. Osborn, and D. H. Lister (2014), Updated high-resolution grids of monthly climatic observations - the CRU TS3.10 Dataset, *Int. J. Clim.*, *34*(3), 623–642, doi: 10.1002/joc.3711.

Hegerl, G. C., H. Von Storch, K. Hasselmann, B. D. Santer, U. Cubasch, and P. D. Jones (1996), Detecting greenhouse-gas-induced climate change with an optimal fingerprint method, doi: 10.1175/1520-0442(1996)009<2281:DGGICC>2.0.CO;2.

Hegerl, G. C., K. Hasselmann, U. Cubasch, J. F. B. Mitchell, E. Roeckner, R. Voss, and J. Waszkewitz (1997), Multi-fingerprint direction and attribution analysis of greenhouse gas, greenhouse gas-plus-aerosol and solar forced climate change, *Clim. Dyn.*, *13*, 613–634, doi: 10.1007/s003820050209.

Hegerl, G. C., O. Hoegh-Guldberg, G. Casassa, M. Hoerling, S. Kovats, C. Parmesan, D. Pierce, and P. Stott (2010), Good practice guidance paper on Detection and Attribution related to anthropogenic climate change, *Meet. Rep. Intergov. Panel Clim. Chang. Expert Meet. Detect. Attrib. Anthropog. Clim. Chang.*, pp. 1–9.

Held, I. M., and B. J. Soden (2006), Robust responses of the hydrological cycle to global warming, *J. Clim.*, *19*(21), 5686–5699, doi: 10.1175/JCLI3990.1.

Held, I. M., T. L. Delworth, J. Lu, K. L. Findell, and T. R. Knutson (2005), Simulation of Sahel drought in the 20th and 21st centuries, *Proc. Natl. Acad. Sci. U.S.A.*, *102*(50), 17,891–17,896, doi: 10.1073/pnas.0509057102.

Hewitson, B., A. Janetos, T. Carter, F. Giorgi, R. Jones, W.-T. Kwon, L. Mearns, E. Schipper, and M. van Aalst (2014), Regional context, *Clim. Chang. 2014 Impacts, Adapt. Vulnerability. Part A Glob. Sect. Asp. Contrib. Work. Gr. II to*

Fifth Assess. Rep. Intergov. Panel Clim. Chang., pp. 1133–1197, doi: 10.1017/CBO9781107415386.001.

Hoesly, R. M., S. J. Smith, L. Feng, Z. Klimont, G. Janssens-Maenhout, T. Pitkanen, J. J. Seibert, L. Vu, R. J. Andres, R. M. Bolt, T. C. Bond, L. Dawidowski, N. Kholod, J.-i. Kurokawa, M. Li, L. Liu, Z. Lu, M. C. P. Moura, P. R. O'Rourke, and Q. Zhang (2018), Historical (1750-2014) anthropogenic emissions of reactive gases and aerosols from the Community Emission Data System (CEDS), *Geosci. Model Dev. Discuss.*, pp. 1–41, doi: 10.5194/gmd-2017-43.

Hsu, P., T. Li, and B. Wang (2011), Trends in global monsoon area and precipitation over the past 30 years, *Geophys. Res. Lett.*, *38*(L08701), 1–5, doi: 10.1029/2011GL046893.

Huang, B., V. F. Banzon, E. Freeman, J. Lawrimore, W. Liu, T. C. Peterson, T. M. Smith, P. W. Thorne, S. D. Woodruff, and H. M. Zhang (2015), Extended reconstructed sea surface temperature version 4 (ERSST.v4). Part I: Upgrades and intercomparisons, *J. Clim.*, *28*(3), 911–930, doi: 10.1175/JCLI-D-14-00006.1.

Huang, J., A. Adams, C. Wang, and C. Zhang (2009), Black Carbon and West African Monsoon precipitation: Observations and simulations, *Ann. Geophys.*, *27*, 4171–4181, doi: 10.5194/angeo-27-4171-2009,2009.

Hudson, R. D. (2012), Measurements of the movement of the jet streams at midlatitudes, in the Northern and Southern Hemispheres, 1979 to 2010, *Atmos. Chem. Phys.*, *12*(16), 7797–7808, doi: 10.5194/acp-12-7797-2012.

Huggel, C., I. Wallimann-Helmer, D. Stone, and W. Cramer (2016), Reconciling justice and attribution research to advance climate policy, *Nat. Clim. Chang.*, *6*(10), 901–908, doi: 10.1038/nclimate3104.

Hurrell, J. W. (1995), Decadal trends in the North Atlantic Oscillation: Regional temperatures and precipitation, *Science*, *269*(5224), 676–9, doi: 10.1126/science.269.5224.676.

Hurrell, J. W., M. M. Holland, P. R. Gent, S. Ghan, J. E. Kay, P. J. Kushner, J.-F. Lamarque, W. G. Large, D. Lawrence, K. Lindsay, W. H. Lipscomb, M. C. Long, N. Mahowald, D. R. Marsh, R. B. Neale, P. Rasch, S. Vavrus, M. Vertenstein, D. Bader, W. D. Collins, J. J. Hack, J. Kiehl, and S. Marshall (2013), The Community Earth System Model, *Bull. Am. Meteorol. Soc.*, *94*(9), 1339–1360, doi: 10.1175/BAMS-D-12-00121.1.

Hwang, Y.-T., D. M. W. Frierson, and S. M. Kang (2013), Anthropogenic sulfate aerosol and the southward shift of tropical precipitation in the late 20th century, *Geophys. Res. Lett.*, *40*(11), 2845–2850, doi: 10.1002/grl.50502.

Iles, C., and G. Hegerl (2017), Role of the North Atlantic Oscillation in decadal temperature trends Role of the North Atlantic Oscillation in decadal temperature trends, *Environ. Res. Lett.*, *12*, 114,010.

Iles, C. E., and G. C. Hegerl (2015), Systematic change in global patterns of streamflow following volcanic eruptions, *Nat. Geosci.*, *8*(November), 838–844, doi: 10.1038/NGEO2545.

Iles, C. E., G. C. Hegerl, A. P. Schurer, and X. Zhang (2013), The effect of volcanic eruptions on global precipitation, *J. Geophys. Res. Atmos.*, *118*, 8770–8786, doi: 10.1002/jgrd.50678.

IPCC (2007), *Climate Change 2007: The Physical Science Basis. Contribution of Working Group I to the Fourth Assessment Report of the Intergovernmental Panel of Climate Change*, 996 pp., Cambridge University Press, Cambridge, United Kingdom and New York, NY, USA.

IPCC (2012), Managing the risks of extreme events and disasters to advance climate change adaptation, in *A Spec. Rep. Work. Goups I II Intergov. Panel Clim. Chang.*, edited by C. B. Field, V. Barros, T. F. Stocker, D. Qin, D. J. Dokken, K. L. Ebi, M. D. Mastrandrea, K. J. Mach, G.-K. Plattner, S. K. Allen, M. Tignor, and P. M. Midgley, p. 582, Cambridge University Press, Cambridge, United Kingdom and New York, NY, USA.

IPCC (2013), Summary for Policymakers, in *Clim. Chang. 2013 Phys. Sci. Basis. Contrib. Work. Gr. I to Fifth Assess. Rep. Intergov. Panel Clim. Chang.*, edited by T. F. Stocker, D. Qin, G.-K. Plattner, M. Tignor, S. K. Allen, J. Boschung, A. Nauels, Y. Xia, V. Bex, and P. M. Midgley, Cambridge University Press, Cambridge, United Kingdom and New York, NY, USA.

Iversen, T., M. Bentsen, I. Bethke, J. B. Debernard, A. Kirkevåg, Ø. Seland, H. Drange, J. E. Kristjansson, I. Medhaug, M. Sand, and I. A. Seierstad (2013), The Norwegian Earth System Model, NorESM1-M - Part 2: Climate response and scenario projections, *Geosci. Model Dev.*, *6*, 389–415, doi: $10.5194/\mathrm{gmd}\text{-}6\text{-}389\text{-}2013$.

Jeffrey, S., L. Rotstayn, M. Collier, S. Dravitzki, C. Hamalainen, C. Moeseneder, K. Wong, and J. Syktus (2013), Australia's CMIP5 submission using the CSIRO-Mk3.6 model, *Aust. Meteorol. Oceanogr. J.*, *63*, 1–13.

Ji, Z., G. Wang, J. S. Pal, and M. Yu (2016), Potential climate effect of mineral aerosols over West Africa. Part I: Model validation and contemporary climate evaluation, *Clim. Dyn.*, *46*(3), 1223–1239, doi: $10.1007/\mathrm{s}00382\text{-}015\text{-}2641\text{-}\mathrm{y}$.

Kasoar, M., A. Voulgarakis, J.-F. Lamarque, D. T. Shindell, N. Bellouin, W. J. Collins, G. Faluvegi, and K. Tsigaridis (2016), Regional and global temperature response to anthropogenic SO2 emissions from China in three climate models, *Atmos. Chem. Phys.*, *16*(2009), 9785–9804, doi: $10.5194/\mathrm{acp}\text{-}16\text{-}9785\text{-}2016$.

Kavvada, A., A. Ruiz-Barradas, and S. Nigam (2013), AMO's structure and climate footprint in observations and IPCC AR5 climate simulations, *Clim. Dyn.*, *41*(5-6), 1345–1364, doi: $10.1007/\mathrm{s}00382\text{-}013\text{-}1712\text{-}1$.

Kennedy, J. J., N. A. Rayner, R. O. Smith, D. E. Parker, and M. Saunby (2011a), Reassessing biases and other uncertainties in sea surface temperature observations measured in situ since 1850: 1. Measurement and sampling uncertainties, *J. Geophys. Res.*, *116*(D14103), 1–13, doi: $10.1029/2010\mathrm{JD}015218$.

Kennedy, J. J., N. A. Rayner, R. O. Smith, D. E. Parker, and M. Saunby (2011b), Reassessing biases and other uncertainties in sea surface temperature observations

measured in situ since 1850: 2. Biases and homogenization, *J. Geophys. Res.*, *116*(D14104), 1–22, doi: 10.1029/2010JD015220.

Kim, J., J. Shin, Y.-H. Lim, Y. Honda, M. Hashizume, Y. L. Guo, H. Kan, S. Yi, and H. Kim (2016), Comprehensive approach to understand the association between diurnal temperature range and mortality in East Asia, *Sci. Total Environ.*, *539*, 313–21, doi: 10.1016/j.scitotenv.2015.08.134.

Klocke, D., M. Brueck, C. Hohenegger, and B. Stevens (2017), Rediscovery of the doldrums in storm-resolving simulations over the tropical Atlantic, *Nat. Geosci.*, *10*(12), 891–896, doi: 10.1038/s41561-017-0005-4.

Knight, J. R. (2009), The Atlantic multidecadal oscillation inferred from the forced climate response in coupled general circulation models, *J. Clim.*, *22*(7), 1610–1625, doi: 10.1175/2008JCLI2628.1.

Knight, J. R., R. J. Allan, C. K. Folland, M. Vellinga, and M. E. Mann (2005), A signature of persistent natural thermohaline circulation cycles in observed climate, *Geophys. Res. Lett.*, *32*(20), 1–4, doi: 10.1029/2005GL024233.

Knight, J. R., C. K. Folland, and A. A. Scaife (2006), Climate impacts of the Atlantic multidecadal oscillation, *Geophys. Res. Lett.*, *33*(17), 2–5, doi: 10.1029/2006GL026242.

Knudsen, M. F., B. H. Jacobsen, M.-S. Seidenkrantz, and J. Olsen (2014), Evidence for external forcing of the Atlantic Multidecadal Oscillation since termination of the Little Ice Age., *Nat. Commun.*, *5*, 3323, doi: 10.1038/ncomms4323.

Koffi, B., F. Dentener, G. Janssens-Maenhout, D. Guizzardi, M. Crippa, T. Diehl, S. Galmarini, and E. Solazzo (2016), Hemispheric Transport Air Pollution (HTAP): Specification of the HTAP2 experiments Ensuring harmonized modelling, *Tech. rep.*, Joint Research Centre (JRC), Luxembourg, doi: 10.2788/725244.

Kucharski, F., N. Zeng, and E. Kalnay (2013), A further assessment of vegetation feedback on decadal Sahel rainfall variability, *Clim. Dyn.*, *40*, 1453–1466, doi: 10.1007/s00382-012-1397-x.

Kumar, S., J. L. Kinter, Z. Pan, and J. Sheffield (2016), Twentieth century temperature trends in CMIP3, CMIP5, and CESM-LE climate simulations: Spatial-temporal uncertainties, differences, and their potential sources, *J. Geophys. Res. Atmos.*, *121*(16), 9561–9575, doi: 10.1002/2015JD024382.

Lamarque, J.-F., T. C. Bond, V. Eyring, C. Granier, A. Heil, Z. Klimont, D. Lee, C. Liousse, A. Mieville, B. Owen, M. G. Schultz, D. Shindell, S. J. Smith, E. Stehfest, J. Van Aardenne, O. R. Cooper, M. Kainuma, N. Mahowald, J. R. McConnell, V. Naik, K. Riahi, and D. P. van Vuuren (2010), Historical (1850-2000) gridded anthropogenic and biomass burning emissions of reactive gases and aerosols: methodology and application, *Atmos. Chem. Phys.*, *10*(15), 7017–7039, doi: 10.5194/acp-10-7017-2010.

Latham, J. (1990), Control of global warming?, *Nature*, *347*(6291), 339–340.

Lewinschal, A., A. M. L. Ekman, and H. Körnich (2013), The role of precipitation in aerosol-induced changes in northern hemisphere wintertime stationary waves, *Clim. Dyn.*, *41*, 647–661, doi: 10.1007/s00382-012-1622-7.

Lewis, S. C., and D. J. Karoly (2013), Evaluation of historical diurnal temperature range trends in CMIP5 models, *J. Clim.*, *26*(22), 9077–9089, doi: 10.1175/JCLI-D-13-00032.1.

Li, Z., W. K.-M. Lau, V. Ramanathan, G. Wu, Y. Ding, M. G. Manoj, J. Liu, Y. Qian, J. Li, T. Zhou, J. Fan, D. Rosenfeld, Y. Ming, Y. Wang, J. Huang, B. Wang, X. Xu, S.-S. Lee, M. Cribb, F. Zhang, X. Yang, C. Zhao, T. Takemura, K. Wang, X. Xia, Y. Yin, H. Zhang, J. Guo, P. M. Zhai, N. Sugimoto, S. S. Babu, and G. P. Brasseur (2016), Aerosol and monsoon climate interactions over Asia, *Rev. Geophys.*, *54*, 866–929, doi: 10.1002/2015RG000500.

Linderholm, H. W., T. Ou, J.-H. Jeong, C. K. Folland, D. Gong, H. Liu, Y. Liu, and D. Chen (2011), Interannual teleconnections between the summer North Atlantic Oscillation and the East Asian summer monsoon, *J. Geophys. Res.*, *116*(D13), 1–13, doi: 10.1029/2010JD015235.

Lindvall, J., and G. Svensson (2014), The diurnal temperature range in the CMIP5 models, *Clim. Dyn.*, *44*, 405–421, doi: 10.1007/s00382-014-2144-2.

Liu, L., Z. Li, X. Yang, H. Gong, C. Li, and A. Xiong (2016), The long-term trend in the diurnal temperature range over Asia and its natural and anthropogenic causes, *J. Geophys. Res. Atmos.*, *121*, 3519–3533, doi: 10.1002/2015JD024549.

Lo, Y. T., A. J. Charlton-Perez, F. C. Lott, and E. J. Highwood (2016), Detecting sulphate aerosol geoengineering with different methods, *Sci. Rep.*, *6*(December), 1–10, doi: 10.1038/srep39169.

Lobell, D. B., C. Bonfils, and P. B. Duffy (2007), Climate change uncertainty for daily minimum and maximum temperatures: A model inter-comparison, *Geophys. Res. Lett.*, *34*(5), 1–5, doi: 10.1029/2006GL028726.

Makowski, K., M. Wild, and A. Ohmura (2008), Diurnal temperature range over Europe between 1950 and 2005, *Atmos. Chem. Phys. Discuss.*, *8*(2), 7051–7084, doi: 10.5194/acpd-8-7051-2008.

Makowski, K., E. B. Jaeger, M. Chiacchio, M. Wild, T. Ewen, and A. Ohmura (2009), On the relationship between diurnal temperature range and surface solar radiation in Europe, *J. Geophys. Res. Atmos.*, *114*(7), 1–16, doi: 10.1029/2008JD011104.

Marini, C., and C. Frankignoul (2013), An attempt to deconstruct the Atlantic Multidecadal Oscillation, *Clim. Dyn.*, *43*(3-4), 607–625, doi: 10.1007/s00382-013-1852-3.

Marshall, J., A. Donohoe, D. Ferreira, and D. McGee (2014), The ocean's role in setting the mean position of the Inter-Tropical Convergence Zone, *Clim. Dyn.*, *42*(7-8), 1967–1979, doi: 10.1007/s00382-013-1767-z.

Martin, E. R., C. Thorncroft, and B. B. B. Booth (2014), The multidecadal Atlantic SST-Sahel rainfall teleconnection in CMIP5 simulations, *J. Clim.*, *27*(2), 784–806, doi: 10.1175/JCLI-D-13-00242.1.

McNeill, V. F. (2017), Atmospheric aerosols: Clouds, chemistry, and climate, *Annu. Rev. Chem. Biomol. Eng.*, *8*, 427–44, doi: 10.1146/annurev-chembioeng-060816-101538.

Medhaug, I., and T. Furevik (2011), North Atlantic 20th century multidecadal variability in coupled climate models: Sea surface temperature and ocean overturning circulation, *Ocean Sci.*, *7*(3), 389–404, doi: 10.5194/os-7-389-2011.

Meehl, G. A., W. M. Washington, J. M. Arblaster, A. Hu, H. Teng, J. E. Kay, A. Gettelman, D. M. Lawrence, B. M. Sanderson, and W. G. Strand (2013), Climate change projections in CESM1(CAM5) compared to CCSM4, *J. Clim.*, *26*, 6287–6308, doi: 10.1175/JCLI-D-12-00572.1.

Menary, M. B., C. D. Roberts, M. D. Palmer, P. R. Halloran, L. Jackson, R. a. Wood, W. a. Müller, D. Matei, and S.-K. Lee (2013), Mechanisms of aerosol-forced AMOC variability in a state of the art climate model, *J. Geophys. Res. Ocean.*, *118*(4), 2087–2096, doi: 10.1002/jgrc.20178.

Mendelsohn, R., K. Emanuel, S. Chonabayashi, and L. Bakkensen (2012), The impact of climate change on global tropical cyclone damage, *Nat. Clim. Chang.*, *2*(3), 205–209, doi: 10.1038/nclimate1357.

Mignot, J., and C. Frankignoul (2005), The variability of the Atlantic Meridional Overturning Circulation, the North Atlantic Oscillation, and the El Niño-Southern Oscillation in the Bergen Climate Model, *J. Clim.*, *18*, 2361–2375, doi: 10.1175/JCLI3405.1.

Ming, Y., V. Ramaswamy, and G. Chen (2011), A model investigation of aerosol-induced changes in boreal winter extratropical circulation, *J. Clim.*, *24*(23), 6077–6091, doi: 10.1175/2011JCLI4111.1.

Moore, G. W. K. (2013), Tibetan ice core evidence for an intensification of the East Asian jet stream since the 1870s, *Atmos. Sci. Lett.*, *14*(4), 235–242, doi: 10.1002/asl2.445.

Morice, C. P., J. J. Kennedy, N. A. Rayner, and P. D. Jones (2012), Quantifying uncertainties in global and regional temperature change using an ensemble of observational estimates: The HadCRUT4 data set, *J. Geophys. Res.*, *117*(D8), D08,101, doi: 10.1029/2011JD017187.

Munoz, E., B. Kirtman, and W. Weijer (2011), Varied representation of the Atlantic Meridional Overturning across multidecadal ocean reanalyses, *Deep Sea Res. Part II Top. Stud. Ocean.*, *58*(17-18), 1848–1857, doi: 10.1016/j.dsr2.2010.10.064.

Murphy, L. N., K. Bellomo, M. Cane, and A. Clement (2017), The role of historical forcings in simulating the observed Atlantic multidecadal oscillation, *Geophys. Res. Lett.*, *44*, 2472–2480, doi: 10.1002/2016GL071337.

Myhre, G., D. Shindell, F.-M. Bréon, W. Collins, J. Fuglestvedt, J. Huang, D. Koch, J.-F. Lamarque, D. Lee, B. Mendoza, T. Nakajima, A. Robock, G. Stephens, T. Takemura, and H. Zhang (2013), Anthropogenic and natural radiative forcing, in *Clim. Chang. 2013 Phys. Sci. Basis. Contrib. Work. Gr. I to Fifth Assess. Rep. Intergov. Panel Clim. Chang.*, edited by T. Stocker, D. Qin, G.-K. Plattner, M. Tignor, S. Allen, J. Boschung, A. Nauels, Y. Xia, V. Bex, and P. Midgley, Cambridge University Press, Cambridge, United Kingdom and New York, NY, USA.

NASA/Goddard Space Flight Center (2007), GEOS-5 Nature Run Collection.

Neale, R. B., C.-C. Chen, P. H. Lauritzen, D. L. Williamson, A. J. Conley, A. K. Smith, M. Mills, H. Morrison, P. Cameron-Smith, W. D. Collins, M. J. Iacono, R. C. Easter, S. J. Ghan, X. Liu, P. Rasch, and M. A. Taylor (2012), Description of the NCAR Community Atmosphere Model (CAM 5.0), *Tech. rep.*, NCAR Technical Note, NCAR/TN-486+STR.

Nicholson, S. E. (2013), The West African Sahel: A review of recent studies on the rainfall regime and its interannual variability, *ISRN Meteorol.*, *2013*, doi: 10.1155/2013/453521.

Nigam, S., B. Guan, and A. Ruiz-Barradas (2011), Key role of the Atlantic Multidecadal Oscillation in 20th century drought and wet periods over the Great Plains, *Geophys. Res. Lett.*, *38*(16), 1–6, doi: 10.1029/2011GL048650.

Otterå, O. H., M. Bentsen, H. Drange, and L. Suo (2010), External forcing as a metronome for Atlantic multidecadal variability, *Nat. Geosci.*, *3*(10), 688–694, doi: 10.1038/ngeo955.

Pausata, F. S. R., M. Gaetani, G. Messori, S. Kloster, and F. J. Dentener (2014), The role of aerosol in altering North Atlantic atmospheric circulation in winter and air-quality feedbacks, *Atmos. Chem. Phys. Discuss.*, *14*(16), 22,477–22,506, doi: 10.5194/acpd-14-22477-2014.

Pena-Ortiz, C., D. Gallego, P. Ribera, P. Ordonez, and M. Del Carmen Alvarez-Castro (2013), Observed trends in the global jet stream characteristics during the second half of the 20th century, *J. Geophys. Res. Atmos.*, *118*(7), 2702–2713, doi: 10.1002/jgrd.50305.

Penner, J. E., D. Hegg, and R. Leaitch (2001), Unraveling the role of aerosols in climate change, *Environ. Sci. Technol.*, *35*(15), 332A–340A, doi: 10.1021/es0124414.

Persad, G. G., and K. Caldeira (2018), Divergent global-scale temperature effects from identical aerosols emitted in different regions, *Nat. Commun.*, *9*(1), 3289, doi: 10.1038/s41467-018-05838-6.

Philander, S. G. H., D. Gu, D. Halpern, G. Lambert, N.-C. Lau, T. Li, and R. C. Pacanowski (1996), Why the ITCZ is mostly North of the Equator, *J. Clim.*, *9*(12), 2958–2972, doi: 10.1175/1520-0442(1996)009<2958:WTIIMN>2.0.CO;2.

Polson, D., G. C. Hegerl, X. Zhang, and T. J. Osborn (2013), Causes of robust seasonal land precipitation changes, *J. Clim.*, *26*(17), 6679–6697, doi: 10.1175/JCLI-D-12-00474.1.

Polson, D., M. Bollasina, G. C. Hegerl, and L. J. Wilcox (2014), Decreased monsoon precipitation in the Northern Hemisphere due to anthropogenic aerosols, *Geophys. Res. Lett.*, *41*(16), 6023–6029, doi: 10.1002/2014GL060811.

Prather, K. A., C. D. Hatch, and V. H. Grassian (2008), Analysis of atmospheric eerosols, *Annu. Rev. Anal. Chem.*, *1*(1), 485–514, doi: 10.1146/annurev.anchem.1.031207.113030.

Rahmstorf, S., J. E. Box, G. Feulner, M. E. Mann, A. Robinson, S. Rutherford, and E. J. Schaffernicht (2015), Exceptional twentieth-century slowdown in Atlantic Ocean overturning circulation, *Nat. Clim. Chang.*, *5*(5), 475–480, doi: 10.1038/nclimate2554.

Ramanathan, V., P. J. Crutzen, J. T. Kiehl, and D. Rosenfeld (2001), Aerosols, climate, and the hydrological cycle, *Science*, *294*(5549), 2119–2124.

Roberts, A. J., M. J. Woodage, J. H. Marsham, E. J. Highwood, C. L. Ryder, W. McGinty, S. Wilson, and J. Crook (2018), Can explicit convection improve modelled dust in summertime West Africa?, *Atmos. Chem. Phys.*, *18*(12), 9025–9048, doi: 10.5194/acp-18-9025-2018.

Robock, A., and J. Mao (1995), The volcanic signal in surface temperature observations, *J. Clim.*, *8*(5), 1086–1103, doi: 10.1175/1520-0442(1995)008<1086:TVSIST>2.0.CO;2.

Rohde, R., R. A. Muller, R. Jacobsen, E. Muller, S. Perlmutter, A. Rosenfeld, J. Wurtele, D. Groom, and C. Wickham (2013a), A new estimate of the average Earth surface land temperature spanning 1753 to 2011, *Geoinfor Geostat*, *1*(1), 1–7, doi: 10.4172/2327-4581.1000101.

Rohde, R., R. Muller, R. Jacobsen, S. Perlmutter, A. Rosenfeld, J. Wurtele, J. Curry, C. Wickham, and S. Mosher (2013b), Berkeley Earth Temperature averaging process, *Geoinfor Geostat An Overv.*, *1:2*, doi: 10.4172/2327-4581.1000103.

Rotstayn, L. D. (2013), Projected effects of declining anthropogenic aerosols on the southern annular mode, *Environ. Res. Lett.*, *8*(4), doi: 10.1088/1748-9326/8/4/044028.

Rotstayn, L. D., and U. Lohmann (2002), Tropical rainfall trends and the indirect aerosol effect, *J. Clim.*, *15*(15), 2103–2116, doi: 10.1175/1520-0442(2002)015<2103:TRTATI>2.0.CO;2.

Rotstayn, L. D., S. J. Jeffrey, M. a. Collier, S. M. Dravitzki, a. C. Hirst, J. I. Syktus, and K. K. Wong (2012), Aerosol- and greenhouse gas-induced changes in summer rainfall and circulation in the Australasian region: A study using single-forcing climate simulations, *Atmos. Chem. Phys.*, *12*(14), 6377–6404, doi: 10.5194/acp-12-6377-2012.

Rotstayn, L. D., M. A. Collier, and J.-J. Luo (2015), Effects of declining aerosols on projections of zonally averaged tropical precipitation, *Environ. Res. Lett.*, *10*(4), 44,018, doi: 10.1088/1748-9326/10/4/044018.

Saeed, S., N. Van Lipzig, W. A. Müller, F. Saeed, and D. Zanchettin (2014), Influence of the circumglobal wave-train on European summer precipitation, *Clim. Dyn.*, *43*(1-2), 503–515, doi: 10.1007/s00382-013-1871-0.

Salby, M. L. (2012), *Physics of the Atmosphere and Climate*, Cambridge University Press, New York, NY, USA.

Salter, S., G. Sortino, and J. Latham (2008), Sea-going hardware for the cloud albedo method of reversing global warming, *Philos. Trans. R. Soc.*, *366*(August), 3989–4006, doi: 10.1098/rsta.2008.0136.

Salzmann, M., and R. Cherian (2015), On the enhancement of the Indian summer monsoon drying by Pacific multidecadal variability during the latter half of the twentieth century, *J. Geophys. Res. Atmos.*, *120*(18), 9103–9118, doi: 10.1002/2015JD023313.Abstract.

Salzmann, M., H. Weser, and R. Cherian (2014), Robust response of Asian summer monsoon to anthropogenic aerosols in CMIP5 models, *J. Geophys. Res. Atmos.*, *119*, 1–17, doi: 10.1002/2014JD021783.1.

Schmidt, G. A., M. Kelley, L. Nazarenko, R. Ruedy, G. L. Russell, I. Aleinov, M. Bauer, S. E. Bauer, M. K. Bhat, R. Bleck, V. Canuto, Y.-H. Chen, Y. Cheng, T. L. Clune, A. D. Genio, R. D. Fainchtein, G. Faluvegi, J. E. Hansen, R. J. Healy, N. Y. Kiang, D. Koch, A. A. Lacis, A. N. Legrande, J. Lerner, K. K. Lo, E. E. Matthews, S. Menon, R. L. Miller, V. Oinas, A. O. Oloso, J. P. Perlwitz, M. J. Puma, W. M. Putman, D. Rind, A. Romanou, M. Sato, D. T. Shindell, S. Sun, R. A. Syed, N. Tausnev, K. Tsigaridis, N. Unger, A. Voulgarakis, M.-S. Yao, and J. Zhang (2014), Configuration and assessment of the GISS ModelE2 contributions to the CMIP5 archive, *J. Adv. Model. Earth Syst.*, *6*, 141–184, doi: 10.1002/2013MS000265.Received.

Schneider, T., T. Bischoff, and G. H. Haug (2014a), Migrations and dynamics of the intertropical convergence zone, *Nature*, *513*(7516), 45–53, doi: 10.1038/nature13636.

Schneider, U., A. Becker, P. Finger, A. Meyer-Christoffer, M. Ziese, and B. Rudolf (2014b), GPCC's new land surface precipitation climatology based on quality-controlled in situ data and its role in quantifying the global water cycle, *Theor. Appl. Clim.*, *115*, 15–40, doi: 10.1007/s00704-013-0860-x.

Schnur, R., and K. I. Hasselmann (2005), Optimal filtering for Bayesian detection and attribution of climate change, *Clim. Dyn.*, *24*(1), 45–55, doi: 10.1007/s00382-004-0456-3.

Shindell, D., and G. Faluvegi (2009), Climate response to regional radiative forcing during the twentieth century, *Nat. Geosci.*, *2*(4), 294–300, doi: 10.1038/ngeo473.

Shindell, D., M. Schulz, Y. Ming, T. Takemura, G. Faluvegi, and V. Ramaswamy (2010), Spatial scales of climate response to inhomogeneous radiative forcing, *J. Geophys. Res.*, *115*(D19), D19,110, doi: 10.1029/2010JD014108.

Shindell, D., G. Faluvegi, L. Rotstayn, and G. Milly (2015), Spatial patterns of radiative forcing and surface temperature response, *J. Geophys. Res. Atmos.*, *120*, 1–19, doi: 10.1002/2014JD022752.Received.

Shultz, J. M., J. P. Kossin, J. M. Shepherd, J. M. Ransdell, R. Walshe, I. Kelman, and S. Galea (2018), Risks, health consequences, and response challenges for small-island-based populations: Observations from the 2017 Atlantic Hurricane season, *Disaster Med. Public Health Prep.*, *Apr 6*, 1–13, doi: 10.1017/dmp.2018.28.

Smith, D. M., R. Eade, N. J. Dunstone, D. Fereday, J. M. Murphy, H. Pohlmann, and A. A. Scaife (2010), Skilful multi-year predictions of Atlantic hurricane a frequency, *Nat. Geosci.*, *3*(12), 846–849, doi: 10.1038/ngeo1004.

Sperber, K. R., H. Annamalai, I.-S. Kang, A. Kitoh, A. Moise, A. Turner, B. Wang, and T. Zhou (2013), The Asian summer monsoon: An intercomparison of CMIP5 vs. CMIP3 simulations of the late 20th century, *Clim. Dyn.*, *41*, 2711–2744, doi: 10.1007/s00382-012-1607-6.

Srokosz, M., M. Baringer, H. Bryden, S. Cunningham, T. Delworth, S. Lozier, J. Marotzke, and R. Sutton (2012), Past, present, and future changes in the Atlantic Meridional Overturning Circulation, *Bull. Am. Meteorol. Soc.*, *93*(11), 1663–1676, doi: 10.1175/BAMS-D-11-00151.1.

Steinman, B. A., M. E. Mann, and S. K. Miller (2015), Hemisphere temperatures, *Science*, *347*(February), 988–991, doi: 10.5061/dryad.6f576.SUPPLEMENTARY.

Stenchikov, G., T. L. Delworth, V. Ramaswamy, R. J. Stouffer, A. Wittenberg, and F. Zeng (2009), Volcanic signals in oceans, *J. Geophys. Res. Atmos.*, *114*(16), 1–13, doi: 10.1029/2008JD011673.

Stevens, B., and G. Feingold (2009), Untangling aerosol effects on clouds and precipitation in a buffered system, *Nature*, *461*(7264), 607–613, doi: 10.1038/nature08281.

Stjern, C. W., and Jón Egill Kristjánsson (2015), Contrasting influences of recent aerosol changes on clouds and precipitation in Europe and East Asia, *J Clim.*, *28*, 8770–8790, doi: 10.1175/JCLI-D-14-00837.1.

Stjern, C. W., A. Stohl, and J. E. Kristjánsson (2011), Have aerosols affected trends in visibility and precipitation in Europe?, *J. Geophys. Res.*, *116*(D02212), 1–15, doi: 10.1029/2010JD014603.

Storelvmo, T., T. Leirvik, U. Lohmann, P. C. B. Phillips, and M. Wild (2016), Disentangling greenhouse warming and aerosol cooling to reveal Earth's climate sensitivity, *Nat. Geosci.*, *9*(March), 286–291, doi: 10.1038/ngeo2670.

Strong, C., and R. E. Davis (2007), Winter jet stream trends over the Northern Hemisphere, *Q. J. R. Meteorol. Soc.*, *133*, 2109–2115, doi: 10.1002/qj.171.

Sutton, R. T., and D. L. Hodson (2007), Climate response to basin-scale warming and cooling of the North Atlantic Ocean, *J. Clim.*, *20*(5), 891–907, doi: 10.1175/JCLI4038.1.

Swingedouw, D. (2015), Oceanography: Fresh news from the Atlantic, *Nat. Clim. Chang.*, *5*(5), 411–412, doi: 10.1038/nclimate2626.

Sylla, M. B., F. Giorgi, E. Coppola, and L. Mariotti (2013), Uncertainties in daily rainfall over Africa: assessment of gridded observation products and evaluation of a regional climate model simulation, *Int. J. Climatol.*, *33*(7), 1805–1817, doi: 10.1002/joc.3551.

Takahashi, C., and M. Watanabe (2016), Pacific trade winds accelerated by aerosol forcing over the past two decades, *Nat. Clim. Chang.*, *6*, 768–772, doi: 10.1038/NCLIMATE2996.

Tandon, N. F., and P. J. Kushner (2015), Does external forcing interfere with the AMOC's influence on North Atlantic sea surface temperature?, *J. Clim.*, *28*(16), 6309–6323, doi: 10.1175/JCLI-D-14-00664.1.

Tao, L., Y. Hu, and J. Liu (2016), Anthropogenic forcing on the Hadley circulation in CMIP5 simulations, *Clim. Dyn.*, *46*(9-10), 3337–3350, doi: 10.1007/s00382-015-2772-1.

Taylor, K. E., R. J. Stouffer, and G. A. Meehl (2012), An overview of CMIP5 and the experiment design, *Bull. Am. Meteorol. Soc.*, *93*(4), 485–498, doi: 10.1175/BAMS-D-11-00094.1.

The Royal Society (2009), Geoengineering the climate: Science, governance and uncertainty, *Tech. rep.*, London, UK.

Thorne, P. W., M. G. Donat, R. J. H. Dunn, C. N. Williams, L. V. Alexander, J. Caesar, I. Durre, I. Harris, Z. Hausfather, P. D. Jones, M. J. Menne, R. Rohde, R. S. Vose, R. Davy, J. H. Lawrimore, T. C. Peterson, and J. J. Rennie (2016), Reassessing changes in diurnal temperature range: Intercomparison and evaluation of existing global data set estimates, *J. Geophys. Res. Atmos.*, *121*, 5138–5158, doi: 10.1002/2015JD024584.

Ting, M., Y. Kushnir, R. Seager, and C. Li (2009), Forced and internal twentieth-century SST trends in the North Atlantic, *J. Clim.*, *22*(6), 1469–1481, doi: 10.1175/2008JCLI2561.1.

Ting, M., Y. Kushnir, R. Seager, and C. Li (2011), Robust features of Atlantic multi-decadal variability and its climate impacts, *Geophys. Res. Lett.*, *38*(17), doi: 10.1029/2011GL048712.

Ting, M., Y. Kushnir, and C. Li (2014), North Atlantic Multidecadal SST Oscillation: External forcing versus internal variability, *J. Mar. Syst.*, *133*, 27–38, doi: 10.1016/j.jmarsys.2013.07.006.

Tsai, I.-C., W.-C. Wang, H.-H. Hsu, and W.-L. Lee (2016), Aerosol effets on summer monsoon over Asia during 1980s and 1990s, *J. Geophys. Res. Atmos.*, *121*, 11,761–11,776, doi: 10.1002/2016JD025388.Received.

Turner, A. G., and H. Annamalai (2012), Climate change and the South Asian summer monsoon, *Nat. Clim. Chang.*, *2*(August), 587–595, doi: 10.1038/NCLIMATE1495.

Twomey, S. (1977), The influence of pollution on the shortwave albedo of clouds, *J. Atmos. Sci.*, *34*, 1149–1152, doi: 10.1175/1520-0469(1977)034<1149:TIOPOT>2.0.CO;2.

Undorf, S., M. A. Bollasina, and G. C. Hegerl (2018a), Impacts of the 1900-1974 increase in anthropogenic aerosol emissions from North America and Europe on Eurasian summer climate, *J. Clim.*, doi: 10.1175/JCLI-D-17-0850.1.

Undorf, S., D. Polson, M. Bollasina, Y. Ming, A. Schurer, and G. C. Hegerl (2018b), Detectable impact of local and remote anthropogenic aerosols on the 20th century changes of West African and South Asian monsoon precipitation, *J. Geophys. Res. Atmos.*, *123*, 4871–4889, doi: 10.1029/2017JD027711.

UNFCCC. Conference of the Parties (COP) (2015), Adoption of the Paris Agreement, *Tech. Rep. December*, doi: FCCC/CP/2015/L.9/Rev.1.

Villarini, G., G. A. Vecchi, and J. A. Smith (2010), Modeling the dependence of tropical storm counts in the North Atlantic basin on climate indices, *Mon. Weather Rev.*, *138*(7), 2681–2705, doi: 10.1175/2010MWR3315.1.

von Salzen, K., J. F. Scinocca, N. A. McFarlane, J. Li, J. N. S. Cole, D. Plummer, D. Verseghy, M. C. Reader, X. Ma, M. Lazare, and L. Solheim (2013), The Canadian fourth generation Atmospheric global climate Model (CanAM4). Part I: Representation of physical processes, *Atmos.-Ocean*, *51*(1), 104–125, doi: 10.1080/07055900.2012.755610.

von Storch, H., and F. W. Zwiers (1999), *Statistical Analysis in Climate Research*, Cambridge University Press, Cambridge, United Kingdom and New York, NY, USA and Port Melbourne, Australia, doi: 0511010184.

Vuuren, D. P. V., J. Edmonds, M. Kainuma, K. Riahi, N. Nakicenovic, S. J. Smith, and S. K. Rose (2011), The representative concentration pathways: an overview, *Clim. Chang.*, *109*, 5–31, doi: 10.1007/s10584-011-0148-z.

Wang, B., R. Wu, and K.-M. Lau (2001), Interannual variability of the Asian Summer Monsoon: Contrasts between the Indian and the Western North Pacific–East Asian Monsoons, *J. Clim.*, *14*, 4073–4090, doi: 10.1175/1520-0442(2001)014<4073:IVOTAS>2.0.CO;2.

Wang, C., S. Dong, A. T. Evan, G. R. Foltz, and S. K. Lee (2012), Multidecadal covariability of north atlantic sea surface temperature, African dust, Sahel Rainfall, and Atlantic hurricanes, *J. Clim.*, *25*(15), 5404–5415, doi: 10.1175/JCLI-D-11-00413.1.

Wang, H., S. P. Xie, and Q. Liu (2016), Comparison of climate response to anthropogenic aerosol versus greenhouse gas forcing: Distinct patterns, *J. Clim.*, *29*(14), 5175–5188, doi: 10.1175/JCLI-D-16-0106.1.

Wang, J., B. Yang, F. C. Ljungqvist, J. Luterbacher, T. J. Osborn, K. R. Briffa, and E. Zorita (2017), Internal and external forcing of multidecadal Atlantic climate variability over the past 1,200 years, *Nat. Geosci.*, *10*(7), 512–517, doi: 10.1038/ngeo2962.

Westervelt, D. M., A. J. Conley, A. M. Fiore, J. F. Lamarque, D. Shindell, M. Previdi, G. Faluvegi, G. Correa, and L. W. Horowitz (2017), Multimodel precipitation responses to removal of U.S. sulfur dioxide emissions, *J. Geophys. Res.*, *122*(9), 5024–5038, doi: 10.1002/2017JD026756.

Westervelt, D. M., A. J. Conley, A. M. Fiore, J.-F. Lamarque, D. T. Shindell, M. Previdi, N. R. Mascioli, G. Faluvegi, G. Correa, and L. W. Horowitz (2018), Connecting regional aerosol emissions reductions to local and remote precipitation responses, *Atmos. Chem. Phys. Discuss.*, (June), 1–25, doi: 10.5194/acp-2018-516.

Wilcox, L. J., E. J. Highwood, and N. J. Dunstone (2013), The influence of anthropogenic aerosol on multi-decadal variations of historical global climate, *Environ. Res. Lett.*, *8*(2), 24,033, doi: 10.1088/1748-9326/8/2/024033.

Wilcox, L. J., E. J. Highwood, B. B. B. Booth, and K. S. Carslaw (2015), Quantifying sources of inter-model diversity in the cloud albedo effect, *Geophys. Res. Lett.*, *42*, 1568–1575, doi: 10.1002/2015GL063301.

Wild, M., A. Ohmura, and K. Makowski (2007), Impact of global dimming and brightening on global warming, *Geophys. Res. Lett.*, *34*(4), 1–4, doi: 10.1029/2006GL028031.

Xie, S.-P., B. Lu, and B. Xiang (2013), Similar spatial patterns of climate responses to aerosol and greenhouse gas changes, *Nat. Geosci.*, *6*(10), 828–832, doi: 10.1038/ngeo1931.

Yadav, R. K. (2017), On the relationship between east equatorial Atlantic SST and ISM through Eurasian wave, *Clim. Dyn.*, *48*, 281–295, doi: 10.1007/s00382-016-3074-y.

Yuan, T., L. Oreopoulos, M. Zelinka, H. Yu, J. R. Norris, M. Chin, S. Platnick, and K. Meyer (2016), Positive low cloud and dust feedbacks amplify tropical North Atlantic Multidecadal Oscillation, *Geophys. Res. Lett.*, *43*(3), 1349–1356, doi: 10.1002/2016GL067679.

Zelinka, M. D., T. Andrews, P. M. Forster, and K. E. Taylor (2014), Quantifying components of aerosol-cloud-radiation interactions in climate models, *J. Geophys. Res. Atmos.*, *119*(12), 7599–7615, doi: 10.1002/2014JD021710.

Zhang, C., T. L. Delworth, R. Sutton, D. L. R Hodson, K. W. Dixon, I. M. Held, Y. Kushnir, R. Zhang, J. Marshall, Y. Ming, R. Msadek, J. Robson, A. J. Rosati, M. Ting, and G. A. Vecchi (2013), Have aerosols caused the observed Atlantic Multidecadal Variability?, *J. Atmos. Sci.*, *70*(4), 1135–1144, doi: 10.1175/JAS-D-12-0331.1.

Zhang, L., and C. Wang (2013), Multidecadal North Atlantic sea surface temperature and Atlantic meridional overturning circulation variability in CMIP5 historical simulations, *J. Geophys. Res. Ocean.*, *118*(10), 5772–5791, doi: 10.1002/jgrc.20390.

Zhang, R. (2017), On the persistence and coherence of subpolar sea surface temperature and salinity anomalies associated with the Atlantic multidecadal variability, *Geophys. Res. Lett.*, *44*(15), 7865–7875, doi: 10.1002/2017GL074342.

Zhang, R., and T. L. Delworth (2006), Impact of Atlantic multidecadal oscillations on India/Sahel rainfall and Atlantic hurricanes, *Geophys. Res. Lett.*, *33*(17), 1–5, doi: 10.1029/2006GL026267.

Zhang, R., R. Sutton, G. Danabasoglu, T. L. Delworth, W. M. Kim, J. Robson, and S. G. Yeager (2016), Comment on "The Atlantic Multidecadal Oscillation without a role for ocean circulation", *Science*, *352*(6293), 1527, doi: 10.1126/science.aab3980.

Zhang, X., F. W. Zwiers, G. C. Hegerl, F. H. Lambert, N. P. Gillett, S. Solomon, P. A. Stott, and T. Nozawa (2007), Detection of human influence on twentieth-century precipitation trends, *Nature*, *448*(7152), 461–465, doi: 10.1038/nature06025.

Zittis, G. (2018), Observed rainfall trends and precipitation uncertainty in the vicinity of the Mediterranean, Middle East and North Africa, *Theor. Appl. Climatol.*, *134*(3-4), 1207–1230, doi: 10.1007/s00704-017-2333-0.

Appendix A

Supplementary Figures to Chapter 2

Outline. The figures in this chapter support further the analysis in Chapter 2. Figs. A.1-A.4 complement Figs. 2.1 and 2.2a-b by showing the historical spatio-temporal changes in emissions of black carbon (Figs. A.1-A.2) and organic carbon (Figs. A.3-A.4). The joint EOF results (Fig. 2.3) are supported by additional empirical orthogonal function (EOF) analyses of sulphate load and near-surface temperature separately (Fig. A.5). Mid-latitude mean atmospheric temperature trends (Fig. A.6) add information on upper-level changes to the changes in near-surface temperature (Fig. 2.4), while linear trend maps for sea level pressure (Fig. A.7) show the robustness of the trends shown as contour lines in Fig. 2.4. Trends in cloud fraction in the aerosol-only ensemble (Fig. A.8) then support the hypothesis of aerosol-driven cloud changes contributing to the changes diurnal temperature range. How the patterns of change during 1900-1950 compare to those over the longer period of 1900-1974 (Figs. 2.4, 2.6, and 2.7) is finally shown with linear trends in near-surface temperature and sea level pressure (Fig. A.9), precipitation (Fig. A.10), and diurnal temperature range (Fig. A.11).

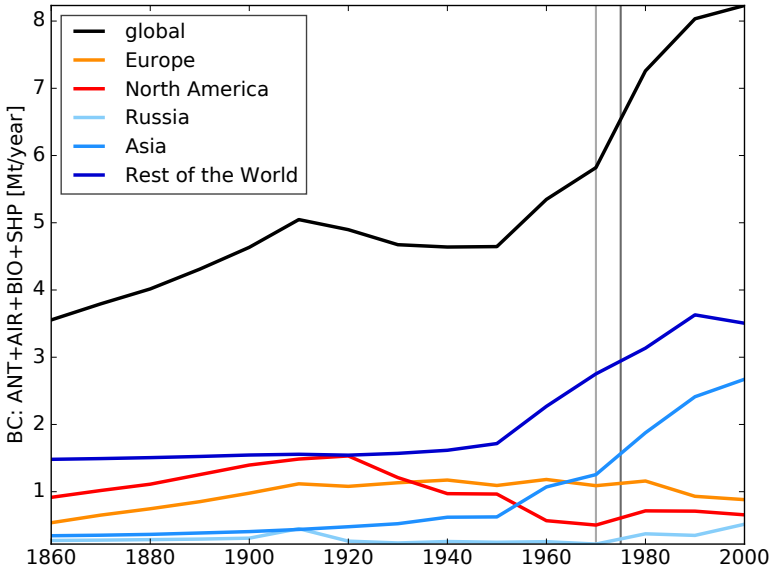

Figure A.1: Same as Fig. 2.1, but for black carbon. Data from *Lamarque et al.* (2010).

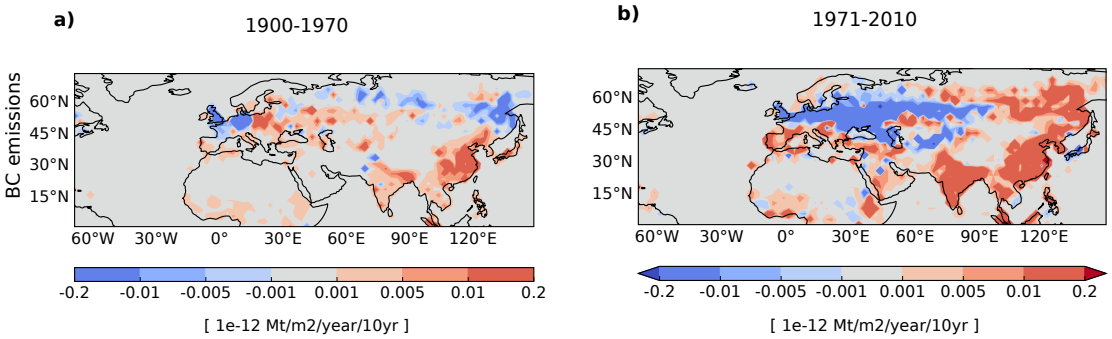

Figure A.2: Same as Fig. 2.2a-b, but for black carbon. Data from *Lamarque et al.* (2010).

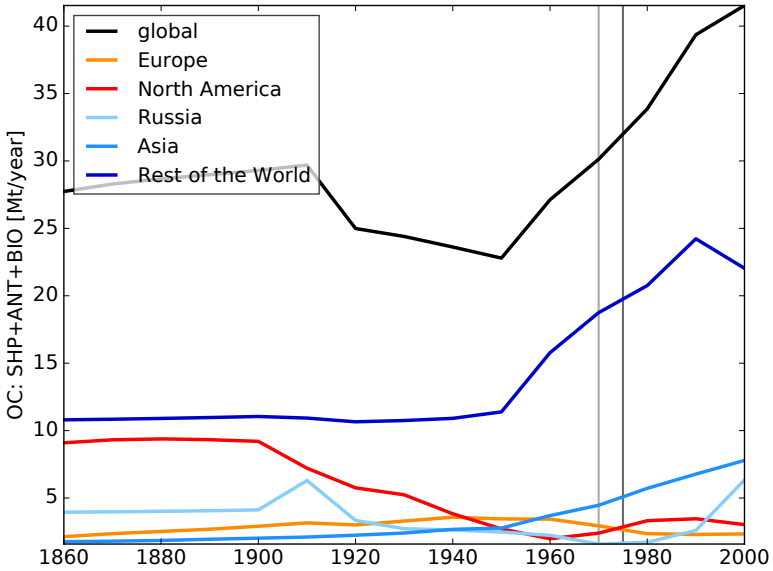

Figure A.3: Same as Fig. 2.1, but for organic carbon. Data from *Lamarque et al.* (2010).

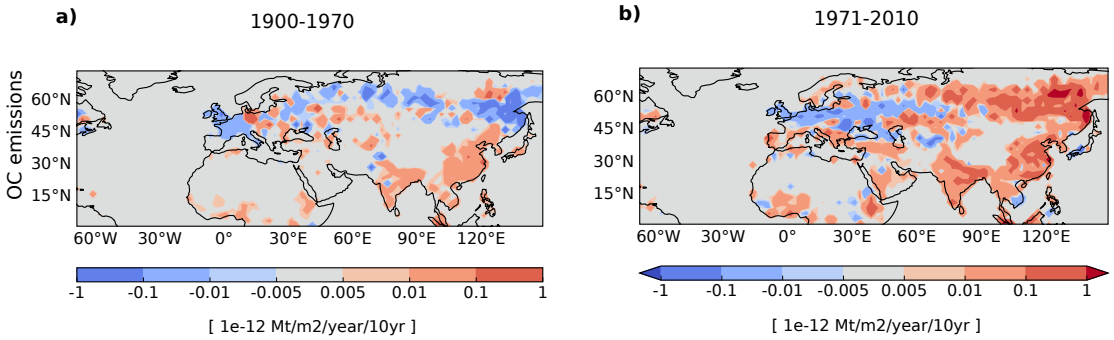

Figure A.4: Same as Fig. 2.2a-b, but for organic carbon. Data from *Lamarque et al.* (2010).

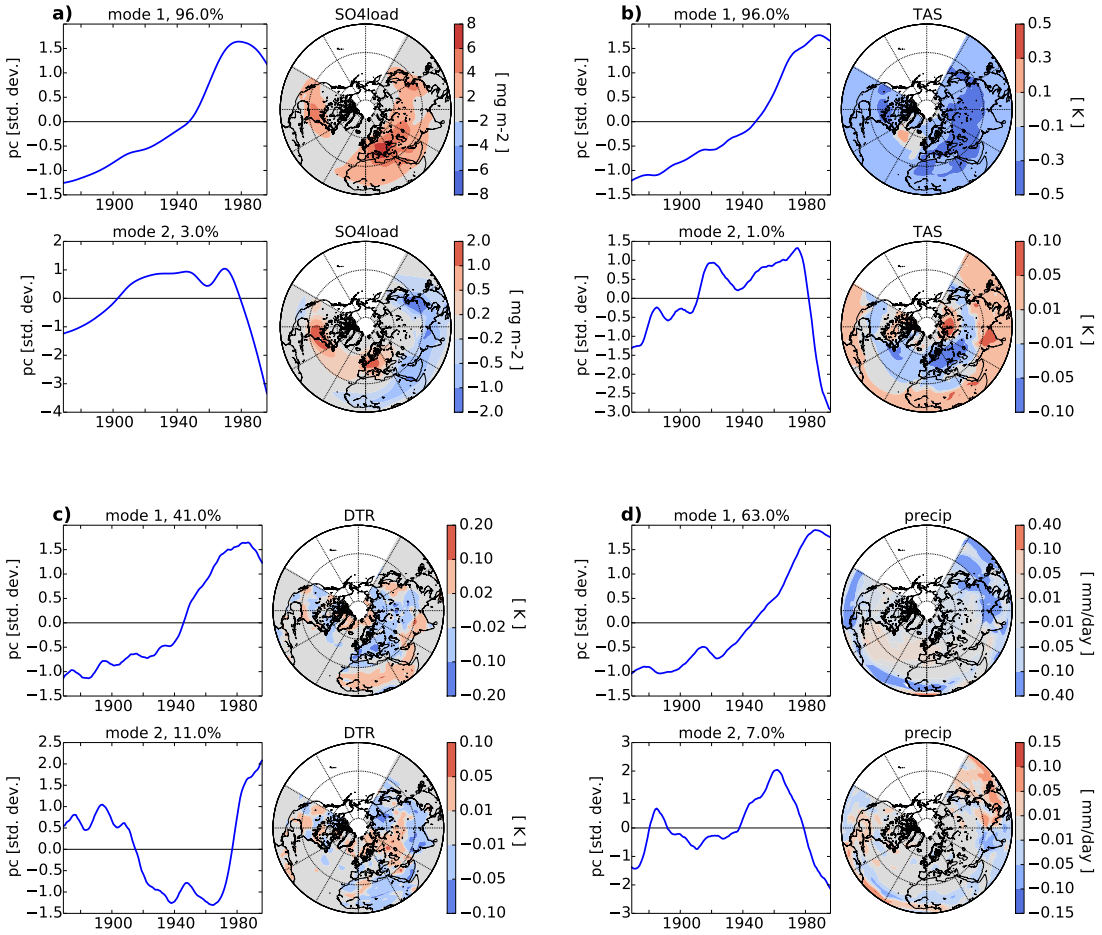

Figure A.5: EOF analysis for JJA (a) sulphate loading (SO4load), (b) near-surface temperature (TAS), (c) diurnal temperature range (DTR), and (d) precipitation from the multi-model mean of the aerosol-only CMIP5 simulations. The (left) principal components and (right) associated patterns of the (top) first and (bottom) second mode are shown. The models used are those in Tab. 1.1 for TAS, and those except HadGEM2-ES (no data available) for SO4load. We take 11- and 7-year running means one after the other prior to the analysis. Here, EOFs for SO4load and TAS are calculated for each variable in isolation, while Fig. 2.3 shows the results from a combined EOF approach.

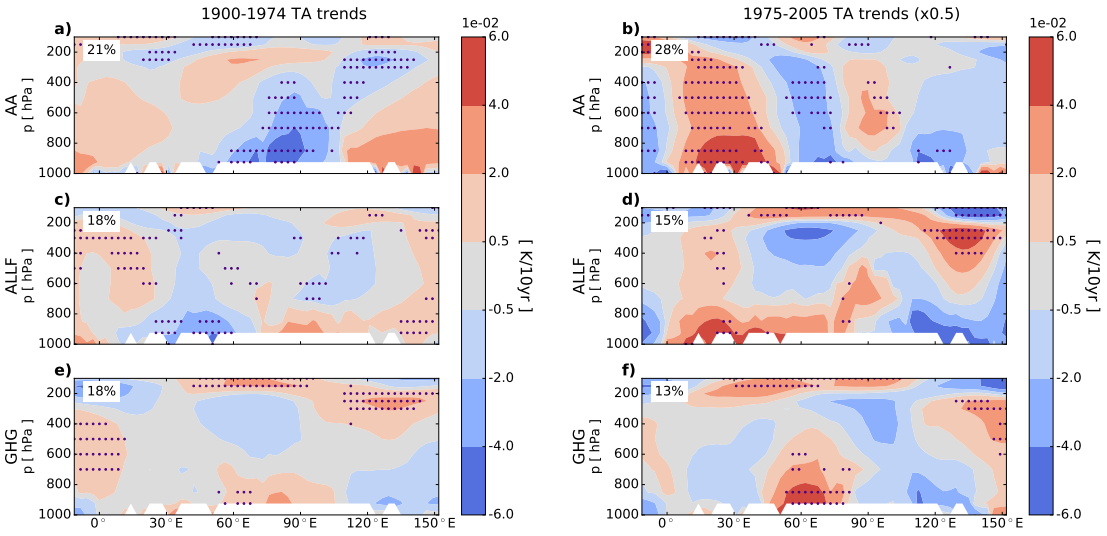

Figure A.6: Linear trends in JJA atmospheric temperature (TA, in K/decade), averaged between 30-60°N during (left) 1900-1974 and (right) 1975-2005 for the multi-model mean of the (top) AA, (middle) ALLF, (bottom) GHG simulations for the models listed in Tab. 1.1. Data are not shown where at least one latitude is masked by orography. Stippling indicates where at least 6 out of the 7 models' ensemble means agree on sign. Anomalies from the area-mean trend per level are shown. Note that trends during the second period are scaled by 1/2 for easier comparison with those during the first period.

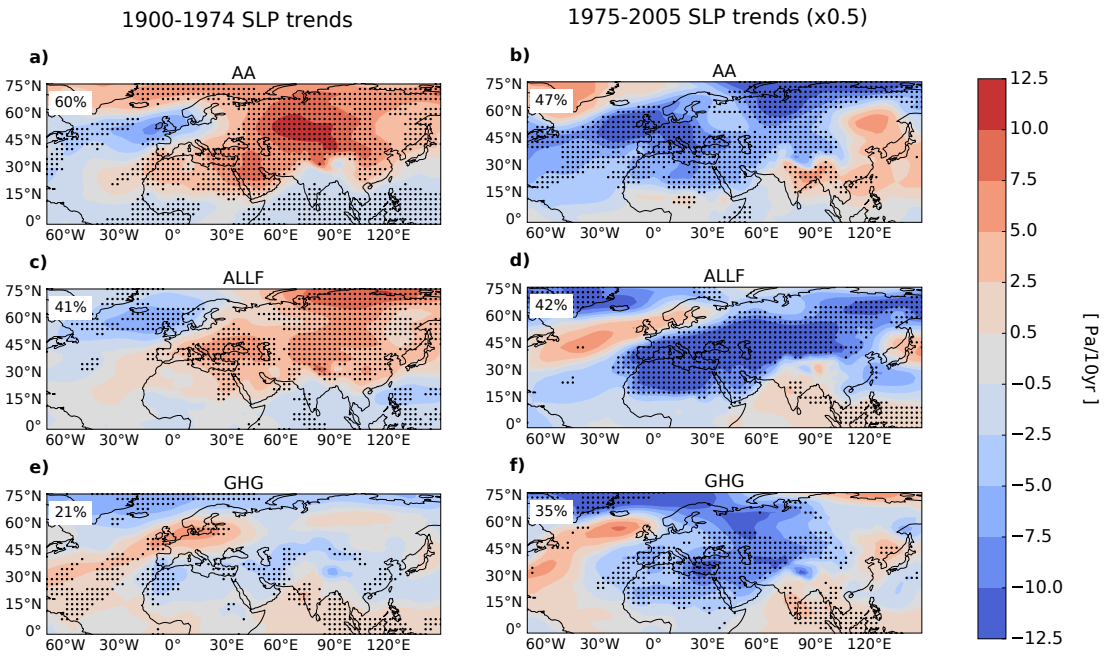

Figure A.7: As Fig. 2.4, but for sea level pressure (SLP, in Pa/decade) in colour instead of as contour lines to show the robustness of the trends. Note that trends during the second period are scaled by 1/2 for easier comparison with those during the first period.

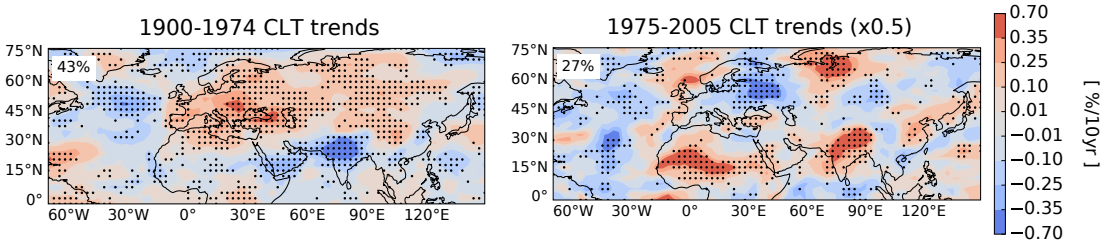

Figure A.8: As Fig. 2.7, but for total cloud fraction (CLT, in %/decade) for the aerosol-only simulations (AA) only. Note that trends during the second period are scaled by 1/2 for easier comparison with those during the first period.

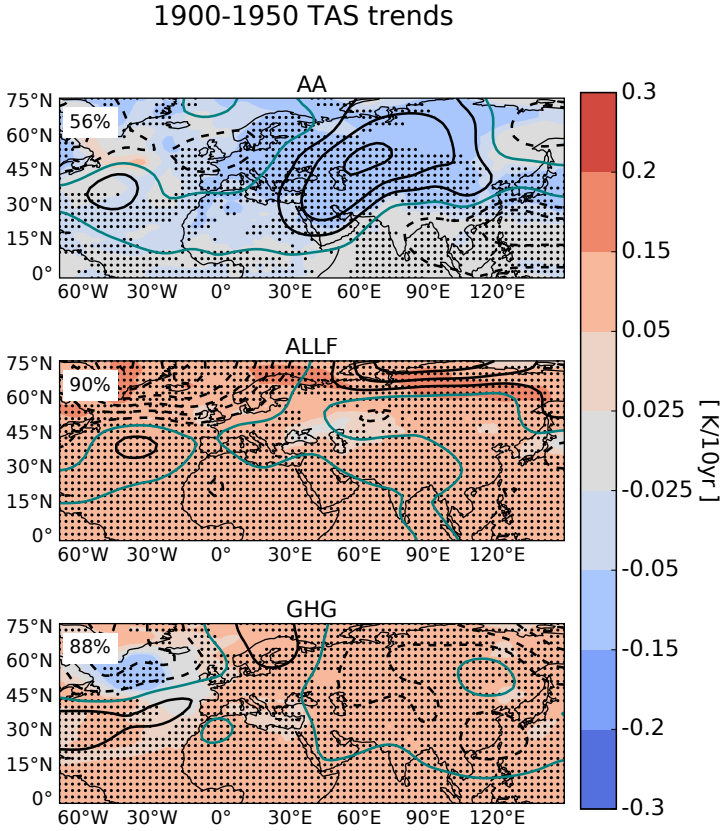

Figure A.9: As Fig. 2.4, but for 1900-1950.

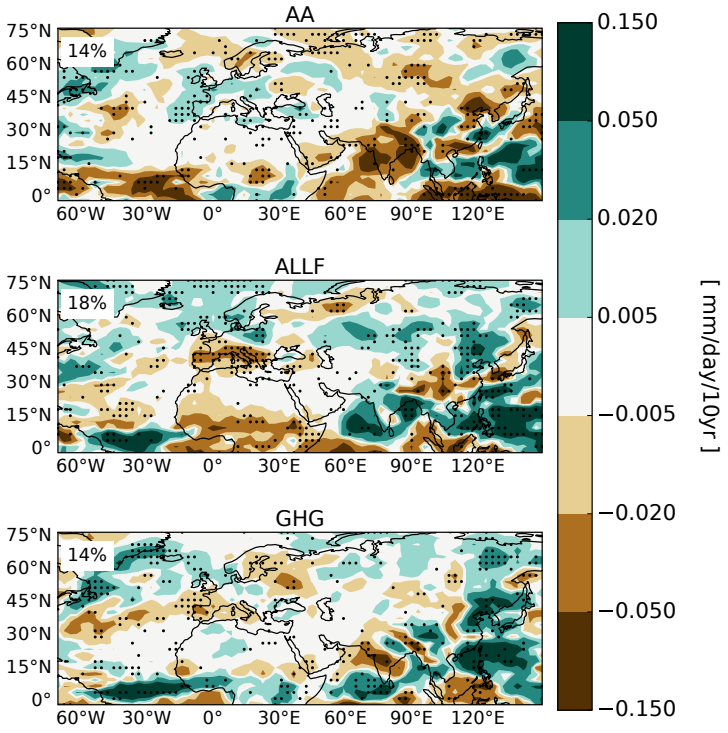

Figure A.10: As Fig. 2.6, but for 1900-1950.

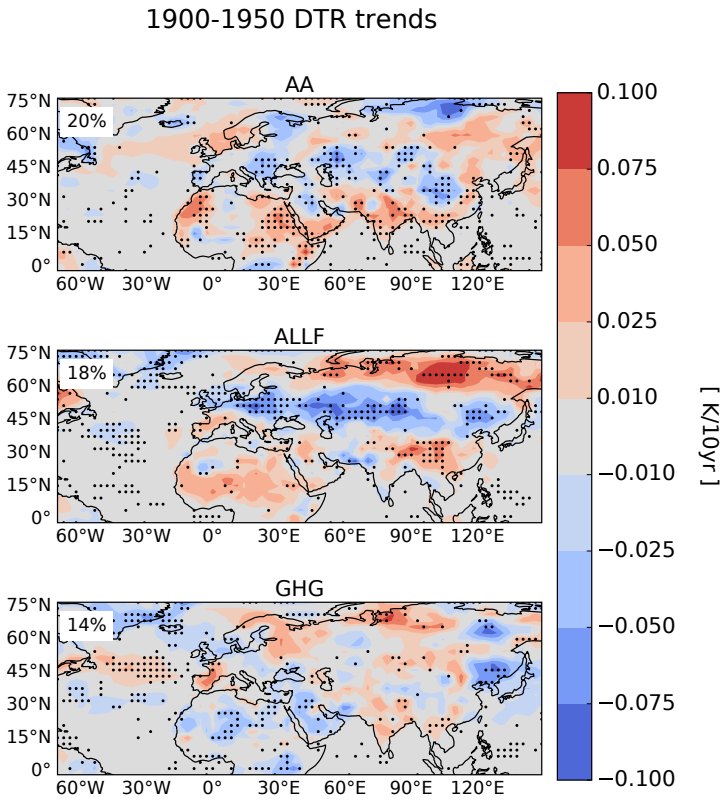

Figure A.11: As Fig. 2.7, but for 1900-1950.

Appendix B

Supplementary Figures to Chapter 3

Outline. The figures in this chapter support further the analysis in Chapter 3. We illustrate the emission source regions used for the regional-aerosol simulations with GFDL-CM3 (Fig. B.1) and the approximate linearity in the response to the regional-aerosol forcing for emissions from South Asian vs. elsewhere (Fig. B.2). The monsoon regions used in our analysis as defined in Section 3.2 are then displayed (Fig. B.3). The historical evolution of aerosol emissions by source region and aerosol species are shown (Fig. B.4), and the resulting radiative forcings (RFs) are shown thereafter – for the regional-aerosol experiments we can only calculate the instantaneous RF, but are reassured in its representativeness by the similarity between the effective RF and the instantaneous RF for the global aerosol simulations (Figs. B.5-B.6). The approximate linearity in the response to the different global forcings is also shown (Fig. B.7). In addition to the precipitation trends during 1920-2005 shown in the main document, we show here the trends for the shorter time periods 1920-1975 (Fig. B.8) and 1975-2005 (Fig. B.9) and the trends during all three periods only in the monsoon regions (Figs. B.10-B.12). This is followed by the response to the regional aerosol changes compared not only to global aerosol emissions but also to other forcing agents (Fig. B.13). The detected time series of monsoon precipitation over the West African (Fig.

B.14) and the South Asian (Fig. B.16) monsoon region are shown, scaled according to the factor which represents best the observations in the one-signal detection and attribution (D&A) analysis. The station data coverage is illustrated exemplarily for one of the observational datasets (Fig. B.15). Additional D&A results are shown in Figs. B.17-B.20, with Fig. B.17 showing the scaling factors for GHG forcing, and Figs. B.18-B.20 those from the two-signal study. Long-term trends in sea surface temperatures (SSTs) over the Atlantic region illustrate the hemispheric contrast of temperature change (Fig. B.21), as shown as time series in Section 3.4. Changes in West African aerosol emissions and aerosol optical depths are also shown (Fig. B.22). To demonstrate circulation changes related to the precipitation changes in the GFDL experiments, we also show long-term trends in near-surface winds (Fig. B.23), sea level pressure (Fig. B.24), and surface temperature (Fig. B.25). Time series of precipitation and surface variables related to the monsoon mechanism in South Asia are furthermore displayed (Fig. B.26). Linear trends of the same circulation measures are additionally calculated for reanalysis data as well as simulations with the same model as used in the study but SSTs fixed to observed values (Fig. B.27); this tests the consistency as well as the relative importance of the slow and fast components of the response.

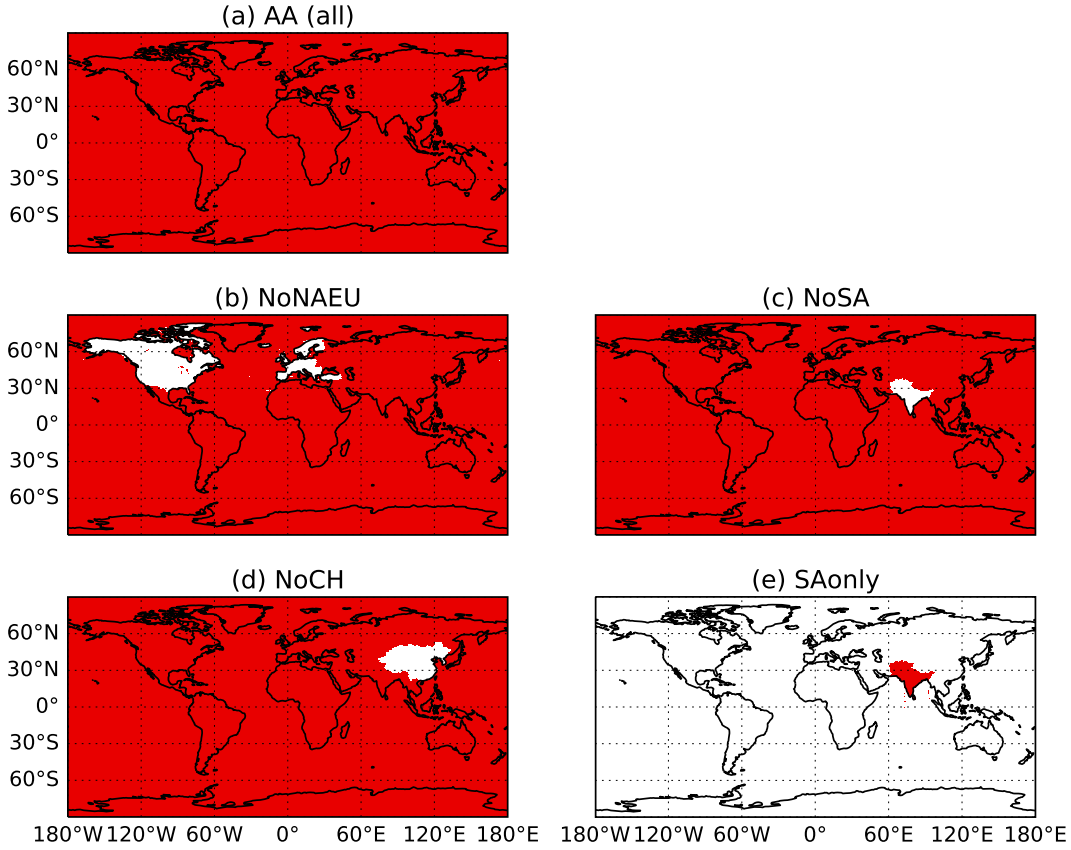

Figure B.1: Aerosol emission regions used for the simulations. Emissions -if any- from regions shown in red evolve according to the historical emission inventories from *Lamarque et al.* (2010), while those from regions shown in white are set to pre-industrial levels.

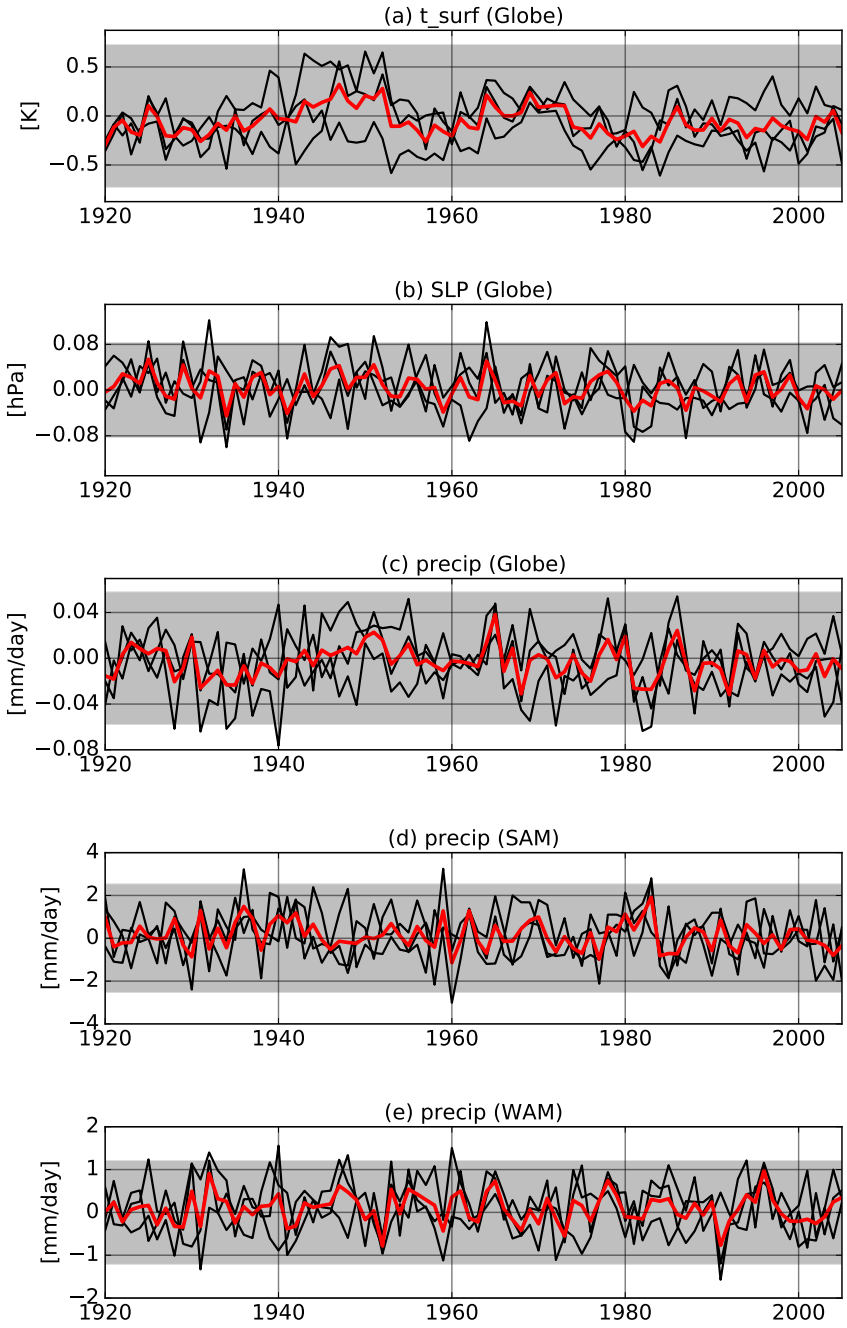

Figure B.2: Linearity of the response to regional aerosol forcing: Difference between the time series from the global aerosol simulations (AA) and the sum of the time series from simulations with South Asian aerosols only (SAonly) and all but South Asian aerosols (NoSA) for summer (JJAS) (a) global surface temperature, (b) global sea level pressure, (c) global precipitation, (d) South Asian monsoon precipitation, and (e) West African monsoon precipitation. Black lines show the results, AA-(SAonly+NoSA), for individual ensemble members, and the red line those for the ensemble means. (d-e) refer to the monsoon regions shown in Fig. B.3a. Anomalies with respect to climatological mean values from a 500-year pre-industrial control simulation with GFDL-CM3 are used, and grey shading indicates the respective 5-95% range of expected internal variability ($1.96\sqrt{3}\sigma_{\text{PIcontrol}}$).

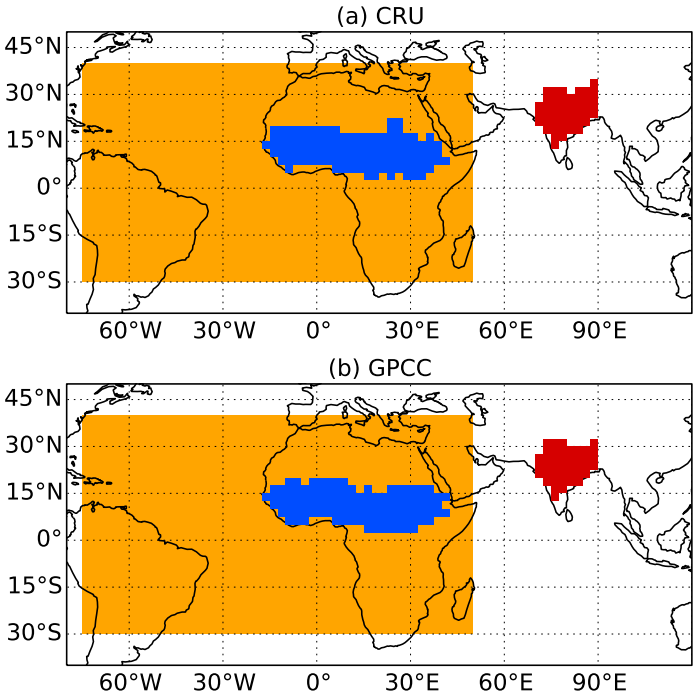

Figure B.3: West African (blue) and South Asian (red) summer monsoon regions calculated for the (a) CRU precipitation dataset (*Harris et al.*, 2014) and (b) GPCC precipitation dataset (*Schneider et al.*, 2014b). The yellow box (30°S-40°N, 75°W-50°E) shows the region for which zonal mean precipitation is calculated for Fig. 3.6.

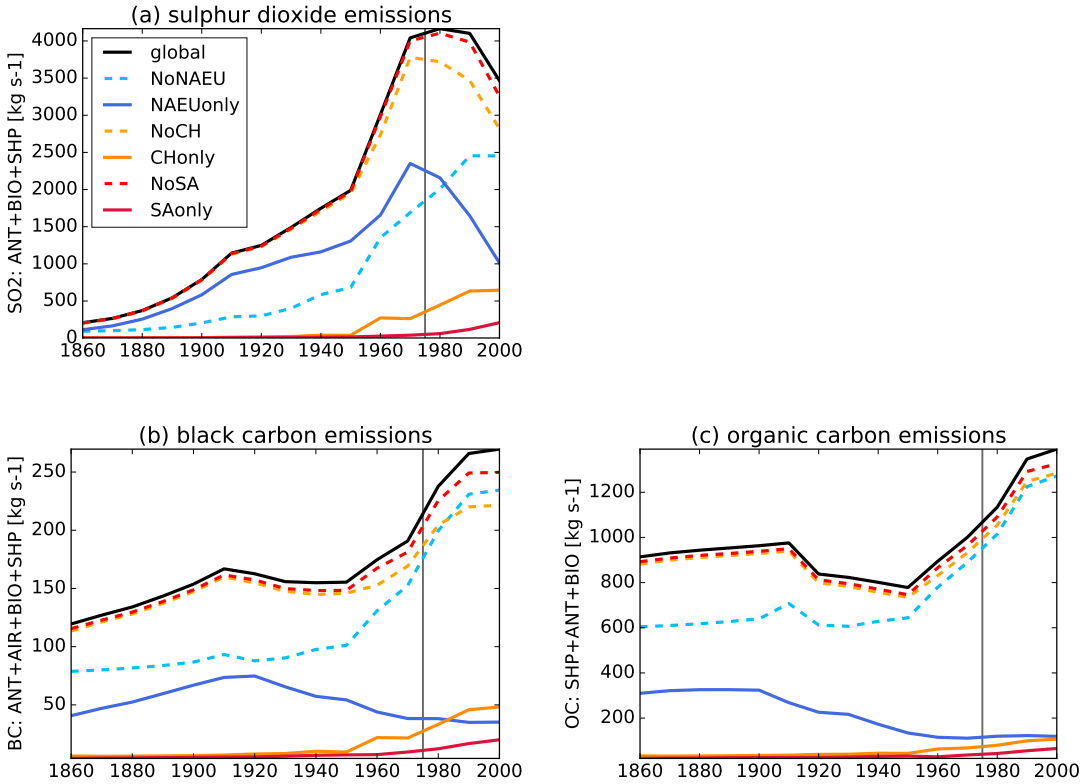

Figure B.4: Regional sum of decadal emissions from all sectors in boreal summer (JJAS) of (a) the sulphate aerosol precursor SO2, (b) black carbon aerosols, and (c) organic carbon aerosols. Global emissions (black) are shown as well as the emissions as they are evolving in the different simulations: Emissions from everywhere but North America and Europe (NoNAEU, light blue, dashed), from everywhere but China (NoCH, yellow, dashed), from everywhere but South Asia (NoSA, red, dashed), and from South Asia only (SAonly, dark red, solid). Emissions from North America and Europe only (NAEUonly dark blue, solid) and from China only (CHonly, orange, solid) are shown as well. The regions are shown in Fig. B.1. The grey vertical line indicates the year 1975 which divides the first and second time period for which trends are calculated. Data from *Lamarque et al.* (2010).

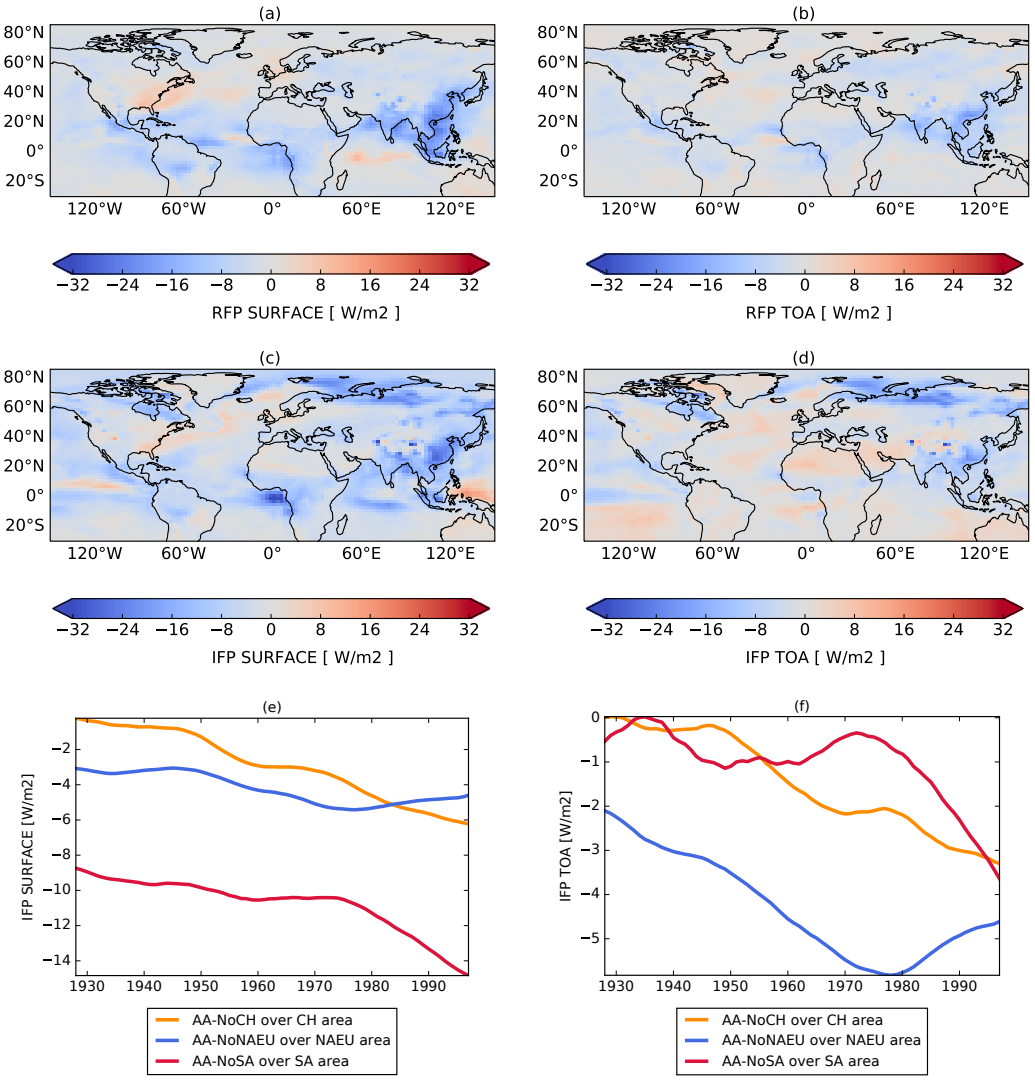

Figure B.5: Simulated JJAS radiative forcing (RF, W/m^2): AA ensemble mean (a-b) radiative flux perturbation (RFP, same as effective RF; *Hansen et al.*, 2005) and (c-f) instantaneous RF (defined as the sum of net short-wave and net long-wave radiation) at the (left) surface and (right) top of the atmosphere (TOA). (a-d) Spatial patterns of RF due to changes in global aerosol emissions between [1996-2005] and [1920-1929]. (e-f) Time series of instantaneous RF over the aerosol emission regions (China (yellow), NAEU (blue), and South Asia (red)) due to local emissions. Shown are the differences in the area-mean time series between the global aerosol (AA) ensemble and the ensemble without time-evolving emissions from that respective region (NoCH, NoNAEU, NoSA), smoothed with 11-7 running means.

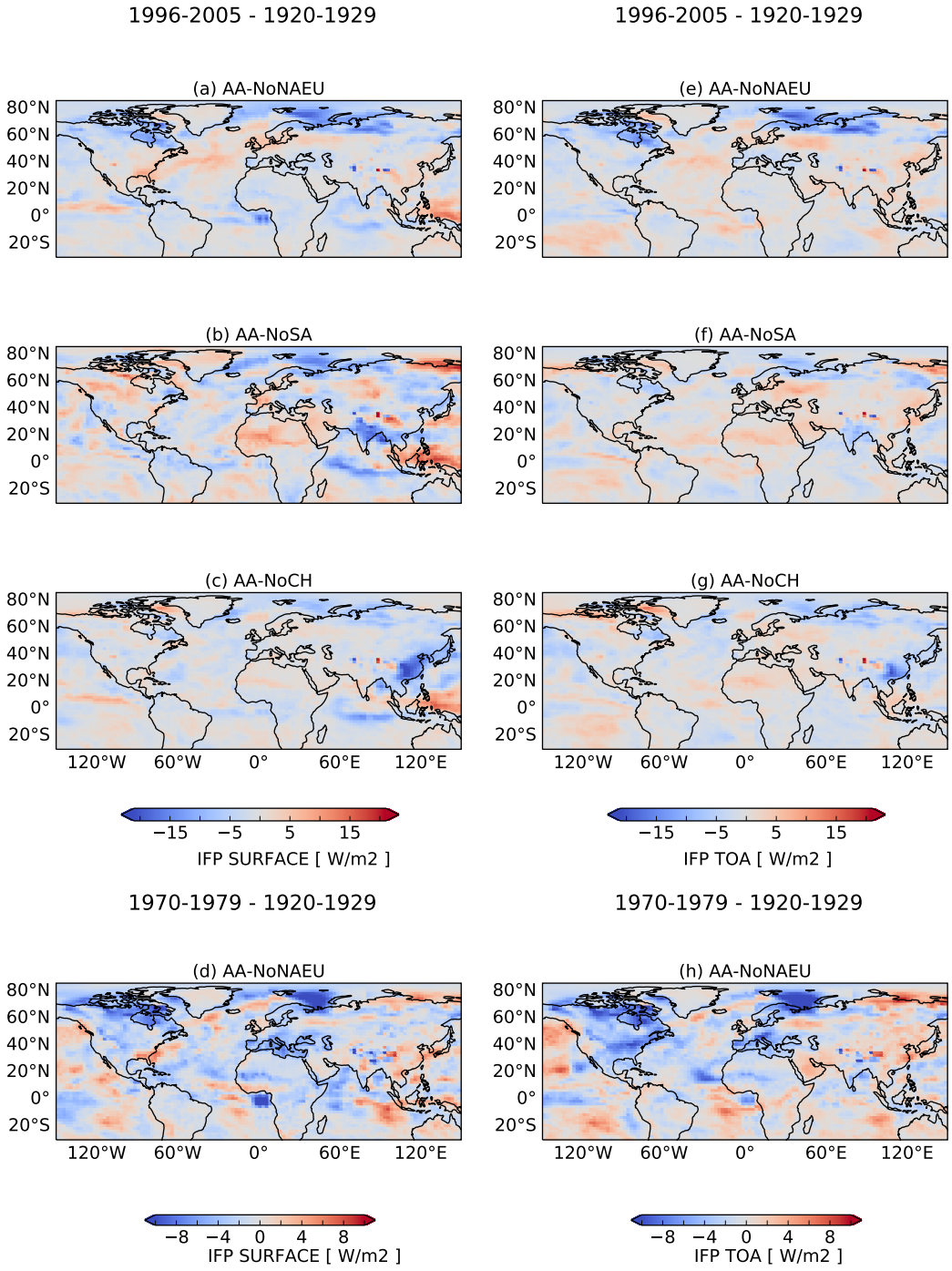

Figure B.6: Difference between the JJAS instantaneous RF in the AA ensemble mean and the ensemble means of the regional anthropogenic aerosol simulations (W/m^2) between (top) [1996-2005] and [1920-1929] and (bottom) [1970-1979] and [1920-1929] indicating the impact of (a,d,e,h) North American and European aerosols, (b,f) South Asian aerosols, and (c,g) Chinese aerosols.

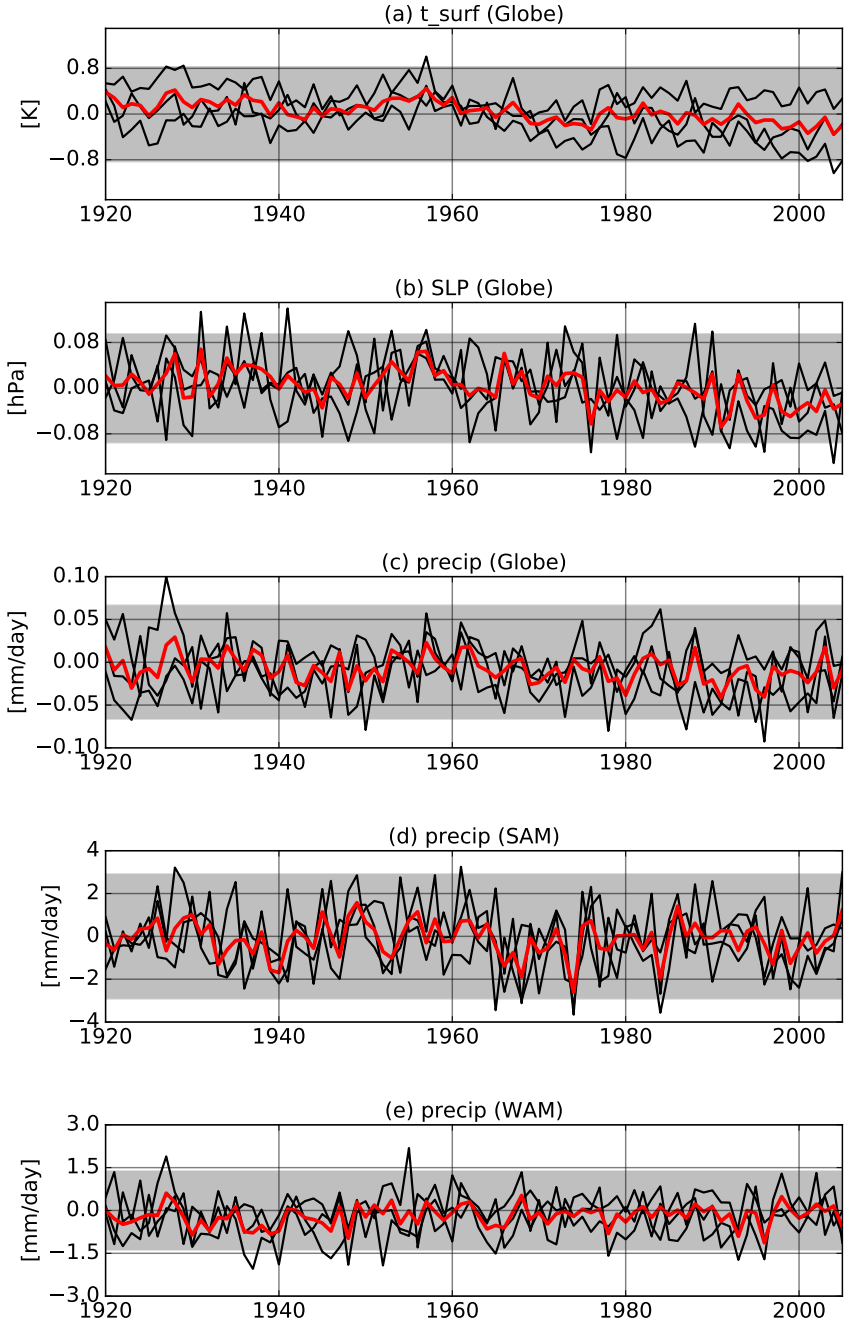

Figure B.7: Linearity of the response to different forcings: Difference between the time series from the all-forcing simulations (ALL) and the sum of the time series from the global aerosol-only simulations (AA), greenhouse-gas only simulations (GHG), and natural forcings only (NAT) for the same variables as in Fig. B.2. Anomalies with respect to climatological mean values from a 500-year pre-industrial control simulation with GFDL-CM3 are used, and grey shading indicates the respective 5-95% range of expected internal variability ($1.96\sqrt{4}\sigma_{\text{PIcontrol}}$).

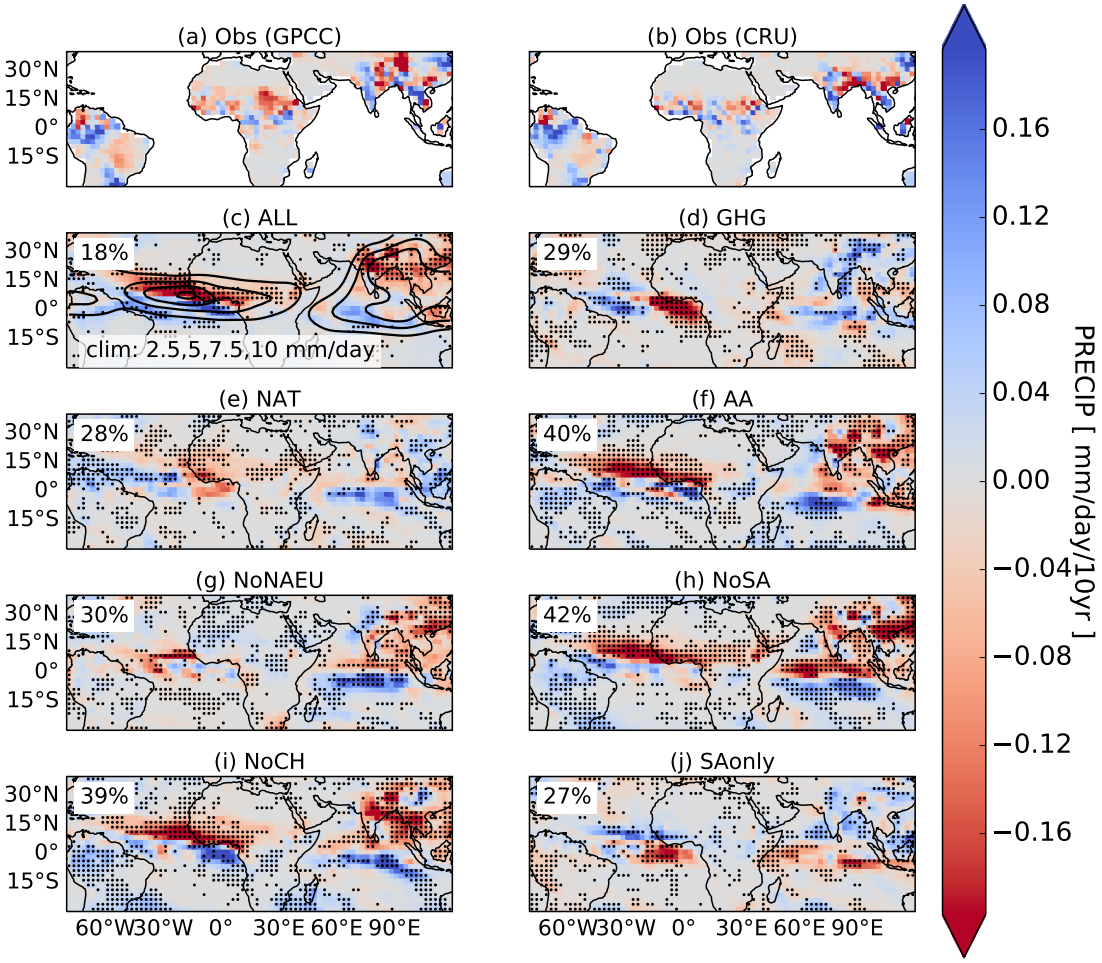

Figure B.8: As Fig. 3.1, but for 1920-1975: Observed and modeled summer (JJAS) precipitation linear trends (mm/day/decade) for 1920-1975. Shown are observed (a) CRU and (b) GPCC, and ensemble mean for (c) all external forcings (ALL), (d) greenhouse gas forcing (GHG), (e) natural forcing (NAT), (f) global anthropogenic aerosol only forcing (AA), (g-j) global anthropogenic aerosol only forcing with regional emissions set to pre-industrial levels for (g) North America and Europe (NoNAEU), (h) South Asia (NoSA), (i) China (NoCH), and (j) all but South Asia (SAonly). Stippling shows where the respective ensemble agrees on the sign of the trend. See also Fig. B.11, which shows the same data only for the considered monsoon regions.

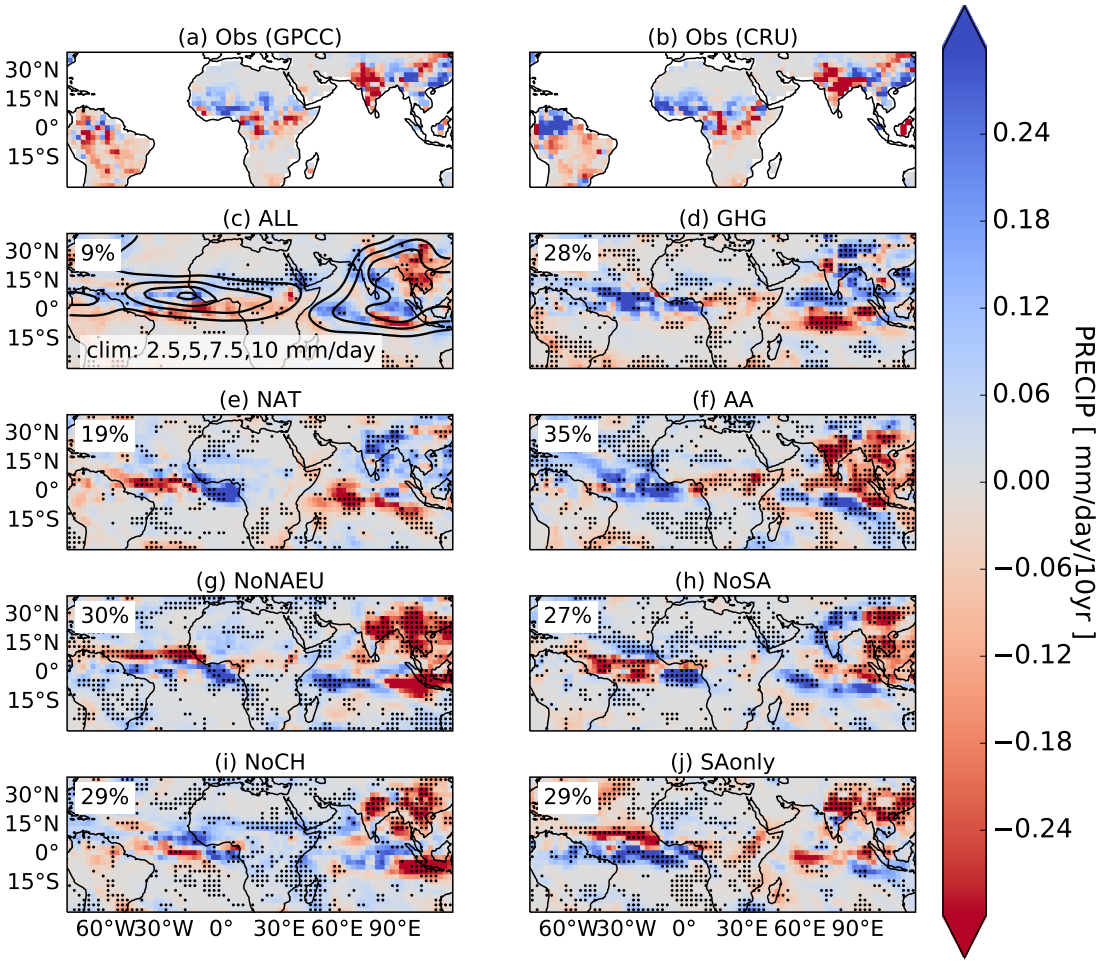

Figure B.9: As Fig. B.8 except precipitation linear trends (mm/day/decade) are for 1975-2005. See also Fig. B.12, which shows the same data only for the considered monsoon regions.

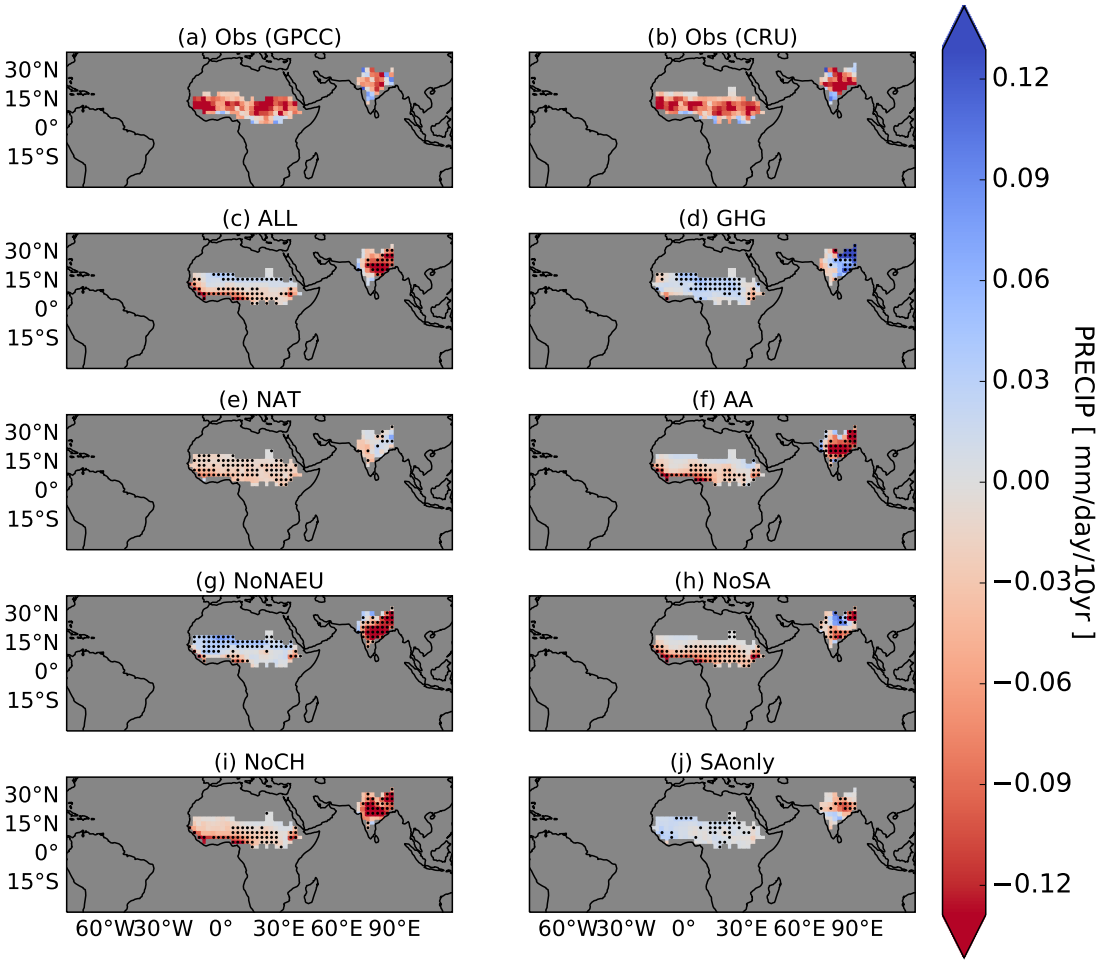

Figure B.10: As Fig. B.8 except linear trends (mm/day/decade) are for 1920-2005 and only data in the monsoon regions are shown. The simulated trends (c-j) are masked using the monsoon region derived from the CRU observations.

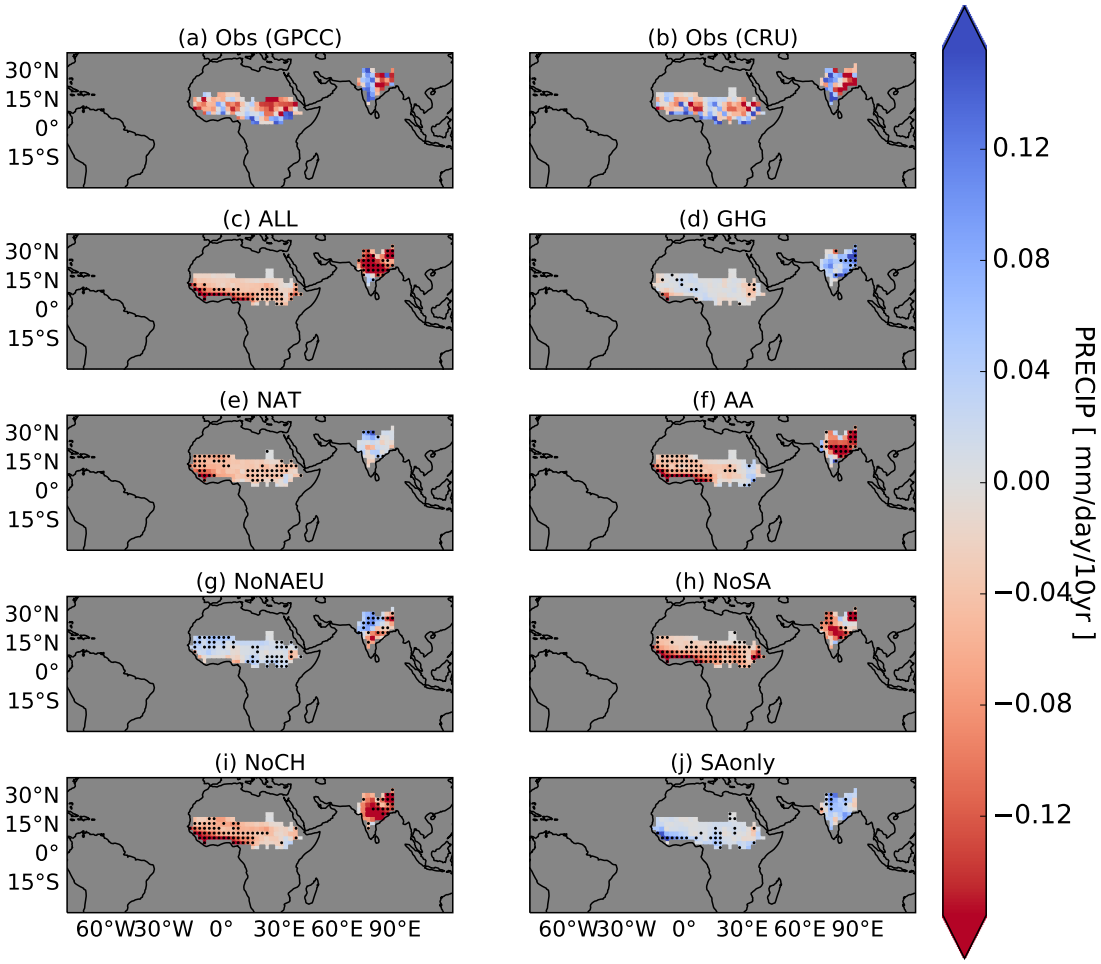

Figure B.11: As Fig. B.10 except linear trends (mm/day/decade) are for 1920-1975.

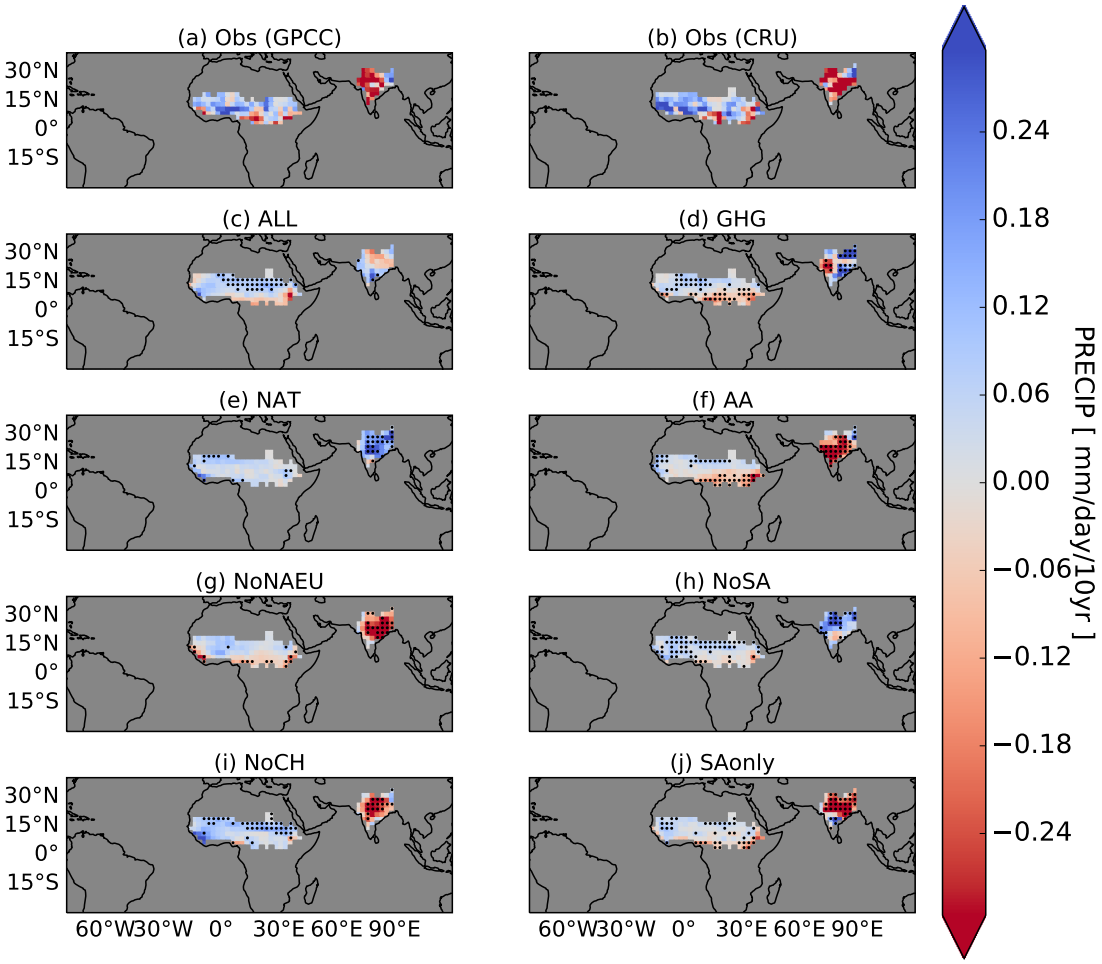

Figure B.12: As Fig. B.10 except linear trends (mm/day/decade) are for 1975-2005.

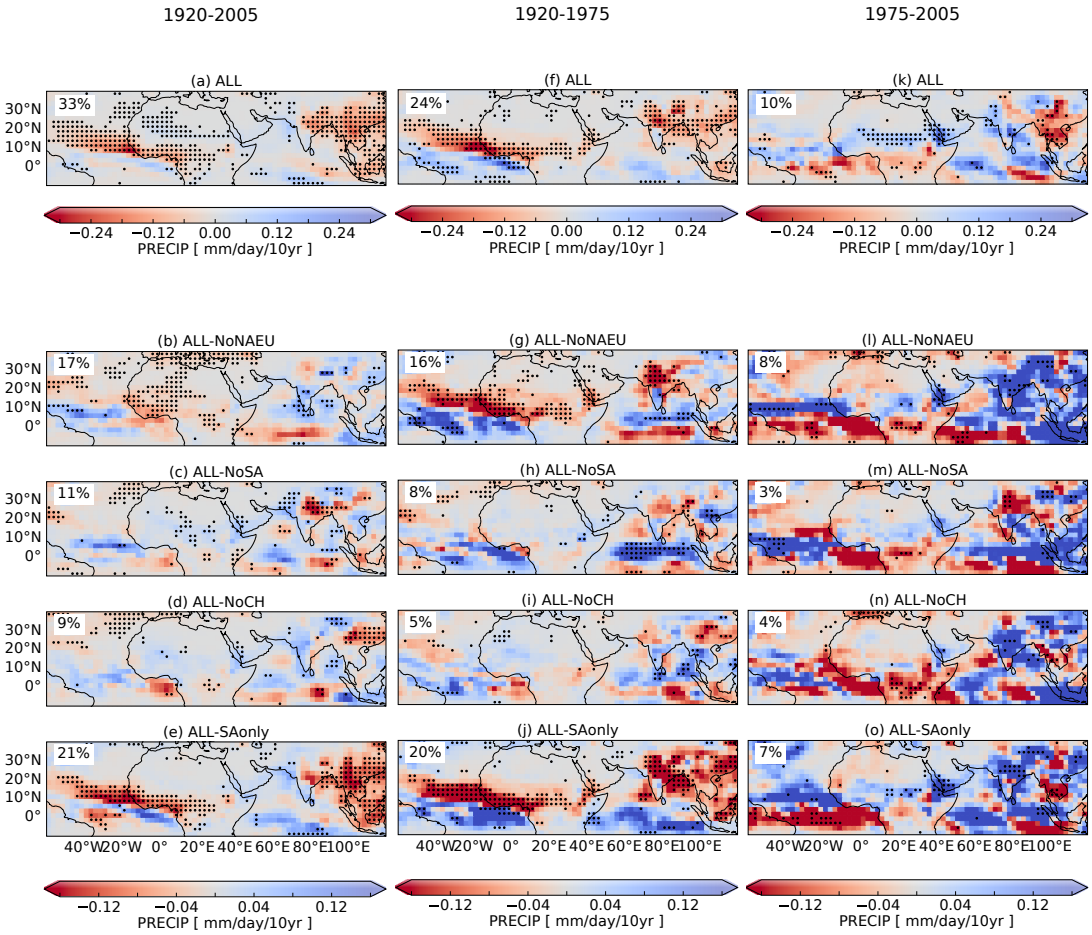

Figure B.13: Simulated summer (JJAS) precipitation linear trends (mm/day/decade) in the all-forcing (ALL) ensemble mean (first row) and the difference between the precipitation trends in the ALL ensemble mean and the ensemble means of the regional anthropogenic aerosol simulations (mm/day/decade) for (a-e) 1920-2005, (f-j) 1920-1975, and (k-o) 1975-2005. The second row shows (b,g,l) ALL-NoNAEU, indicating the impact of North American and European aerosols. The other rows show (c,h,m) ALL-NoSA for South Asian aerosols; (d,i,n) ALL-NoCH for Chinese aerosols; and (e,j,o) ALL-SAonly for all but South Asian aerosols. Stippling in (a,f,k) shows where the ALL ensemble agrees on the sign of the trend, and stippling in (b-e,g-j,l-o) shows where differences between the ALL ensemble and regional aerosol ensemble are statistically significant at the 95% confidence level using a t-test. Numbers in the top left corner give the fraction of stippled points within the displayed area.

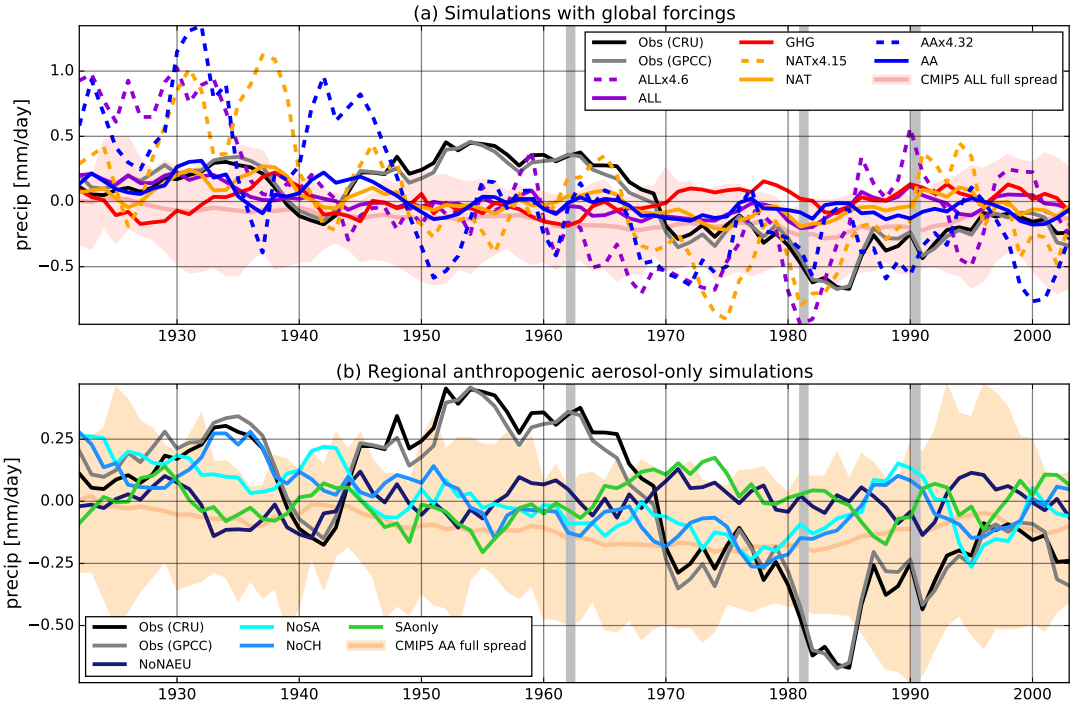

Figure B.14: As Fig. 3.3, but with the detected fingerprints (time series) multiplied by the respective best-guess scaling factors from the 1-signal detection and attribution analysis (Fig. 3.5) as dashed lines: West African summer (JJAS) monsoon precipitation anomalies (mm/day) with respect to the 1920-2005 climatology.

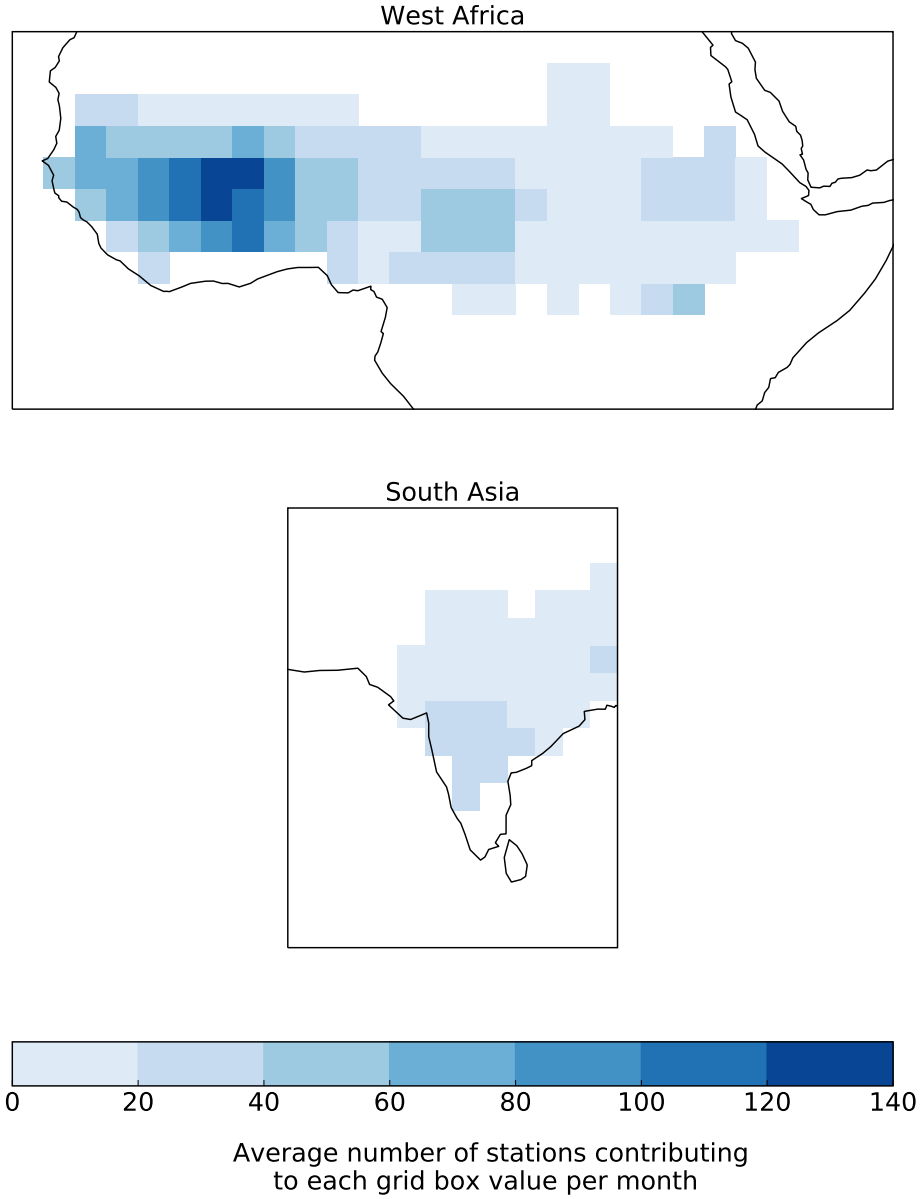

Figure B.15: Station coverage of CRU precipitation observations. Number of stations per month contributing to the respective grid box value, averaged over all JJAS months between 1920 and 2005 in the (top) West African and (bottom) South Asian monsoon region.

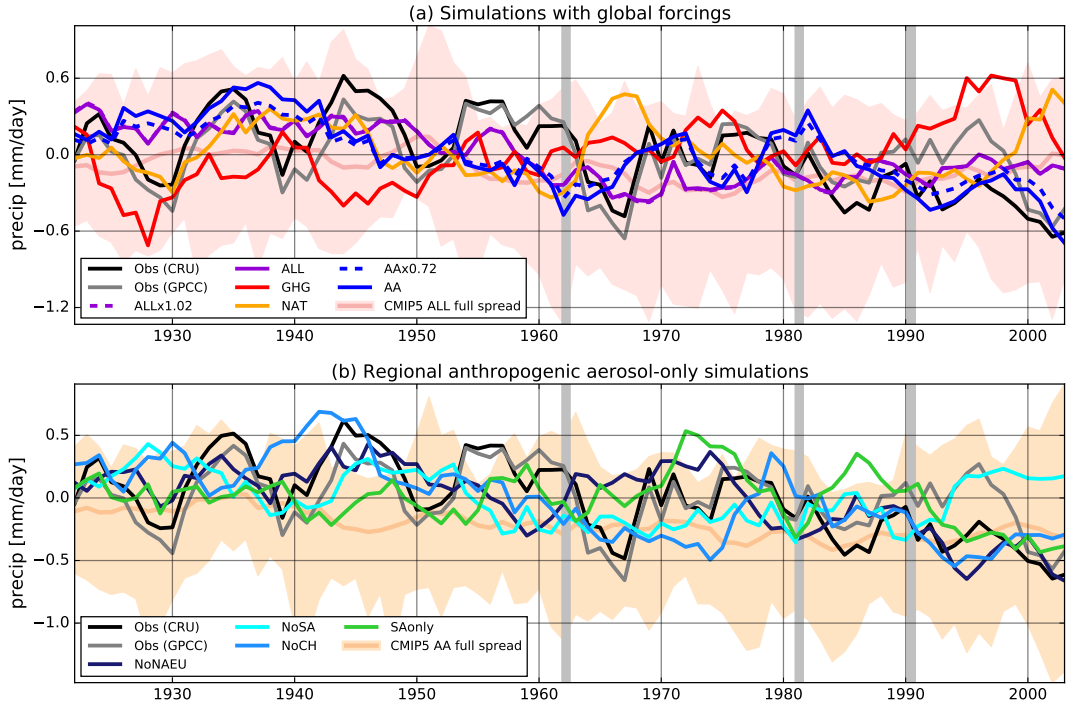

Figure B.16: As Fig. 3.4, but with the detected fingerprints (time series) multiplied by the respective best-guess scaling factors from the 1-signal detection and attribution analysis (Fig. 3.5) as dashed lines: South Asian summer (JJAS) monsoon precipitation anomalies (mm/day) with respect to the 1920-2005 climatology.

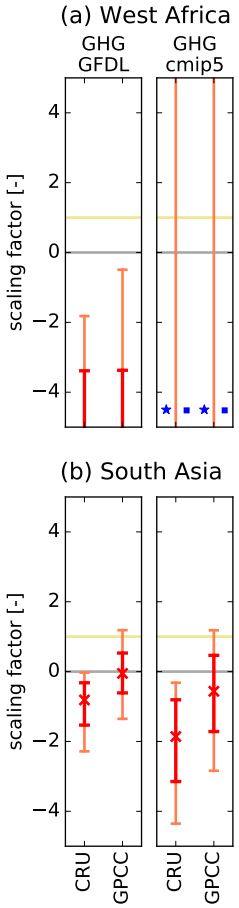

Figure B.17: As Fig. 3.5, detection and attribution of observed changes in (a) West Africa and (b) South Asia summer monsoon precipitation, but for greenhouse gas (GHG) forcing from GFDL-CM3 (GFDL) and the CMIP5 models (cmip5).

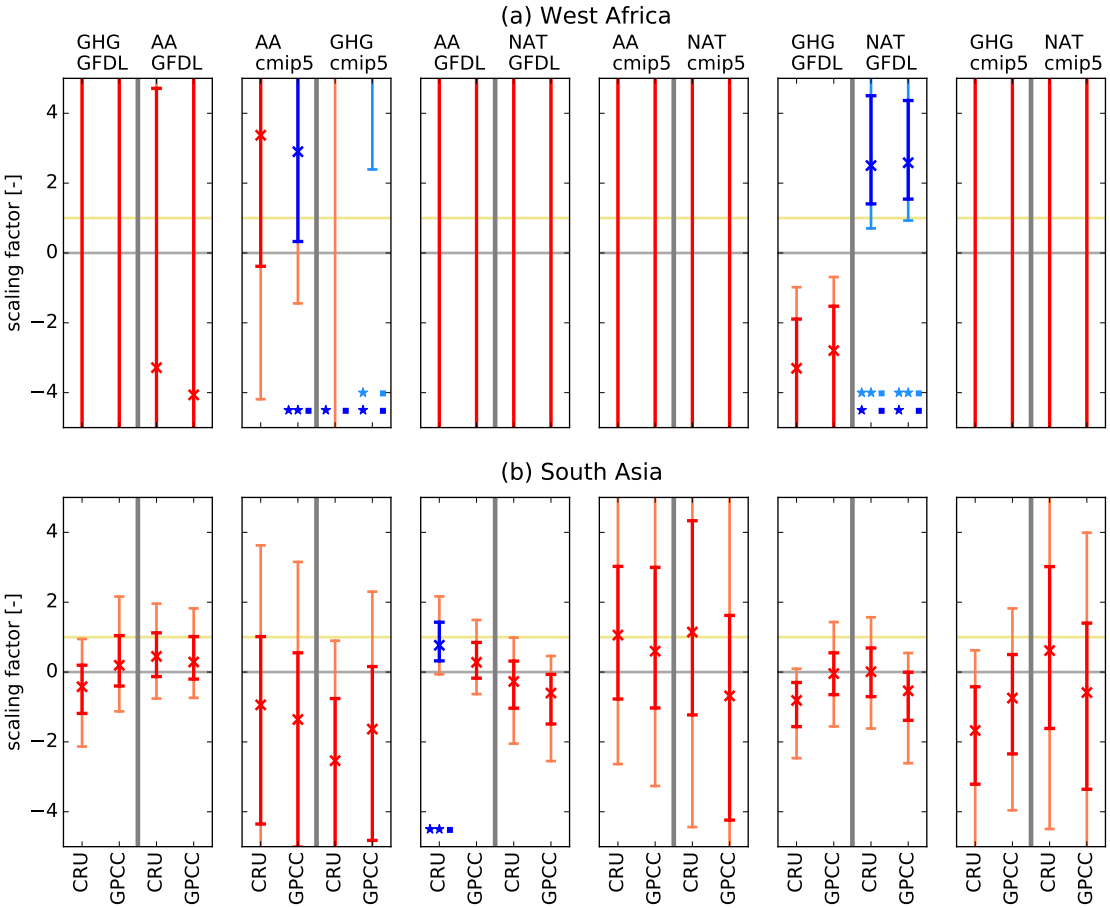

Figure B.18: As Fig. 3.5, detection and attribution of observed changes in (a) West Africa and (b) South Asia summer monsoon precipitation, but from a two-signal analysis. Scaling factors for different combinations of anthropogenic aerosol forcing (AA), greenhouse gas forcing (GHG), and natural forcing (NAT) from GFDL-CM3 (GFDL) and the CMIP5 models (cmip5).

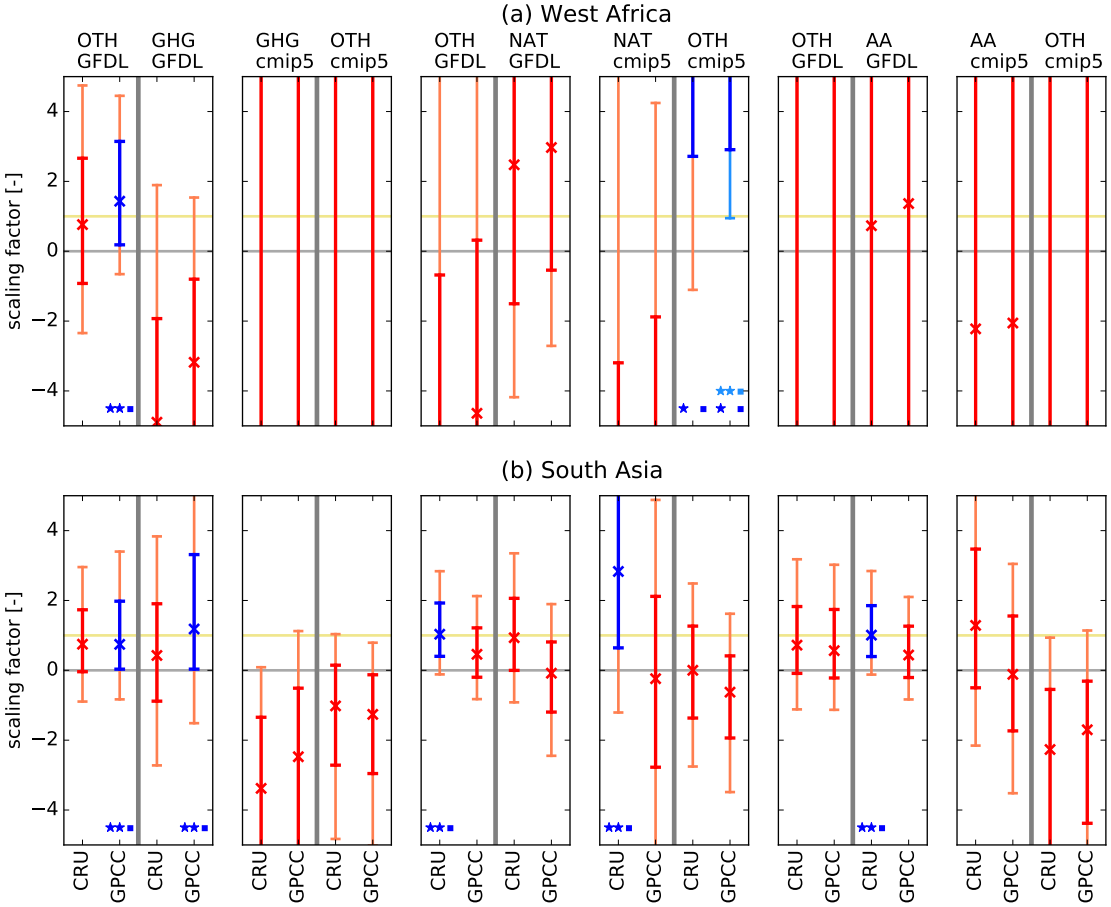

Figure B.19: As Fig. B.18 except historical forcings (ALL) are regressed together with anthropogenic aerosol forcing (AA), greenhouse gas forcing (GHG), natural forcing (NAT). The scaling factors are translated into those for the respective regional aerosol forcing and all but this forcing (OTH).

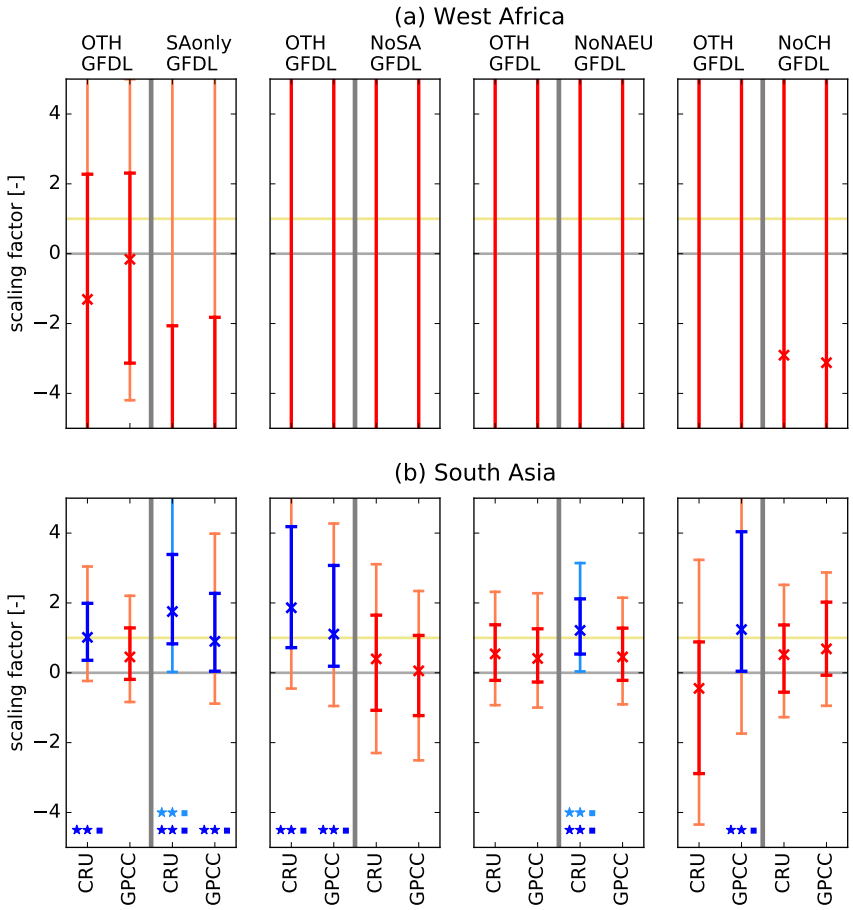

Figure B.20: As Fig. B.18, except historical forcings (ALL) are regressed together with regional anthropogenic aerosol only forcing for South Asian emissions only (SAonly), no historical South Asian emissions (NoSA), no historical North American and European emission (NoNAEU), and no historical Chinese emissions (NoCH), respectively, from GFDL-CM3. The scaling factors are translated into those for the respective regional aerosol forcing and all but this forcing (OTH).

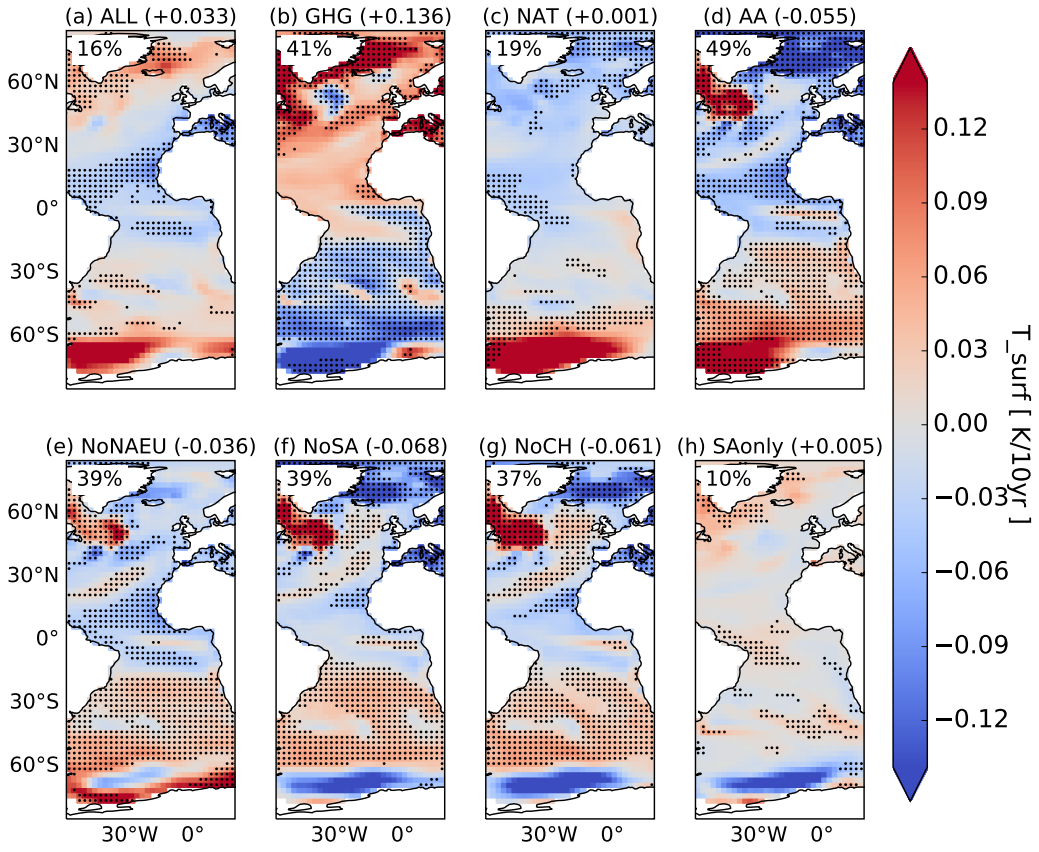

Figure B.21: As Fig. B.8 except linear trends (K/decade) are for sea surface temperature for 1920-2005 for the Atlantic sector (85°S-85°N, 60°W-20°E). The area mean, given above each panel, is removed before calculating the agreement of the ensemble on sign per simulation.

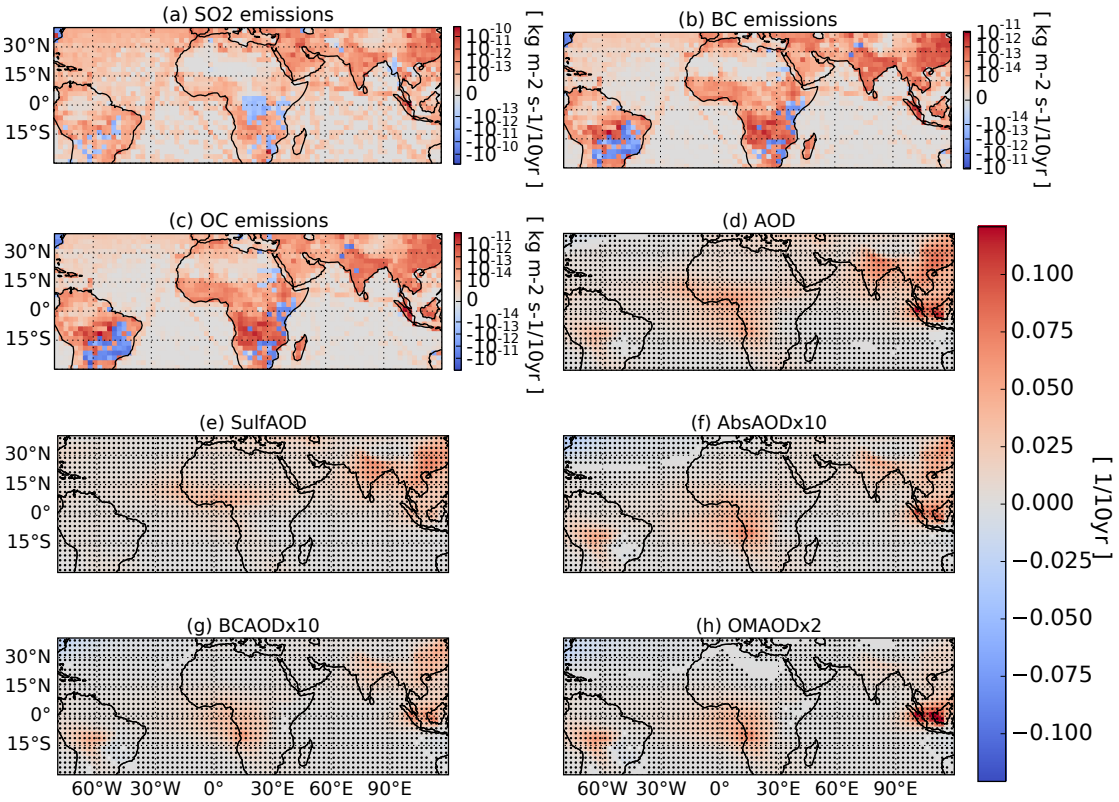

Figure B.22: As Fig. B.8 except linear trends (a-c) kg/m2/s/decade, (d-g) 1/decade) are for 1920-2005 for emissions of (a) the sulphate aerosol precursor sulphur dioxide, (b) black carbon, and (c) organic matter, from *Lamarque et al.* (2010), and simulated (d) total aerosol optic depth (AOD) as well as AOD from (e) sulphate aerosols (i.e. the scattering AOD), (f) black carbon and organic matter (i.e. the absorbing AOD), (g) black carbon separately, and (h) organic matter. In (d-h), stippling shows where all simulations give trend of the same sign. In (f-h), values are multiplied by a constant factor (given above the plot) to make the trends better visible.

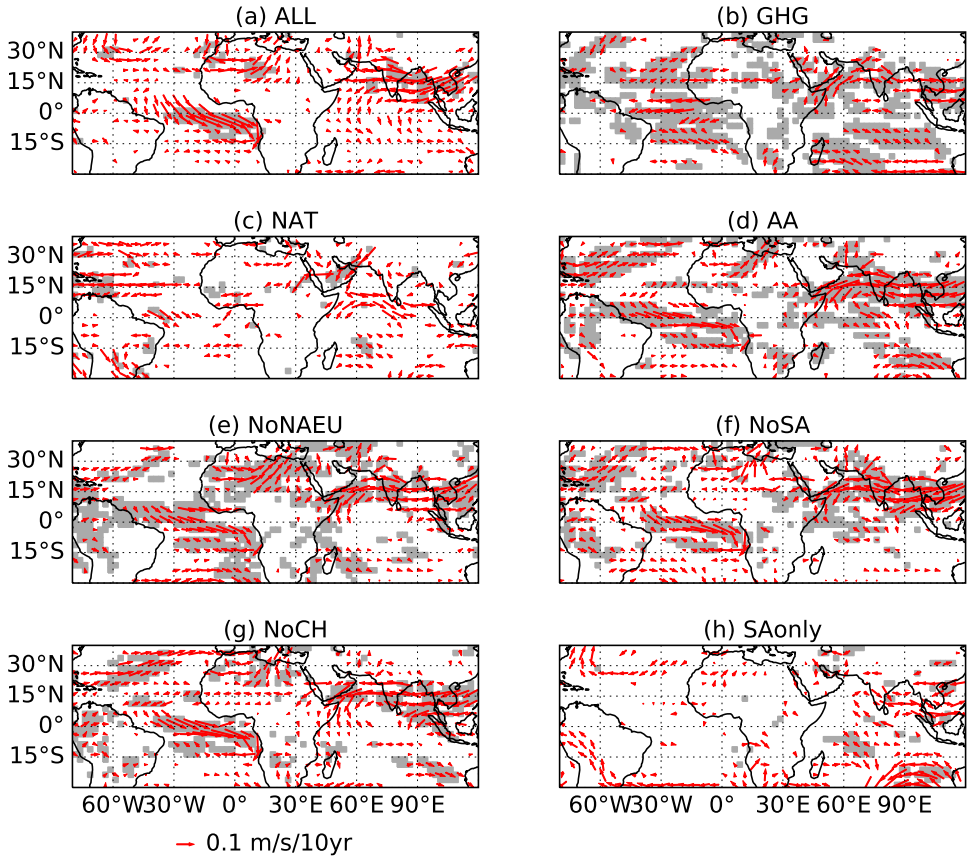

Figure B.23: As Fig. B.8 except linear trends (m/s/decade) are for wind speed at 850 hPa for 1920-2005. Grey shading shows where the AA ensemble agrees on the sign of the trends in zonal wind speed, meridional wind speed, and total wind speed.

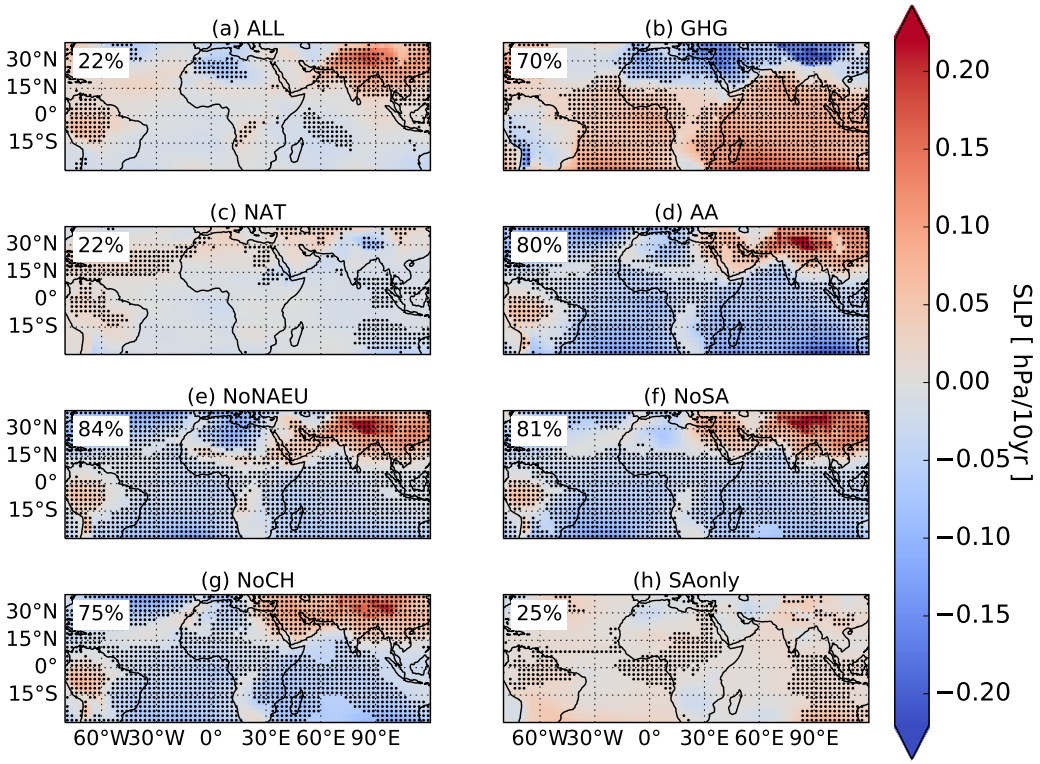

Figure B.24: As Fig. B.23 except linear trends (hPa/decade) are for sea level pressure for 1920-2005.

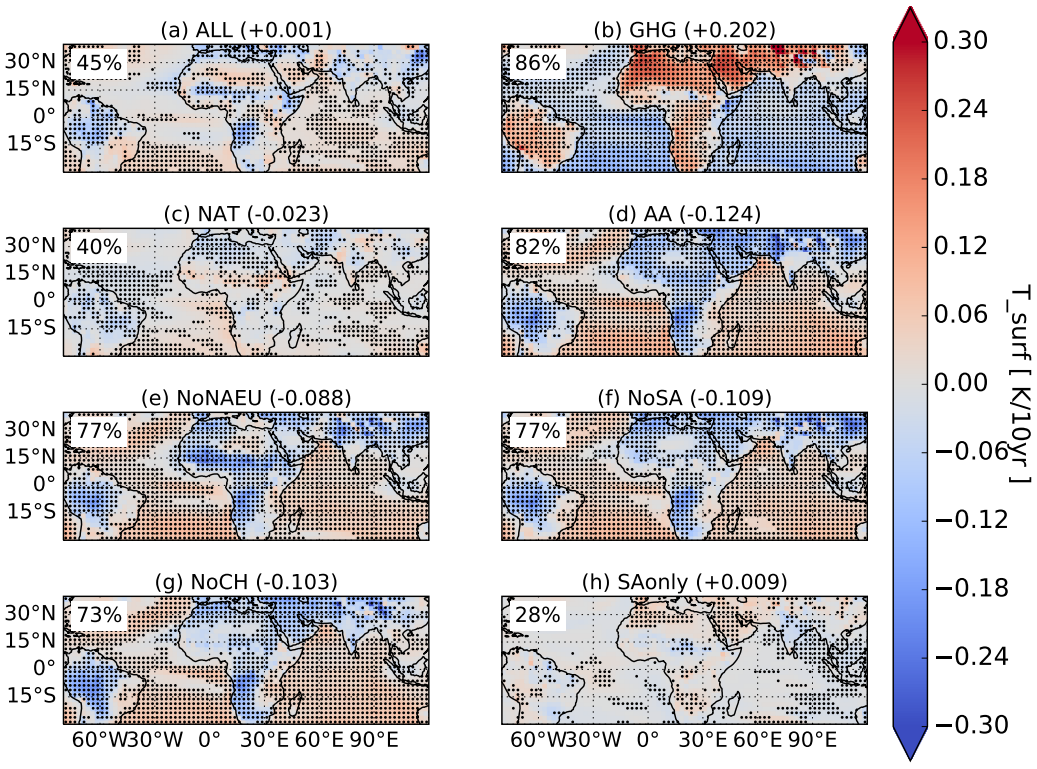

Figure B.25: As Fig. B.23 except linear trends (K/decade) are for surface temperature for 1920-2005. The area mean, given above each panel, is removed before calculating the agreement of the ensemble on sign per simulation.

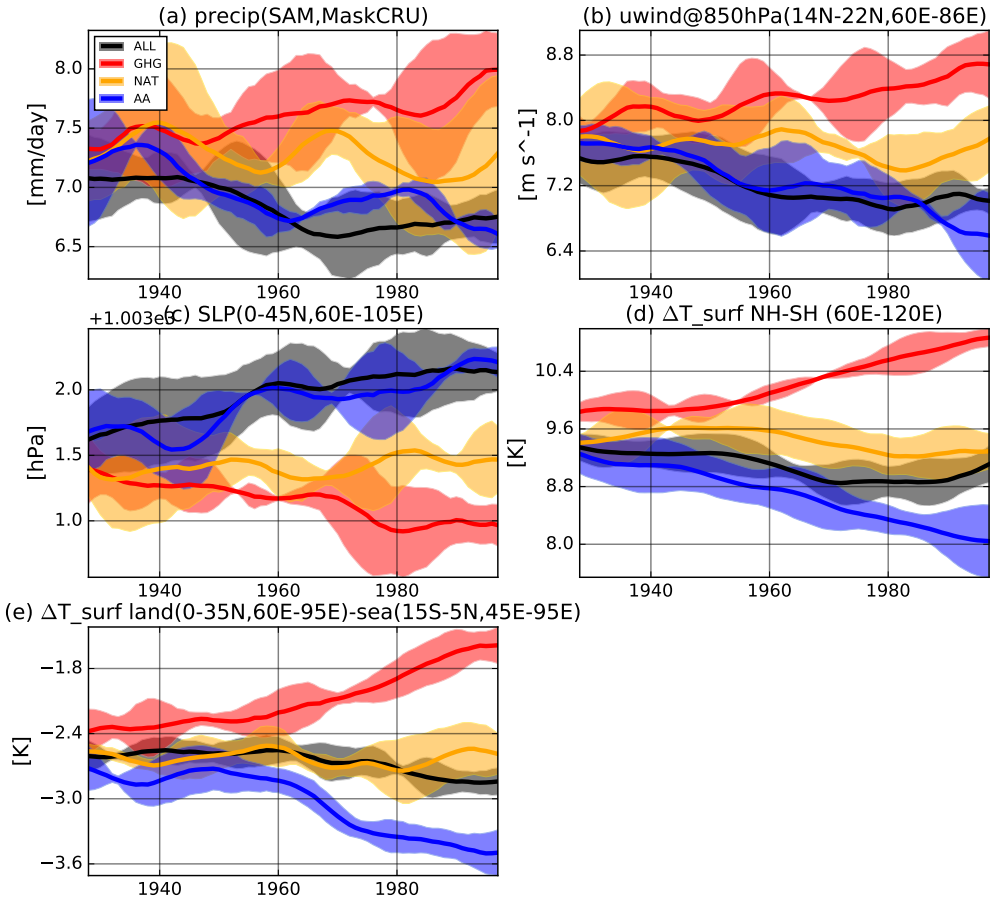

Figure B.26: South Asian summer (JJAS) (a) monsoon precipitation, (b) zonal wind speed over India and the Arabian Sea, (c) sea level pressure over a northerly extended South Asian land region, (d) the inter-hemispheric surface temperature gradient at Asian longitudes, and (e) the South Asian land-ocean contrast as simulated with all historical forcings (ALL, black), greenhouse gas forcing (GHG, red), natural forcing (NAT, yellow), and global anthropogenic aerosol only forcing (AA, blue) with 11-7-year running mean along with the respective 95% range of the individual simulations (shading).

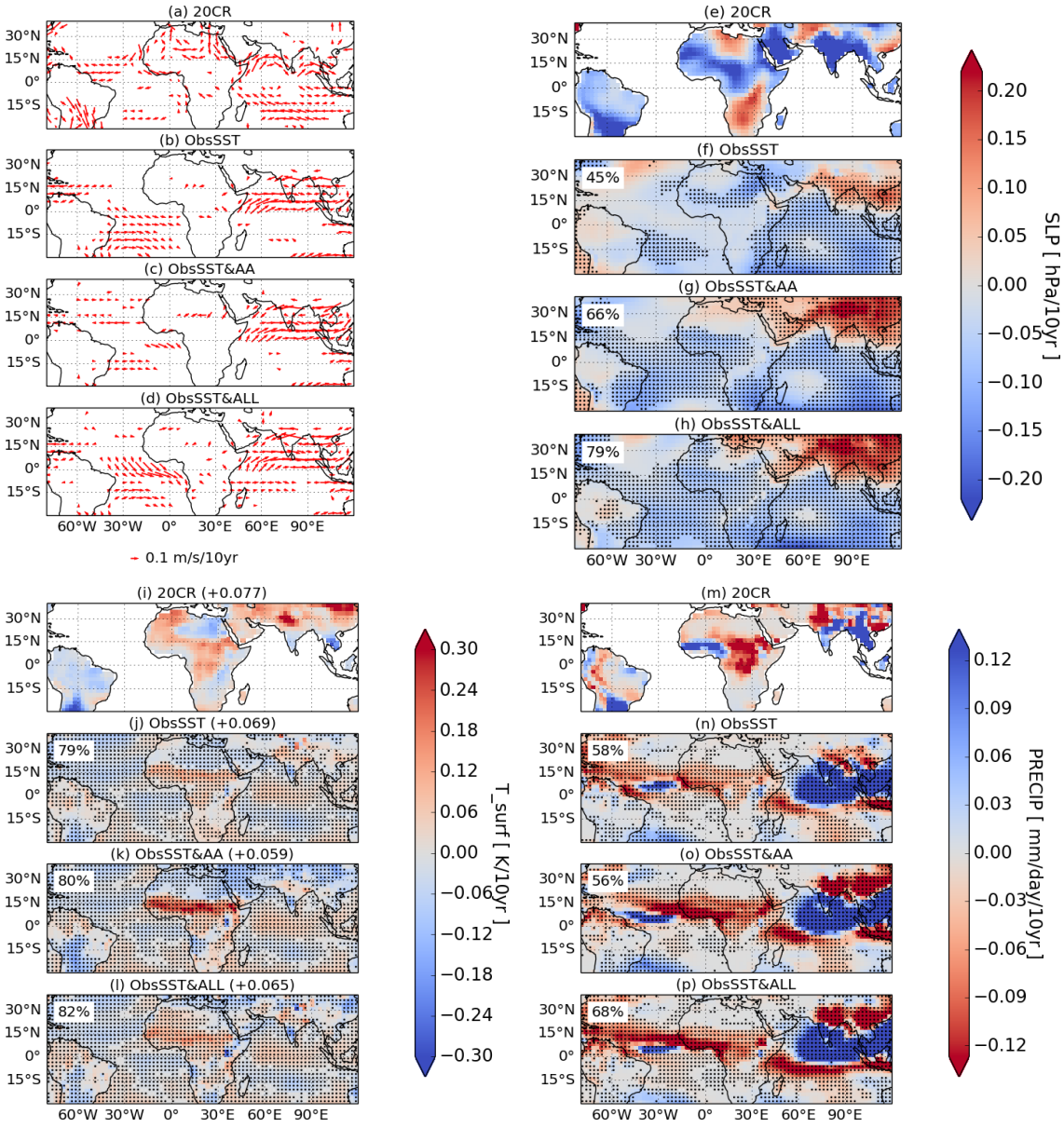

Figure B.27: As. Figs. B.23-B.25 except linear trends are calculated for (a,e,i,m) 20th Century Reanalysis V2 data (20CR) reanalysis (*Compo et al.*, 2011), simulations with the atmosphere-only component of the GFDL model used in this study, forced by (b,f,j,n) observed sea surface temperatures (ObsSST), (c,g,k,o) ObsSST and anthropogenic aerosol emissions (AA), and (d,h,l,p) ObsSST, AA, and other external forcings (GHG, NAT). The colourbars are cropped in order to be consistent with Figs. B.24, B.25, and 3.1, respectively. Note that 20CR is less able of reproducing the observed precipitation trends (Fig. 3.1) than the model simulations, so that differences between the circulation trends in 20CR and the model may not be considered model deficiencies.

Appendix C

Supplementary Figures to Chapter 4

Outline. The figures in this chapter support further the analysis in Chapter 4. The model experiment design is visualised further by showing the ocean initial states of the ensemble members by means of their Atlantic Meridional Overturning Circulation (AMOC) index, and by showing the annual-mean evolution of sulphur dioxide (SO_2) emissions used in the simulations (Fig. C.1). Simulated changes in sea surface temperatures and upper-ocean heat content over the Atlantic and elsewhere supplement Fig. 4.1a-c (Fig. C.2). The spatial SST patterns associated with the Atlantic Multidecadal Variability (AMV) index are then shown both for the pre-industrial control simulation (Fig. C.3) and for the historical observations and simulations, including the impact of observational data coverage on the pattern and the hemisphere-wide character of the AMV (Fig. C.4). The global patterns of simulated long-term change in aerosol optical depth (AOD) and near-surface temperature in response to the anthropogenic SO_2 emissions from North America (NA) and Europe (EU) (Fig. C.5) complement the patterns over the Atlantic shown in Figs. 4.3a,b and 4.1d-e. Simulated long-term changes in cloud cover at different heights in response to SO_2 emissions from NA and EU (Fig. C.6) support the analysis of aerosol effects over the Atlantic, while simulated (changes in the) sea salt and dust burden refer to the possi-

ble interactions between the effects of anthropogenic and natural aerosols (Fig. C.7). The simulated North Atlantic Oscillation (NAO) is also shown (Fig. C.8) due to its potential role in AMV-AMOC interactions. Temporal changes in sea surface salinity, averaged over the subpolar and the tropical Atlantic and compared to observations (Fig. C.9), are finally shown as an exemplary measure of the realism of the model's ocean changes. Unless otherwise stated, all time series are smoothed with 5-year running means as are the figures in Chapter 4.

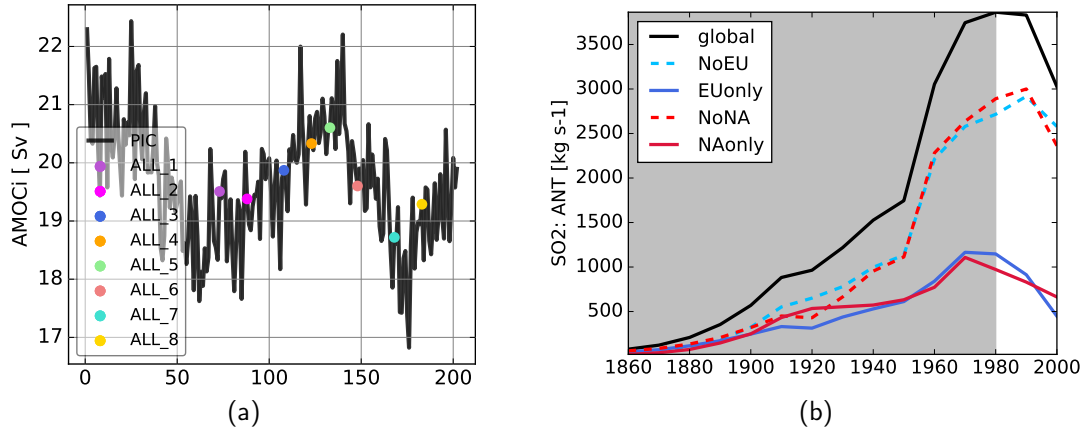

Figure C.1: Simulation set-up: (a) Atlantic Meridional Overturning Circulation (AMOC) index at 30°N, with its state at the times used as initial conditions for the members of the historical (ALL, noNA, and noEU) ensembles marked as coloured dots. (b) Historical emissions of sulphur dioxide (SO_2): Global anthropogenic (ANT) emissions as used in the ALL experiment (black solid), as well as emissions from Europe only (EUonly, blue solid) and North America only (NAonly, dark red solid). The global emissions in the regional-aerosol experiments (noEU, light blue dashed and noNA, red dashed) result from allowing emissions to evolve historically everywhere but in Europe and North America, respectively. Total SO_2 emissions, i.e. including those from ships (SHP) and biomass burning (BIO), are also shown (grey, solid). Data from *Lamarque et al.* (2010).

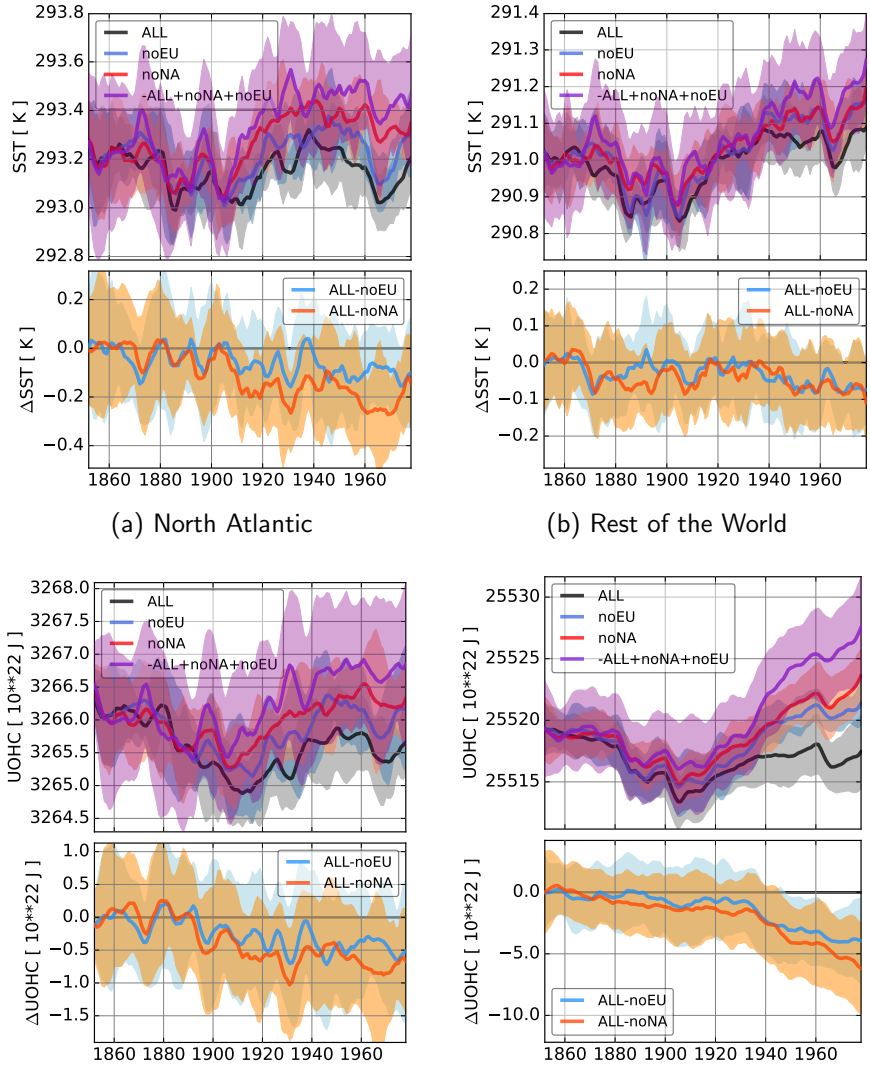

(a) North Atlantic (b) Rest of the World

(c) North Atlantic (d) Rest of the World

Figure C.2: Simulated annual-mean time series of (a-b) area-averaged sea surface temperatures and (c-d) area-summed upper ocean (0-700m) heat content (UOHC) over (a,c) the North Atlantic [0-65°N; 0-80°W] and (b,d) the rest of the world ocean i.e. all but [0-65°N; 0-80°W]. The ensemble-mean values of the (top) simulations with global anthropogenic SO_2 emissions (ALL; black with grey shading for the 90% range of the 8-member ensemble) and those from the simulations without European (noEU; blue line and shading) and North American (noNA; red line and shading) anthropogenic SO_2 emissions are shown as well as the (bottom) differences between ALL and noEU (light blue line and shading) and ALL and noNA (orange line and shading). (Top) We also show -ALL+noNA+noEU (purple) here, which, again assuming linearity in the response to the single forcings, is the simulated response to greenhouse gases, natural forcings, sulphate aerosols from anywhere but NA or EU, and other aerosol species.

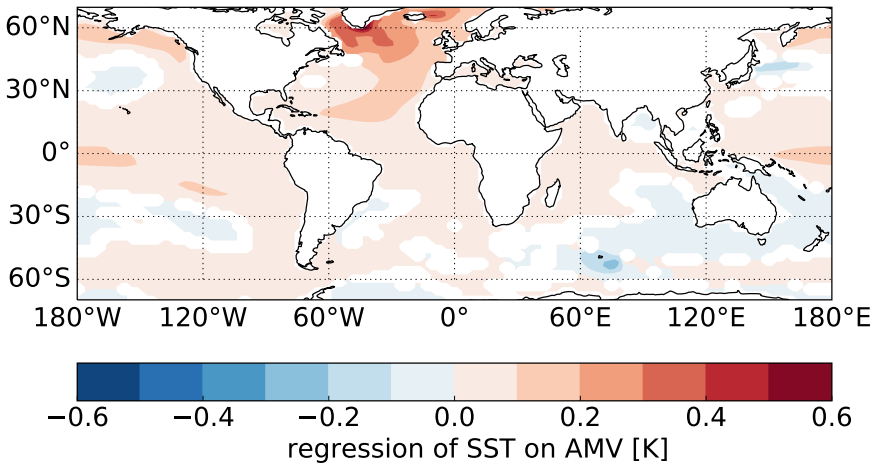

Figure C.3: Spatial AMV pattern in the pre-industrial control simulation, obtained by regressing SSTs on the standardised AMV index. The SSTs are 10-year Lanczos low-pass filtered and detrended prior to the analysis. Data is masked where $p \geq 0.1$.

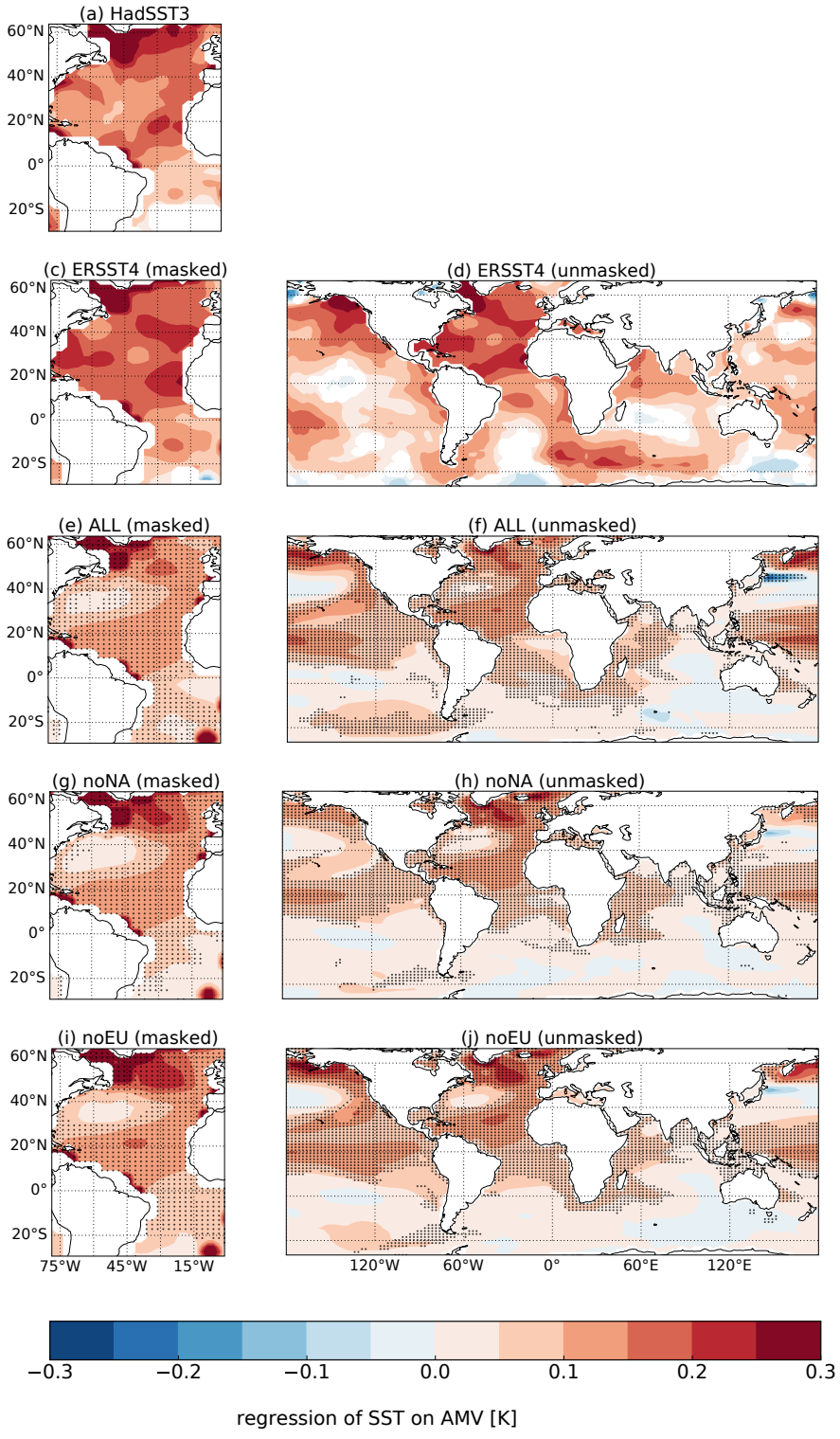

Figure C.4: Spatial AMV pattern as in Fig. C.3, but for the historical (1854-1980) period. for (a-d) observations and (e-j) simulations. In (a-d), data is masked where $p \geq 0.1$. In (e-j), stippling shows where all 8 ensemble members agree on sign. (Left) For ERSST4 and the model data, SSTs are regridded and masked to the coverage of HadSST3 before the analysis.

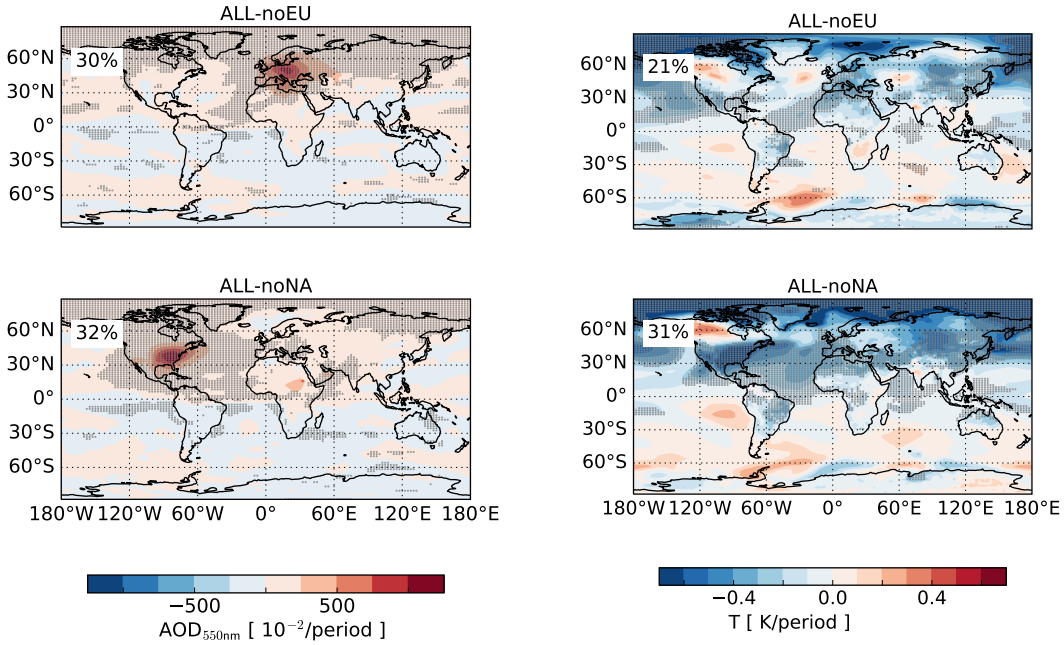

Figure C.5: Simulated long-term changes in (left) AOD and (right) near-surface temperature (T) in response to anthropogenic SO_2 emissions: Differences in the linear trends during 1850-1975 between the global aerosol ensemble (ALL) and the ensemble without (top) European emissions (noEU) and without (bottom) North American emissions (noNA). Stippling shows where differences between ALL and noEU/noNA are significant at the 5% level using a t-test. Numbers in the top left corner give the fraction of stippled points within the displayed area. (Right) The colourbar is cropped as to make the pattern better visible; minimum trends are up to 1.5 K/period.

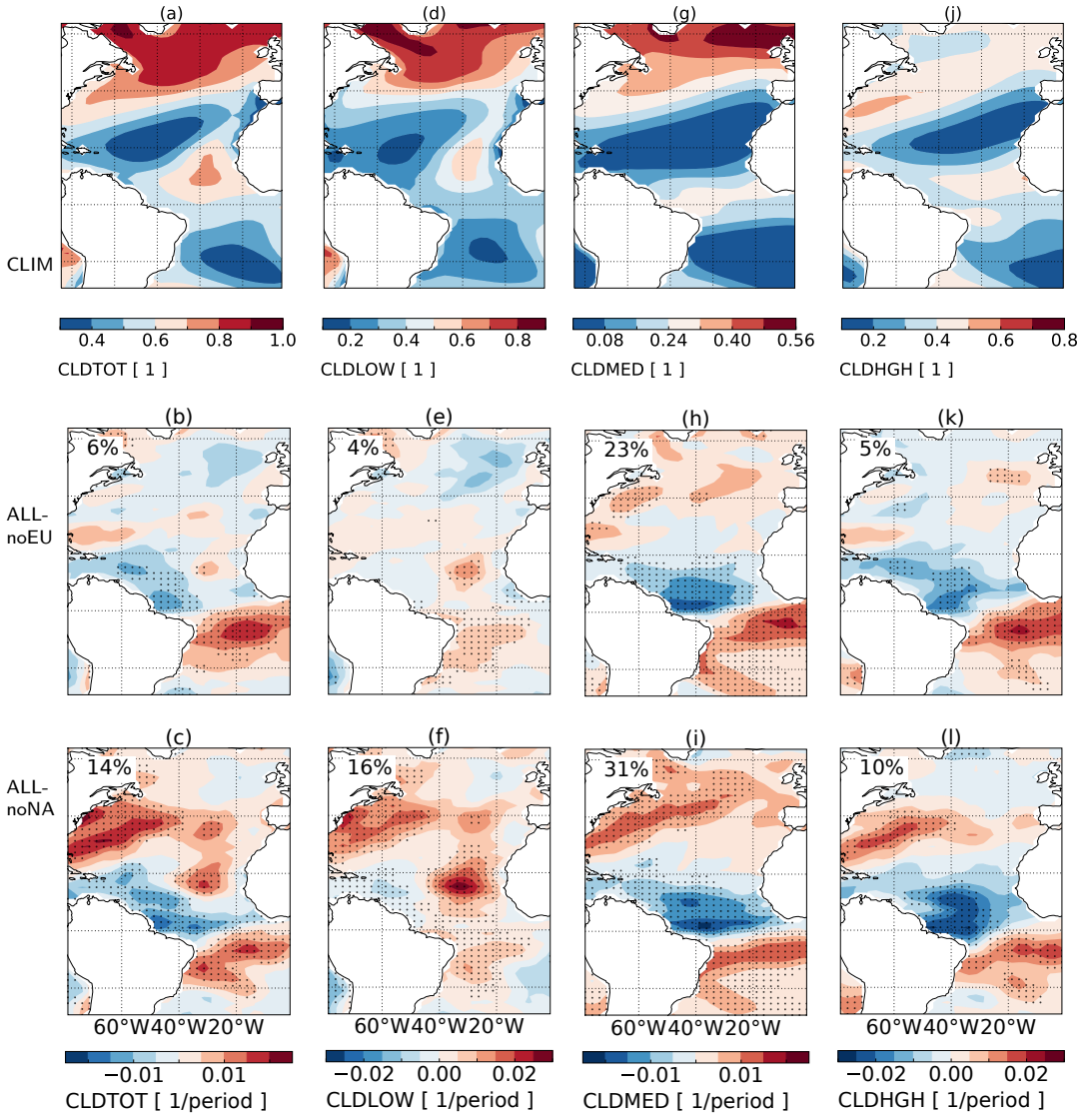

Figure C.6: Cloud cover (changes): (top) climatology from the pre-industrial control simulation and difference in the linear trends during 1850-1975 between ALL and (middle) noEU and (bottom) noNA for (a-c) total (CLDTOT), (d-f) low (CLDLOW), (g-i) mid-level (CLDMED), and (j-l) high (CLDHGH) cloud fraction. Stippling as in Fig. C.5.

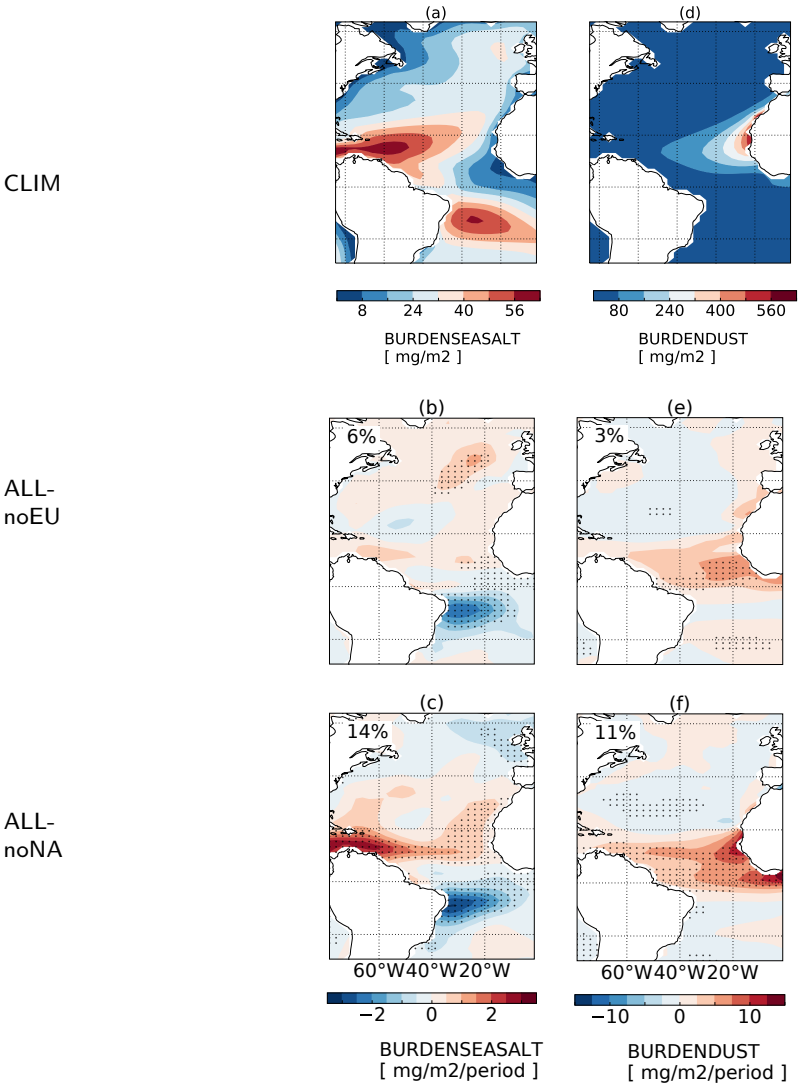

Figure C.7: Simulated changes in natural aerosol load: As Fig. C.6, but for (a-c) sea salt and (d-f) dust burden.

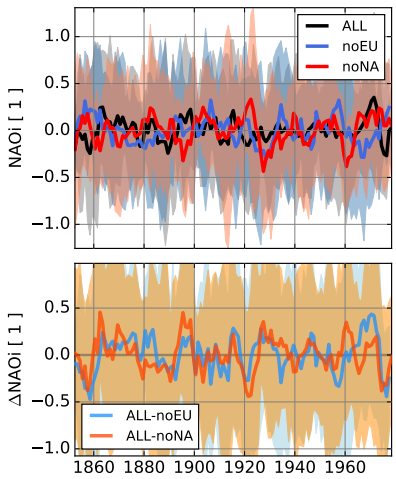

Figure C.8: Simulated North Atlantic Oscillation (NAO) index, calculated as principal component of the first Empirical Orthogonal Function (EOF) of December-March (DJFM) sea level pressure over [20°-80°N; 90°W-40°E] (*Hurrell*, 1995); colours and shading as in Fig. C.4.

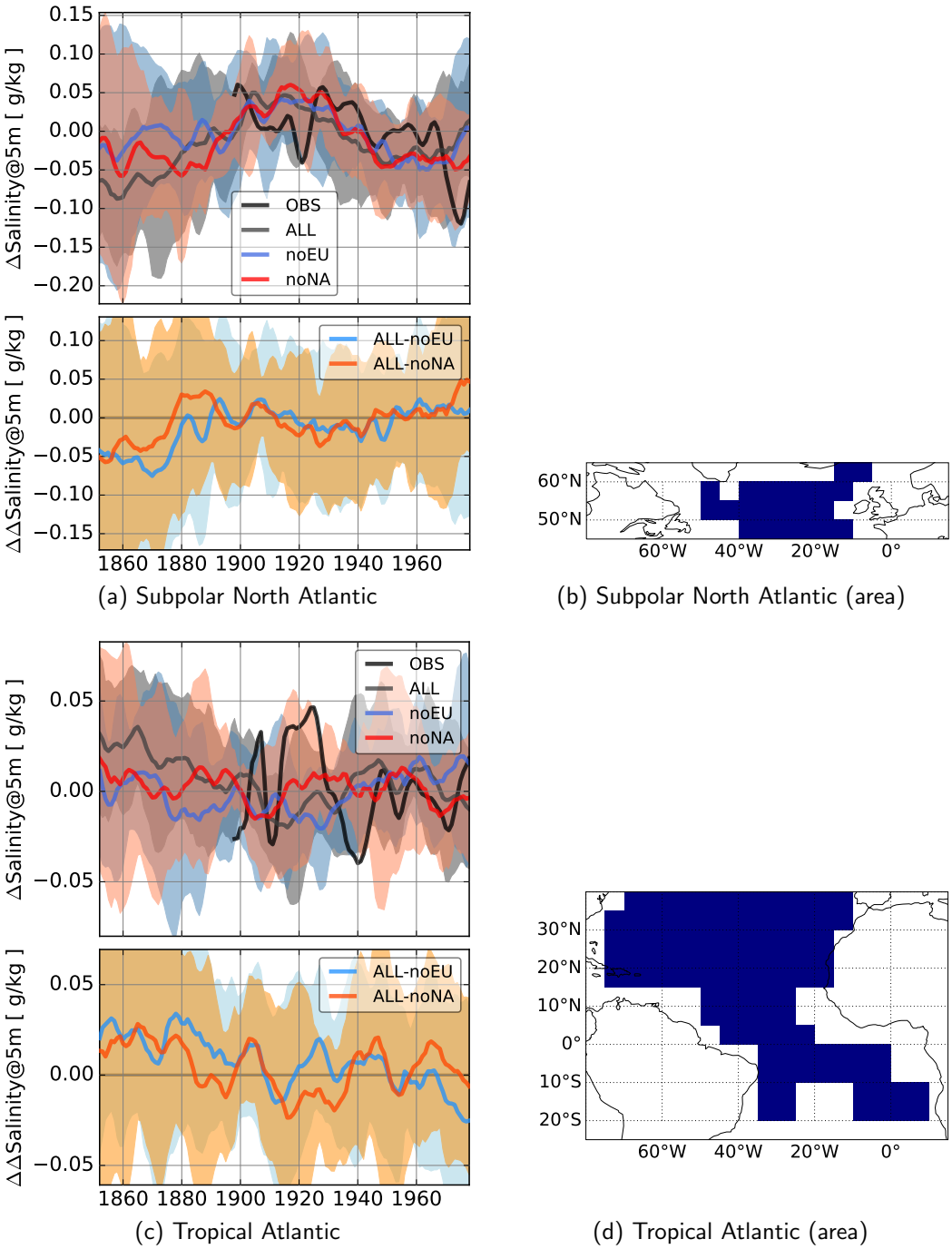

(a) Subpolar North Atlantic

(b) Subpolar North Atlantic (area)

(c) Tropical Atlantic

(d) Tropical Atlantic (area)

Figure C.9: Observed and simulated sea surface salinity area-averaged over the (a) subpolar North Atlantic area shown in (b), and (c) the tropical Atlantic area shown in (d). The model data is regridded and masked to the observational resolution and coverage, respectively. Anomalies with respect to 1896-1979 are shown. Colours and shading as in Fig. C.4, expect observations in black and ALL simulations in grey as in Fig. 4.1a. The observational dataset used is from *Friedman et al.* (2017).